

Flow control for oblique shock wave reflections

Giepman, Rogier

DOI

[10.4233/uuid:597489bb-0b41-4da2-8ec4-b1bc390f8d2c](https://doi.org/10.4233/uuid:597489bb-0b41-4da2-8ec4-b1bc390f8d2c)

Publication date

2016

Document Version

Final published version

Citation (APA)

Giepman, R. (2016). *Flow control for oblique shock wave reflections*. [Dissertation (TU Delft), Delft University of Technology]. <https://doi.org/10.4233/uuid:597489bb-0b41-4da2-8ec4-b1bc390f8d2c>

Important note

To cite this publication, please use the final published version (if applicable).
Please check the document version above.

Copyright

Other than for strictly personal use, it is not permitted to download, forward or distribute the text or part of it, without the consent of the author(s) and/or copyright holder(s), unless the work is under an open content license such as Creative Commons.

Takedown policy

Please contact us and provide details if you believe this document breaches copyrights.
We will remove access to the work immediately and investigate your claim.

FLOW CONTROL FOR OBLIQUE SHOCK WAVE REFLECTIONS

FLOW CONTROL FOR OBLIQUE SHOCK WAVE REFLECTIONS

Proefschrift

ter verkrijging van de graad van doctor
aan de Technische Universiteit Delft,
op gezag van de Rector Magnificus prof. ir. K.C.A.M. Luyben,
voorzitter van het College voor Promoties,
in het openbaar te verdedigen op 9 juni 2016 om 15:00 uur

door

Rogier Hendrikus Maria GIEPMAN

Ingenieur Luchtvaart- en Ruimtevaart,
Technische Universiteit Delft, Nederland
geboren te 's Gravenhage, Nederland

Dit proefschrift is goedgekeurd door de

Promotor: Prof. dr. F. Scarano
Copromotor: Dr. ir. B.W. van Oudheusden
Copromotor: Dr. ir. F.F.J. Schrijer

Samenstelling promotiecommissie:

Rector Magnificus,	voorzitter
Prof. dr. F. Scarano,	Technische Universiteit Delft
Dr. ir. B.W. van Oudheusden,	Technische Universiteit Delft
Dr. ir. F.F.J. Schrijer,	Technische Universiteit Delft

Onafhankelijke leden:

Prof. dr. H. Babinsky,	Cambridge University
Prof. dr. S. Hickel,	Technische Universiteit Delft
Dr. P. Dupont,	Institut Universitaire des Systèmes Thermiques Industriels
Dr. L.J. Souverein,	Airbus Defence and Space
Prof. dr. L.L.M. Veldhuis,	Technische Universiteit Delft, reservelid



This project has received funding from the European Union's Seventh Framework Programme for research, technological development and demonstration under grant agreement no. 265455.

Keywords: Shock waves, boundary layers, flow control, transition, separation, supersonic flows

Printed by: Sieca Repro Delft

Front & Back: A series of schlieren visualizations showing the start-up process of a supersonic wind tunnel

Copyright © 2016 by R.H.M. Giepman

ISBN 978-94-6186-679-0

An electronic version of this dissertation is available at
<http://repository.tudelft.nl/>.

SUMMARY

Shock wave-boundary layer interactions are prevalent in many aerospace applications that involve transonic or supersonic flows. Such interactions may lead to boundary layer separation, flow unsteadiness and substantial losses in the total pressure. Flow control techniques can help to mitigate these adverse effects and stabilize the interaction. This thesis focuses on passive flow control techniques for oblique shock wave reflections on flat plates and presents experimental results for both laminar (part I) and turbulent interactions (part II). Particle image velocimetry (PIV) measurements were used as the main flow diagnostics tool throughout this thesis, where especially the laminar case proved to be challenging due to its very small boundary layer thickness of ~ 0.2 mm.

Laminar boundary layers are extremely prone to separation and long separation bubbles ($\sim 50\delta_{99}$) were recorded even for relatively weak shock waves ($p_3/p_1 \sim 1.2$). The bubble has a flat / triangular shape and extends mostly upstream of the incident shock wave. The incoming boundary layer is lifted over the bubble and remains in an apparent quasi-laminar state up to the incident shock wave, after which the boundary layer quickly transition into a turbulent state ($30-40\delta_{99}$). Only for very weak shock waves it was found that the boundary layer can remain laminar up to reattachment.

The separation bubble for laminar interactions can be removed by enforcing boundary layer transition a short distance upstream of the interaction. Transition strips that introduce three-dimensional features in the flow were found to be more effective at this task than purely two-dimensional trips (e.g. a step) and could therefore be placed closer to the interaction while still maintaining their effectiveness. Forced boundary layer transition, however, comes at the price of having a substantially thicker ($\sim 50\%$) turbulent boundary layer downstream of the interaction, which is the result of losses at the trip, a larger portion of turbulent flow and higher shock-induced losses. It therefore appears that there is no added value to tripping the boundary layer for laminar flat plate interactions, especially given the fact that the untripped laminar interaction shows no signs of any large-scale type of unsteadiness.

For the turbulent interactions, micro-ramp vortex generators were studied as flow control devices. Micro-ramps transport high-momentum fluid towards the near-wall region of the flow by the action of streamwise vortices, thus creating a fuller boundary layer profile that is less prone to separation. A net transport of streamwise momentum has been observed up to $5-7\delta_{99}$ downstream of the micro-ramp, after which a plateau level is reached in which, on average, no momentum is added or removed from the near-wall region of the flow. Consequently, a similar distance between the trailing edge of the micro-ramp and the onset of the interaction is required to ensure a maximum reduction in separation bubble size and shock unsteadiness. The application of micro-ramps leads to a spanwise modulation of the separation bubble, with the micro-ramp being most effective along its centreline. The control effectiveness of the micro-ramp is virtually independent of the Reynolds number and is slightly reduced for higher Mach numbers.

SAMENVATTING

Schokgolf-grenslaag interacties komen veel voor in lucht- en ruimtevaart toepassingen waarbij sprake is van transsonen dan wel supersonen snelheden. Dergelijke interacties kunnen leiden tot een loslating van de grenslaag, stromingsinstabiliteiten en verliezen in de totale druk. Stromingscontrole technieken kunnen helpen om deze negatieve effecten te beperken. Deze thesis bespreekt passieve stromingscontrole technieken voor schuine schokgolf reflecties op een vlakke plaat, waarbij zowel laminaire (deel I) als turbulente interacties (deel II) zijn bestudeerd. Particle image velocimetry metingen dienden als belangrijkste meettechniek in deze thesis, waarbij vooral de laminaire interactie uitdagend was door de zeer geringe grenslaagdikte van ~ 0.2 mm.

Laminaire grenslagen zijn extreem gevoelig voor loslating en lange loslatingsbubbels ($\sim 50\delta_{99}$) zijn waargenomen zelfs voor vrij zwakke schokgolven ($p_3/p_1 \sim 1.2$). De bubbel heeft een vlakke / driehoekige vorm en strekt zich vooral uit in stroomopwaartse richting van de schokgolf. De inkomende grenslaag wordt over de loslatingsbubbel heen getild en blijft in een quasi-laminaire staat tot aan de impact locatie van de inkomende schokgolf, waarna de grenslaag snel omslaat ($30-40\delta_{99}$) en een turbulente staat bereikt. Enkel voor zeer zwakke schokgolven is een volledig laminaire interactie waargenomen.

De loslatingsbubbel kan geëlimineerd worden door de grenslaag geforceerd om te laten slaan enige afstand voor de inkomende schokgolf. Transitie-elementen die driedimensionale structuren in de stroming introduceren presteerden hierin beter dan tweedimensionale elementen (zoals een 2D stap) en konden zodoende dichter op de interactie geplaatst worden zonder hun effectiviteit te verliezen. Het forceren van transitie zorgt echter wel voor een dikkere ($\sim 50\%$) turbulente grenslaag stroomafwaarts van de interactie. Deze waarneming kan teruggeleid worden op verliezen in de directe nabijheid van het transitie-element, de eerdere omslag van de grenslaag en schok geïnduceerde verliezen. Het forceren van grenslaag transitie heeft daarom weinig toegevoegde voor laminaire interacties op een vlakke plaat, vooral ook omdat de laminaire interactie geen tekenen van grootschalige instabiliteit vertoont.

Micro-ramp wervel generatoren zijn gebruikt als stromingscontrole elementen voor turbulente schuine schokgolf grenslaag interacties. Deze elementen introduceren wervels in de stromingsrichting, waardoor hoog impulsieve lucht naar de wand wordt getransporteerd. Een netto transport van impuls is waargenomen tot $5-7\delta_{99}$ achter de micro-ramp, waarna een plateau wordt bereikt waarin, gemiddeld genomen, geen impuls wordt toegevoegd of weggenomen uit de grenslaag vlak aan de wand. Een vergelijkbare afstand is daarom nodig tussen de achterzijde van de micro-ramp en het begin van de schokgolf grenslaag interactie, om zodoende een maximale reductie in loslatingsbubbelgrootte en schokinstabiliteit te bewerkstelligen. Micro-ramps introduceren een spanwijze modulatie in de bubbel, waarbij de beste resultaten zijn geregistreerd in het symmetrievlak van de micro-ramp. De effectiviteit van de micro-ramp is vrijwel onafhankelijk van het Reynolds getal en neemt lichtelijk af voor hogere Mach getallen.

CONTENTS

Summary	v
Samenvatting	vii
1 Introduction	1
1.1 Historical background	1
1.2 Shock wave-boundary layer interactions in the engineering practice	5
1.3 Laminar oblique shock wave reflections	9
1.4 Turbulent oblique shock wave reflections	11
1.5 Flow control for oblique shock wave reflections	17
1.6 Thesis objectives	30
1.6.1 Flow control for laminar oblique shock wave reflections	30
1.6.2 Flow control for turbulent oblique shock wave reflections	31
1.7 Thesis outline	31
2 Experimental methods	33
2.1 Schlieren visualizations	33
2.2 Oil-flow visualizations	35
2.3 Infrared thermography measurements	36
2.3.1 Equipment and calibration	36
2.3.2 Data reduction	37
2.4 Hot wire anemometry measurements	39
2.4.1 Energy balance	39
2.4.2 Operating modes	41
2.4.3 Linear modal analysis and static calibration	42
2.4.4 Dynamic calibration	43
2.4.5 Data reduction	45
2.5 Particle image velocimetry	47
2.5.1 Flow seeding	47
2.5.2 Particle imaging	50
2.5.3 Data reduction	51
I Flow control for laminar and transitional oblique shock wave reflections	55
3 Experimental setup and data reduction techniques	57
3.1 Flow facility	58
3.2 Wind tunnel models	60
3.3 PIV arrangement	60
3.4 Pre-processing the PIV data	63
3.4.1 Correction for fixed-pattern camera read-out noise	63

3.4.2	Correction for plate vibrations	63
3.4.3	Normalization of particle intensities	64
3.5	Processing the PIV data	64
3.6	Uncertainty analysis	66
3.6.1	Particle slip and shock smearing	66
3.6.2	Aero-optical distortions	66
3.6.3	Cross-correlation errors	67
3.6.4	Uncertainties on the measured reversed flow height	68
3.6.5	Uncertainties on the shape factor development	70
4	Boundary layer study	71
4.1	Oil-flow visualization	71
4.2	Spark-light schlieren visualizations	72
4.3	Particle image velocimetry	72
4.4	Infrared thermography	79
4.5	Comparison of techniques	85
5	Oblique shock wave reflections under natural transition conditions	87
5.1	Laminar, transitional and turbulent interactions	87
5.1.1	Oil-flow visualizations	88
5.1.2	Schlieren visualizations	88
5.1.3	Particle image velocimetry	89
5.2	Flow deflection angle, Mach and Reynolds number effects	94
5.2.1	Interpretation of the velocity fields.	96
5.2.2	The connection between boundary layer separation and transition	97
5.2.3	The applicability of the free-interaction theory	104
5.3	A note on the unsteadiness of laminar interactions	106
5.4	Conclusions.	108
6	Oblique shock wave reflections under forced transition conditions	111
6.1	Transition control devices.	112
6.2	PIV camera configuration	113
6.3	Study of transition control devices	114
6.4	The effects of forced transition on an oblique shock wave reflection	116
6.5	Conclusions.	121
II	Flow control for turbulent oblique shock wave reflections	127
7	New insights in the flow topology of micro-ramp vortex generators	129
7.1	The absence / presence of a leading-edge horseshoe vortex	131
7.1.1	Experimental arrangement	132
7.1.2	Results	132
7.2	Schlieren visualizations of Kelvin-Helmholtz vortex shedding	134

8	Micro-ramp flow control	141
8.1	Experimental arrangement	141
8.1.1	Flow facility	141
8.1.2	Micro-ramp configurations and experimental matrices	142
8.1.3	PIV arrangement	144
8.1.4	Uncertainty analysis	145
8.2	Results	146
8.2.1	Assessment of the undisturbed boundary layer	146
8.2.2	Effects of the micro-ramp on the interaction region	147
8.2.3	Interaction control mechanism	152
8.3	Conclusions.	156
9	Mach and Reynolds number effects	159
9.1	Experimental setup	159
9.1.1	Test matrix.	159
9.1.2	PIV setup.	160
9.2	Data reduction	161
9.2.1	PIV processing	162
9.2.2	Vortex modelling.	162
9.2.3	PIV uncertainty analysis	163
9.3	Undisturbed boundary layer measurements	164
9.4	Results	165
9.4.1	Schlieren and oil-flow visualizations	166
9.4.2	PIV results	170
9.4.3	Comparison with other studies	173
9.5	Conclusions.	174
10	Conclusions	185
10.1	Flow control for laminar oblique shock wave reflections	185
10.2	Flow control for turbulent oblique shock wave reflections	190
11	Recommendations	193
11.1	The unsteadiness of laminar oblique shock wave reflections	193
11.2	A synthesis of all flat plate TFAST data	194
11.3	Kelvin-Helmholtz vortex formation downstream of micro-ramps.	194
11.4	A 3D visualization of a micro-ramp controlled interaction	195
11.5	Total pressure measurements of a micro-ramp controlled interaction	195
11.6	Variations on the micro-ramp geometry	195
A	PIV wall treatment	197
	References	199
	Acknowledgements	209
	List of publications	213
	Biographical note	217

1

INTRODUCTION

1.1. HISTORICAL BACKGROUND

Research on high-speed flows started with the basic observation that sound takes a finite amount of time to travel from one location to the next. Although mankind was aware of this phenomenon since the stone age, Isaac Newton was the first to systematically investigate the speed of sound by analysing artillery test data and formulating a theory around the propagation of sound waves. He described this theory as part of his world-changing *Principia Mathematica* in 1687. The speed of sound that followed from Newton's theory was, however, systematically 15% lower than the values measured during the artillery tests. At the time, Newton could not find a proper explanation for this discrepancy and assumed that it was due to dust particles present in the air. It was not until Laplace (1816), more than one century later, that the error in Newton's theory was found. Newton incorrectly assumed the propagation of sound waves to be an isothermal process instead of being an adiabatic process. Laplace corrected this mistake and finally experimental data and theory were found to be in good agreement.

The work on compressible flows continued in the 19th century, although mostly from a mathematical point of view. Rankine (1870) and Hugoniot (1887) independently derived the equations describing the change in flow properties over a normal shock wave. It was, however, not until half way the 20th century that their mathematical model could be validated against experimental wind tunnel data. Their work is still being used in today's engineering practice, where the equations governing the flow across a normal shock wave are called the Rankine-Hugoniot equations, in honour of these two pioneering scientists.

The first convincing experimental evidence of shock waves came from the work of Mach (1887), who performed for the very first time shadowgraphy measurements on a bullet travelling at supersonic speeds. This classical image is presented in Fig.1.1 and provided a wealth of information for researchers at that time. A bow shock is present at the leading edge of the bullet and further downstream expansion waves can be distinguished at the bullet's expansion corner. Shock waves are formed at the trailing edge of

the bullet to again realign the flow and a clear turbulent wake is formed downstream of the bullet.

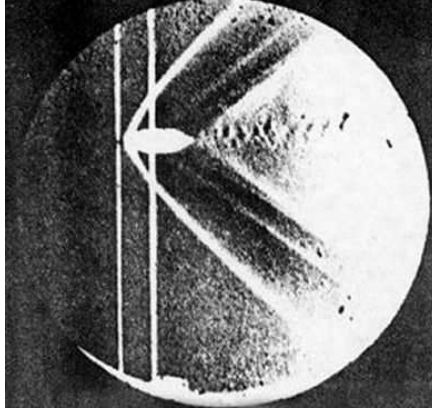


Figure 1.1: Shadowgraph of a bullet flying at supersonic speed, imaged by Mach (1887)

It was not long after the work of Ernst Mach that a second major discovery was made in the field of fluid dynamics. This time it was the discovery of the boundary layer by German physicist Ludwig Prandtl in 1904. The boundary layer concept divides the flow around a body in two parts: 1) a thin layer of fluid in the direct vicinity of the body where viscous effects play an important role and 2) an outer flow where viscous effects can be neglected. This idea provided a major simplification compared to the full Navier-Stokes equations and also provided answers to many yet poorly understood flow phenomena, such as flow reversal and the lift / drag distributions of airfoils.

However, at that time no one could imagine the interaction between these two recently discovered phenomena: shock waves and boundary layers. The first evidence for such interactions to exist came from World War I airplanes. The airplanes itself at that time were still flying in the low subsonic regime, but the propellers that were used could under some conditions reach transonic or locally supersonic speeds at the tips. It was noticed by pilots that there would be a sudden drop in propeller performance when operating them at high rotational speeds. After World War I this was also confirmed by the lab experiments of Caldwell and Fales (1921) for a range of different airfoils. They noticed a significant drop in lift and a rise in airfoil drag when passing a certain 'critical speed'. The physical explanation for this critical speed was, however, still missing.

In the 1930's it became a top priority at NACA to better understand compressible flows and the problems encountered by airplanes at high speed. A young NACA engineer, John Stack, led the way on high-speed flight and shock wave-boundary layer research in those early days. Fig.1.2 shows one of the first schlieren visualization of a shock wave-boundary layer interaction on a transonic airfoil, when operated above the critical speed. It was realized by Stack (1933) that shock waves were responsible for the sudden change in airfoil characteristics when passing the critical speed (see Fig.1.3). The adverse pressure gradient induced by the normal shock wave would separate the incoming boundary layer (see Fig.1.4), thus reducing the lift production of the airfoil and increasing its pres-

sure drag. Also the centre of pressure was found to shift downstream substantially when operating the airfoil beyond the critical Mach number.

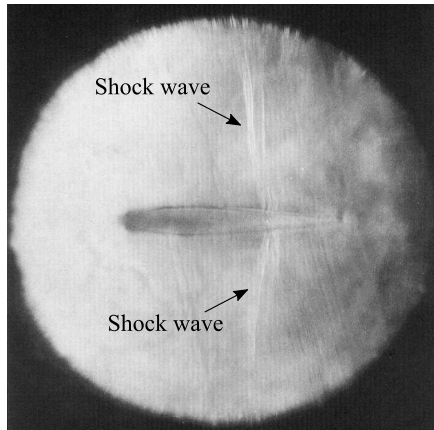


Figure 1.2: Schlieren photograph of the air flow over a NACA 0012 airfoil, when operated above the critical speed. The image was acquired by John Stack in 1934 and modified from the work of Anderson (1999)

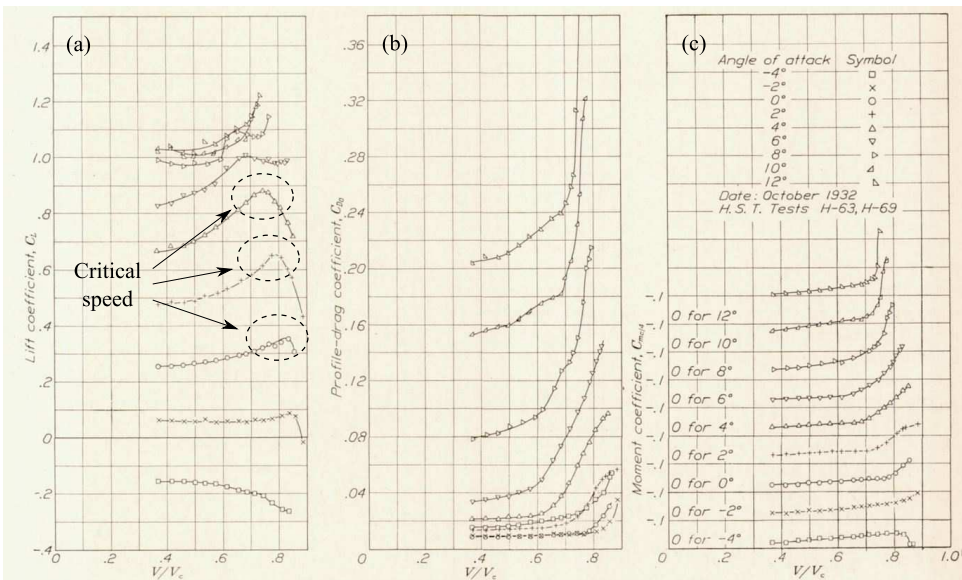


Figure 1.3: Aerodynamic characteristics of the 3C6 airfoil, showing the lift-coefficient (a), drag-coefficient (b) and moment-coefficient (c). The flow speed V on the horizontal axis is normalized with the speed of sound V_c , thus effectively showing the Mach number M . The picture was modified from the work of Stack (1933).

The potential dangers of shock wave-boundary layer interactions during in-flight situations were experienced first-hand by German Luftwaffe pilot Guido Mutke. Although not validated, Mutke was probably the first pilot to break the sound barrier during a steep

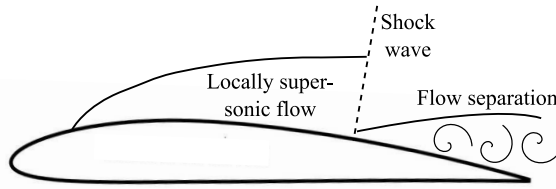


Figure 1.4: A schematic representation of the flow field over a transonic airfoil operated above the critical speed.

dive with his Messerschmitt Me-262 airplane in the year 1945. Mutke reported that his speedometer was stuck against its limit of 1100 km/h, with a speed of sound of ~ 1060 km/h at an altitude of 12 km. The airplane was shaking violently during the dive and Mutke temporarily lost control of his airplane. Mutke was trying to pitch up his airplane, but the elevator flaps were not providing him with any control authority. To regain control of his airplane he therefore decided to take advantage of one of the Messerschmitt's special features: a fully movable horizontal tail plane. By changing the incidence angle of the entire horizontal tail plane he was able to again pitch up and reduce the speed of his airplane.

The loss of control authority can be traced back to the occurrence of shock wave-boundary layer interactions on the wings and horizontal tail plane. These interactions can lead to a sudden shift in the centre of pressure (see also Fig.1.3(c)), therefore drastically changing the stability characteristics of the airplane. The movable horizontal tail plane proved to be of life-saving quality and was later also implemented in the design of the Bell X-1 airplane, which was used by Chuck Yeager in 1947 to reach supersonic speeds, for the first time, during horizontal flight conditions.

In the late 1940's most aerospace engineers were aware of the dangers of shock wave-boundary layer interactions and systematic studies were performed on transonic wings, oblique shock wave reflections, compression surfaces, axi-symmetric bodies and several other configurations. These experiments provided a wealth of information and also formed the basis of the celebrated free-interaction theory by Chapman et al. (1957). The free-interaction theory states that the first part of the interaction should only depend on upstream flow properties and not on the downstream flow conditions. The initial pressure rise through the interaction should therefore, in principle, be independent of the shock strength and the type of interaction (e.g. oblique shock wave reflection or compression corner).

Experimentalists in the 1950's mostly focused on the mean flow properties of shock wave-boundary layer interactions. The unsteady aspects could not be resolved with the technology available at that time and shock wave-boundary layer interactions were typically thought of as stable phenomena with very little shock unsteadiness (Chapman et al. (1957)). This turned out to be incorrect and in the 1960's, with the advancements in high-speed pressure transducers and data acquisition systems, it became possible to also study the unsteady properties of shock wave-boundary layer interactions. Kistler (1964) found that the turbulent shock-separation bubble system displays some low-frequency

(0.1 - 1 kHz) large amplitude oscillations over time; low-frequency in the sense that the recorded frequencies are approximately two orders of magnitude smaller than those encountered in the incoming turbulent boundary layer ($\sim U/\delta_{99}$). The low-frequency shock motion can interact with the eigenmotion of structural elements, potentially leading to aero-structural fatigue and an early failure of the particular component (Clemens and Narayanaswamy (2014)).

Therefore, in recent decades there has been made a tremendous effort by the research community to better understand turbulent SWBLI unsteadiness. This development has been aided by major advancements in both experimental and numerical techniques, with the latest evidence suggesting that for large separation bubbles the process is mostly driven by downstream instabilities, whereas for smaller separation bubbles it is affected by upstream disturbances (Clemens and Narayanaswamy (2014)). A more elaborate description of shock wave-boundary layer unsteadiness is provided in section 1.4.

From this brief historical perspective it is clear that shock wave-boundary layer interactions can have a major impact on the performance of transonic and supersonic flight vehicles. Flow control devices are therefore crucial for ensuring the safe and efficient operation of engines, airplanes or rockets under transonic or supersonic conditions. A summary of recent flow control efforts for SWBLIs is provided in section 1.5. This thesis builds further on this work by analysing a range of flow control devices for laminar, transitional and turbulent oblique shock wave reflections. A full outline of the objectives of this thesis is provided in section 1.6.

1.2. SHOCK WAVE-BOUNDARY LAYER INTERACTIONS IN THE ENGINEERING PRACTICE

Shock wave-boundary layer interactions can be encountered in a wide range of applications relevant to the high-speed flight regime, such as transonic wings (see the previous section), compressor and turbine blades of turbomachinery (Figs.1.5-1.6) and in supersonic jet intakes (Fig.1.7). This section provides a short description of the last three applications and highlights how shock wave-boundary layer interactions impact the design choices of engineers.

Fig.1.5(a) shows a Schlieren visualization of the transonic compressor cascade tunnel at the DLR in Cologne (Germany). The inlet Mach number was set to 1.09 and the stage pressure ratio to 1.45 (Weber et al. (2002)). The supersonic inflow conditions lead to the formation of a near-normal shock wave at the leading edge of each blade. This shock wave impinges on the lower blade at an approximately half-chord location. Since the flow is accelerated over the blade, relatively high Mach numbers of ~ 1.4 are recorded directly upstream of the shock wave (see Fig.1.5(b)). The shock separates the laminar incoming boundary layer and a separation bubble is formed that extends over approximately 20% of the chord length.

Boundary layer separation is typically hard to avoid in the compressor environment, which is characterized by strong adverse pressure gradients. A high pressure ratio per stage is desirable, since it limits the number of stages required to reach the operating pressure of the combustion chamber, thereby reducing both the size and the weight of an engine. On the other hand, the larger the pressure ratio per stage, the harder it becomes

to avoid the formation of large shock-induced separation bubbles. In general, such large separation regions are to be avoided, because of their associated total pressure losses and high levels of flow unsteadiness (Dolling (2001)). It is therefore often necessary to make a trade-off between the compactness and the efficiency of an engine. Of course, this is just one of the many trade-offs that turbomachinery experts are faced with.

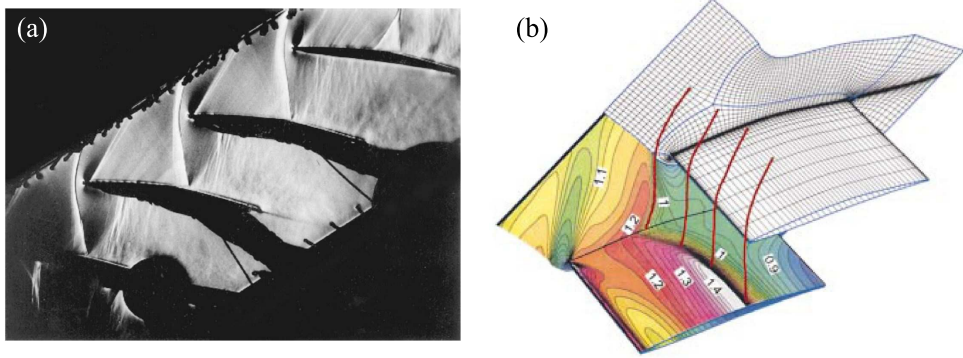


Figure 1.5: A schlieren visualization of a transonic compressor cascade operated at $M_{\infty} = 1.09$ (a) and the results of a numerical simulation for the same configuration with DLR's Navier-Stokes code TRACE (b). Images were taken from the work of Weber et al. (2002)

Fig.1.6 shows a schlieren visualization of a turbine cascade that was tested at DLR's rectilinear cascade wind tunnel in Göttingen (Graham and Kost (1979)). The exit Mach number was set to a low supersonic value of $M = 1.15$ and the inlet angle with respect to the horizontal was set to 60 degrees. The supersonic exit speed leads to the formation of oblique shock waves at the trailing edge of the turbine blades. These shock waves impinge on the neighbouring turbine blade and result in the formation of a substantial separation bubble. The bubble itself cannot be observed from the schlieren visualizations, but its impact on the overall flow field is clearly visible. The black lines mark the separation and reattachment shock waves and the vague white region marks an expansion fan that emanates from the top of the separation bubble (see also the topological discussion of oblique shock wave reflections in section 1.3). The trailing edge shocks become stronger with increasing Mach numbers and larger separation bubbles are observed. Consequently, Graham and Kost (1979) found that total pressure losses can increase by $\sim 50\%$ for the tested blade profiles when changing the exit Mach number from 1 to 1.4.

Blade cooling is another factor that needs to be taken into account when analysing the performance of turbine blades. Due to the high thermal loading of the turbine blade it is often necessary to apply some type of film cooling. The injection of cold air has a stabilizing effect on the boundary layer that develops over the turbine blade. Laminar boundary layer interactions are therefore more likely to occur and large separation bubbles may result because of that (Janke and Wolf (2010)).

Finally, Fig.1.7(a) shows a bi-cone, mixed-compression, axi-symmetric inlet, which was designed by NASA (Wasserbauer et al. (1975)) to be used on the TF30-P-3 turbofan engine (used on the F111 Aardvark jet fighter). The inlet is of a mixed-compression type,

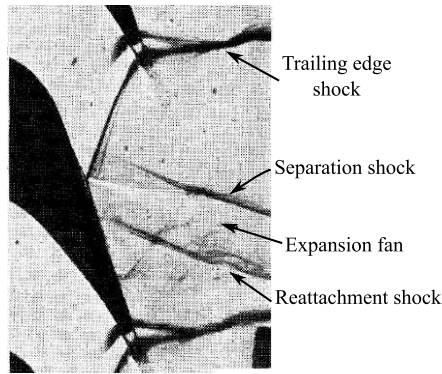


Figure 1.6: Schlieren visualization over a turbine blade for an exit Mach number of 1.15. Image was modified from the work of Graham and Kost (1979).

which implies that supersonic compression is achieved both internally (downstream of the cowl lip) and externally (upstream of the cowl lip). The bi-cone configuration allows for a supersonic compression of the incoming flow by means of two oblique shock waves. The angle of the second cone can be varied, as such allowing for a variation in the contraction ratio of the inlet. The two oblique shock waves impinge on the leading edge of the cowl and a further compression is achieved by means of isentropic compression waves formed at the smoothly curved surface of the cowl. A weak normal shock wave is formed at the throat of the inlet and further subsonic compression is obtained by means of a smoothly diverging channel.

Multiple shock wave-boundary layer interactions are encountered throughout the supersonic inlet. A compression corner is formed on the vertex between the first and second cone of the inlet. Boundary layer separation may occur at this location, depending upon the state of the boundary layer (i.e. laminar / turbulent) and the strength of the oblique shock wave (i.e. the relative flow deflection angle between both cones). Further downstream we find the interaction between an axi-symmetric boundary layer and oblique shock waves / isentropic compression waves. Finally, an interaction between a normal shock wave and a boundary layer is recorded in the throat of the inlet.

To ensure the safe and efficient operation of the inlet it is usually necessary to apply flow control techniques to counter the potential adverse consequences of separated shock wave-boundary layer interactions. For the inlet of Fig.1.7(a) use was made of both boundary layer bleed and vortex generators. Boundary layer bleed is applied on the center-body cone only, close to the impingement location of the normal shock wave on the surface. Bleeding slots are provided, which remove the low-momentum part of the boundary layer and as such reduce the extent of the separation bubble. The vortex generators (half a NACA-0012 airfoil) were installed both on the inlet's centre-body and on the cowl's inner surface. The purpose of these devices is to re-energize the boundary layer by transporting high momentum fluid from within the freestream towards the wall. This leads to a fuller turbulent boundary layer, which is less prone to separation.

The effects of boundary layer bleed are clearly demonstrated in Fig.1.7(b), which shows the total pressure recovery ratio p_5/p_0 over the inlet for a range of bleed mass

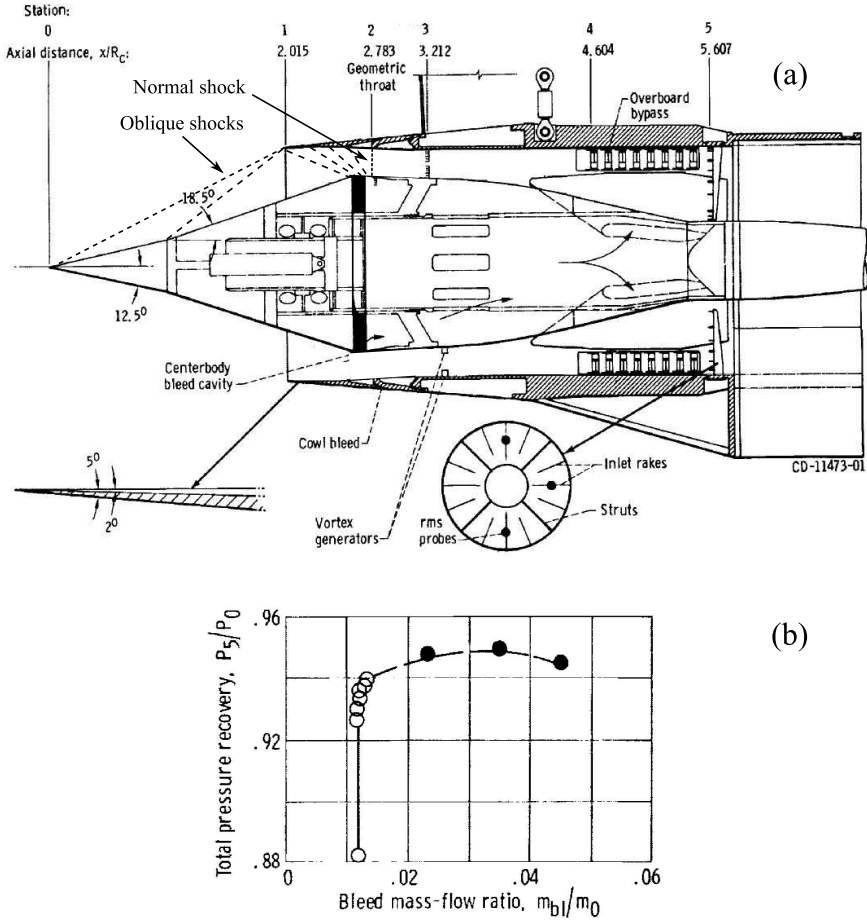


Figure 1.7: A detailed drawing of a mixed-compression supersonic jet inlet (a) and the total pressure recovery over the inlet as a function of bleed mass flow ratio (b). Images were modified from the work of Wasserbauer et al. (1975).

flow ratios m_{bl}/m_0 . At least 1.4% of the capture mass flow m_0 should be bled from the inlet to achieve a satisfactory total pressure recovery ratio of 0.95. A strong decrease in the total pressure recovery ratio can be observed for lower bleeding ratios ($p_5/p_0 = 0.88$ for $m_{bl}/m_0 = 1.2\%$).

Boundary layer bleed furthermore has a very pronounced effect on the stability margin of the inlet. The results of Fig.1.7(b) were obtained for a zero incidence angle of the inlet and a Mach number of 2.0. Results may vary significantly when altering one of these parameters and the inlet might unstart under certain conditions. Wasserbauer et al. (1975) reported that the unstart incidence angle is 2.55° for a bleed mass flow ratio of $m_{bl}/m_0 = 2\%$ and an operating Mach number of 2.5. This angle can be increased to 6.85° by increasing the bleed mass flow ratio to 5%. Boundary layer bleed therefore not

only impacts the efficiency of the inlet, but also its stability margin.

The goal of this thesis is not to simulate the flow throughout an entire engine or over a row of compressor / turbine blades. Instead it will focus on describing the details of laminar and turbulent oblique shock wave reflections and investigating the potential benefits and limitations that flow control devices may pose in this respect. The next sections will cover in more detail the topology of laminar / turbulent oblique shock wave reflections (sections 1.3 and 1.4) and the topic of flow control (section 1.5).

1.3. LAMINAR OBLIQUE SHOCK WAVE REFLECTIONS

Laminar boundary layers are more prone to separation than turbulent boundary layers (White (2005)) and even weak shock waves (flow deflection angles of $\theta \approx 1^\circ - 2^\circ$) can already result in the formation of a large separation bubble. Gadd et al. (1954), Hakkinen et al. (1959) and Chapman et al. (1957) were among the first workers to experimentally investigate laminar oblique shock wave reflections. Their work provided a wealth of data and insight into the topology of such interactions. Fig.1.8 has been derived from the work of Hakkinen et al. (1959) and presents the flow field typically encountered for laminar oblique shock wave reflections.

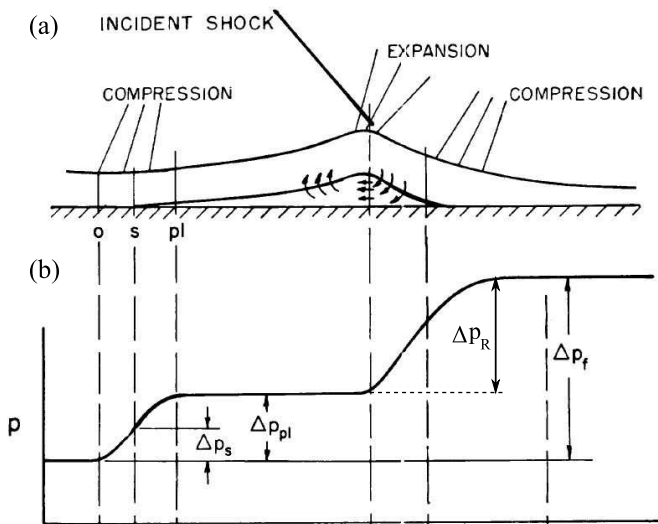


Figure 1.8: A sketch of the typical flow field encountered for laminar oblique shock wave reflections (a) and the corresponding pressure distribution (b). The images were modified from the work of Hakkinen et al. (1959).

The incident shock wave imposes a strong adverse pressure gradient on the flow and this information is communicated upstream via the subsonic channel of the incoming laminar boundary layer. This pressure rise leads to a thickening of the subsonic channel, which in itself again leads to the formation of a series of compression waves. The compression waves induce an adverse pressure gradient on the boundary layer, which leads to a further dilatation of the subsonic channel. So, clearly there is a mutual interaction between the viscous boundary layer and the inviscid freestream. At some mo-

ment though a balance will be obtained between the pressure rise in the freestream and the frictional effects in the thickening boundary layer. This process can be described as a free-interaction process (Chapman et al. (1957)) and is completely independent of downstream flow properties (e.g. shock strength, interaction type).

As a consequence of this free interaction concept, a stronger incident shock wave will not affect the plateau pressure, but it will lead to a higher pressure rise at reattachment, which necessitates the formation of a longer pressure plateau. The longer the pressure plateau, the more momentum will be present on the dividing streamline (the streamline connecting the separation and reattachment point) and the more capable the boundary layer will be to overcome the pressure rise at reattachment Δp_R . If one neglects the effects of compressibility and approaches the problem from an incompressible Bernoulli type of perspective (a major simplification), then one can write down the following condition for the dividing streamline (see also Babinsky and Harvey (2011)):

$$\Delta p_R = 0.5\rho V_{div}^2 \quad (1.1)$$

Here V_{div} is the velocity along the dividing streamline. Starting from the separation point, V_{div} is found to increase gradually when moving in the downstream direction. Reattachment sets in (approximately) when V_{div} satisfies the condition given by Eq.1.1.

The laminar interaction of Fig.1.8 displays a long and flat separation bubble with a near-triangular type of shape. The incident shock wave reflects from the top of the separation bubble as a centred expansion fan which turns the flow towards the wall. At reattachment a series of compression waves is formed to again realign the flow with the wall. The laminar boundary layer during this process is lifted over the bubble and typically remains in a laminar state up to the incident shock wave (Hakkinen et al. (1959)), after which transition sets in (see also chapter 5).

However, for weak shock waves and low Reynolds numbers, it is possible for the boundary layer to remain laminar throughout the entire interaction region. The work of Le Balleur and Déleroy (1973) showed that the transition front gradually moves upstream with increasing shock strength. For pressure jumps larger than 1.4 they found that, independent of the Reynolds number, transition sets in at the impact point of the incident shock. A mixed type of interaction is then obtained, with a laminar boundary layer upstream of the shock and the downstream part of the interaction exhibiting a transitional behaviour. This transitional behaviour of the boundary layer results in increased mixing and supports the boundary layer to overcome the pressure rise at reattachment, therefore reducing the size of the separation bubble. The size of the separation bubble shows a near-linear dependence with the driving pressure coefficient (total pressure jump minus pressure required for incipient separation) and the local displacement thickness (Gadd et al. (1954); Hakkinen et al. (1959); Katzer (1989)). Typically, researchers have recorded only weak Reynolds number effects on the size of the separation bubble. For a fully laminar interaction the separation bubble is found to increase in size with Reynolds number, while for the mixed type of interaction this trend is reversed.

Most experimental studies have dealt with the mean flow properties of laminar shock wave-boundary layer interactions. Its unsteady features were mainly touched upon by a series of recent numerical studies by, amongst others, Robinet (2007) and Sansica et al. (2014). The DNS study of Robinet (2007) showed that the laminar interaction can be-

come unstable under certain conditions. Key factors here are the shock strength and the spanwise extent of the computational domain. Computations performed on a wide domain were found to become unsteady for weaker shock waves than computations performed on a narrow, near 2-D domain. For relatively wide domains ($L_z > 0.8x_{sh}$, with x_{sh} the distance from the leading edge to the shock impingement location) it was found that the interaction becomes unsteady for shock angles of $\beta > 31.7^\circ$, which for their test conditions ($M = 2.15$, $Re_{x_{sh}} = Re_\infty \cdot x_{sh} = 10^5$) corresponds to flow deflection angles of $\theta > 4.8^\circ$.

The laminar separation bubble was found to exhibit some complex unsteady behaviour, with patches of attached and separated flow in the spanwise direction of the domain. A strong waterspout type of vortex was furthermore discovered that connects the flow at the wall in the separation bubble with the downstream shear layer. This vortex shows self-sustained low-frequency (700 Hz) oscillations and is expected to be one of the main causes of laminar SWBLI unsteadiness.

The simulations of Robinet (2007) were performed for a noise-free environment to study the global instability mechanisms of the interaction. In practice, freestream disturbances will always be present and are known (Van Driest and Blumer (1962)) to have a significant impact on the stability of the boundary layer. The simulations of Sansica et al. (2014) therefore focused on studying the receptivity of the laminar separation bubble to outside disturbances. Their DNS simulations showed the development of Kelvin-Helmholtz vortices on the detached shear layer, which are expected to be responsible for the onset of boundary layer transition. Similar to the findings of Robinet (2007), also a low-frequency type of unsteadiness was discovered at the separation point of the interaction. This type of low-frequency behaviour appears to be very similar to what has been recorded for turbulent interactions (Sansica et al. (2014)). Therefore studying the unsteadiness of laminar shock wave-boundary layer interactions may, indirectly, also shed some light on the unsteadiness of turbulent interactions.

1.4. TURBULENT OBLIQUE SHOCK WAVE REFLECTIONS

Turbulent boundary layers are much less prone to separation than their laminar counterparts, because of their fuller velocity profile and higher skin friction coefficient. Consequently, stronger shock waves are required to separate turbulent boundary layers. Many criteria exist for predicting the separation onset, but in this thesis we will rely upon the following well-validated criterion (Babinsky and Harvey (2011)), which has been derived from the free-interaction theory:

$$\frac{p_{inc}}{p_\infty} = 1 + C_{sep} \gamma M_0^2 \sqrt{\frac{2C_{f_0}}{(M_0^2 - 1)^{0.5}}} \quad (1.2)$$

With M_0 and C_{f_0} the freestream Mach number and skin friction coefficient at the interaction onset, respectively. For laminar interactions it is found that $C_{sep} \approx 1$ (Hakkinen et al. (1959)) and for turbulent interactions $C_{sep} \approx 3$ (Babinsky and Harvey (2011)). Evaluation of Eq.1.2 for the experimental conditions considered in chapters 3 - 6 ($M_0 = 1.7$, $Re_{x_{sh}} = 1.8 \times 10^6$) yields incipient separation pressure ratios of 1.11 ($\theta = 1.0^\circ$) and 1.77 ($\theta = 5.7^\circ$) for the laminar and turbulent interaction, respectively. This simple calculation

again highlights the laminar boundary layers extreme sensitivity to adverse pressure gradients.

Fig.1.9 shows the typical flow topology for an unseparated turbulent oblique shock wave reflection. The presence of the incident shock wave propagates upstream via the subsonic channel of the boundary layer. The upstream influence is very limited though compared to that of the typical laminar interaction (see Fig.1.8), which to a great extent is due to the much thinner subsonic channel for turbulent boundary layers. The thickening boundary layer leads to the formation of a series of compression waves, which quickly coalesce to form the reflected shock wave. The slope of the compression waves is not constant, but changes throughout the boundary layer as the Mach number varies. The same behaviour is also observed for the incident shock wave which curves and becomes more normal as it gets closer to the sonic line, where it is reflected as an expansion fan. The boundary layer recovers downstream of the interaction and the flow is again aligned with the wall by means of a series of weak compression waves.

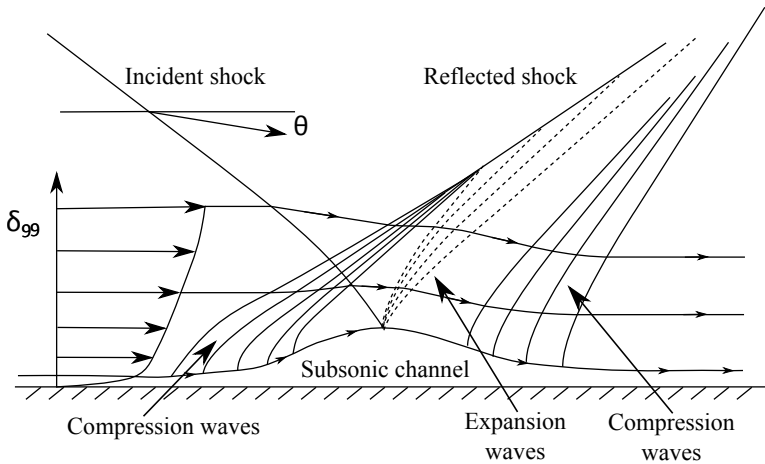


Figure 1.9: Flow topology of an attached turbulent oblique shock wave reflection, based upon the work of Détery and Bur (2000).

Fig.1.9 provides a simplified description of the flow topology of an attached oblique shock wave reflection. In reality, the flow field will be further complicated by the effects of shock wave refraction, which occurs when an oblique shock wave enters a rotational layer of fluid (i.e. the boundary layer). The process of shock wave refraction is schematically represented in Fig.1.10, where the boundary layer is divided in a series of parallel constant-pressure streams of varying Mach number. Shock wave refraction occurs at the intersection of these streams and leads to the formation of both a transmitted and a reflected wave (very similar to the process of light refraction). The nature of the reflected waves depends, to a great extent, upon the fullness of the incoming boundary layer profile (Henderson (1967)). Empty profiles typically lead to a mix of expansion and compression waves, whereas full velocity profiles result in a refraction pattern of mere compression waves. In reality this pattern of discrete expansion / compression waves will be replaced by a smooth continuous shock refraction pattern. A more elaborate de-

scription on the topic of shock refraction can be found in the work of Henderson (1967).

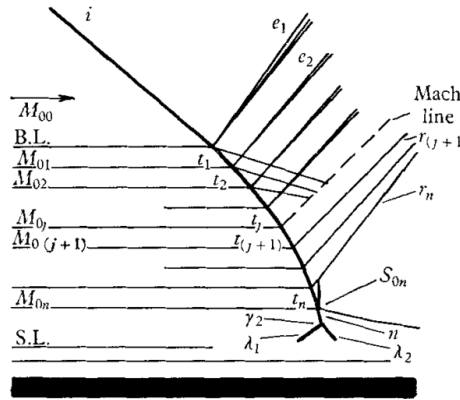


Figure 1.10: Shock refraction inside of a turbulent supersonic boundary layer. Adjusted from the work of Henderson (1967).

Fig.1.11 presents the flow topology for a separated turbulent oblique shock wave reflection. The formation of a separation bubble results in a strong upstream shift of the reflected shock wave, which now intersects the incident shock wave at some distance outside of the boundary layer. This intersection leads to the formation of a slip line, across which the flow direction and pressure are equal, but entropy and density levels may differ. The transmitted incident shock impinges on the top of the separation bubble and reflects as a series of expansion waves, because of the near-constant pressure level in the separation bubble. Afterwards the flow is deflected towards the wall and compression waves are formed at reattachment.

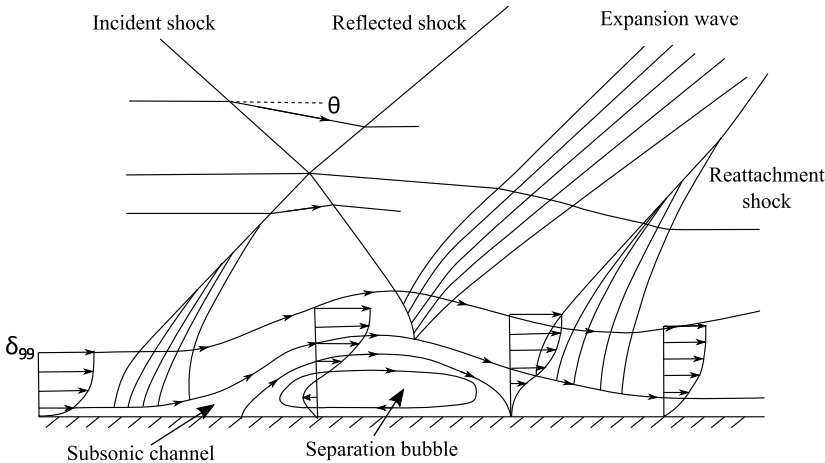


Figure 1.11: Flow topology of a separated turbulent oblique shock wave reflection, based upon the work of Déleury and Bur (2000).

The boundary layer thickness increases substantially over the shock system and the same holds true for the velocity fluctuations in the boundary layer. This is very clearly depicted in the Particle Image Velocimetry (PIV) measurements of Humble et al. (2007), who investigated an incipiently separated turbulent oblique shock wave reflection ($M_\infty = 2.1$ and $Re_{\delta_{99}} = 7.0 \times 10^5$). Fig.1.12 shows the mean velocity field and Fig.1.13 the velocity fluctuations throughout the interaction. Very high velocity fluctuations are recorded in the detached shear layer, with $\langle u' \rangle \sim 0.2U_\infty$ and $\langle v' \rangle \sim 0.05U_\infty$; thus showing the strongly anisotropic nature of turbulence in the interaction region. The very high values of $\langle u' \rangle$ are mostly due to the pulsating motion of the separation bubble. The bubble shows a low-frequency oscillatory motion (Clemens and Narayanaswamy (2014)), which leads to strong local variations in the streamwise velocity component. This pulsating motion has a much weaker effect on $\langle v' \rangle$, since the variations in v are much smaller in the streamwise direction than those recorded for u . Further downstream much stronger fluctuations of $\langle v' \rangle$ are recorded, which show very little recovery over the region from $x = 0 - 2\delta_{99}$ and are caused by vortex shedding in the shear layer of the interaction (Humble et al. (2007)). These vortices can have a very long life time and elevated turbulence levels are expected to survive at least $O(10)$ boundary layer thicknesses downstream of the interaction (Wu and Martin (2007b)).

High velocity fluctuations are also recorded in the vicinity of the reflected shock wave. These fluctuations can be traced back to the pulsating motion of the separation bubble, which moves the reflected shock wave back and forth and results in high values for $\langle u' \rangle$ and $\langle v' \rangle$ in Fig.1.13. Slightly elevated fluctuation levels are also recorded in the vicinity of the incident shock wave. These fluctuations are, however, not physical but can be traced back to the higher PIV measurement uncertainties in regions with strong velocity gradients.

One of the most puzzling aspects of separated turbulent shock wave-boundary layer interactions is the low-frequency unsteadiness behaviour of the reflected shock wave (Clemens and Narayanaswamy (2014)). The oscillation frequency of the reflected shock wave increases with freestream velocity U_∞ and decreases with the length of the separation bubble L_{sep} . This behaviour can be expressed in terms of a Strouhal number St and it was found by Dussauge et al. (2006) that $St = f_c \cdot L_{sep} / U_\infty = 0.03 - 0.05$ for a wide range of operating conditions. In this definition, f_c denotes the dominant frequency in the pre-multiplied power spectrum of the pressure fluctuations, as measured at the location of the reflected shock foot. Alternatively one could also define a Strouhal number based on the oscillation amplitude L_i of the shock system. This delivers typical Strouhal numbers of $St_{L_i} = 0.01 - 0.03$ (Clemens and Narayanaswamy (2014)).

However, the fluctuations that are recorded in the incoming boundary layer are of a much higher frequency: $O(U_\infty / \delta_{99})$ Hz; and typically two orders of magnitude higher than the oscillation frequency of the reflected shock. So, the puzzling part here is the conversion of high-frequency boundary layer fluctuations to low-frequency shock oscillations. The physical mechanism behind this behaviour has long been unclear and there were basically two alternative explanations for this behaviour. The low-frequency unsteadiness is either caused by large-scale upstream disturbances or it is a downstream phenomenon coupled with the dynamics of the separation bubble.

Many studies (Erengil and Dolling (1993), Ganapathisubramani et al. (2007), Wu and

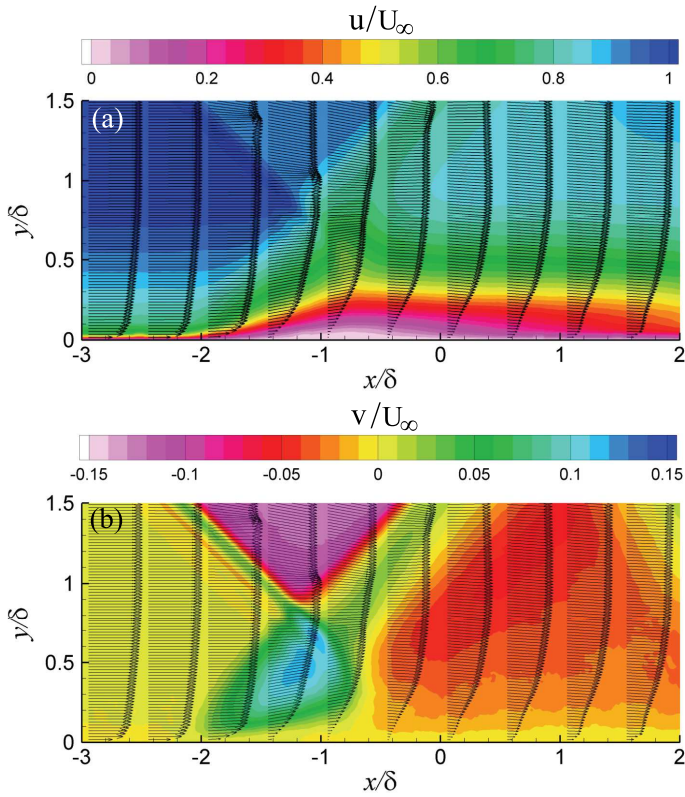


Figure 1.12: The mean velocity field of an incipiently separated turbulent oblique shock wave reflection (after Humble et al. (2007)). Streamwise velocity component u/U_∞ (a) and the wall-normal velocity component v/U_∞ (b)

Martin (2007a), Humble et al. (2009)) have shown that there is a clear correlation (0.4-0.5) between the instantaneous fullness of the velocity profile and the size of the separation bubble. A full boundary layer with a large amount of momentum in the near-wall region typically leads to a smaller separation bubble and a downstream displacement of the reflected shock wave. Furthermore, experimental evidence by Ganapathisubramani et al. (2007) revealed the existence of very long ($L > 8\delta_{99}$) low and high-speed streaks in supersonic turbulent boundary layers. The passage of a high-speed streak pushes the separation onset location downstream and results in a spanwise rippling of the separation bubble and the reflected shock wave (see Fig.1.14). This evidence therefore suggests that the recorded shock unsteadiness is mostly due to upstream effects.

The LES simulations of Touber and Sandham (2009), however, shed a different light on this discussion. Their LES simulations showed a low-frequency unsteadiness of the reflected shock wave even without the presence of very long streaks in the incoming boundary layer. This would suggest that the low and high-speed streaks might not be the driving factor for interaction unsteadiness. This idea was further substantiated by the

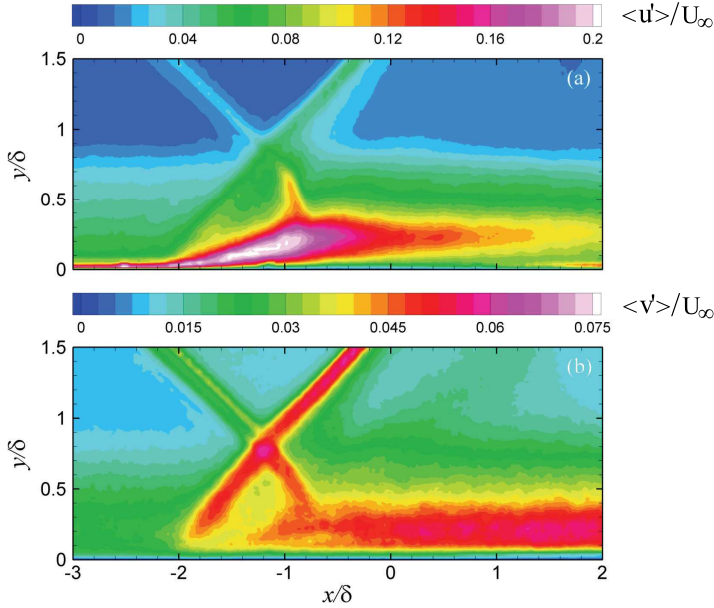


Figure 1.13: RMS velocity fluctuations measured within the interaction region (after Humble et al. (2007)). Streamwise fluctuating component $\langle u' \rangle / U_\infty$ (a) and the wall-normal fluctuating component $\langle v' \rangle / U_\infty$ (b)

experimental work of Piponniau et al. (2009), who developed a model based upon mass flow entrainment rate in the separation bubble. On average, there should be a constant amount of mass contained within the separation bubble, however, instantaneously there will be a transfer of mass between the bubble and the shear layer. The latter can result in a flapping motion of the shear layer and under some conditions the complete collapse of the separation bubble (Priebe and Martin (2012)). Piponniau et al. (2009) defined a characteristic time scale for the entrainment process by dividing the amount of mass in the reverse flow region by the rate of mass flow entrainment. This characteristic time scale was found to be closely related to the flapping motion of the shear layer and the low-frequency unsteadiness found for the reflected shock wave.

The work of Touber and Sandham (2009), Piponniau et al. (2009) and Priebe and Martin (2012) provides compelling evidence for the existence of a downstream mechanism driving the low-frequency unsteadiness. However, their work did not yet provide a satisfactory answer to the high correlations measured between the upstream boundary layer and the separation bubble by many other researchers. This open question was addressed in the recent numerical work of Touber and Sandham (2011). They artificially introduced velocity fluctuations in the upstream turbulent boundary layer by white noise forcing. First, they used a broadband white-noise spectrum and next they used a high-pass filtered white-noise spectrum. The first simulation again triggered low-frequency oscillations of the reflected shock wave, whereas in the second simulation these oscillations were absent. An upstream forcing of the low-frequency dynamics of the system

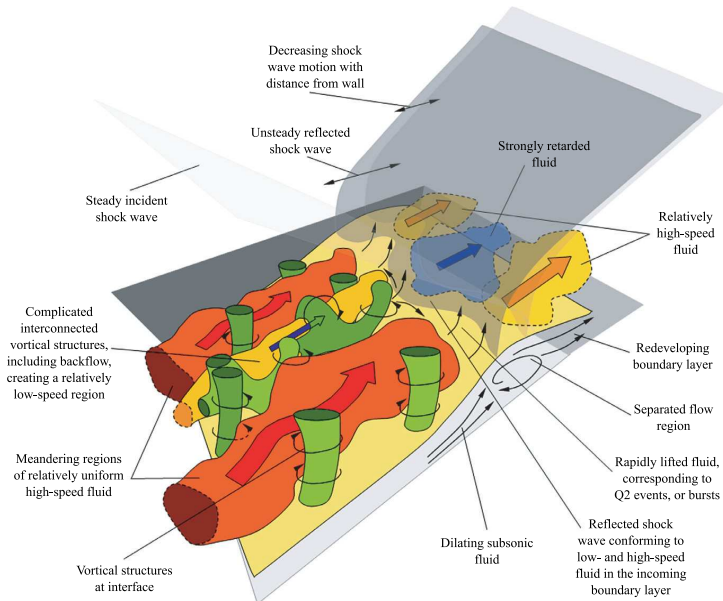


Figure 1.14: A physical description of turbulent shock wave-boundary layer interaction unsteadiness by Humble et al. (2009). The incoming boundary layer features low- and high-speed streaks, which lead to a rippling of the reflected shock wave and a spanwise modulation of the separation bubble. Low-momentum in the incoming boundary layer is correlated with an upstream movement of the reflected shock and high-momentum is correlated with a downstream movement.

therefore appears to be necessary, but the forcing does not have to appear in the form of coherent high-speed streaks. The presence of weak incoherent low-frequency features is sufficient for triggering the low-frequency dynamics of the interaction. This view of the shock wave-boundary layer interaction as a forced dynamical system also explains the high correlations that have been recorded between the incoming boundary layer and the separation bubble for relatively weak interactions (Souverein et al. (2010)).

1.5. FLOW CONTROL FOR OBLIQUE SHOCK WAVE REFLECTIONS

The previous sections showed that shock wave-boundary layer interactions can severely compromise the efficiency and safety of transonic and supersonic flight vehicles. Evidently there is a need for flow control, which is the ability to change the flow for the better by using either passive or active flow control devices (Gad-el Hak (2000)). The term 'better' is relatively vague and depends upon the specific application and requirements of the user. For a supersonic inlet it is of prime importance to have low total pressure losses, whereas for transonic wings one would like to have a high lift to drag ratio for a wide range of operating conditions. Many of these requirements can be traced back to the occurrence of a shock-induced separation bubble.

This central role of boundary layer separation within the chain of events is depicted in Fig.1.15, which shows the relations between some key flow control goals. Fig.1.15

has been derived from the work of Gad-el Hak (2000) and has been extended to also include ‘total pressure recovery’, ‘flow unsteadiness’ and ‘shock smearing’, which are important factors when considering shock wave-boundary layer interactions. Separation is of course strongly connected with the process of boundary layer transition. Laminar boundary layers are prone to separation and large separation bubbles are formed even for very weak shock waves. The detached shear layer on the other hand also forms a region of high receptivity where transition is more likely to occur (Saric et al. (2002)). If transition occurs on the shear layer, then this results in an increased mixing and an early reattachment of the boundary layer.

Large separation bubbles are typically to be avoided, because they can lead to a loss in lift, a drastic increase in drag, high total pressure losses and high levels of flow unsteadiness. However, under certain circumstances it may also be beneficial to have a large separation bubble. That is because the presence of a separation bubble tends to smear the shock system. The gradual thickening of the boundary layer leads to the formation of a series of compression waves, which introduce lower total pressure losses than those caused by a single concentrated shock wave. So, aiming for complete separation removal may not always be the best approach. This statement will be substantiated further in Chapter 6, which shows that a large shock-induced laminar separation bubble can be less harmful than an attached turbulent interaction, under the same test conditions.

Clearly, a good understanding of separation is of major importance when developing flow control applications for shock wave-boundary layer interactions. In this context it is useful to review the streamwise boundary layer momentum equation for a steady flow, given by:

$$\frac{\partial p}{\partial x} + \rho u \frac{\partial u}{\partial x} + \rho v \frac{\partial u}{\partial y} - \frac{\partial \mu}{\partial T} \frac{\partial T}{\partial y} \frac{\partial u}{\partial y} = \mu \frac{\partial^2 u}{\partial y^2} \quad (1.3)$$

Evaluation of this equation at the wall delivers the following relation:

$$\left. \frac{\partial p}{\partial x} \right|_{y=0} + \rho_w v_w \left. \frac{\partial u}{\partial y} \right|_{y=0} - \left. \frac{\partial \mu}{\partial T} \right|_{y=0} \left. \frac{\partial T}{\partial y} \right|_{y=0} \left. \frac{\partial u}{\partial y} \right|_{y=0} = \mu_w \left. \frac{\partial^2 u}{\partial y^2} \right|_{y=0} \quad (1.4)$$

Where ρ_w , v_w and μ_w define the density, wall-normal velocity and the dynamic viscosity at the wall, respectively.

The term $\left. \frac{\partial^2 u}{\partial y^2} \right|_{y=0}$ on the right-hand side of the equation can be viewed as a separation indicator. A large negative value indicates a full profile that is far from separation, whereas a positive value indicates a profile that is either separated or close to separation (see also Fig.1.16). So, in order to prevent separation, one should try to make one or more terms on the left-hand side of Eq.1.4 negative as well.

The first term on the left-hand side of Eq.1.4 is the pressure gradient. A favourable pressure gradient ($\left. \frac{\partial p}{\partial x} < 0 \right)$ will prevent separation, whereas an adverse pressure gradient promotes separation. For some applications it might be possible to prevent boundary layer separation by correctly shaping the aerodynamic surfaces. However, for many other applications, the adverse pressure gradient is a ‘given factor’, which cannot be changed easily. The adverse pressure gradient in a supersonic jet intake is for instance

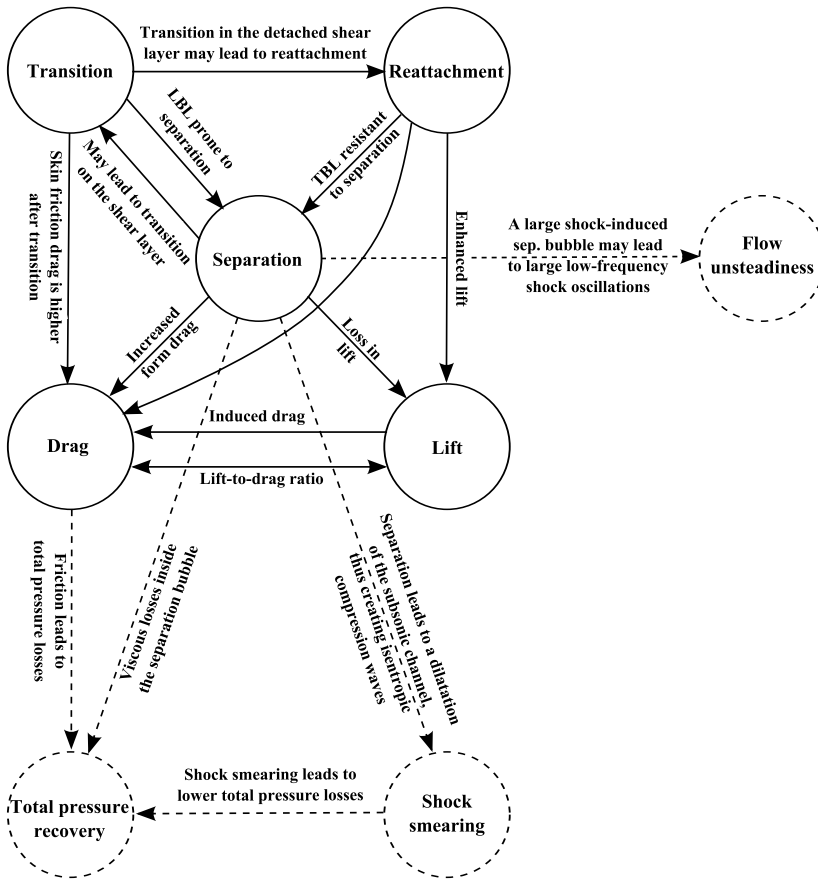


Figure 1.15: Connections between the different flow control goals. The image is inspired upon the work of Gad-el Hak (2000) and extended to also include features typical for shock wave-boundary layer interactions (dashed lines).

governed by the strength of the oblique shock waves. Weaker shocks are less likely to introduce flow separation, but more shocks are needed to reach the same level of flow compression, thus increasing the length of the inlet, which is often not acceptable.

An alternative approach is offered by the second term on the left-hand side of Eq.1.4: $\rho_w v_w \frac{\partial u}{\partial y} \Big|_{y=0}$, which defines flow control by means of suction or blowing. Suction ($v_w < 0$) removes the low-momentum portion of the boundary layer and thus yields a fuller velocity profile, which is less prone to separation. Blowing ($v_w > 0$) on the other hand has the opposite effect and promotes separation.

A third option of control is offered by the term $-\frac{\partial \mu}{\partial T} \Big|_{y=0} \frac{\partial T}{\partial y} \Big|_{y=0} \frac{\partial u}{\partial y} \Big|_{y=0}$. Here $\frac{\partial u}{\partial y} \Big|_{y=0}$ is positive for attached boundary layers and $\frac{\partial \mu}{\partial T} \Big|_{y=0}$ is positive for gaseous types of flows (for liquids $\frac{\partial \mu}{\partial T} \Big|_{y=0}$ is negative). A positive wall temperature gradient $\frac{\partial T}{\partial y} \Big|_{y=0}$ therefore

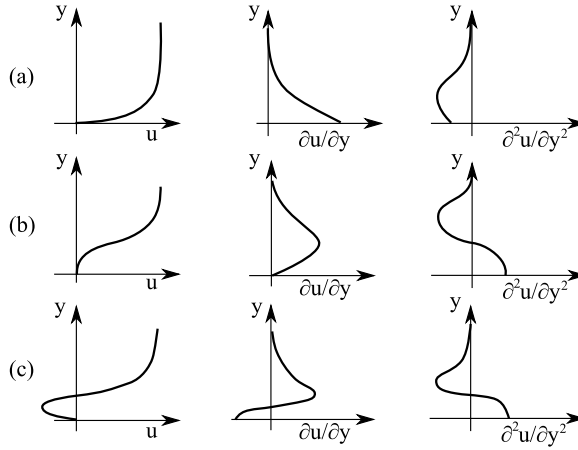


Figure 1.16: Typical boundary layer profiles for an attached profile (a) incipiently separated profile (b) and a separated profile. From left to right, the streamwise velocity component u , the first derivative $\partial u/\partial y$ and the second derivative $\partial^2 u/\partial y^2$.

has a stabilizing effect on the boundary layer and tends to postpone separation. The defining factor here is the ratio of the wall temperature T_w to the adiabatic wall temperature T_{aw} , where the adiabatic wall temperature is calculated as:

$$T_{aw} = T_e (1 + 0.5r(\gamma - 1)M_\infty^2) \quad (1.5)$$

With T_e the temperature in the freestream, γ the ratio of specific heats and r the recovery factor of the boundary layer. For laminar boundary layers $r \approx 0.84$ and for turbulent boundary layer $r \approx 0.89$.

If $T_w/T_{aw} < 1$ (cold wall), then the gradient $\left. \frac{\partial T}{\partial y} \right|_{y=0}$ becomes positive and separation will be postponed according to Eq.1.4. For a hot wall ($T_w/T_{aw} > 1$) the opposite holds true and separation will be promoted.

The three flow control methods that were identified in the foregoing discussion work for both laminar and turbulent flows. Now to gain some extra insight in the control of turbulent flows it is useful to revisit the streamwise momentum equation presented in Eq.1.3. This equation only holds true instantaneously for turbulent flows. A discussion of the mean flow properties is therefore only possible by Favre averaging (Wilcox (1994)) Eq.1.3, which delivers the following result for a 2D turbulent boundary layer:

$$\frac{\partial \bar{p}}{\partial x} + \bar{\rho} \bar{u} \frac{\partial \bar{u}}{\partial x} + \bar{\rho} \bar{v} \frac{\partial \bar{u}}{\partial y} - \frac{\partial \bar{\mu}}{\partial T} \frac{\partial \bar{T}}{\partial y} \frac{\partial \bar{u}}{\partial y} + \frac{\partial \overline{\rho u' v'}}{\partial y} = \bar{\mu} \frac{\partial^2 \bar{u}}{\partial y^2} \quad (1.6)$$

Where $[\bar{\quad}]$ denote mean quantities and $[\quad]'$ denote fluctuating quantities. The equation looks very similar to Eq.1.3, except for the addition of the Reynolds shear stress term $\overline{\rho u' v'}$ on the left-hand side of the equation. The Reynolds shear stress is the most important dynamic quantity in turbulent boundary layers and to a great extent responsible for the mixing processes taking place in the turbulent boundary layer. Mixing is important

for the redistribution of low and high-momentum fluid throughout the boundary layer and makes the boundary layer more resistant to separation. This can readily be seen by integrating Eq.1.6 over the boundary layer thickness (only excluding the near-wall viscous sublayer from the integration procedure, below δ_v):

$$\frac{d}{dx} \int_{\delta_v}^{\delta_{99}} \bar{\rho} \bar{u}^2 dy + \left[\overline{\rho u' v'}(\delta_{99}) - \overline{\rho u' v'}(\delta_v) \right] \approx -\frac{d\bar{p}}{dx} (\delta_{99} - \delta_v) \quad (1.7)$$

Here it has been assumed that the wall-normal velocity component v is small with respect to the streamwise velocity component u and can be neglected upon integration. Also it has been assumed that the viscous stresses are small compared to the Reynolds shear stresses. The latter assumption is only valid outside of the viscous sublayer for attached turbulent boundary layers. From Eq.1.7 it is clear that boundary layer momentum and Reynolds shear stresses compete with the pressure gradient. Boundary layer separation can therefore be prevented, or at least reduced, if the incoming turbulent boundary layer has a full velocity profile and shows a high degree of mixing. A fuller boundary layer profile, however, does not translate one-on-one to a reduced separation probability of the flow. A fuller boundary layer profile has a smaller sonic channel, which limits the propagation of the pressure rise imposed by the shock system in the upstream direction. The same pressure rise will therefore be felt by the boundary layer over a shorter distance in space and thus the $\frac{d\bar{p}}{dx}$ term in Eq.1.7 will increase in magnitude, as such partially cancelling the positive effect of the high momentum fluid present close to the wall (Delery and Marvin (1986)).

A full velocity profile can be obtained by means of boundary layer suction, which removes the low-momentum portion of the boundary layer from the flow, thus leaving a fuller velocity profile that is rich in momentum. Although proven to be highly effective (Gad-el Hak (2000)), this system does have the disadvantage of removing part of the incoming mass flow. In the case of supersonic inlets this implies that a larger (heavier) inlet is needed to obtain the same amount of mass flow through the engine core. An attractive alternative to boundary layer bleed is offered by vortex generators (VGs). A vortex generator redistributes streamwise momentum throughout the boundary layer by introducing a macro scale type of vortex. Low-momentum fluid is transported away from the wall, whereas high-momentum fluid is transported towards the wall, thus creating a fuller velocity profile that is less prone to separation.

Vortex generators come in different shapes and sizes. Typically they are shaped as small airfoils of low aspect ratio which are mounted normal to the wall of the object. They are often placed under a small angle of attack with respect to the incoming flow, thus causing a pressure difference between the suction and pressure side of the airfoil and the formation of a streamwise vortex. This process is nicely illustrated in Fig.1.17, which shows vorticity contour levels downstream of a pair of straight rectangular-shaped vortex generators. The VGs were positioned such that a counter-rotating vortex pair is generated that re-energizes the near-wall region of the flow. A region of strong downwash is created along the symmetry plane of the VG pair, whereas upwash occurs away from the symmetry plane.

Although VGs energize the near-wall boundary layer they are also responsible for a considerable drag contribution. In the early days of vortex generators it was common to

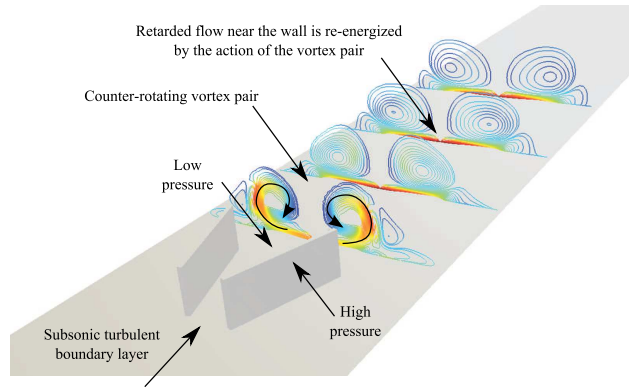


Figure 1.17: Simulation of the flow field downstream of two straight rectangular vortex generators. Iso-vorticity contours are plotted and coloured according to the turbulent kinetic energy. Image was modified from the work of Florentie (2015).

use VG heights on the order of the boundary layer thickness δ_{99} . However, over the past two decades research has focused on relatively small vortex generators with heights of about $0.1\text{--}0.5\delta_{99}$ (Lin (2002)), which have a considerably lower drag contribution. Vortices generated by these so-called sub-boundary layer VGs stay close to the surface for a longer distance downstream, whereas vortices generated by large VGs quickly lift off from the surface. Small VGs can therefore still be effective at preventing separation, since energizing the near-wall region is most critical in separation control.

The development of the vortex strength downstream of vortex generators of different heights in low-speed incompressible flows ($U_\infty = 10 - 40$ m/s) was investigated by Ashill et al. (2001). Fig.1.18 shows the normalized circulation strength $\Gamma/h_{eff}u_\tau$ of the primary vortex as measured $5h$ downstream of the device. The horizontal axis shows the Reynolds number $Re_{h_{eff}} = u_\tau h_{eff}/\nu$ based upon the effective height h_{eff} of the vortex generator and the friction velocity u_τ . The effective height is a non-physical parameter that has been introduced by Ashill et al. (2001) to collapse the data of different VG configurations. A larger h_{eff} therefore implies that a stronger vortex is induced for the same physical height h of the vortex generator. From the analysis of Ashill et al. (2001) it follows that joined CFU (Common Flow Up) vanes are the most effective at generating strong vortices. Common flow up in this context describes the formation of two counter-rotating vortices that generate a ‘common’ upwash component along the symmetry plane of the two devices. Another important finding of their work is that vortex strength scales linearly with the height of the vortex generator for $Re_{h_{eff}} > 1.4 \times 10^3$.

Vortex strength is, however, not the only parameter to consider when choosing a vortex generator for the purpose of separation control. Factors that also should be considered are 1) the location of the vortex with respect to the wall, 2) the longevity of the vortex and 3) the robustness of the vortex generator. Ashill et al. (2001) showed that although strong vortices are generated by the joined CFU vane pair, they also tend to migrate away from the surface much faster than the vortices generated by for instance the non-joined CFU vane pair ($n > 0$) or one of the wedge configurations. Additionally, the vortices gen-

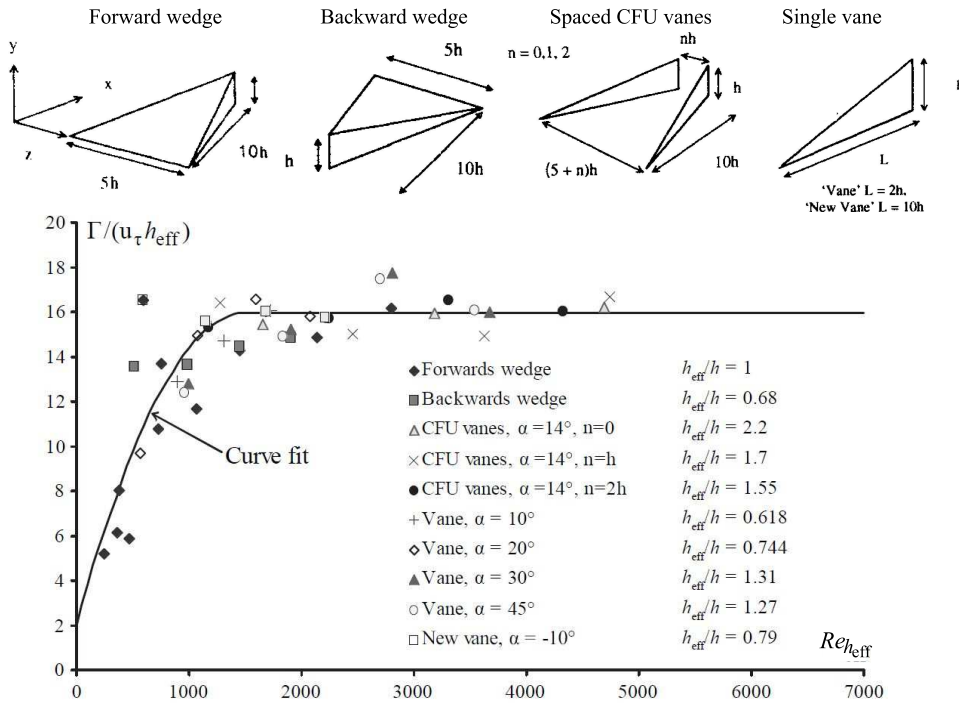


Figure 1.18: A correlation between the vortex circulation strength Γ and vortex generator height h , measured $5h$ downstream of the trailing edge of the devices. The axes are normalized with the friction velocity u_τ and the effective height h_{eff} , where the latter is a non-physical scaling parameter introduced by Ashill et al. (2001) to collapse the data of different types of VGs. The figure was reproduced from the work of Ashill et al. (2001) and Nolan and Babinsky (2012).

erated by the joined CFU vane pair tend to decay very rapidly, therefore quickly losing their ability to transport momentum towards the near-wall region of the flow. These observations can be traced back to the close proximity of the two vortices with respect to each other for the joined CFU vane pair. The mutual interference between the vortices is the main reason for the vortices to migrate away from the wall and to lose their strength.

An additional factor that needs to be taken into account is the robustness of the vortex generator. Although vanes are typically more effective at generating strong vortices than wedges (Ashill et al. (2001)), they are also relatively fragile. Especially when applied in supersonic jet intakes, where pressure and thermal loads can be very high, it is important to have a robust device that is unlikely to fail and to be ingested by the compressor stage of the engine. Micro-ramp vortex generators (see Fig.1.19(a)) fit these requirements very well and have been designed specifically to deliver optimal performance (i.e. a low incompressible shape factor) under supersonic operating conditions (Anderson et al. (2006)). Micro-ramps have therefore been selected as the method of choice for the control of turbulent oblique shock wave reflections described in part II of this thesis.

A micro-ramp is a small triangular, wedge-shaped type of vortex generator, with

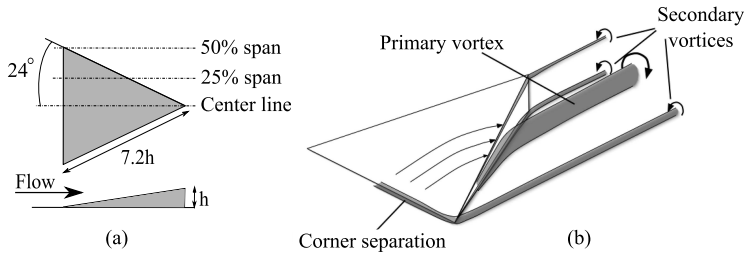


Figure 1.19: Micro-ramp geometry (a) and the corresponding flow topology (b). (Adjusted from the work of Babinsky et al. (2009))

a typical height of $\sim 0.5\delta_{99}$. The main flow features of the micro-ramp are presented schematically in Fig.1.19(b). Since the flow field is, on average, symmetrical around the centreline of the micro-ramp, only the right-half of the flow field is depicted. The control authority of the micro-ramp comes mostly from the two counter-rotating (CFU) primary vortices it introduces in the boundary layer. These vortices create a strong upwash component along the symmetry plane of the micro-ramp and a downwash component towards the edges of the ramp (see Fig.1.20). This leads to a redistribution of streamwise momentum and an influx of high-momentum fluid in the centreline region of the micro-ramp.

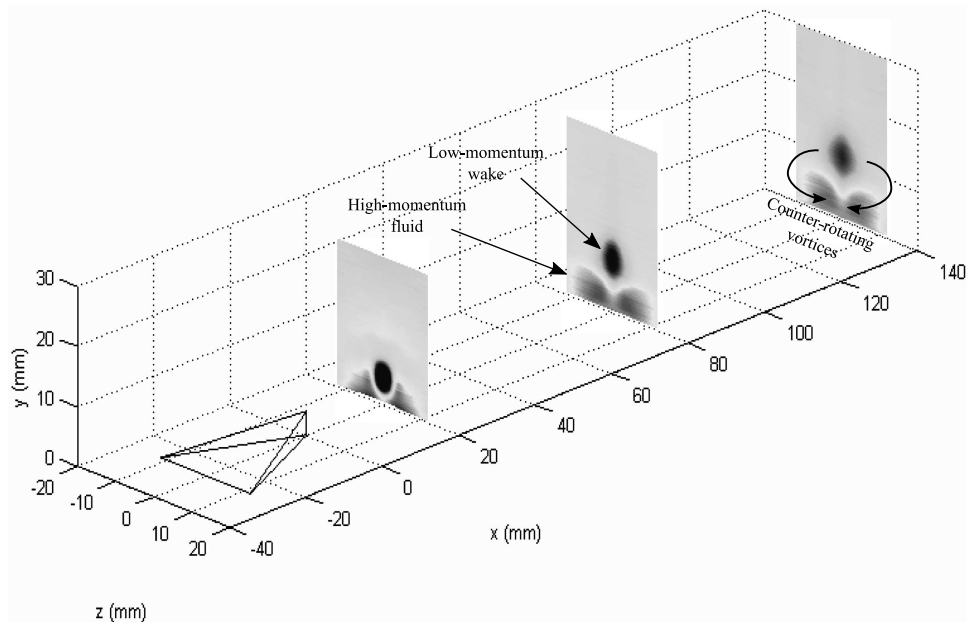


Figure 1.20: Redistribution of streamwise momentum downstream of the micro-ramp. (Adjusted from the work of Babinsky et al. (2009))

The strong primary vortices induce secondary vortices at the side-wall / tunnel-wall

junction and at the side-wall / top surface junction. These secondary vortices are significantly weaker than the primary vortices and rotate in the opposite direction (Lu et al. (2012)). Additionally, multiple studies on micro-ramp vortex generators (Babinsky et al. (2009); Herges et al. (2009); Saad et al. (2012); Lu (2015)) have recorded the presence of a weak horseshoe vortex that wraps around the leading edge of the micro-ramp and that trails downstream along its edges. A detailed description of the horseshoe vortex is provided in section 7.1 of this thesis, which presents oil-flow visualizations for a number of micro-ramp flow deflection angles and for different initial oil distributions.

In the recent work of Sun et al. (2012) tomographic particle image velocimetry measurements were performed on the flow field downstream of a micro-ramp positioned in a turbulent supersonic boundary layer. The tracer particles are imaged by multiple cameras during a tomographic PIV measurement, thus allowing for a three-dimensional reconstruction of the velocity field in a small volume downstream of the micro-ramp. Sun et al. (2012) thoroughly analysed this dataset and were able to visualize the two primary vortices and an overarching train of Kelvin-Helmholtz vortices (see Fig.1.21). The Kelvin-Helmholtz vortices are instabilities that are formed in the shear layer of the low-momentum wake downstream of the micro-ramp (see also Fig.1.20). The Kelvin-Helmholtz vortices introduce strong local mixing effects and are, to a great extent, responsible for the high Reynolds shear stresses that have been recorded by researchers (Sun et al. (2014); Herges et al. (2010)) within the shear layer of the low-momentum wake.

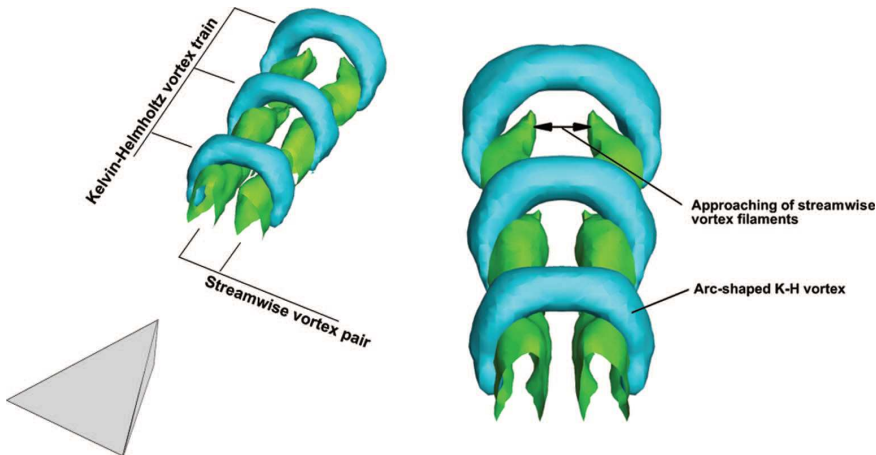


Figure 1.21: Conditional average of the vorticity distribution downstream of a micro-ramp vortex generator. The streamwise vortex pair is depicted in green and the overarching Kelvin-Helmholtz vortices in blue. From the work of Sun et al. (2012).

Although the shedding of Kelvin-Helmholtz (K-H) vortices affects the transfer of streamwise momentum towards the low-momentum wake, K-H vortices are not expected to substantially influence the micro-ramp's ability to reduce flow separation. Referring back to Eq.1.7, separation can be prevented by either having a full velocity profile or by having large negative values for the Reynolds shear stress near the wall. The studies of Sun et al. (2014) and Herges et al. (2010) revealed that although Reynolds shear

stresses can be large on the bottom ($\overline{u'v'} > 0$) and top ($\overline{u'v'} < 0$) shear layer of the low-momentum wake, the Reynolds shear stresses that are recorded near the wall are typically not much higher than those recorded for the undisturbed boundary layer. The main mechanism by which micro-ramps affect shock-induced separation therefore is the transportation of high-momentum fluid towards the wall, by which a fuller velocity profile is obtained.

Micro-ramps have been used as flow control devices for oblique shock wave reflections in a number of studies (Anderson et al. (2006); Babinsky et al. (2009); Blinde et al. (2009); Lee et al. (2010); Ghosh et al. (2010)). In the landmark study of Babinsky et al. (2009) micro-ramps were used to control an oblique shock wave reflection (flow deflection angle: $\theta = 7^\circ$) in a $M_\infty = 2.5$ flow. For the same conditions, Ghosh et al. (2010) performed a series of Reynolds-averaged Navier Stokes computations, for which the results were found to be in reasonable agreement with the experimental data of Babinsky et al. (2009). Fig. 1.22 shows a side-by-side comparison of their results, with and without the presence of a micro-ramp. The left hand side of the figure shows oil-flow visualizations performed by Babinsky et al. (2009) and the right-hand side a streamwise velocity contour level extracted 2.5 μm from the wall by Ghosh et al. (2010).

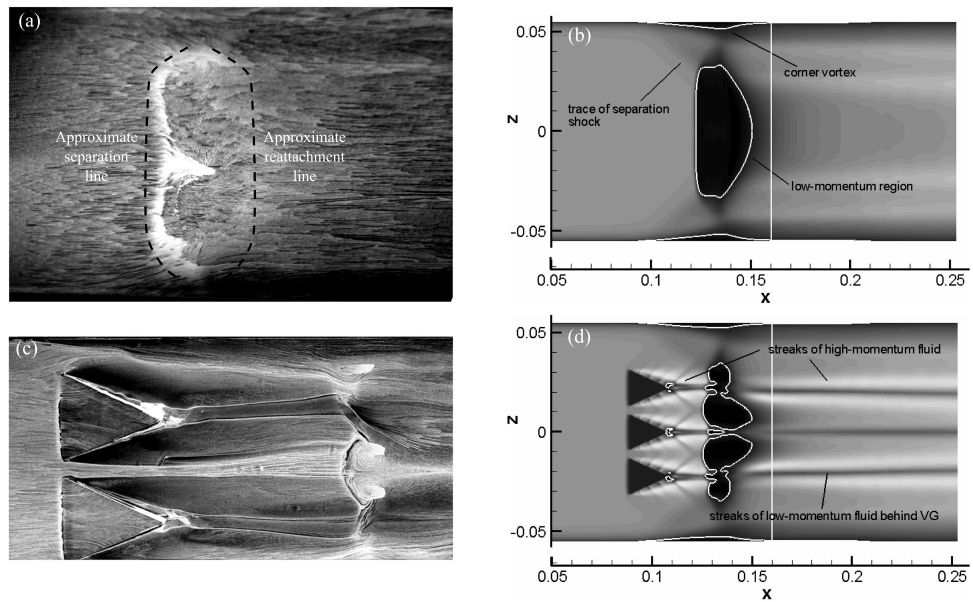


Figure 1.22: The wall flow topology for an oblique shock wave reflection without (a-b) and with (c-d) the presence of a micro-ramp positioned upstream of the interaction. The left column (a,c) presents the oil-flow visualizations by Babinsky et al. (2009) and the right column (b,d) the near-wall velocity contours by Ghosh et al. (2010). The experiment by Babinsky et al. (2009) and the numerical simulation by Ghosh et al. (2010) were conducted for the same test configuration and tunnel operating conditions.

Without the presence of micro-ramps a large separation bubble is formed that spans a substantial portion of the tunnel. The interaction of the oblique shock wave with the sidewall boundary layer leads to a crossflow type of separation, which results in a thick-

ening of the side-wall boundary layer and the formation of a series of compression waves upstream of the interaction. The bottom wall boundary layer therefore experiences a more gradual compression towards the edges of the domain, which precludes boundary layer separation and leads to the occurrence of channels of attached flow.

Installing micro-ramps upstream of the interaction does not lead to a complete removal of the separation bubble, but instead breaks up the bubble in a number of individual cells. The oil-flow visualizations of Babinsky et al. (2009) show that a channel of attached flow is created around the centreline region of the micro-ramp. The separation bubble that is formed between the centrelines of the two micro-ramps appears to be highly three-dimensional with strong waterspout type of vortices forming at the edges of the reversed flow region. These vortices are clearly visible in Fig.1.23, which shows a selection of near-surface streamlines for this particular interaction. The waterspout vortices that are created in-between the micro-ramps are found to entrain momentum from both the centreline region of the tunnel and from the region close to the side-walls.

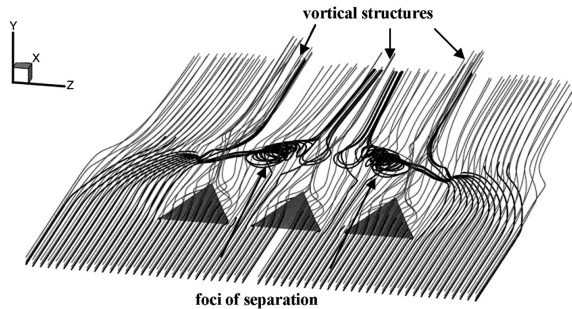


Figure 1.23: Near-surface streamlines for an oblique shock wave reflection controlled with micro-ramp vortex generators. From the work of Ghosh et al. (2010).

Babinsky et al. (2009) furthermore performed a series of pressure measurements and laser Doppler anemometry (LDA) measurements. The LDA measurements were used to track the state of the boundary layer throughout the interaction. Fig.1.24(a) shows the incompressible displacement thickness δ_i^* and the incompressible shape factor H_i for the baseline case (without a micro-ramp) and for the case of a $h = 3$ mm ($\sim 0.5\delta_{99}$) micro-ramp installed $\sim 17h$ upstream of the shock impingement location. Measurements with a micro-ramp were performed at three different spanwise locations: the centreline ($z = 0$ mm), 25% span ($z = 4.5$ mm) and 50% span ($z = 9$ mm).

The highest values of the displacement thickness are found at the shock impingement location, which is due to the thickening of the boundary layer experienced when crossing the shock system. Downstream of shock impingement, all cases show a pronounced recovery of the boundary layer and thus lower values for the displacement thickness. The micro-ramp introduces a strong spanwise modulation in the boundary layer downstream of the shock system. This is because the two primary counter-rotating vortices yield a strong upwash component along the centreline region of the micro-ramp and a downwash component towards its edges, which leads to a thickening / thinning of the boundary layer, respectively.

Fig.1.24(b) shows the incompressible shape factor H_i , which is a measure of the fullness of the velocity profile and thus an indicator of how close the boundary layer is to separation. It is therefore promising to see that the shape factor has been reduced in the interaction region over the entire span of the micro-ramp, compared to that of the baseline case. The strongest reduction in shape factor is obtained along the centreline of the micro-ramp, which agrees with the oil-flow visualizations of Babinsky et al. (2009) and the CFD simulations of Ghosh et al. (2010) presented earlier in Fig.1.22.

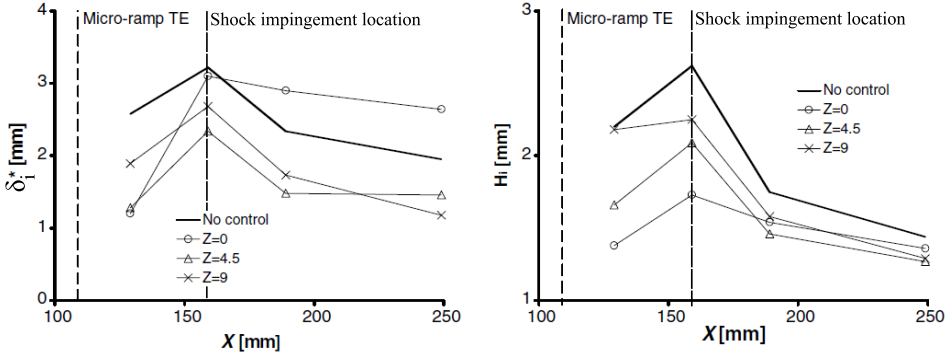


Figure 1.24: Development of the incompressible displacement thickness δ_i^* (a) and the incompressible shape factor H_i (b) throughout an oblique shock wave reflection. Modified from the work of Babinsky et al. (2009).

The foregoing discussion shows that micro-ramps can reduce the size of the separation bubble and that the strongest control effect is obtained along the centreline of the micro-ramp. As discussed earlier in this section, separation control is strongly connected to several other flow control goals (see Fig.1.15). Separation may trigger transition or cause large losses in lift and an increased pressure drag contribution. However, if we consider the case of a turbulent flat plate boundary layer (e.g. a supersonic jet intake) then our main concerns are 1) the (un)steadiness of the interaction and 2) the total pressure recovery over the shock system.

The unsteadiness of a micro-ramp controlled oblique shock wave reflection was investigated by Blinde et al. (2009), who performed Stereo PIV measurements in planes parallel to the wall. Similar to Babinsky et al. (2009), they also found a pronounced spanwise modulation of the separation bubble, where regions with a high separation probability were found to be correlated with high levels of shock unsteadiness. On average, the separation probability was reduced by 20%–30% and the reflected shock oscillation amplitude by 20%, compared to the uncontrolled case.

The total pressure recovery downstream of a normal shock wave boundary layer interaction ($M_\infty = 1.6$) controlled by Wheeler vortex generators was investigated by McCormick (1993). Fig.1.25 is extracted from his work and shows total pressure profiles $20\delta_{99}$ downstream of the shock impingement location. Compared to the baseline case, vortex generators were found to improve the total pressure recovery in the near-wall region of the flow, but worsen the recovery further away from the wall. Both observations can be traced back to the smaller separation bubble that is present when vortex generators are installed. Viscous losses will be lower for a smaller separation bubble and conse-

quently lower total pressure losses will be recorded close to the wall. A large separation bubble on the other hand is beneficial because it leads to the formation of isentropic compression waves in the freestream. By reducing the size of the separation bubble, these waves are replaced by a single shock wave which introduces higher total pressure losses. Finally, the vortex generator case displays an additional total pressure loss in the region of $0.6 < Y/R < 0.8$, which is the imprint of the low-momentum wake. Y in this definition is the wall-normal coordinate and R the local test section radius.

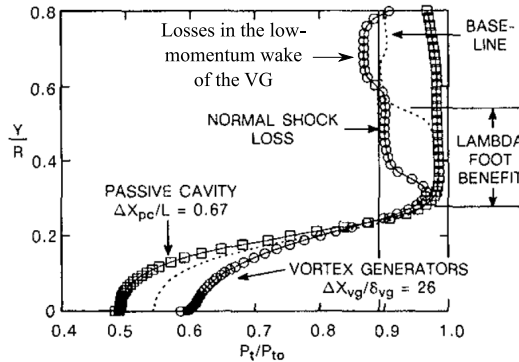


Figure 1.25: Total pressure recovery downstream of a normal shock wave boundary layer interaction, with and without flow control techniques. Adjusted from the work of McCormick (1993).

It is therefore often not directly clear if the application of vortex generators will improve or deteriorate the total pressure recovery over a shock wave-boundary layer interaction. In the numerical work (LES) of Lee et al. (2010) micro-ramps of $0.25\delta_{99}$ and $0.5\delta_{99}$ were used to control an oblique shock wave reflection at a Mach number of 3.0. They integrated the total pressure losses over a spanwise plane far downstream of the interaction and found that total pressure recovery was, on average, improved by 7% for the small $0.25\delta_{99}$ micro-ramps and worsened by 5% for the larger $0.5\delta_{99}$ micro-ramps. They also found that the smaller micro-ramps are more effective at reducing the size of the separation bubble than the larger micro-ramps. The latter finding is, however, not in agreement with the work of Babinsky et al. (2009), who found the opposite trend. The main disadvantage of larger micro-ramps is that they also introduce higher total pressure, as a result of the stronger downstream wake. In practice, one could therefore select an optimal micro-ramp height, which provides the right balance between the control of the separation bubble size and the incurred total pressure losses. The recent review of Titchener and Babinsky (2015) showed that the best performance is typically obtained for vortex generators heights h in the order of $0.2 - 0.5\delta_{99}$.

The review of Titchener and Babinsky (2015) also looked into the connection between the location of the vortex generator (VG) and its effectiveness at reducing the size of the shock-induced separation bubble. In general it appears that the best results are obtained for VG-to-separation bubble distances in the order of $15 - 30h$. However, it should be noted here that these results were obtained for widely varying VG configurations under widely varying test conditions. Chapter 8 of this thesis will look further into the positioning of the micro-ramp with respect to the shock wave and will try to es-

1 establish the connection between vortex-induced momentum transport and the optimal micro-ramp location.

1.6. THESIS OBJECTIVES

The governing theme of this PhD thesis is that of flow control for oblique shock wave reflections at relatively low supersonic Mach number ($M_\infty = 1.5 - 3$). Within the scope of this work, both *laminar* and *turbulent* interactions will be treated, with and without the presence of flow control devices.

1.6.1. FLOW CONTROL FOR LAMINAR OBLIQUE SHOCK WAVE REFLECTIONS

Since turbulent interactions are more often found in flight conditions (Babinsky and Harvey (2011)), most researchers have focused their attention to this particular type of interaction. However, with the economic and environmental challenges facing the aerospace sector there has been an ongoing effort for laminarizing both the internal and external components of aircraft and spacecraft. Laminar / transitional SWBLI are therefore expected to become more prevalent in the decades to come and additional research is needed on the potential drawbacks of these interactions when compared to turbulent ones.

Although laminar boundary layers have the advantage of a low skin friction, they are also more prone to separation than turbulent boundary layers. A turbulent boundary layer carries more momentum in the near-wall region of the flow, which is beneficial for overcoming the adverse pressure gradient imposed by the shock system. Turbulent boundary layers can therefore withstand stronger shocks without separation than laminar boundary layers. Boundary layer separation in general is to be avoided, because of the associated unsteadiness and potential system performance losses in terms of drag and total pressure. From a performance point of view it therefore would seem optimal to trip the laminar boundary layer a short distance upstream of the impinging shock wave. This concept, however, raises the following questions:

1. How detrimental is the baseline laminar SWBLI?
2. How far should the transition control devices be placed upstream of the interaction to completely avoid separation?
3. What is the most effective way of tripping the boundary layer?

These questions are being addressed within the collaborative research framework of TFAST (as part of the European FP7 program), which investigates the effects of boundary layer transition on a SWBLI in the low supersonic regime. Several test cases are considered within the project, ranging from fundamental flat plate interactions (normal / oblique SWBLIs) to SWBLIs on more complex geometries, such as compressor / turbine cascades and on transonic wings. This PhD thesis focuses on the fundamental flat plate case with a reflecting oblique shock wave.

An additional goal here was to further develop particle image velocimetry as a measurement technique for small-scale flow features in supersonic flows. Laminar supersonic boundary layers are extremely thin (~ 0.2 mm for the test conditions considered in

this thesis) and difficult to measure by means of particle image velocimetry due to the very high shear rates and typical strongly non-uniform particle seeding distributions. Advancements were made here both on the software (data analysis) and hardware side of the experimental approach.

1.6.2. FLOW CONTROL FOR TURBULENT OBLIQUE SHOCK WAVE REFLECTIONS

The goal of flow control for turbulent SWBLIs is to have a fuller boundary layer profile at the onset of the interaction, which is more capable of withstanding the imposed adverse pressure gradient by the shock system. To this end, micro-ramp vortex generators were investigated in this PhD thesis. The micro-ramps were placed a short distance upstream of the interaction and redistribute low- and high-speed momentum throughout the boundary layer, as such yielding a fuller boundary layer profile. The most important questions here were:

1. How do micro-ramp height and location affect the size of the shock-induced separation bubble and the interaction unsteadiness?
2. What is the physical mechanism behind the (in)effectiveness of micro-ramp vortex generators?
3. How do the Mach and Reynolds number affect the flow mixing properties of micro-ramp vortex generators?

1.7. THESIS OUTLINE

The thesis is divided into two parts, the first part (chapter 3 to 6) focuses on the understanding and control of laminar / transitional oblique shock wave reflections, whereas the second part (chapter 7 to 9) focuses on the control of fully turbulent oblique shock wave reflections.

The oblique shock wave reflections were studied with a range of experimental techniques. Chapter 2 discusses the working principles of these techniques, followed by a brief description of the experimental setup and the subsequent data processing steps.

Chapter 3 describes the experimental setup that was designed for investigating laminar oblique shock wave reflections. An important part of the setup was the installation of a full-span flat plate in the wind tunnel for growing a laminar boundary layer. A dedicated study was carried out to characterize the undisturbed boundary layer, the results of which are summarized in chapter 4.

Chapter 5 continues on this topic by installing a shock generator in the flow and having an oblique shock wave impinge on the surface of the flat plate. The shock wave was positioned in the laminar, transitional or turbulent region of the boundary layer for a range of shock strengths and Mach numbers. Experimental data was acquired via particle image velocimetry measurements, oil-flow visualizations and schlieren visualizations. A large experimental database has been obtained, providing new insights into the relation between separation and transition in oblique shock wave reflections.

After having obtained a good understanding of the baseline laminar interaction, the next step was to apply flow control techniques to reduce the size of the shock-induced

separation bubble. In chapter 6 three tripping devices were investigated that were installed a short distance upstream of the interaction. Particle image velocimetry measurements were used to study the size of the shock-induced separation bubble and the overall development of the boundary layer.

Chapter 7 forms the start of part II of this PhD thesis and introduces the micro-ramp vortex generator as flow control device for turbulent oblique shock wave reflections. Although this part of the PhD thesis focuses mostly on the application of micro-ramp vortex generators for SWBLI control, also some new insight were gained in the fundamental flow topology of these devices. In particular, Chapter 7 discusses the presence / absence of a horseshoe vortex at the leading edge of the micro-ramp and the formation of Kelvin-Helmholtz vortices in the low-momentum wake of the ramp.

Chapter 8 continues on the 'control' aspect of micro-ramps and presents the results of a parametric study that has been conducted into the effects of micro-ramp height and location on the size of the separation bubble and the associated shock unsteadiness. Some configurations were found to work very well, whereas other configurations only tend to make the system more separated and unsteady. To better understand the (in)effectiveness of micro-ramp vortex generators, a study was performed into the flow mixing properties of micro-ramp vortex generators.

Chapter 9 builds further upon this description by also studying the effects of Mach and Reynolds number on the flow mixing and wake properties of micro-ramp vortex generators of various heights.

Chapter 10 concludes this work by summarizing the most important findings and discussing their physical relevance in relation to the engineering practice. Finally, chapter 11 gives an outlook for the future, identifying several interesting research opportunities.

2

EXPERIMENTAL METHODS

2.1. SCHLIEREN VISUALIZATIONS

Schlieren is an optical technique which can be used to visualize density gradients in air flows. The technique is an excellent tool for visualizing shock waves, expansion waves, boundary layers and even the process of boundary layer transition. Although it can be used as a quantitative tool to measure density variations in flows (Elsinga et al. (2003)), it is still most often used as a qualitative technique for better understanding the general flow topology.

Schlieren visualizations rely upon the principles of light refraction in a medium with varying indices of light refraction n :

$$n = \frac{c_v}{c} \quad (2.1)$$

Where c_v in the speed of light in vacuum and c the speed of light through the medium under investigation. For air the index of refraction n has a typical value of ~ 1.00029 , with n being a function of the air density ρ :

$$n = 1 + K\rho \quad (2.2)$$

Where K is the Gladstone-Dale constant, which for air equals approximately $K = 0.2274 \text{ cm}^3/\text{g}$ (for a wavelength $\lambda = 0.5 \text{ }\mu\text{m}$).

A light ray is bend (refracted) when it encounters a gradient in the refractive index of the medium along its lateral plane (x, y). On the other hand, gradients in the refractive index n in the direction of light ray propagation (z) do not lead to a bending of the light ray. The curvature of the light ray can be expressed by the following relations for the two directions lateral to the light ray:

$$\frac{\partial^2 x}{\partial z^2} = \frac{1}{n} \frac{\partial n}{\partial x} \quad \text{and} \quad \frac{\partial^2 y}{\partial z^2} = \frac{1}{n} \frac{\partial n}{\partial y} \quad (2.3)$$

Upon integration this leads to the following relations for the deflection angle ϵ of the light ray:

$$\epsilon_x = \frac{1}{n} \int \frac{\partial n}{\partial x} dz \quad \text{and} \quad \epsilon_y = \frac{1}{n} \int \frac{\partial n}{\partial y} dz \quad (2.4)$$

From Eq.2.4 it follows that light rays deflect towards the region with the higher density. These deflections can be visualized by means of a Z-type of schlieren setup (as also used in the ST-15 and TST-27 wind tunnels) presented schematically in Fig.2.1.

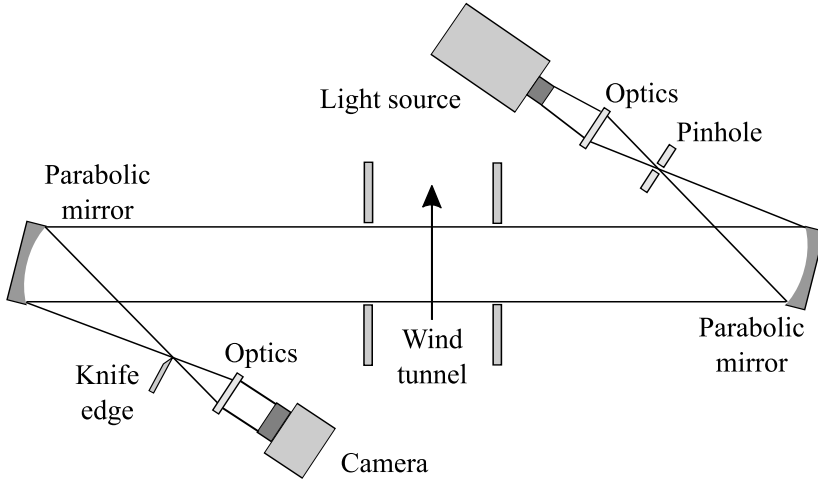


Figure 2.1: Sketch of a Z-type of schlieren setup

A light source in combination with lenses and a pinhole is used to create a point-like light source. The pinhole is placed in the focal point of the first parabolic mirror, which therefore creates a collimated beam of light that passes through the wind tunnel test section. A second parabolic mirror then focusses the beam of light on a knife edge (schlieren knife) and the generated image is recorded by means of a camera. The knife edge typically blocks about half on the incoming light, when not operating the wind tunnel. When running the tunnel, part of the light rays will be deflected by the density gradients present in the fluid. The deflected light rays will either pass or be blocked by the knife edge, depending upon its orientation. Density gradients will therefore either show up as white or black features in the produced schlieren visualizations.

The sensitivity of the system depends to a great extent upon the size of the pinhole. An infinitely small pinhole would in principle lead to an infinitely sensitive schlieren system. Even the weakest density gradients would cause light rays to be blocked completely by the knife edge or to pass completely. This type of behaviour is not desirable and therefore finite size pinholes (typically in the order of 3 mm for the visualizations performed in the TST-27) are used to improve the measurement range of the flow visualization. The larger the size of the pinhole, the smaller the change will be to a particular density gradient encountered by the light rays in the test section.

The schlieren system can be operated both with a continuous light source or with a spark light source. The spark light source generates a very short pulse (~ 20 ns), which freezes the flow field in the schlieren visualization and thus captures the instantaneous features of the flow. This approach was used to capture boundary layer transition (section 4.2) and to capture the vortices introduced by micro-ramp vortex generators (section 7.2).

2.2. OIL-FLOW VISUALIZATIONS

Surface oil-flow visualizations are widely applied in the field of fluid dynamics (Merzkirch (1987)) and provide the experimentalist with a powerful tool to quickly examine the surface flow topology of their model. The technique relies upon the application of a thin layer of a carrier fluid (oil, kerosene, etc...) to the surface of the test object. The carrier fluid is typically mixed with a colouring agent to improve the contrast of the measurement and to allow for a clear visualization of the surface flow topology. The oil film layer is subjected to the following forces during a wind tunnel experiment

- Shear stresses
- Pressure forces
- Gravity
- Surface tension

The effects of gravity and surface tension are typically very small and play a negligible role in the development of the oil film layer during wind tunnel experiments. Squire (1961) furthermore showed that the pressure forces for most applications can also safely be neglected. It is only in the presence of large pressure gradients (e.g. separation) that the pressure forces are expected to play a substantial role in the flow of the oil-film layer. The dominant term in the description of oil-flow visualizations is therefore the wall shear stress exerted by the boundary layer on the oil sheet. The oil flows in the direction of the local skin friction vector (Squire (1961)) and as such maps out skin friction lines. Since, the oil flowing between two skin friction lines must be conserved (for non-evaporating fluids) it follows that the oil film height can increase by two factors: 1) a reduction of the skin friction coefficient, which reduces the convection speed of the oil and 2) converging skin friction lines. A large accumulation of oil therefore does not necessarily have to be associated with a low skin friction coefficient or the presence of a vortex, instead it can also be the result of closely spaced skin friction lines.

The oil moves downstream at a speed of $U_o = \tau_x h_o / \mu_o$, where τ_x is the wall shear stress in the streamwise direction, h_o the height of the oil-film and μ_o the dynamic viscosity of the oil (Brown and Naughton (1999)). The convection speed of the oil thus varies proportionally with the wall shear stress and inversely proportional with the viscosity of the oil. For experiments on laminar boundary layers it is therefore recommendable to use a low-viscosity oil mixture, whereas for turbulent boundary layers one should use a higher viscosity mixture. A high viscosity mixture has the advantage of not being influenced substantially by tunnel start-up and shut-down effects. On the otherhand, high-

viscosity mixtures may lead to excessive tunnel run times and may not capture some of the weaker features of the flow.

For the oil-flow visualizations performed in this thesis a mixture of Shell Tellus type 22 oil and TiO₂ particles (Sachtleben UV-TITAN L-530, 30 nm crystal size) was used. To this mixture a couple of drops of oleic acid were added in order to obtain an oil film layer with the right viscosity for the intended application. The typical tunnel run time while performing an oil-flow visualization would be approximately 15 seconds.

2

2.3. INFRARED THERMOGRAPHY MEASUREMENTS

Infrared thermography measurements are commonly used to assess the state of a boundary layer developing over a surface. By measuring the temperature development of the model, information can be inferred about the local state of the boundary layer. This section will first give a brief description of the infrared thermography camera and the camera calibration procedure. Next, the data reduction procedure will be outlined for converting the measured temperature maps to surface heat flux maps.

2.3.1. EQUIPMENT AND CALIBRATION

All infrared thermography experiments in this thesis were performed with a CEDIP Titanium 530L infrared camera, which uses a MCT sensor having 320x256 pixels. The camera is sensitive in the spectral range of 7.7 - 9.3 μm . A Stirling cycle is used to cool the sensor, which brings down the noise equivalent temperature difference (NETD) to 25 mK. An integration time of 340 μs was used and images were recorded at a frequency of 25 Hz. During the experiments the camera was placed under an angle with respect to the window and the model (see Fig.2.2(a)), in order to avoid any self-reflections from the camera.

The camera records the thermal radiation level emitted by the wind tunnel model. A calibration procedure is as such necessary to convert the measured thermal radiation to surface temperatures. This calibration is accomplished by using a black body simulator: a box with a small opening on the top, painted black from the inside and equipped with a series of tubes with hot water to allow the uniform heating of the simulator (see Fig.2.2(b)). The emissivity ϵ of the black walls equals ~ 0.9 , however, due to the design of the simulator (narrow opening, wide cavity) multiple reflections will occur inside the cavity and the emissivity of the complete system will be close to 1 (Mayer (2000)), therefore making it a suitable calibration object. In the calibration process, also the germanium window is included, which during the measurements will be located between the camera and the model in the tunnel. In this way the reduced transmissivity ($\tau \sim 0.8$, Schrijer (2010)) of the germanium window is also included in the calibration. The black body simulator is then heated to a range of different temperatures and a calibration curve is obtained which links the thermal radiation recorded by the camera with the temperature of the black body simulator.

The flat plate model that is used during the wind tunnel experiments is, however, not a perfect black body radiator. The thermal energy budget states that:

$$\epsilon + \tau + \rho = 1 \quad (2.5)$$

For an opaque object the transmissivity τ equals zero and consequently the reflectivity ρ equals $\rho = 1 - \epsilon$. The thermal radiation I_m that is measured by the camera therefore consists of two components: the radiation emitted by the object I_o and the radiation of the ambient environment I_a that is reflected by the test object. This can be expressed by the following formula:

$$I_m = \epsilon \cdot I_o + (1 - \epsilon) \cdot I_a \quad (2.6)$$

If the emissivity of the test object and the radiation from the ambient environment are known, then the following relation can be used to determine I_o .

$$I_o = \frac{I_m - (1 - \epsilon) \cdot I_a}{\epsilon} \quad (2.7)$$

Via the earlier determined calibration curve, these values can then be converted to surface temperatures.

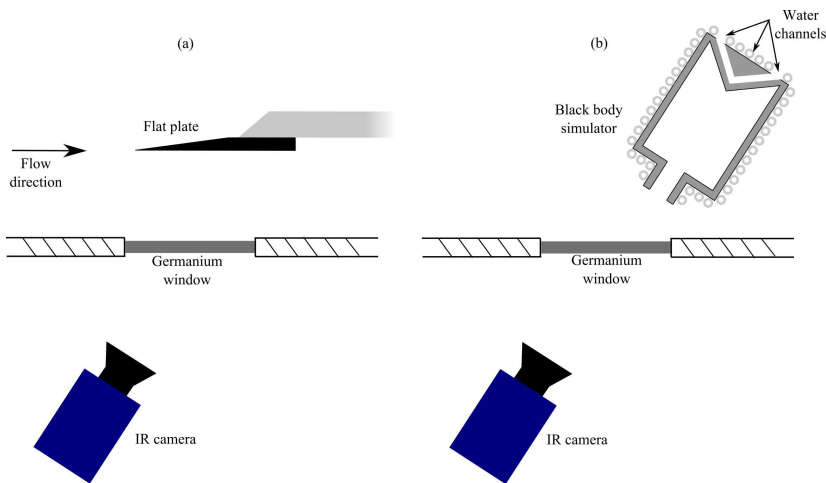


Figure 2.2: Sketch of the infrared thermography measurement setup in the wind tunnel (a) and while performing the calibration (b).

2.3.2. DATA REDUCTION

Turbulent boundary layers display a higher rate of convective heat transport than laminar boundary layers (White (2005)) and consequently larger variations are expected in the measured wall temperatures for the turbulent boundary layer. So, in principle, it is possible to infer the transition location of a boundary layer directly from the temperature distribution on the model. In practice this analysis might, however, be complicated when the model has a non-uniform thickness. The thinner parts of the model tend to cool down more rapidly, obscuring the representation of the transition location. Furthermore, the temperature distribution provides only a delayed representation of the transition location due to the temporal variation in the surface heat flux and the effects

of lateral conduction. Therefore to obtain the instantaneous transition location it is necessary to directly have access to the value of the convective heat flux.

To obtain the heat flux from the measured time-transient temperature distribution, various data reduction techniques are available, which can be grouped in three classes according to Walker and Scott Walker and Scott (1998). Type 1 methods solve the unsteady one-dimensional (1-D) heat conduction equation in closed form and deliver an analytical solution for the convective heat flux as function of the surface temperature. Well-known examples of this type of method are the approaches from Cook and Felderman (1966) and Kendall et al. (1967). Although robust and fast, these methods assume a 1-D semi-infinite slab, and so it is not possible to take into account the effect of the finite, non-uniform thickness of the model nor the effect of lateral conduction. Type 2 methods are more flexible and the convective heat fluxes are derived from a direct numerical solution of the unsteady two- or three-dimensional heat conduction equation inside the discretized geometry of the wind-tunnel model. Finally, type 3 methods solve the full-inverse problem, usually via an adjoint-type solution (Özisik and Orlande (2000)) which also provides the sensitivities of the solution.

The data reduction method used in this thesis can be classified as a type 2 method. The unsteady heat conduction equation is solved in a 2-D slice of the flat plate model (see Fig.2.3), with prescribed time-dependent surface temperatures as a boundary condition (BC). On the top of the flat plate, the measured surface temperatures are applied. Because there is no measurement data available for the bottom side (which is not watched by the camera during the experiments), the same measured temperature signal is also applied there. On the rear face of the plate, a uniform temperature condition is applied, equal to the values measured at the trailing edge of the plate. As initial condition it is assumed that the temperatures measured before starting the tunnel are constant throughout the thickness of the plate.

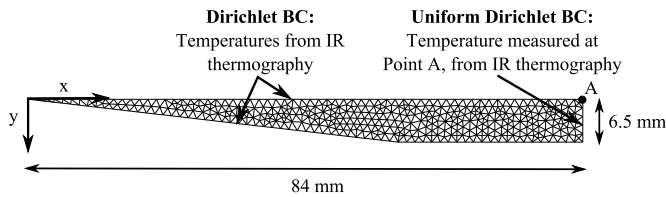


Figure 2.3: Coarse version of the mesh used for solving the unsteady heat conduction equation

The aforementioned assumptions are not perfect and there will be temperature differences between the top and bottom of the plate, both at the start and during the run, which are not taken into account. However, the goal of calculating the surface heat flux is not to obtain quantitative information about the state of the boundary layer (skin friction, thickness, etc.), but to get an estimate of the transition location and its behaviour in time.

The 2-D heat equation is solved on an unstructured grid with triangular cells. The mesh has 80 cells in the y direction and 1200 cells in the x direction. The surface heat

flux is calculated from the temperature gradient at the surface, which is estimated using a second-order-accurate stencil. A mesh convergence study was performed and essentially no variations in the calculated surface heat flux were found when using more than 40 cells in the y direction.

2.4. HOT WIRE ANEMOMETRY MEASUREMENTS

Hot wire anemometry (HWA) systems allow for the measurement of mass flux $(\rho u)'$ and total temperature fluctuations T_0' in supersonic flows at a high acquisition frequency (10 - 100 kHz). The working element is a thin metallic wire (see Fig.2.4), which is heated by passing an electric current through it. Cooling is provided by the effects of convection when performing a wind tunnel experiment. Higher velocities yield a stronger cooling effect, which translates into a higher output voltage when the wire is operated at a constant temperature. The voltage signal can therefore be used to infer information on the flow conditions in the wind tunnel.

First, a description is given of the wire's energy balance in section 2.4.1, discussing the input by Joule heating and losses induced by convection, conduction and radiation effects. The HWA system can be operated as a constant current anemometer (CCA), a constant voltage anemometer (CVA) or as a constant temperature anemometer (CTA) system. Section 2.4.2 provides a short description of these different operating modes and highlights the pros and cons of the different modes. Next, the static and dynamic calibration procedure of the HWA system are discussed in sections 2.4.3 and 2.4.4, respectively. Finally, section 2.4.5 covers the conversion of freestream mass flux fluctuations $(\rho u)'$ to freestream pressure fluctuations p' .

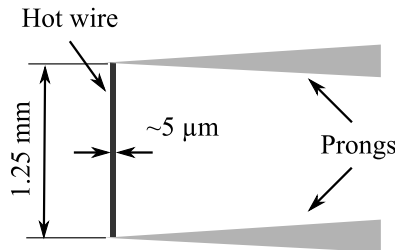


Figure 2.4: Dimensions of the Dantec 55P11 single-wire probe

2.4.1. ENERGY BALANCE

The energy balance for the hot wire can be written as:

$$C \cdot \frac{dT_w}{dt} = W - (Q_{conv} + Q_{cond} + Q_{rad}) \quad (2.8)$$

Where C is the heat capacity of the wire and T_w the wire temperature. The hot wire gains thermal energy by the effects of Joule heating W and loses heat via the mechanisms of convection Q_{conv} , conduction Q_{cond} and radiation Q_{rad} . All four contributions will be discussed shortly in this section.

JOULE HEATING

The heat that is added to the wire W can be expressed in terms of the current flowing through the wire I_w and the resistance of the wire R_w :

$$W = I_w^2 R_w \quad (2.9)$$

$$I_w = \frac{E}{R_w + R_s} \quad (2.10)$$

Where R_s is the resistance of all components that are connected in series with the hot wire and E the operating voltage of the system.

CONVECTION

The effects of heat convection can be described by the following equation:

$$Q_{conv} = \pi \cdot l_w \cdot d_w \cdot h \cdot (T_w - T_r) \quad (2.11)$$

Where l_w is the length of the wire, d_w the diameter of the wire, h the convective heat transfer coefficient and T_r the recovery temperature. The recovery temperature T_r is the temperature that the wire would reach during a wind tunnel experiment when not being heated. The recovery temperature is related to the total temperature T_0 by the following simple relation: $T_r = \eta T_0$, where η is the recovery factor. For the hot wire experiments presented in this thesis a recovery factor of $\eta = 0.95 \pm 0.01$ was found. This value is very comparable to the recovery factor $\eta = 0.94 \pm 0.01$ found by Smits et al. (1983) in their supersonic ($M = 2.9$) hot wire experiments.

Eq.2.11 will now be rewritten in a more standardized form by introducing some commonly used definitions in the field of HWA measurements. The wire temperature T_w is often expressed in terms of the overheat ratio a_w :

$$a_w = \frac{T_w - T_r}{T_r} \quad (2.12)$$

And the convective heat transfer coefficient h is often normalized by the wire diameter d_w and the heat conductivity of the fluid k_{f_0} evaluated at total temperature conditions, giving the Nusselt number:

$$Nu = \frac{h \cdot d_w}{k_{f_0}} \quad (2.13)$$

Substituting Eqs.2.12 and 2.13 in Eq.2.11 delivers the following general relation for heat losses due to convection:

$$Q_{conv} = \pi \cdot l_w \cdot Nu \cdot k_{f_0} \cdot a_w \cdot T_r \quad (2.14)$$

The Nusselt number is a function of the wire Reynolds number ($Re_w = Re_\infty \cdot d_w$) and the Mach number (Dewey (1965)). Based upon the work of Dewey (1965) it is expected that the Nusselt number will equal approximately $Nu \sim 5$ for the hot wire experiments presented in this thesis.

END-CONDUCTION LOSSES

A portion of the energy that is generated by Joule heating leaks away via the prongs of the hot wire by the effects of conduction Q_{cond} . This is undesirable, since it is well-known (Bruun (1995)) that large end-conduction effects lead to a strong attenuation of the measured output signal, which is unwanted when studying the properties of a turbulent flow field. For end-conduction effects to have a negligible impact on the output voltage, the following criterion (after Hultmark et al. (2011)) needs to be satisfied:

$$\Gamma = \frac{l_w}{d_w} \sqrt{\frac{4(a_w + 1)k_{f_w}Nu}{k_w}} > 14 \quad (2.15)$$

Where k_{f_w} is the heat conductivity of the fluid evaluated at the wire temperature and k_w is the heat conductivity of the wire evaluated at the wire temperature. The parameter Γ scales linearly with the aspect ratio (l_w/d_w) of the wire and with the square root of the overheat ratio. It is therefore beneficial to work with long thin wires operated at a high overheat ratios, when trying to avoid wire end-conduction effects. The measurements that are described in this thesis were performed at overheat ratios a_w of 0.4 and 0.93, for which Γ equals 18 and 25, respectively. End-conduction effects are therefore expected to have a negligible effect on the recorded output voltage.

RADIATION LOSSES

The heat radiated by the wire can be calculated via Stefan-Boltzmann's law:

$$Q_{rad} = \epsilon \cdot \sigma \cdot \pi \cdot d_w \cdot l_w \cdot (T_w^4 - T_e^4) \quad (2.16)$$

Where ϵ is the emissivity of the wire, $\sigma = 5.67 \times 10^{-8} \text{ W/m}^2/\text{K}^4$ the Stefan-Boltzmann constant and T_e the freestream temperature. The radiation losses are less than 0.1% of the convective heat losses for the experiments described in this thesis and can therefore safely be neglected when considering the thermal balance of the hot wire.

2.4.2. OPERATING MODES

The hot wire can be operated as a constant temperature anemometer (CTA), a constant current anemometer (CCA) or as a constant voltage anemometer (CVA). The latter two operating modes have the disadvantage that the wire temperature depends on the flow conditions. The wire temperature is therefore not known (exactly) in advance and consequently there is a risk of overheating and burning the wire. Also not having the hot wire temperature fixed puts a limit on the frequency response characteristics of the hot wire system. Although the wire is very thin ($\sim 5 \mu\text{m}$) it still has a non-negligible thermal capacity. The speed with which the hot wire system can respond to turbulent fluctuations in the flow is as such limited by the thermal inertia of the hot wire. However, this can at least partially be compensated for by using in-line frequency compensation modules, which allow for obtaining an excellent frequency response ($>100 \text{ kHz}$) even when the hot wire is operated in CCA or CVA mode (Tropea et al. (2007)).

In CTA mode one runs a much smaller risk of overheating the hot wire, since the operating temperature of the wire is set directly by the experimentalist and is not the outcome of unknown flow conditions. In the electrical circuitry a Wheatstone bridge

is used to keep the resistance of the hot wire R_w at a constant value, where the wire resistance is a direct function of the wire temperature:

$$R_w = R_0(1 + \alpha_0(T_w - T_a)) \quad (2.17)$$

With R_0 the resistance of the wire at given reference conditions and α_0 the temperature coefficient of resistance. Therefore by fixing the wire resistance, also the wire temperature is kept at a constant value and a good frequency response can be obtained due to the absence of thermal inertia effects, which are compensated for by using the Wheatstone bridge setup.

A drawback of the CTA operating mode is the non-linear response of the wire to temperature fluctuations at low overheat ratios, which makes the linear modal analysis described in section 2.4.3 no longer adequate. Smits et al. (1983) therefore argued that the hot wire should only be operated in CTA mode for overheat ratios larger than 0.4.

2.4.3. LINEAR MODAL ANALYSIS AND STATIC CALIBRATION

All hot-wire measurements described in this thesis were performed in CTA operating mode. In CTA mode the wire temperature is fixed and Eq.2.8 can therefore be simplified to:

$$W = H \quad (2.18)$$

Now substituting Eqs.2.9-2.10 and Eq.2.14 for heat addition and convection losses delivers, respectively:

$$E^2 = pi \cdot l_w \cdot Nu \cdot k_{f_0} \cdot a_w \cdot T_r \cdot \frac{(R_w + R_s)^2}{R_w} \quad (2.19)$$

Applying logarithmic differentiation to Eq.2.19 and assuming small disturbances []' with respect to a mean state [] , one can write:

$$\frac{E'}{E} = S_{T_0} \frac{T'_0}{T_0} + S_u \frac{u'}{u} + S_\rho \frac{\rho'}{\rho} \quad (2.20)$$

Here S_{T_0} , S_u and S_ρ are the sensitivity coefficients to fluctuations in the total temperature, velocity and the density, respectively. Morkovin (1956) showed that Eq.2.20 can be simplified for Mach numbers larger than 1.2. For $M > 1.2$, the Nusselt number becomes virtually independent (Dewey (1965)) of the Mach number, from which it can be derived that $S_\rho = S_u = S_{\rho u}$. The hot wire is therefore only sensitive to fluctuations in the total temperature T_0 and to fluctuations in the mass flux ρu :

$$\frac{E'}{E} = S_{T_0} \frac{T'_0}{T_0} + S_{\rho u} \frac{\rho u'}{\rho u} \quad (2.21)$$

The calibration of a hot wire for supersonic applications consequently involves the determination of the two sensitivity coefficients: S_{T_0} and $S_{\rho u}$. The sensitivity coefficient $S_{\rho u}$ can be determined fairly easy by varying the total pressure in the tunnel and thus the mass flow rate in the test section, of course while keeping the total temperature constant. The sensitivity coefficient S_{T_0} is, however, harder to determine, since

most supersonic wind tunnels do not provide the capability to actively control the total temperature. Morkovin (1956) therefore proposed a different procedure, where the total temperature of the wind tunnel is kept constant, but instead the wire temperature is varied. The sensitivity coefficient S_{T_0} can then be calculated by means of the following equation:

$$S_{T_0} = \frac{1}{2} \left(n_0 + 1 - \frac{1 + A_w}{A_w} \chi' - \frac{1}{2} m_0 \right) \quad (2.22)$$

Where $n_0 = \partial \ln(k_{f_0}) / \partial \ln(T_0) \approx 0.91$ and $m_0 = \partial \ln(\mu_{f_0}) / \partial \ln(T_0) \approx 0.79$ for air at a total temperature of $T_0 = 278$ K. The coefficient χ' defines the logarithmic differential of the temperature coefficient of resistance α_0 evaluated at total temperature conditions. The Dantec 55P11 single-wire probe used in this thesis has an $\alpha_0 = 0.0036 \text{ K}^{-1}$, which translates into $\chi' \approx 1.0$. Finally, A_w defines the generalized overheat ratio which is calculated by the following relation:

$$A_w = \frac{1}{2} \frac{I_w}{R_w} \frac{\partial R_w}{\partial I_w} \quad (2.23)$$

The experimentally determined sensitivity coefficients $S_{\rho u}$ and S_{T_0} are presented in Fig.2.5 for a range of overheat ratios. The figure furthermore shows a comparison with the theoretical model described by Tropea et al. (2007) for a typical hot-wire system operated in supersonic flow in CTA mode. Notice that $S_{\rho u}$ is positive, whereas S_{T_0} is negative. That is, an increase in the mass flux leads to a stronger cooling of the wire and consequently a higher voltage is necessary to keep the wire at the same temperature. An increase in the total temperature on the other hand reduces the cooling of the wire and leads to a reduced output voltage. The sensitivity coefficient $S_{\rho u}$ reaches a value of $\sim 0.26 \pm 0.01$ for overheat ratios larger than 0.5, which is in good agreement with the theoretically predicted value of 0.25. The sensitivity coefficient S_{T_0} is also in good agreement with the theoretical model and shows a near-hyperbolic behaviour when approaching $a_w = 0$.

From Fig.2.5 it is clear that the fluctuations in the total temperature are best measured at a low overheat ratio, whereas the fluctuations in the mass flux should be determined at a high overheat ratio. For measuring the fluctuations in the total temperature an overheat ratio of $a_w = 0.4$ is used, for which the hot wire is 5.0 times more sensitive to fluctuations in the total temperature than to fluctuations in the mass flux. Lower values of the overheat would yield an even more favourable factor, but as described in section 2.4.2, linear modal analysis breaks down for hot wires operated in CTA mode for $a_w < 0.4$. For measuring the fluctuations in the mass flux an overheat ratio of $a_w = 0.93$ is used, for which the hot wire is 3.1 times more sensitive to fluctuations in the mass flux than to fluctuations in the total temperature. Higher overheat ratios were not considered safe, given the risks of overheating and burning the wire.

2.4.4. DYNAMIC CALIBRATION

The frequency response of the hot wire setup can be investigated by performing a square-wave test. A step change in the bridge voltage is applied, simulating a near-discrete

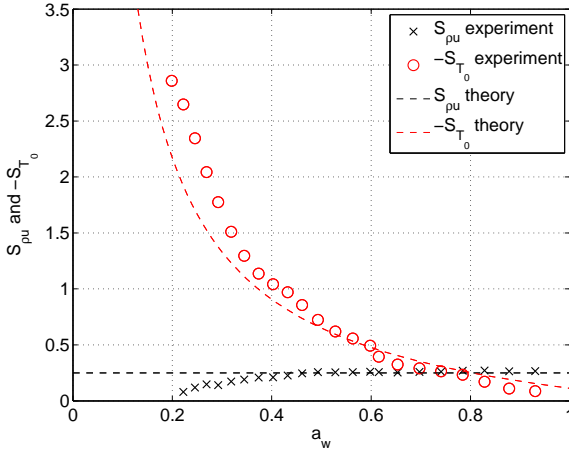


Figure 2.5: Sensitivity coefficients of the hot wire anemometer system for a range of overhear ratios, when operated in CTA mode. *System:* Dantec 55P11 single-wire probe in combination with a DISA 55M10 CTA bridge. *Tunnel operating conditions:* $M = 1.7$ and $Re_\infty = 35 \times 10^6 \text{ m}^{-1}$.

change in the velocity. The recorded output voltage (usually via a connected oscilloscope) then gives the user critical information on the stability and cut-off frequency of the hot-wire system. Fig.2.6 shows the response of the hot wire system to a square wave test for tunnel-off and tunnel-on ($M = 1.7$, $Re_\infty = 35 \times 10^6 \text{ m}^{-1}$) conditions. All experiments were performed with a Dantec 55P11 single-wire probe in combination with a DISA 55M10CTA bridge, which was set to an overhear ratio $a_w = 0.93$. The Dantec system allows for an adjustment of the servo loop's amplifier gain. A high value of the gain results in a fast response of the system, but also leads to a large undershoot in the hot wire response. For a stable operation of the hot wire system it is important that the amplitude of the undershoot is less than 15% of h , which is the amplitude of the initial voltage overshoot (Bruun (1995)). This is only the case when operating the hot wire system at a gain of $G = 222$, for which an undershoot of $0.12h$ is recorded. The cut-off frequency f_c can be calculated from the width τ_w of the initial overshoot by the following relation:

$$f_c = \frac{1}{1.3\tau_w} \quad (2.24)$$

For a gain setting $G = 222$ and tunnel-on conditions the wire response time equals $\tau_w = 11 \mu\text{s}$ and the cut-off frequency thus equals $f_c = 70 \text{ kHz}$. The cut-off frequency of the wire is much smaller under tunnel-off conditions ($f_c = 15 \text{ kHz}$), but on the other hand also more stable, in the sense that the undershoot is smaller (<5%). Under tunnel-off conditions it is therefore possible to operate the system at higher gains, while still keeping a stable response (undershoot less than $0.15h$). It is therefore important to always perform the dynamic calibration procedure while running the wind tunnel.

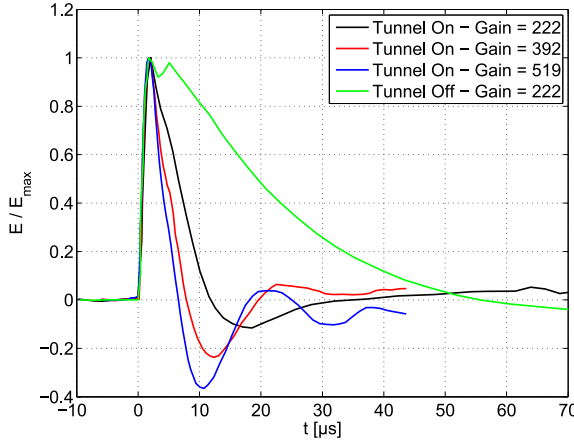


Figure 2.6: Square-wave test for tunnel-on ($M = 1.7$, $Re_\infty = 35 \times 10^6 \text{ m}^{-1}$) and tunnel-off conditions, using different gain settings.

2.4.5. DATA REDUCTION

Hot wire anemometer measurements are used in this thesis to study the freestream turbulence spectrum of the wind tunnel. In section 2.4.3 it was shown that, depending upon the overheat settings, the hot wire is sensitive to either fluctuations in the mass flux and/or to fluctuations in the total temperature. For describing the freestream conditions it would, however, also be useful to have the freestream pressure fluctuations available. The pressure fluctuations can be derived from the mass flux fluctuations under the assumption of having a purely acoustic disturbance field. This is a reasonable assumption for most supersonic wind tunnels, for which the fluctuations in the freestream are mostly caused by the acoustic waves radiated by the turbulent wall boundary layers (Laufer (1961)).

The goal of this section is therefore to find an explicit relation between the mass flux and pressure fluctuations. The first step here is to linearize the equation for the mass flux m :

$$m_\infty + m' = (\rho_\infty + \rho') \cdot (U_\infty + u') \quad (2.25)$$

$$\frac{m'}{m_\infty} = \frac{\rho'}{\rho_\infty} + \frac{u'}{U_\infty} \quad (2.26)$$

From the isentropic relations it is known that:

$$p = C \cdot \rho^\gamma \quad (2.27)$$

Which upon linearization and substitution in Eq.2.26 gives:

$$\frac{m'}{m_\infty} = \frac{1}{\gamma} \frac{p'}{p_\infty} + \frac{u'}{U_\infty} \quad (2.28)$$

The next step is to rewrite u'/U_∞ in terms of the acoustic pressure fluctuations. For that, consider the flow field sketched in Fig.2.7(a) for a stationary acoustic source placed in a supersonic flow field. The envelope of the acoustic waves forms a Mach wave, which is inclined under an angle μ with respect to the freestream. The Mach angle μ is calculated as:

$$\mu = \text{asin}\left(\frac{a \cdot t}{M_\infty \cdot a \cdot t}\right) = \text{asin}\left(\frac{1}{M_\infty}\right) \quad (2.29)$$

In a supersonic turbulent boundary layer noise is radiated by large-scale pressure-carrying eddies (Duan et al. (2014)), which are not stationary in time, but convect with the flow at a bulk Mach number M_b . Laufer (1964) showed that the bulk Mach number M_b varies in a near-linear fashion with the freestream Mach number, with $M_b = 0.34$ for $M_\infty = 2$ and $M_b = 0.57$ for $M_\infty = 5$. From the extrapolation of this trendline it is found that at a Mach number of 1.7, the bulk Mach number equals $M_b \approx 0.32$.

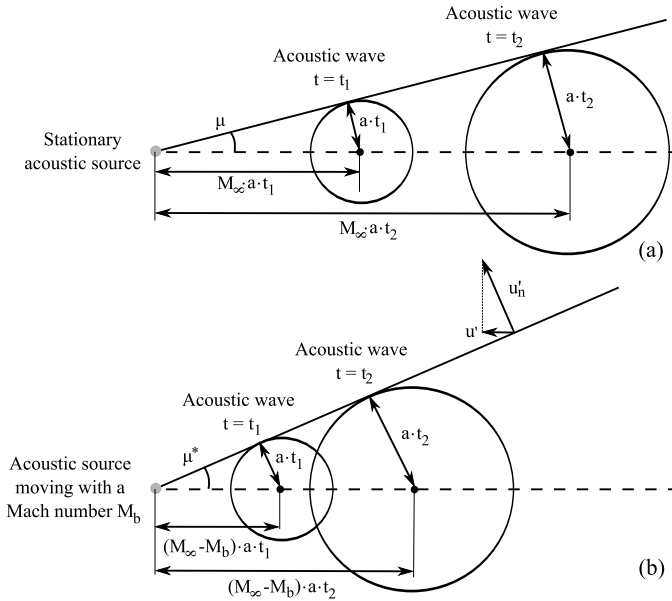


Figure 2.7: The formation of the Mach envelope for a stationary (a) and moving acoustic source (b)

Given this information it is necessary to correct Eq.2.29 for the effects of the non-stationary acoustic sources. Fig.2.7(b) shows an updated sketch of the flow field. From this figure an updated Mach angle μ^* is calculated as follows:

$$\mu^* = \text{asin}\left(\frac{1}{M_\infty - M_b}\right) \quad (2.30)$$

The pressure jump p' over the acoustic wave can be related to the velocity jump normal to the wave u'_n by the following relation (Liepmann and Roshko (1957)):

$$\frac{u'_n}{U_\infty} = -\frac{1}{\gamma M_\infty} \frac{p'}{p_\infty} \quad (2.31)$$

The hot wire is, however, only sensitive to fluctuations in the streamwise direction u' of the flow:

$$\frac{u'}{U_\infty} = \sin(\mu^*) \frac{u'_n}{U_\infty} = \frac{-1}{\gamma M_\infty (M_\infty - M_b)} \frac{p'}{p_\infty} \quad (2.32)$$

Substitution of Eq.2.32 in Eq.2.28 delivers a direct relation between the pressure and mass flux fluctuations in a supersonic flow for acoustic disturbances:

$$\frac{p'}{p_\infty} = \left(\frac{\gamma M_\infty (M_\infty - M_b)}{M_\infty (M_\infty - M_b) - 1} \right) \frac{m'}{m_\infty} \quad (2.33)$$

2.5. PARTICLE IMAGE VELOCIMETRY

Particle Image Velocimetry (PIV) is an essentially non-intrusive technique which relies upon the addition of small tracer particles to the fluid. A sketch of a typical PIV arrangement is presented in Fig.2.8. The camera in Fig.2.8 acquires two images in short succession of each other (the time delay is typically $\Delta t \sim 1\mu s$ in supersonic flows), such that the same particles are recorded in both images although shifted by a small amount. To capture these tiny and fast moving particles on film, a large amount of light is required, which is typically delivered by a laser that can produce two high-energy pulses for the given time separation Δt and ‘freezes’ the location of the particles in both frames. Using computer algorithms the particle movement from the first to the second image can be obtained. Since the time separation between both images is known, the velocity of the particle and thus of the flow can be computed.

Within this measurement chain three critical components can be identified: the flow seeding (section 2.5.1), particle imaging and illumination (section 2.5.2) and the data processing techniques (section 2.5.3). All three components will be addressed in the following sections.

2.5.1. FLOW SEEDING

The selection of the right seeding particles is of great importance when performing a PIV experiment. A key parameter here is the diameter of the particle d_p , which impacts both the light scattering properties of the particles and the response time of the particle τ_p . The amount of light scattered by the particles varies with d_p^2 in the Mie scattering regime (Raffel et al. (2007)). Mie scattering occurs when the diameter of the particle d_p is larger than the wavelength λ of the light it is reflecting, which is the case for most PIV experiments. Larger particles are therefore much easier to detect by camera and this consequently eases the requirements on the sensitivity of the camera and/or the power output of the laser. It should be mentioned here though that the light scattering properties of tracer particles are not solely determined by their diameter. Also their refractive index with respect to the surrounding fluid and their orientation of the camera with respect to the laser can greatly affect the recorded light intensity.

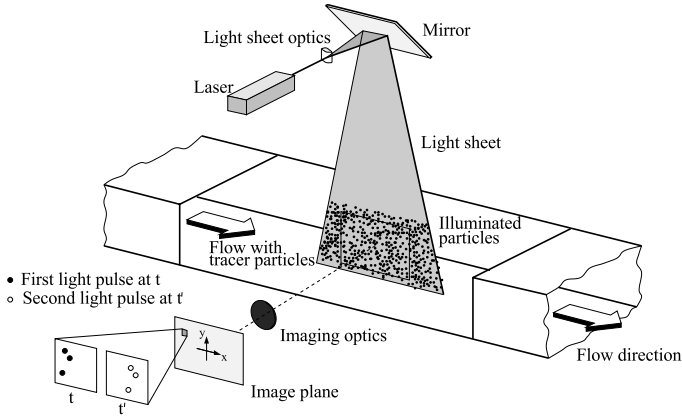


Figure 2.8: Schematic overview of a particle image velocimetry arrangement in a wind tunnel (Raffel et al. (2007))

Unfortunately, however, larger particles also suffer from having a longer response time. This is an important characteristic to take into account, especially in supersonic flows where sharp discontinuities and strong velocity gradients may occur. The motion of small spherical particles is governed by two major factors: inertia and viscous drag, as expressed by the following first order differential equation (after Melling (1997)):

$$\frac{dU_p}{dt} = -\frac{3}{4}c_d Re_{d_p} \frac{\mu_f}{\rho_p d_p^2} (U_p - U) = -K(U_p - U) \quad (2.34)$$

with c_d being the drag coefficient of the particle, ρ_p the density of the particle, Re_{d_p} the Reynolds number based on the particle diameter d_p and μ_f the dynamic viscosity of the fluid. U_p presents the velocity of the particle and U the actual velocity of the flow. The difference between U_p and U presents the slip velocity and the factor K can be viewed as the 'gain' of the system. The smaller the particle diameter, the larger the gain K and the faster the particles will respond to sudden accelerations in the flow.

In this PhD thesis, two types of seeding were used: Di-ethyl-hexyl-sebacate (DEHS) and Titaniumdioxide (TiO_2 , 30 nm grain size). DEHS is an oil-based type of seeding with a particle life time of several hours. The particles were generated by a PIVTEC PIVpart45 seeding generator. The seeding generator consists of a container with oil and a series of 45 Laskin nozzles which are dipped into the oil reservoir. The Laskin nozzles are connected via a pressure regulator to the high-pressure air supply of the laboratory. For an effective operation of the Laskin nozzles typically an overpressure of 1 bar is provided compared to the settling chamber pressure of the wind tunnel. The Laskin nozzles introduce sonic jets inside the oil reservoir, which result in the formation of small bubbles. The bubbles contain even smaller ($\sim 1 \mu\text{m}$) DEHS droplets, which are carried to the surface of the oil reservoir by the bubbles. Typically an impactor plate is installed inside of the seeder to block the larger particles and only allow the smaller particles to enter the wind tunnel.

TiO_2 particles are of a solid nature and readily available due to their many applica-

tions in industry (for instance sun screen). They have the advantage of reflecting significantly more light than the DEHS particles, while typically only having a slightly larger particle response time (Ragni et al. (2010)). The particles are injected in the tunnel by means of a home-built pressurized cyclone seeder. The advantage of a cyclone type of seeder is that a much higher seeding concentration can be obtained than with the DEHS seeder, which especially for the experiments described in part I of this thesis on thin (~ 0.2 mm) laminar boundary layer turned out to be of critical importance. The disadvantage of TiO_2 particles is that they do not evaporate like DEHS particles and remain in the tunnel for an indefinite amount of time. This can be problematic when, for instance, performing hot-wire experiments in a later stage of an experimental campaign. Large TiO_2 particles can easily break a thin hot wire. Another disadvantage of TiO_2 particles is that they tend to form agglomerates, which have a much larger response time than the original particles. These agglomerates can be broken up, at least partially, by heating (120°C for 40 minutes) the particles prior to usage.

The particle response time was assessed by means of an oblique shock wave test (Ragni et al. (2010)). A shock wave provides a near-discontinuous ($\sim 10^2$ nm) jump in the flow velocity and is therefore ideal to check the response time of the particles. The shock tests on the DEHS and TiO_2 tracer particles were performed for the same tunnel operating conditions ($M_\infty = 1.7$, $Re_\infty = 35 \times 10^6 \text{ m}^{-1}$, $\theta = 3^\circ$), but during two separate experimental campaigns with a different experimental setup. For the DEHS test case a 16 megapixel Lavision Imager Pro LX camera was used, which was operated in auto-correlation mode (i.e. both laser pulses were acquired in the first frame). For the TiO_2 test case a 2 megapixel Lavision Imager LX camera was used, which was operated in cross-correlation mode. More details on the experimental setups can be found in Table 2.1.

The particle images were rotated over the shock angle and the interrogation windows were aligned with the oblique shock wave. Processing was done by means of a home-built PIV code (Fluere), using the ensemble correlation technique and 32×128 windows (75% overlap), the windows being stretched in the direction that is tangential to the shock wave. The particle response over the shock for DEHS and TiO_2 tracer particles is presented in Figs. 2.9(a) and 2.9(b), where u_n^* is defined as:

$$u_n^* = \frac{u_n - u_{n,post}}{u_{n,pre} - u_{n,post}} \quad (2.35)$$

u_n being the velocity component normal to the shock wave and $u_{n,pre}$ and $u_{n,post}$ the normal velocity component before and after the shock, respectively.

Fig. 2.9(a) shows the velocity drop over the shock ($x_n = 0$ mm) in linear scaling. Close to the shock wave location some oscillations are observed in the velocity profile recorded for the DEHS particles, which can be attributed to aero-optical aberrations due to variations in the refractive index field (Elsinga et al. (2005a)). These distortions are less clearly present in the data acquired for the TiO_2 particles, due to a different viewing angle α of the camera with respect to the shock wave (DEHS: $\alpha = -0.6^\circ$, TiO_2 : $\alpha = -3.1^\circ$). A more elaborate discussion on how optical aberrations are affected by the viewing angle is provided in section 3.6.2. It is worth mentioning though that the estimated particle response time is virtually independent of the used camera viewing angle.

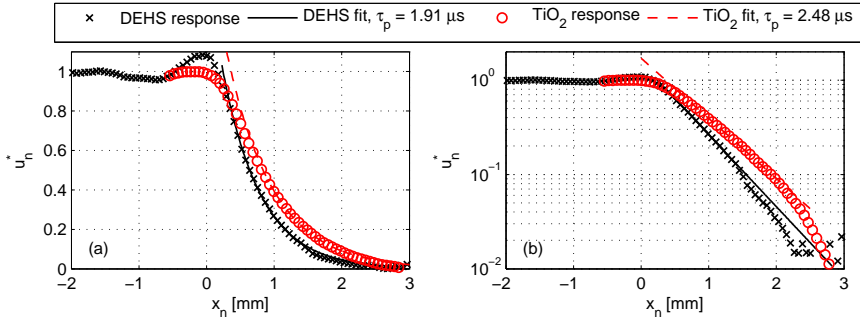


Figure 2.9: Results of the shock test in (a) linear scaling (b) semi-logarithmic scaling

In Fig.2.9b the same data as Fig.2.9a is plotted but now using a logarithmic scaling which allows for obtaining an unambiguous value of the particle response time (Ragni et al. (2010)). The exponential behaviour of the velocity decay is clearly visible and a fitting procedure delivers particle response lengths ξ_p of 0.57 mm and 0.68 mm for the DEHS and TiO_2 tracer particles, respectively. This translates into particle response times τ_p of 1.91 μs and 2.48 μs , respectively. These values agree reasonably well with the particle response time measurements performed by Ragni et al. (2010). For DEHS they measured typical response times of 1.92 - 2.02 μs and for TiO_2 (30 nm crystal size) slightly longer response times of 2.13 - 2.27 μs were reported.

Ragni et al. (2010) also found that for an accurate estimate of ξ_p and τ_p , one has to satisfy the following conditions: $WS/\xi_p < 1$ and $\Delta t/\tau_p < 1$, with WS being the window size and Δt the pulse separation. These conditions are satisfied for both the measurements on the DEHS and TiO_2 seeding particle (see Table 2.1).

Table 2.1: Experimental settings for the seeding assessment

	DEHS	TiO_2
Camera	Lavision Imager Pro LX (16 MP)	Lavision Imager LX (2MP)
Operation mode	Auto-correlation	Cross-correlation
Object focal distance f	200 mm	105 mm
F-number $f_\#$	11	16
Magnification	1.02	0.57
Spatial resolution	138 pix/mm	130 pix/mm
Pulse separation time Δt	250 ns	430 ns
WS/ξ_p	0.41	0.18
$\Delta t/\tau_p$	0.13	0.17

2.5.2. PARTICLE IMAGING

The tracer particles are projected on the CCD chip of the camera by means of a single lens or a series of lenses. The resolution of any finite sized lens is limited by the effects of

Fraunhofer diffraction. That is, a point-like feature will not be imaged as a point on the CCD chip, but as an Airy disk of finite diameter d_{diff} :

$$d_{diff} = 2.44 f_{\#} (M + 1) \lambda \quad (2.36)$$

Where $f_{\#}$ defines the ratio of lens focal distance to aperture, M defines the magnification of the recording and λ defines the wavelength of the recorded light. The recorded diameter of a finite size tracer particle d_{τ} is therefore the combined result of both geometric (d_g) and diffraction limited imaging (d_{diff}), and is calculated as:

$$d_{\tau} = \sqrt{d_g^2 + d_{diff}^2} \quad \text{with} \quad d_g = M d_p \quad (2.37)$$

Where d_p is the physical size of the tracer particle. Since most PIV applications involve very small particles ($d_p \sim 1 \mu\text{m}$) it usually holds true that $d_{diff} \gg d_g$ and thus $d_{\tau} \sim d_{diff}$. The recorded particle diameter can therefore be tuned by altering the magnification of the measurement or by operating the camera at a higher / lower $f_{\#}$. The wavelength λ can usually not be changed and is fixed by the available laser system. The ideal particle diameter for PIV measurements is on the order of ~ 2 pixels (Raffel et al. (2007)), because sub-pixel interpolation schemes usually fail for particles that are of a much smaller or larger diameter, as such limiting the accuracy of the velocity measurements.

Another important factor to consider in setting up a PIV experiment is the depth of focus δ_z of the system, which can be estimated by the following relation:

$$\delta_z = 4.88 \lambda \left(\frac{f_{\#} (M + 1)}{M} \right) \quad (2.38)$$

In-focus imaging of the particles is only possible when the lasersheet thickness is smaller than the depth of focus of the imaging system. From Eq.2.38 it follows that for high-magnification measurements it is typically necessary to also use a high value for $f_{\#}$, in order to maintain a sufficient depth of focus to image all particles in the laser sheet in focus. However, a high value for $f_{\#}$ also implies a smaller aperture and thus a reduced light intensity for the recording, which can have a negative impact on the signal-to-noise ratio of the measurement.

2.5.3. DATA REDUCTION

A PIV experiment delivers the user a series of raw PIV image pairs. Before these images can be used for the extraction of velocity field data, usually first some pre-processing steps are required to improve the quality of the recorded particles. The required pre-processing steps are tailored to the specific application and may differ from experiment to experiment. For some experiments one might want to correct for wall reflections by applying a sliding minimum filter over time (see section 8.1.3), whereas in other experiments one needs to correct for camera read-out noise or oscillating walls (see section 3.4). The specific pre-processing steps will therefore be discussed per experiment.

The pre-processed images in this thesis were further analysed by the commercially available software package Davis and / or by our in-house built PIV code Fluere. The

core of both codes is formed by the cross-correlation operator, which allows for the calculation of particle displacements from the raw PIV image pairs. To apply the cross-correlation operator, the image pairs are first divided in a 2D array of rectangular interrogation windows of size $M \times N$ pixels. Per interrogation window one velocity vector is calculated based upon the average motion of the particles contained within the volume. Most of the particles recorded in frame 1 (acquired at time t_1) should therefore also be present in frame 2 (acquired at time $t_2 = t_1 + \Delta t$), though shifted by a number of pixels (dx, dy) in the horizontal and vertical direction, respectively. The particle shift per interrogation window can be calculated by evaluating the cross-correlation coefficient between frame 1 and frame 2 for a range of particle shifts (the search radius):

$$C(dx, dy) = \frac{\sum_{i=0}^M \sum_{j=0}^N (I_1(i, j) - \mu_{I_1}) (I_2(i + dx)(j + dy) - \mu_{I_2})}{\sigma_1 \sigma_2} \quad (2.39)$$

Here I presents the intensity map of the interrogation window and μ_I presents the average intensity of that particular interrogation window. The correlation coefficient is normalized with the standard deviation σ , defined as:

$$\sigma = \sqrt{\sum_{i=0}^M \sum_{j=0}^N (I(i, j) - \mu_I)^2} \quad (2.40)$$

The location (dx, dy) with the highest correlation coefficient corresponds to the correct particle displacement for that particular interrogation window. Although correlation coefficients are usually only calculated for integer pixel shifts, sub-pixel accuracy can still be obtained by fitting a 3-point Gaussian curve to the correlation peak and its direct neighbours (Willert and Gharib (1991)). This approach typically delivers correct particle displacements within a 0.1 pixel accuracy range Raffel et al. (2007).

The size of the interrogation windows in this approach is limited by the rule-of-thumb that not more than 25% of the particles may leave the interrogation window between frame 1 and 2 (Raffel et al. (2007)). However, smaller interrogation windows and thus higher spatial resolutions are possible if a multi-grid approach is used. The particle displacements are first calculated for large interrogation windows, as such delivering the global movement of the flow. These global displacement vectors then act as a predictor for the next iteration, for which smaller interrogation windows can be used without running the risk of losing an excessive number of particles between frames. The multi-grid approach therefore makes it possible to combine the requirements of having 1) a large dynamic measurement range and 2) recording particle displacements at high resolution.

In shear flows it is furthermore very useful to apply the window deformation technique described by Scarano and Riethmuller (2000). A strong in-plane velocity gradient leads to a stretched correlation peak, for which it is harder to determine with sub-pixel accuracy the location of the peak. This can be improved by not working with rigid rectangular interrogation windows, but by deforming the windows with the local shear rate of the flow. A further decrease in correlation noise can be obtained by applying (Gaussian) window weighting to the interrogation windows (Astarita (2007)). As such putting more emphasis on the movement of the particles in the centre of the interrogation window, instead of those at the edges.

The measurement and processing uncertainties related to PIV measurements are discussed in detail in section 3.6 of this thesis, where special emphasis is placed on the difficulties involved with measuring thin (~ 0.2 mm) laminar supersonic boundary layers.

I

FLOW CONTROL FOR LAMINAR AND TRANSITIONAL OBLIQUE SHOCK WAVE REFLECTIONS

3

EXPERIMENTAL SETUP AND DATA REDUCTION TECHNIQUES

This part of the thesis focuses on a series of experiments that were performed on laminar and transitional oblique shock wave reflections. All the experiments were performed in the TST-27 transonic / supersonic blowdown wind tunnel of the TU Delft. The tunnel and flow conditions are discussed in section 3.1 of this chapter, where special attention is given to the characterization of the freestream fluctuations.

The study of laminar shock wave-boundary layer interactions necessitated the design of a new experimental setup (see section 3.2), which consists of a flat plate for growing a new laminar boundary layer and a shock generator for generating an impinging oblique shock wave. The models can be translated with respect to each other and the angle of attack of the shock generator can be changed, therefore allowing the study of laminar, transitional and turbulent interaction for a wide range of shock strengths.

Particle Image Velocimetry (PIV) served as the main flow diagnostics tool in this study, supported by oil-flow visualizations, schlieren visualizations and infrared thermography measurements. Measuring supersonic transitional boundary layers with PIV for high Reynolds number supersonic flows proved to be very challenging due to the extremely thin laminar boundary layer (~ 0.2 mm), the high shear rates (~ 0.9 pixel/pixel) and the non-uniform seeding distribution. Special attention has therefore been given to the experimental setup and the subsequent data (pre-)processing, which are described in section 3.3 and 3.4-3.5, respectively. Finally, section 3.6 provides an overview of the main sources of uncertainty and their impact on the recorded velocity field, the reversed flow region and the main boundary layer parameters.

Parts of this chapter have been published in Experiments in Fluids **56(6)** (Giepman et al. (2015b)) and parts were presented at the 44th AIAA Fluid Dynamics Conference (Giepman et al. (2014c)) and the 17th International Symposium on Application of Laser Techniques to Fluid Mechanics (Giepman et al. (2014a)).

3.1. FLOW FACILITY

The experiments were carried out in the TST-27 blowdown transonic / supersonic wind tunnel of Delft University of Technology, see Fig.3.1. The facility is able to generate flows in the Mach number range of 0.5 to 4.2 in the test section. The Mach number is set by means of a continuous variation of the throat section and flexible nozzle walls. The air is supplied from a storage vessel of 300 m³ charged to 42 bar and stored at ambient temperature, which allows a blow-down operating use of the tunnel of approximately 300 seconds maximum (depending on operating conditions), before recharging is required. Typical run times applied in practice are restricted to less than 30 sec. Due to the emptying of the storage vessel the total temperature decreases slightly during the course of a run, by approximately 4-5 K for a 30 second wind tunnel run. On average, test section total temperatures of $T_0 \approx 278$ K were recorded.

In the present experiments, tunnel operation is in the low-supersonic regime with freestream Mach numbers in the range of 1.6 - 2.3. The freestream Reynolds was fixed to a value of $Re_\infty = 35 \times 10^6 \text{ m}^{-1}$, which corresponds to stagnation pressures of 2.2 bar and 3.0 bar for freestream Mach numbers of 1.6 and 2.3, respectively.

The settling chamber of the wind tunnel has a square cross section of 800 mm \times 800 mm. In the first section of the converging nozzle the flow channel contracts in lateral direction only, to the final (constant) channel width of 280 mm. Subsequently, the nozzle upper and lower walls provide the (continuously adjustable) contoured converging-diverging shape, symmetrical with respect to the tunnel centre line, to produce the required Mach number in the test section. The distance from the throat to the centre of the test section measures approximately 2 meters. The major components and dimensions of the nozzle and test section are indicated in the technical drawing of Fig.3.1.

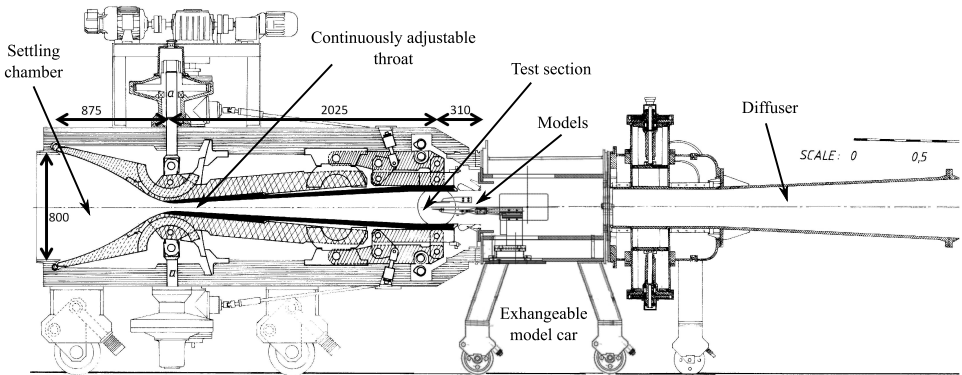


Figure 3.1: Geometry of the TST-27 transonic / supersonic blowdown wind tunnel.

As this study deals with boundary layer transition, which is sensitive to external flow disturbances (Van Driest and Blumer (1962)), hot-wire measurements were performed to quantify the freestream turbulence level of the tunnel at the baseline operating conditions ($M_\infty = 1.7$ and $Re_\infty = 35 \times 10^6 \text{ m}^{-1}$). The hot wire was operated at a relatively high overheat ratio of 0.93, in order to make sure it is mostly sensitive to fluctuations in the mass flux $(\rho u)'$ and not to fluctuations in the total temperature (see the discussion

in section 2.4). From the measurements it followed that the r.m.s. level of the freestream mass flux equals $7.7 \times 10^{-3} \rho_{\infty} u_{\infty}$.

The measured mass flux fluctuations can be converted to pressure fluctuations under the assumption that the disturbances in the tunnel are purely acoustic (Laufer (1964)), which is a reasonable assumption for a non-quiet supersonic wind tunnel (Laufer (1961)). Following the approach outlined in section 2.4.5 it is found that the r.m.s. level of the pressure fluctuations equals $1.9 \times 10^{-2} p_{\infty}$.

To further investigate the nature of the freestream disturbances, the shape of the spectrum of the pressure fluctuations has been compared to the spectra measured in the works of Laufer (1964) and Duan et al. (2014) (see Fig.3.2). Duan et al. (2014) performed DNS simulations on a supersonic ($M = 2.5$) turbulent boundary layer and analysed the radiated acoustic pressure field. Laufer (1964) performed hot wire measurements in the freestream of a $M = 2$ supersonic wind tunnel and converted the measured mass flux fluctuations to pressure fluctuations. Fig.3.2 presents the normalized power spectral density. The data of Laufer (1964) and Duan et al. (2014) is not available for $\omega\delta/U_{\infty} < 0.2$. Therefore to allow a fair comparison with the current dataset, the spectrum normalization is performed such that the integral over the frequency range $\omega\delta/U_{\infty} > 0.2$ equals unity for all three cases. For the current measurements $p_{rms}(\omega\delta/U_{\infty} > 0.2) = 1.06 \times 10^{-2} p_{\infty}$. The non-dimensional frequency bound of 0.2 corresponds to a dimensional frequency of 0.7 kHz. This is based upon a freestream velocity of $U_{\infty} = 452$ m/s and a tunnel wall boundary layer thickness of $\delta = 2.0$ cm.

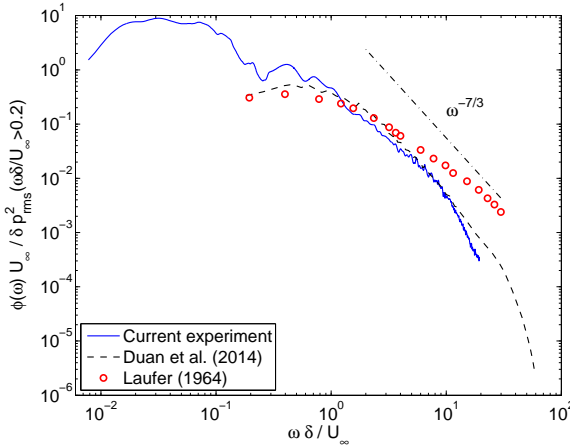


Figure 3.2: Energy spectrum of the freestream pressure fluctuations

In the work of Laufer no exact values were given for the boundary layer thickness δ . It is only mentioned that δ varies from 2.5 to 5.6 cm when increasing the freestream Mach number from 1.5 to 5. Duan et al. analysed the data of Laufer and came to the conclusion that the boundary layer thickness should have been ~ 3.1 cm for a Mach number of 2. This value has also been used here for presenting the data of Laufer in Fig.3.2.

The spectral data of the current experiment is in good agreement with the numerical data of Duan et al. Both datasets display a $\omega^{-7/3}$ frequency dependence for $1 < \omega\delta/U_{\infty} <$

10. For higher frequencies the data from the current measurement starts to deviate from the $-7/3$ scaling and starts approximating a -4.5 scaling. The data from Duan et al. breaks away from the $-7/3$ scaling for slightly higher frequencies ($\omega\delta/U_\infty > 30$) and then shows a -5 scaling. The data from Laufer shows a reasonable agreement with the data from the current experiment and the data of Duan et al. in the lower frequency range, but starts to deviate for $\omega\delta/U_\infty > 4$.

Finally, it may be observed that the data of the current experiment shows a relatively large low-frequency portion ($\omega\delta/U_\infty < 0.2$), which contains 44% of all the energy. This low-frequency noise cannot be attributed to the tunnel wall boundary layers and is probably related to a form of valve noise. Although the energy that is contained in this low-frequency band is not insignificant, it is not expected that it drastically alters the transition behaviour of a flat plate boundary layer. A stability analysis (Groot et al. (2014)) performed for this particular case shows that the growth rate of the most unstable mode in the laminar boundary layer is four orders of magnitude larger than the growth rate of modes with a frequency of $\omega\delta/U_\infty < 0.2$.

3.2. WIND TUNNEL MODELS

The experimental setup consists of two models, a full-span flat plate with a sharp leading edge ($R \sim 0.15$ mm), which is used to generate a laminar boundary layer, and a partial-span shock generator (see Fig.3.3). The shock generator is connected to the tunnel with a fixed support, underneath which sloped blocks can be fitted allowing for a discrete variation of the flow deflection angle θ . Experiments were carried out for angles in the range of $\theta = 1 - 5^\circ$. The holders of the full-span flat plate contain holes and a sliding mechanism that allows for an accurate placement of the impinging shock wave in the laminar, transitional or turbulent part of the flat plate the boundary layer.

The models were designed to be as slender as possible to limit the amount of blockage and to ensure a steady operation of the wind tunnel at this relatively low supersonic Mach number of 1.7. Schlieren visualizations were used to verify that the tunnel was started properly. Fig.3.4 shows a case where the oblique shock wave is impinging approximately 31 mm from the leading edge of the flat plate. The flat plate itself creates a very weak leading edge shock wave ($\theta \sim 0.1^\circ$), which first reflects on the shock generator and then on the flat plate (sufficiently far downstream of the area of interest).

3.3. PIV ARRANGEMENT

The PIV measurements were performed with two Lavision Imager LX cameras, placed on either side of the tunnel. The fields of view (12.5×5 mm²) of the two cameras overlap by approximately 3 mm, to allow for the proper recombination of the images. The cameras have a CCD chip of 1624×1236 pixels, which is cropped in the wall normal direction from 1236 to 651 pixels to increase the data acquisition rate (acquisition frequency of 10.2 Hz). The cameras were equipped with a 105 mm micro Nikkor lens ($f_\# = 16$), resulting in a magnification of 0.57 and a spatial resolution of 130 pixels/mm. At this resolution a 0.2 mm thick laminar boundary layer (conditions at $x = 40$ mm) is imaged onto 26 pixels. An even higher spatial resolution therefore might seem beneficial, however, increasing the magnification also implies a smaller depth of focus, which has to be compensated for by

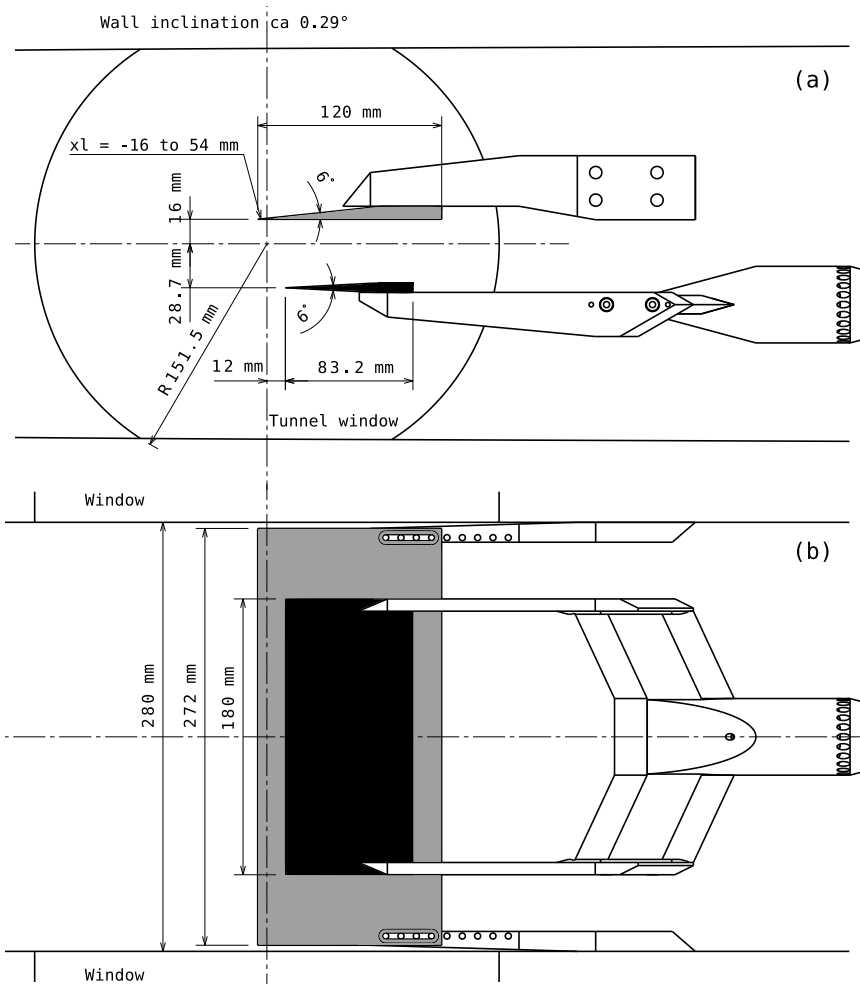


Figure 3.3: Side view (a) and bottom view (b) of the wind tunnel configuration (in grey: flat plate model, in black: shock generator)

an increase of the $f_{\#}$ to avoid out-of-focus particles. The latter has the disadvantage of lower intensity particles with a larger particle diameter. A trade-off was made between these conflicting requirements and the presented settings were found to be optimal for these particular measurement conditions.

An important advantage of the cameras that are used is the short interframe time of 430 ns that can be achieved. At the given spatial resolution, this value results in a freestream particle displacement of ~ 24 pixels between two successive frames and a shear ratio of ~ 0.9 pixel/pixel for conditions that apply to a laminar boundary layer at 40 mm from the leading edge. Although this is a relatively high value for the shear ratio (typically it is preferred to keep it below 0.3 (Meunier and Leweke (2003))), the correlation

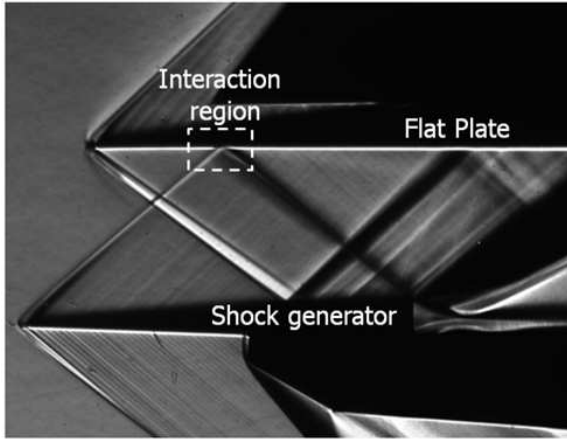


Figure 3.4: Schlieren visualization of the wind tunnel configuration

peak can still be constructed with good accuracy. For an overview of the camera settings see Table 3.1.

Illumination is provided by a double-pulse Nd:YAG Spectra Physics Quanta Ray PIV-400 laser, which is operated at a laser power of 140 mJ per pulse. The pulse duration is less than 7 ns, which translates into a particle displacement during illumination of less than 0.4 pixel and therefore introduces negligible particle blur. The flow was seeded with TiO_2 particles (30 nm crystal size), which have a response time of $\tau_p = 2.48 \mu\text{s}$ after dehydration (the seeding was heated for 40 minutes at 120°C before usage). In the region of the incident shock wave this translates into a response length of $\xi_p = 0.7 \text{ mm}$. The response time / length were determined by performing an oblique shock wave test (see also section 2.5.1).

Table 3.1: Viewing configuration of the PIV cameras

Parameter	Value
Measurement area	$12.5 \times 5.0 \text{ mm}^2$ $1624 \times 651 \text{ pixel}^2$
Laser sheet thickness	1.5 mm
Digital imaging resolution	130 pixels/mm
Object focal length	$f = 105 \text{ mm}$
F-number	$f_\# = 16$
Laser pulse separation	430 ns
Freestream particle displacement	24 pixel

3.4. PRE-PROCESSING THE PIV DATA

3.4.1. CORRECTION FOR FIXED-PATTERN CAMERA READ-OUT NOISE

The mean noise level of the Lavision Imager LX cameras is approximately 150 counts with a random component of 13 counts. Superimposed on this random noise is a constant fixed-pattern noise caused by the progressive-scan readout of the CCD chip. This noise is very weak in individual images (1-3 counts) and exhibits a negligible effect on the correlation peak for single-pair correlation. The situation is, however, different when employing the ensemble correlation technique Meinhart et al. (2000). The ensemble correlation of constant fixed-pattern noise builds up to yield a coherent component of the correlation whose height is of the order of the correlation peak resulting from the particle displacement.

Fig.3.5(a) shows an example of a typical correlation peak without the removal of the fixed-pattern noise. Diagonal lines are present in the correlation plane running from the top left to the bottom right part of the image. To estimate the location of correlation peak with sub-pixel accuracy, a 3-point Gaussian fit is employed, which uses the central peak and its direct neighbours. The accuracy of this fit is deteriorated by the presence of the diagonal lines and consequently so is the accuracy of the estimated velocity vector.

The source of these diagonal lines is expected to be related to the progressive scan read out process of the camera. Therefore, a dark camera image (no laser or particles) was analysed in the frequency domain to capture the pattern without interference from the particle images (see Fig.3.6(a)). A number of distinct peaks appear in the frequency domain, which were found to coincide with secondary peaks present in the images acquired during the experiment (see Fig.3.6(b)). The peaks are spaced by 1/8th of a wave number in x-direction and by 1/4th of a wave number in y-direction. It is therefore possible to transform all camera images to the frequency domain, remove the peaks corresponding to the read-out noise and to transform the images back using an inverse Fourier transform. After this processing step the correlation peak looks much cleaner as can be seen in Fig.3.5(b).

3.4.2. CORRECTION FOR PLATE VIBRATIONS

The plate vibrates slightly during the run (0.03 mm r.m.s.), however, due to the high magnification measurements this corresponds to wall displacements of ~ 4 pixels in the images. As a result, particle reflections from the wall sometimes enter the domain used for calculating the velocity profiles. While conversely actual particle pairs are sometimes covered by the mask that is applied to mitigate laser reflections. Therefore a procedure has been implemented that identifies the wall location in every image and then shifts all images to a nominal reference position. The wall identification method takes advantage of the particle reflections that are present in the image and positions the wall at the midpoint between the particles and their reflections.

The determination of the wall location is an iterative process. First, a wall location is assumed and the particle images below the wall are mirrored and correlated to the particle images above the wall. Ideally, for the correct wall location, the process should return a correlation peak in the origin and a correlation coefficient of 1. In practise, however, the exact location of the peak cannot be determined accurately enough due to

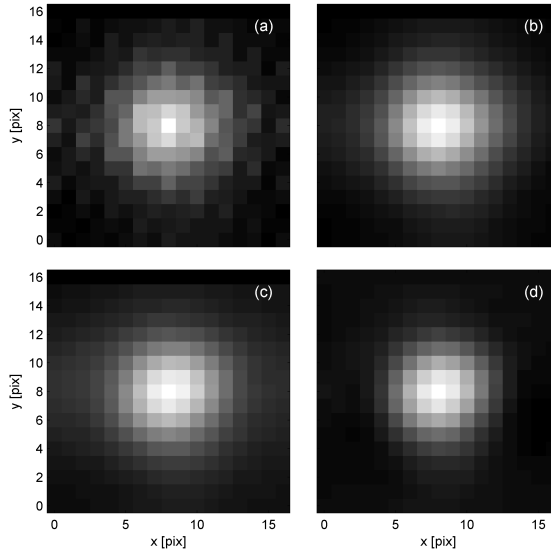


Figure 3.5: Correlation peaks obtained by means of the ensemble correlation technique in a turbulent boundary layer approximately 90 mm from the leading edge of the flat plate at $0.4\delta_{99}$. (a) No pre-processing (b) Read-out noise removed (c) Corrected for wall movements (d) Min-max filtered.

vertical streaks in the reflections and therefore only the correlation peak coefficient is used as indicator. So, for a range of possible wall locations the correlation coefficients are computed and the location that results in the highest coefficient is identified as the best approximation of the wall location.

3.4.3. NORMALIZATION OF PARTICLE INTENSITIES

The raw PIV images contain particles of widely varying intensities. To normalize the image contrast, a min-max filter is employed with a kernel size of 6 pixels, which is empirically found to deliver the best results. Min-max filtering reduces the intensity of the large / bright particles and increases the intensity of the smaller and weaker particles. This consequently reduces the average particle image diameter from 3.6 pixels before filtering to 2.4 pixels after filtering. This effect is clearly visible in the correlation peak of Fig.3.5(d), which is narrower than the one obtained without min-max filtering (Fig.3.5(c)). It is generally conceived that the three-point Gaussian peak estimators work best for particle diameter of 2-3 pixels (Raffel et al. (2007)).

3.5. PROCESSING THE PIV DATA

Because of the very thin boundary layer (~ 0.2 mm at 40 mm from the leading edge), only a limited number of pixels are available that can be used to reconstruct the velocity profile. At the given spatial resolution of 130 pixels/mm (see Table 3.1), this results in 26 pixels. Thin and elongated interrogation windows are therefore required to have a suffi-

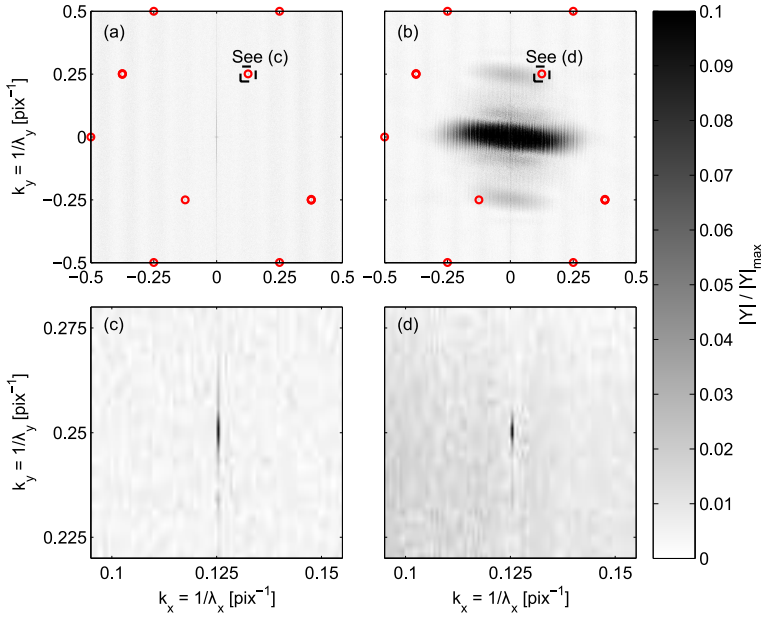


Figure 3.6: Fourier transformed camera images, presented is the normalized magnitude $|Y|/|Y|_{max}$ as a function of the wave number in x and y -direction, respectively, k_x and k_y . The red circles mark the read-out noise peaks that were identified in the dark image. (a) Dark image (b) Typical PIV image (c) Zoom of dark image at peak location (0.125, 0.25) (d) Zoom of the PIV image at peak location (0.125, 0.25).

cient number of measurement points inside the boundary layer. For the boundary layer study, windows of 256×8 pixels were used, which corresponds to 1.97 mm in the streamwise direction and 0.06 mm in the wall-normal direction. A window overlap of 75% was used in the streamwise direction and an overlap of 87.5% was used in the wall normal direction, resulting in vector pitches of 0.49 mm and 7.7 μm , respectively. These settings are summarized in Table 3.2, together with the settings that were used for processing the data from the shock wave-boundary layer interaction measurements.

Furthermore (Gaussian) window weighting is applied in order to further decrease correlation noise (Astarita (2007)). The resulting velocity fields are post-processed with a normalized median filter to remove spurious vectors (Westerweel and Scarano (2005)) and vector relocation (Theunissen et al. (2008)) is performed on vectors for which the interrogation window is overlapping the wall mask. The exact implementation of the vector-relocation algorithm of Theunissen et al. (2008) in our PIV code is discussed in Appendix A.

Because of the thin elongated interrogation windows and the relatively low seeding density close to the wall (see section 4.3), single image pair correlation is not well suited for resolving the laminar / turbulent boundary layer profile. Instead an ensemble correlation approach (Meinhart et al. (2000)) is used, which builds up the correlation plane by calculating and summing up the correlation results for all the image pairs. For the boundary layer study a total of 300 image pairs and for the measurements on the shock

wave-boundary layer interaction 600 image pairs were collected per field of view.

The image pre-processing steps were performed in Matlab and the ensemble correlation technique was implemented in our in-house built iterative multi-grid window deformation PIV code Fluere, which is based upon the work of Scarano and Riethmuller (2000).

Table 3.2: PIV processing settings

Configuration	Interrogation windows		Vector pitch	
	pixels	mm ²	<i>x</i> -dir [mm/vec]	<i>y</i> -dir [mm/vec]
Boundary layer study	256 × 8	1.97 × 0.06	0.49	7.7 × 10 ⁻³
Oblique shock wave reflection	96 × 8	0.74 × 0.06	0.18	15 × 10 ⁻³

3.6. UNCERTAINTY ANALYSIS

The PIV measurements are subject to various sources of uncertainty. This section identifies the main sources of uncertainty and discusses their impact on the measured velocity fields (sections 3.6.1 - 3.6.3). Special attention is furthermore given to the extraction of boundary layer data from the mean velocity fields (sections 3.6.4 - 3.6.5).

3.6.1. PARTICLE SLIP AND SHOCK SMEARING

The TiO₂ particles that were used for the PIV experiments described in this part of the thesis have a response time of 2.5 μs, which for the laminar flat plate boundary layer corresponds to a Stokes number of ~5.6. This is a high value, which according to the study of Samimy and Lele (1991) may result in slip velocities of up to 30% of the instantaneous local velocity. The present investigation will therefore only address the time-averaged velocity fields and will not deal with the unsteady effects associated with boundary layer transition. Also this means that under the present conditions no meaningful velocity fluctuation statistics can be obtained for the boundary layer and the interaction region. On the mean flow field, particle slip results in a smearing of flow regions that display a high streamwise velocity gradient. The incident shock wave is for instance spread over a region of ~2 mm in space.

3.6.2. AERO-OPTICAL DISTORTIONS

The presence of a shock wave in the domain of interest results in a sudden change of the refractive index n of the medium, which typically results in a blurring of the imaged tracer particles (Raffel and Kost (1998)). Blurring stretches the particles in the direction normal to the oblique shock wave and significantly increases the width of the cross-correlation peak, hereby reducing the achievable signal-to-noise ratio. The effects of blurring can be alleviated by positioning the camera under a small angle with respect to the shock wave (Elsinga et al. (2005b)). The blurred region shifts downstream in the image when the camera is looking in the downstream direction (i.e. from low to high density). The exact opposite holds true when the camera is looking in the upstream direction. Since the field of view of the current measurements is relatively small (12.5 × 5

mm²) compared to the viewing distance (~30 cm) only a small angle ($\alpha \pm 3^\circ$) is needed to shift the blurred region outside of the field of view. This significantly improves the quality of the PIV images and allows for a more accurate calculation of the velocity field.

However, as has been shown by Elsinga et al. (2005a), the shock wave not only introduces a blurring effect on the particle images, it also results in a systematic error on the velocity field in the vicinity of the shock wave, which cannot be removed by altering the angle α of the camera with respect to the shock wave. Fig.3.7 presents the measured velocity profile across the oblique shock wave for a range of different viewing angles. The viewing angle with respect to the oblique shock wave is obtained by the following goniometric relation: $\sin(\alpha) = \sin(\beta)\sin(\alpha_x)$, with α_x the rotation angle of the camera and $\beta = 39^\circ$ the shock angle. U_n in Fig.3.7 is the velocity component normal to the oblique shock wave and s the coordinate normal to the shock wave. The camera operating settings for these measurements are listed in Table 3.1 and are the same as those used for all other experiments presented in this study.

Due to the particle inertia, all velocity profiles in Fig.3.7 show an exponential decay when crossing the shock wave. Besides this well-known relaxation effect, also some additional distortions of the velocity profile are present upstream and downstream of the shock. For positive viewing angles (looking downstream) the distortion is located downstream of the shock wave and for negative viewing angles it is located upstream of the shock, which has also been observed by Elsinga et al. (2005b). For the current experimental setup a positive viewing angle delivers the worst results, with a large overshoot of 4% on U_n approximately 2.7 mm downstream of the shock wave. Slightly better results are obtained for negative viewing angles, with maximum overshoots of approximately 2.5% on U_n . Based upon this result it was decided to use negative viewing angles (α is -1 to -3°) for all measurements performed in this study.

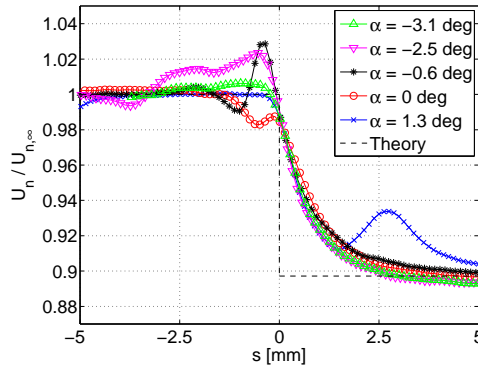


Figure 3.7: Aero-optical distortions recorded in the vicinity of the shock wave for a range of camera viewing angles

3.6.3. CROSS-CORRELATION ERRORS

The ensemble correlation approach (Meinhart et al. (2000)) is used to determine the average velocity fields for all cases investigated in this study. The quality of the velocity

field improves when more images are included in the dataset, but is limited by the finite accuracy of the 3-point Gaussian peak fitting procedure used for locating the correlation peak. An a-posteriori approach to determine the corresponding uncertainty is possible by considering the velocity variations in the freestream. In an ideal situation the converged ensemble averaged velocity in the freestream should yield the same value, small spatial variations with respect to this value can be attributed to the finite accuracy of the peak-fitting procedure. The r.m.s. value of the velocity variations is found to be 0.096% of U_∞ or equivalently 0.023 pixels for a dataset of 600 images. This value forms a lower bound on the uncertainty introduced by the ensemble correlation approach.

In a turbulent boundary layer it is much harder to build up a correlation peak than in the freestream due to the effects of shear and velocity fluctuations, which both tend to broaden the correlation peak (Scharnowski et al. (2011)). By considering the measured velocity variations with respect to the log-law an approximate upper bound can be given for the ensemble correlation uncertainty. For a fully-turbulent boundary layer ($x = 100$ mm, no impinging shock wave) it is found that the velocity variations with respect to a fitted Van Driest log-law equal 0.73% of the local U , or equivalently 0.12 pixels. The uncertainties introduced by the ensemble correlation approach are therefore expected to fall in between 0.096% and 0.73% of the local velocity U .

3.6.4. UNCERTAINTIES ON THE MEASURED REVERSED FLOW HEIGHT

The laminar boundary layer is prone to separation and consequently many of the investigated laminar SWBLIs reveal the presence of a long and flat separation bubble. The height of the reversed flow region ($u = 0$ isoline) is typically not much more than 0.2 mm, making it subject to experimental uncertainties. The three main sources of uncertainty in this respect are: 1) the estimation of the wall location, 2) cross-correlation noise and 3) uncertainties on the wall-extrapolation procedure. These factors will be discussed in this section.

The accuracy with which the wall location can be determined directly affects the accuracy with which the size of the reversed flow region can be determined. As discussed in section 3.4.2, a method has been developed that identifies the wall location in every PIV image and shifts the images to a nominal reference position. The accuracy of this method is conservatively estimated to be 1 pixel. This corresponds to approximately 8 μm , which translates into a typical uncertainty of $\sim 4\%$ on the height and length of the reversed flow region.

The velocity fields were constructed by employing the ensemble correlation technique on the PIV dataset. The laminar / transitional boundary layer displays a high velocity gradient (~ 0.9 pixel/pixel), while seeding conditions are harsh in the near-wall region and aero-optical distortions are present in the vicinity of the shock wave. It is difficult to estimate, a priori, how these individual factors will influence the reversed flow height determination. So, instead an a posteriori estimate of the uncertainty is given by investigating the amount of scatter on the reversed flow regions, as presented in Fig.5.18(a). Straight lines were fitted to the upstream portion of the reversed flow region and the cross-correlation uncertainty is estimated by calculating the r.m.s. difference between this straight line and the experimental data points. For Mach numbers of 1.6, 1.7, 2.0 and 2.3, uncertainties of, respectively, 2%, 3%, 4% and 6% with respect to max-

imum reversed flow height, were recorded. The seeding conditions in the interaction region deteriorate with increasing Mach number and also the aero-optical distortions were found to become more significant at the higher Mach numbers, as such explaining the increased uncertainties for the higher Mach numbers.

Due to a very low level of seeding in the near-wall region of laminar separation bubbles it was not possible to determine the size of the reversed flow region ($u = 0$ isoline) directly from the PIV data (see section 5.1.3). Therefore an extrapolation procedure was developed (see section 5.1.3 for more details), which fits Falkner-Skan (F-S) velocity profiles to the velocity vectors obtained in the range of $0.2 - 0.6U_\infty$. The height of the reversed flow region is then derived from the F-S fitted velocity profiles. F-S velocity profiles have been used before by other researchers (Lees and Reeves (1964)) to approximate the velocity field of laminar SWBLIs, but it remains questionable to what extent they correctly capture the flow field. Within the scope of this work it is important to know the accuracy with which we can determine the height of the reversed flow region, using this F-S extrapolation procedure.

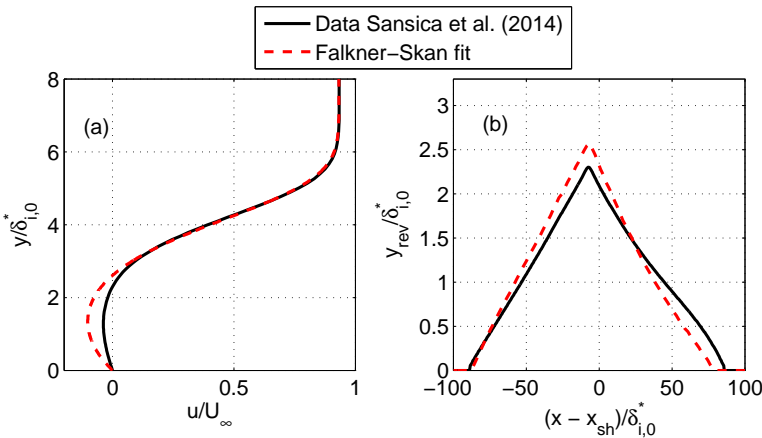


Figure 3.8: Application of the Falkner-Skan fitting procedure to the data of Sansica et al. (2014). (a) Velocity profiles compared at $x-x_{sh}/\delta_{i,0}^* = -7$. (b) Comparison of the $u = 0$ isolines

It was therefore decided to apply the F-S extrapolation procedure to the DNS data of Sansica et al. (2014), who simulated a laminar oblique shock wave reflection ($\theta = 2^\circ$) at a Mach number of 1.5 and Reynolds number of $Re_{x_{sh}} = 6.6 \times 10^5$. The reversed flow region is directly available from the numerical data and is compared with the reversed flow region that follows from the F-S extrapolation procedure (see Fig.3.8(b)), again using only the velocity data within the $0.2 - 0.6U_\infty$ velocity range. The separation location and the wall distance of maximum reversed flow are predicted correctly by the F-S extrapolation procedure. The height of the reversed flow region is, however, overestimated by $\sim 10\%$ when using the F-S extrapolation procedure. The length of the bubble on the other hand is slightly underestimated by $\sim 4\%$. These differences can be traced back to the relatively high backflow velocities predicted by the F-S velocity profiles, which are a factor of 2.7 larger than those of the DNS solution (see also Fig.3.8(a)). F-S velocity

profiles are therefore not well suited to model the details of the (non-similar) flow field inside the separation bubble, but when used as a basis for extrapolation, they do provide a reasonable approximation of the reversed flow height and length.

3.6.5. UNCERTAINTIES ON THE SHAPE FACTOR DEVELOPMENT

The incompressible shape factor H_i is used in this study as an indicator of the state of the boundary layer (laminar/turbulent) developing through the interaction region. The shape factor is subject to three main sources of uncertainty: 1) The estimation of the wall location, 2) Cross-correlation uncertainty and 3) uncertainties coming from the power-law extrapolation procedure for the near-wall region.

As discussed in the previous section, the wall location can be estimated with an accuracy of ~ 1 pixel. For the laminar boundary layer upstream of the interaction onset ($x - x_{sh} = -120\delta_{i,0}^*$, $M_\infty = 1.7$) this translates into an uncertainty of 6% on the incompressible displacement thickness, 3% on the incompressible momentum thickness and 3% on the shape factor. For a fully turbulent boundary layer downstream of the interaction ($x - x_{sh} = 120\delta_{i,0}^*$, $M_\infty = 1.7$) this delivers uncertainties of 5% on the incompressible displacement thickness, 3% for the momentum thickness and 2% on the shape factor. The slightly lower uncertainties for the turbulent boundary layer are related to the increased boundary layer thickness, which makes the relative impact of a 1 pixel offset on the integral parameters smaller.

The value of the shape factor is furthermore affected by cross-correlation uncertainties and errors made when performing the near-wall power-law extrapolation of the data. The latter is necessary because velocity vectors are never available all the way down to the wall. It is difficult, however, to estimate beforehand how these two factors will affect the shape factor. Therefore a similar approach is taken as in the previous section. That is, a smoothing spline is fitted to the data of Fig.5.18(b) and the r.m.s. difference between this spline and the experimental data points is taken as an estimate for cross-correlation and power-law modelling uncertainties. For Mach numbers of 1.6, 1.7, and 2.0 uncertainties of 4% were recorded on the shape factor. For the $M_\infty = 2.3$ case slightly higher uncertainties of 6% were recorded, due to the rather adverse seeding conditions. These uncertainties, though not negligible, are still much smaller than the jump in shape factor observed ($\sim 45\%$) at the point of boundary layer transition.

4

BOUNDARY LAYER STUDY

A good characterization of the undisturbed boundary layer and in particular the transition region is of key importance when aiming to study laminar / transitional shock wave boundary layer interactions. A combination of measurement techniques has been employed for this purpose, namely: oil-flow visualizations, spark-light schlieren, particle image velocimetry and infrared thermography measurements, which are described in sections 4.1 - 4.4, respectively. The results are found to be in good agreement with each other (section 4.5), as such delivering accurate estimates for the transition onset location, the average transition location and the transition length. The average transition location is defined as the location where the boundary layer shows a 50% intermittency level, so where the flow is turbulent / laminar half of the time. The infrared thermography measurements furthermore yielded the sensitivity of the transition location to variations in the wall temperature, with the boundary layer of course becoming more stable for lower wall temperature.

4.1. OIL-FLOW VISUALIZATION

The oil-flow visualization (Fig.4.1) shows that, on average, the boundary layer transitions into a turbulent state ~ 70 mm from the leading edge of the flat plate. The first streaks are, however, already formed upstream of this location and the transition onset location appears to be located around $x = 55 - 60$ mm. In this particular visualization two large turbulent wedges are observed that start almost directly behind the leading edge. These local regions of turbulent flow are not caused by plate imperfections, as they appear at different locations for different runs. Instead they are the result of small accumulations of TiO_2 particles that are present in the applied oil film layer. Although these accumulations are strictly spoken unwanted, they do make the distinction between laminar and

Parts of this chapter have been published in *Experiments in Fluids* **56(6)** (Giepman et al. (2015b)) and in *AIAA Journal* **53(7)** (Giepman et al. (2015c)). Furthermore, parts of the work were presented at the 44th AIAA Fluid Dynamics Conference (Giepman et al. (2014c)), the 17th International Symposium on Application of Laser Techniques to Fluid Mechanics (Giepman et al. (2014a)) and the 12th International Conference on Quantitative Infrared Thermography (Giepman et al. (2014d)).

turbulent flow very clear. Finally, the transition region is nominally two-dimensional over ± 85 mm from the centreline, which corresponds to approximately 62% of the plate span.

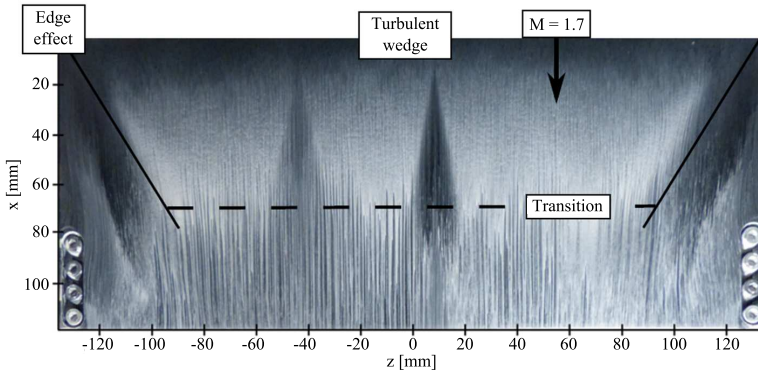


Figure 4.1: Oil-flow visualization for the undisturbed boundary layer

4.2. SPARK-LIGHT SCHLIEREN VISUALIZATIONS

Spark-light schlieren measurements were performed on the flat plate boundary layer. The spark-light delivers a short light pulse of 20 ns, thus instantaneously freezing the flow in the schlieren image. This allows the visualization of the instantaneous turbulent features in the flow and therefore also to distinguish the laminar from the turbulent part of the boundary layer. The transition location is shown (see Fig.4.2) to fluctuate between 55 and 65 mm during the course of a wind tunnel run. Such fluctuations are consistent with the intermittent character of boundary layer transition. Since the schlieren visualizations present a spanwise averaged image of the flow, any turbulent portion of the boundary layer will conceal the laminar portion of the boundary layer. The lower bound ($x = 55$ mm) that is found from the schlieren visualizations should therefore be interpreted as the transition onset location of the boundary layer.

4.3. PARTICLE IMAGE VELOCIMETRY

The major challenge of the PIV measurements proved to be the adequate seeding of the laminar boundary layer. Fig.4.3 illustrates the average seeding distribution in the flow over the plate and is obtained by stitching together a total of 12 fields of view. From this figure it is clear that there is a deficiency of seeding in the near-wall region of the flow up to about 80 mm downstream of the leading edge, which corresponds to the laminar and transitional region of the boundary layer. This behaviour is attributed to the high local streamline curvature near the leading edge (1) and the high level of rotation (large $\partial u/\partial y$) in the newly formed laminar boundary layer (2).

Regarding point (2), a particle entering the boundary layer initially moves faster than the surrounding fluid and under these conditions the particles are subjected to a positive lift force, pushing them away from the wall. Auton (1987) showed that (for incompress-

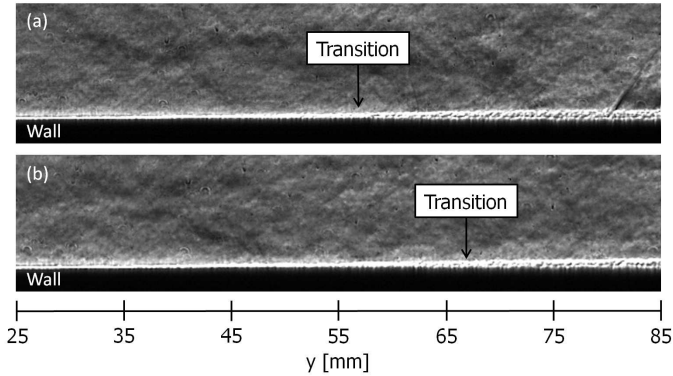


Figure 4.2: Spark-light schlieren visualization of boundary layer transition. Two snapshots are presented to highlight the intermittent character of the transition region.

ible / inviscid fluid) the acceleration experienced by the particle is proportional to the velocity gradient $\partial u / \partial y$ and the slip velocity, the latter being a function of the particle size. Larger particles have a longer response time and will experience larger slip velocities. The boundary layer therefore acts like a filter, with the smallest particles located closest to the wall and the largest particles pushed away from the wall. Since there is no mixing taking place in a laminar boundary layer, there is no mechanism that moves the ejected particles back towards the wall. So, the gap initially present between the wall and the properly seeded flow region remains and even grows when moving downstream. The latter is due to the fact that as the boundary layer grows the streamlines move away from the wall.

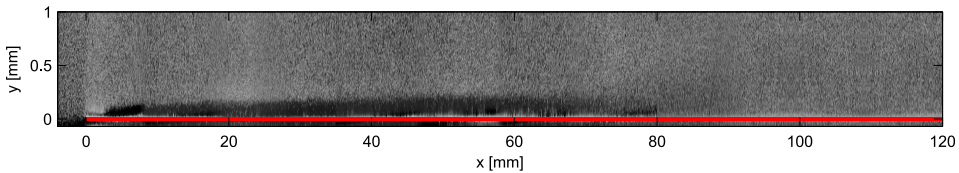


Figure 4.3: Average seeding distribution along the plate. The solid red line indicates the wall location.

A further illustration of the seeding distribution is given in Fig.4.4(a), which shows the average particles per pixel (ppp) per image at 40 mm from the leading edge, where the ppp level is calculated as the number of maxima that is, on average, detected at a particular distance from the wall. An intensity threshold was set to avoid the counting of non-physical background noise peaks, where peaks were considered to be physical when the peak intensity level was at least three times higher than the random background noise component.

From Fig.4.4(a) it is clear that virtually no seeding is detected in the first 10 pixels from the wall (which corresponds to $\sim 40\%$ of δ_{95}). Just outside of the boundary layer, at approximately 35 pixels (0.27 mm) from the wall, an accumulation of particles is found

that is the result of the particles having migrated away from the wall. At 40 mm from the leading edge δ_{95} is reached at ~ 25 pixels from the wall. The lower 10 pixels provide virtually no information for reconstructing the velocity field due to the lack of seeding, but the remaining 15 pixels can still be used to extract the top 60% of the boundary layer profile.

The resulting boundary layer profile is presented in Fig.4.4(b) together with the theoretical compressible Blasius solution (obtained by applying the Illingworth (1950) transformation to the incompressible Blasius solution). For $u \leq 0.95U_\infty$ an excellent agreement is obtained between the experimental data and the Blasius solution. Note here that the Blasius solution has not been fitted to the experimental data, but follows directly from theory. For $u \geq 0.95U_\infty$ a small discrepancy can be noted between the experimental data and the Blasius solution. The theoretical Blasius profile quickly reaches its freestream velocity, whereas the experimental data shows a longer and smoother transition to the freestream velocity. Some characteristic properties of the laminar boundary layer are summarized in Table 4.1.

4

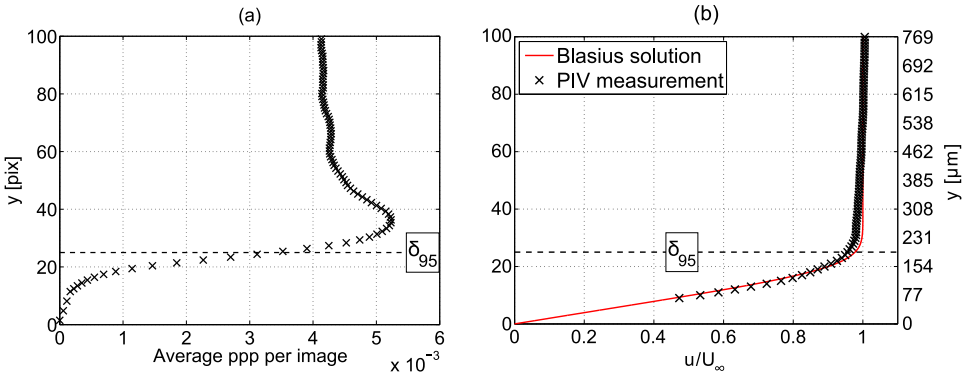


Figure 4.4: Average particle distribution in the laminar boundary layer, 40 mm from the leading edge (a) and the corresponding velocity profile (b)

Table 4.1: Boundary layer properties at $x = 40$ mm

	PIV	Blasius
δ_i^*	$87 \pm 5 \mu\text{m}$	$80 \mu\text{m}$
θ_i	$30 \pm 2 \mu\text{m}$	$29 \mu\text{m}$
H_i	2.9 ± 0.1	2.7
δ_{95}	$200 \pm 8 \mu\text{m}$	$170 \mu\text{m}$

So, even though there is virtually no seeding present in the 10 pixels closest to the wall, it is still possible to resolve the remaining 60% of the boundary layer profile. Since the experimental results agree well with the compressible Blasius solution, it can be used as a basis to extrapolate the experimental data to the wall. In Fig.4.3 one can also see that the gap without seeding slowly disappears in the region of 60 to 80 mm from the leading edge. These values agree well with the extent of the transition region as determined

by means of oil-flow and spark-light schlieren visualizations. Fig.4.3, however, provides an averaged view of the laminar-to-turbulent transition process. When considering individual images, taken at the same downstream position, an intermittent behaviour is observed (see Fig.4.5), in which the empty near-wall region is present in some images and absent in others. This confirms that in the transition regime the boundary layer is switching between a laminar and turbulent state. In the images that show a lack of seeding near the wall the boundary layer is likely to be laminar, whereas in images showing seeding all the way towards the wall as a result of increased mixing the flow is most likely turbulent.

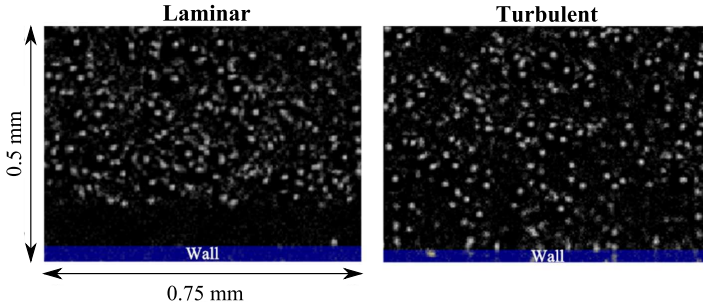


Figure 4.5: Comparison between laminar / turbulent seeding conditions in the near-wall region of the flow. The field of view is centered around $x = 70$ mm from the leading edge.

To further analyse this intermittent behaviour, the ppp levels were calculated in windows covering the region from 5-15 pixels of the wall (256 pixels were used in stream-wise direction, 75% overlap) for every individual image. If the ppp level in the window reached a value higher than 30% of the freestream ppp level for that particular image, it was qualified as turbulent and otherwise it would be qualified as laminar. The threshold value of 30% is based upon the fact that upstream of the transition region the intermittency γ should approach a value of 0, whereas downstream of the transition region it should approach a value of 1. Selecting the threshold value too low / high results in too many samples being classified as turbulent / laminar. The exact level of the threshold has little effect though on the average transition location. For threshold values in the range of 15% - 45% a variation of ± 2 mm is noted on the estimated average transition location.

Fig.4.6 shows the results of the intermittency analysis and although there is some scatter present in the experimental data, one can clearly discern a smooth transition from laminar to turbulent flow taking place over approximately 35 mm. The distribution shows an inflection point around $x = 71$ mm, where the boundary layer is laminar half of the time and turbulent the other half of the time. The experimental data is compared to the semi-empirical intermittency distribution of Dhawan and Narasimha (1958), which is given by the following relation:

$$\gamma = 1 - e^{-0.412\xi^2} \quad (4.1)$$

with γ being the intermittency and $\xi = (x - x_T)/\lambda$. Here x_T is the onset location of

the transition region and $\lambda = x_{\gamma=0.75} - x_{\gamma=0.25}$, which denotes the distance between the x -locations where the flow is turbulent 75% and 25% of the time. Based upon the experimental data from Fig.4.6, $x_T = 55$ mm and $\lambda = 13$ mm. Equation 4.1 is based on the hypothesis of a localized laminar breakdown and the formation of turbulent spots in a very small restricted region around x_T , an assumption valid for most 2D laminar flat plate boundary layers (Narasimha (1957)).

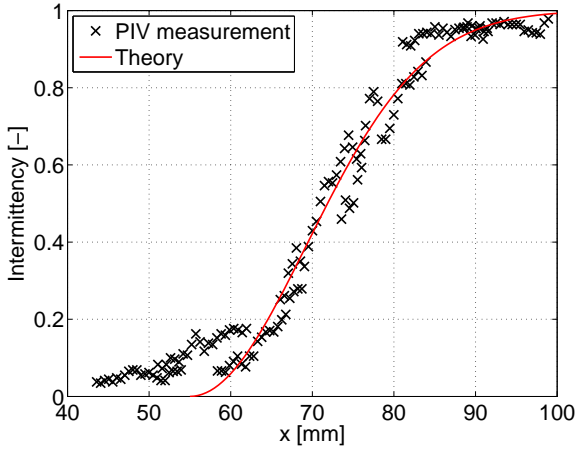


Figure 4.6: Intermittency distribution throughout the interaction region

Both the experimental data and the model of Dhawan and Narasimha (1958) are subject to a certain degree of empiricism and some discrepancies may be noted near the onset and the end of the transitional regime. The theoretical model predicts that the intermittency approaches zero at $x_T = 55$ mm, whereas the experimental data appears to level off at an intermittency level of $\gamma \approx 0.04$. This is due to the fact that in some of the images wall reflections are entering the search domain ($y = 5 - 15$ pixels) and are classified as real particles, resulting in a non-zero intermittency level. Notwithstanding these differences, it appears that the experimental data and the model of Dhawan and Narasimha (1958) both deliver the same general trend, which indicates that the seeding density in the near wall region is a suitable indicator for the state of the boundary layer.

This knowledge can be further exploited to improve the quality of the transitional velocity profiles as obtained by cross correlation. In the laminar and turbulent regime, the velocity vectors can be determined in a relatively straightforward manner using the ensemble correlation technique. However, in the transition region, the flow is switching between two distinct flow states, which makes it hard to construct a clean ensemble averaged correlation peak and consequently makes the computation of the location of this peak unreliable. This has motivated to adopt a data-processing procedure in which the image pairs are divided into two sets, of assumed laminar and turbulent flow images, which have a low and high near-wall seeding density, respectively. The ppp level in the region of 5-15 pixels from the wall is used as the indicator for the laminar / turbulent character of the boundary layer (following the same procedure as used for Fig.4.6 of the intermittency distribution). On both datasets the ensemble correlation technique is ap-

plied separately, delivering two velocity fields. For the velocity field corresponding to the laminar subset, no velocity vectors can be calculated in the near-wall region of the flow ($\leq 10 - 15$ pixels). The Blasius solution is therefore used to extrapolate the vectors outside of this region down to the wall. For the velocity field corresponding to the turbulent subset, all vectors are used. A weighted average (based on the intermittency level) of the two velocity fields is subsequently computed to obtain the velocity field in the transition region.

Fig.4.7 illustrates this weighting procedure on a velocity profile located at $x = 66$ mm, where the flow has an intermittency level of approximately 25%. As expected, the subset with the low near-wall seeding density shows an almost laminar profile ($H_i = 2.00$) and the subset with high near-wall seeding density shows a turbulent velocity profile ($H_i = 1.40$). The velocity profile that is obtained by processing the full dataset is very close ($H_i = 1.95$) to the profile that is obtained by processing the images with a low near-wall seeding density. That is because the flow at $x = 66$ mm is still mostly laminar, consequently in the ensemble correlation plane the strongest peak will be formed for the laminar option and not for the turbulent option. The resulting velocity profile is therefore biased towards the laminar solution if no correction is applied. By dividing the dataset into subsets of low and high seeding density and by applying the proper weighting a better approximation can be obtained for the transitional velocity profile. The incompressible shape factor for the weighted solution is $H_i = 1.85$ in this case. The same behaviour is also found for intermittency values larger than 50%, but now the bias is towards the turbulent solution instead of the laminar one.

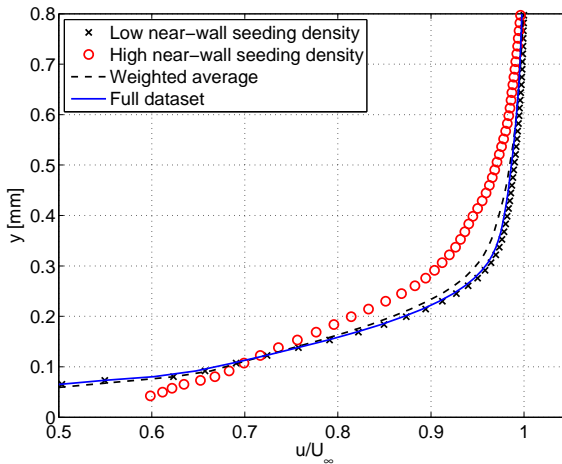


Figure 4.7: Intermittency based weighting of a transitional velocity profile ($x = 66$ mm, $\gamma = 0.25$)

The development of the boundary layer profile, from laminar, transitional to turbulent is illustrated in the six frames of Fig.4.8. At $x = 50$ and 60 mm, the data points are in good agreement with the compressible Blasius solution. In the region from $70 - 90$ mm the data points start to deviate from the laminar profile and approach the theoretical turbulent profile. At 100 mm from the leading edge the boundary layer has reached a

fully turbulent state.

Fig.4.9 shows a semi-logarithmic representation of the latter turbulent profile ($x = 100 \text{ mm}$) in terms of the inner variables $y^+ = yu_\tau/\nu_w$ and $u^+ = u_{eq}/u_\tau$. Here $u_\tau = 19.6 \text{ m/s}$ presents the friction velocity, ν_w the kinematic viscosity evaluated at the wall and u_{eq} is the Van Driest effective velocity (Van Driest (1951)), where the log-law fitting constants κ and B were set to 0.41 and 5.0, respectively. The log region can be clearly distinguished in the PIV data and also the start of the viscous sublayer is resolved. Fig.4.9 also highlights the need for vector relocation (Theunissen et al. (2008)) when performing accurate near-wall measurements. Without relocation, the near-wall velocity vectors are placed too close to the wall and the resulting velocity is biased towards a higher value. This trend is clearly visible in Fig.4.9, which shows that without vector relocation a reliable estimate of the velocity can be given down to y^+ of 27 and with vector relocation it is possible to reach a y^+ of 19. In physical units, this translates into $38 \text{ }\mu\text{m}$ and $27 \text{ }\mu\text{m}$ respectively (or alternatively 5 pixels and 3.5 pixels from the wall).

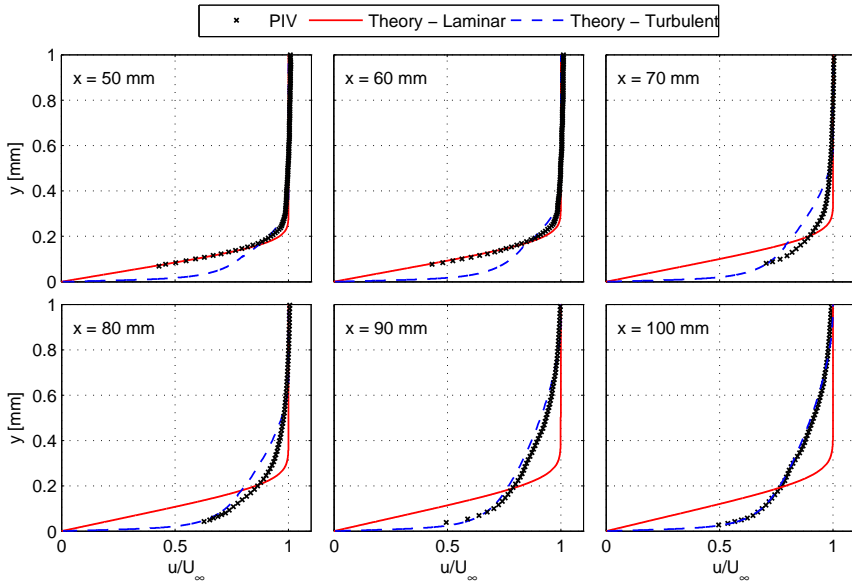


Figure 4.8: Development of the boundary layer profile along the plate

Finally, the development of the incompressible displacement thickness δ_i^* , incompressible momentum thickness θ_i and the incompressible shape factor H_i are displayed in Fig.4.10. The shape factor starts at a value of approximately 2.9 at 40 mm from the leading edge (the Blasius solution predicts a slightly lower shape factor of 2.7 under these conditions) and from 55 - 85 mm experiences a gradual drop to a value of ~ 1.35 , typical for a turbulent boundary layer. The momentum thickness shows a monotonic increase along the flat plate, whereas the displacement thickness experiences a clear drop within the transition region. The displacement thickness reaches a local maximum around $x = 64 \text{ mm}$, decreases in value until $x = 77 \text{ mm}$, and then starts to rise again.

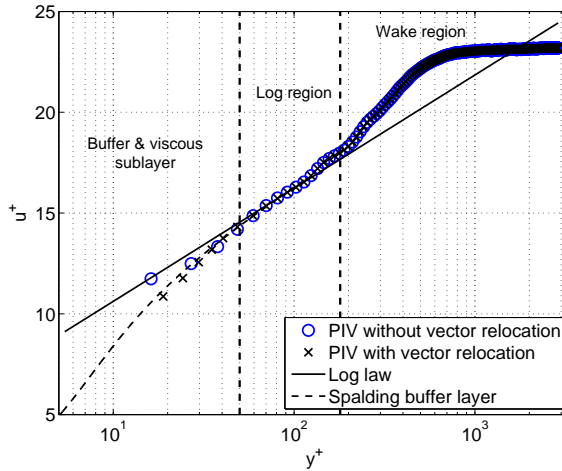


Figure 4.9: The undisturbed turbulent boundary layer profile measured at $x = 100$ mm

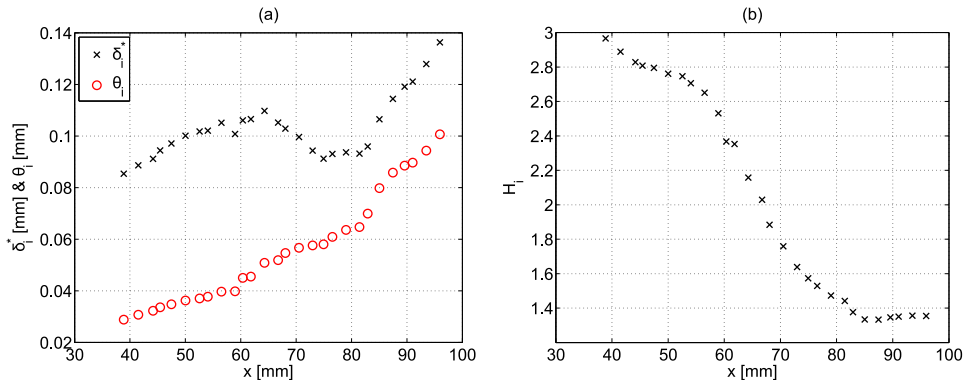


Figure 4.10: Development of the integral parameters for the undisturbed boundary layer. Incompressible momentum θ_i and displacement thickness δ_i^* (a) and incompressible shape factor H_i (b)

4.4. INFRARED THERMOGRAPHY

The infrared thermography measurements were performed on a partial-span flat plate model (see Fig.4.11), instead of on the full-span flat plate model that was used for the measurements described in sections 4.1-4.3. A different model was needed because the full-span model could only be mounted horizontally in the wind tunnel. In this configuration it is not possible for the infrared camera to correctly image the top surface of the model, because the viewing angle is too shallow. It was therefore necessary to design a new flat plate that could be mounted vertically in the wind tunnel. The latter was achieved by making the model sting-mounted and by using the same support system also used for the shock generator (see Fig.3.3).

This new model was designed to have the same leading edge radius ($R \sim 0.15$ mm) as

the full-span flat model and it was given the same surface treatment (polished / painted) as the full-span model. Infrared thermography measurements on the partial-span model furthermore revealed a nearly two-dimensional transition front over a region ± 40 from the centerline. The transition data that has been acquired by means of infrared thermography should therefore, theoretically, be in good agreement with the data acquired by the other three measurement techniques (oil-flow, schlieren and PIV).

The partial-span model was manufactured out of stainless steel T316, which has a density of $\rho = 8000 \text{ kg/m}^3$, a thermal conductivity of $k = 16.2 \text{ W/mK}$ and a specific heat capacity c_p of 500 J/kgK . These values translates into a thermal product of $\rho c_p k = 64.8 \cdot 10^6 \text{ J}^2\text{m}^{-4}\text{K}^{-2}\text{s}^{-1}$, which is two orders of magnitude higher than that of a typical polycarbonate material (for example Makrolon has a thermal product of $\rho c_p k = 0.3 \cdot 10^6 \text{ J}^2\text{m}^{-4}\text{K}^{-2}\text{s}^{-1}$). In general a low thermal product is beneficial, because it maximizes the output temperature signal for a given surface heat flux. However, polycarbonate materials did not meet the structural and aerodynamic requirements and it was therefore necessary to construct the model out of stainless steel. (It should be noted here that the thermal product of stainless steel is still approximately a factor three lower than that of a typical medium carbon alloy steel)

4

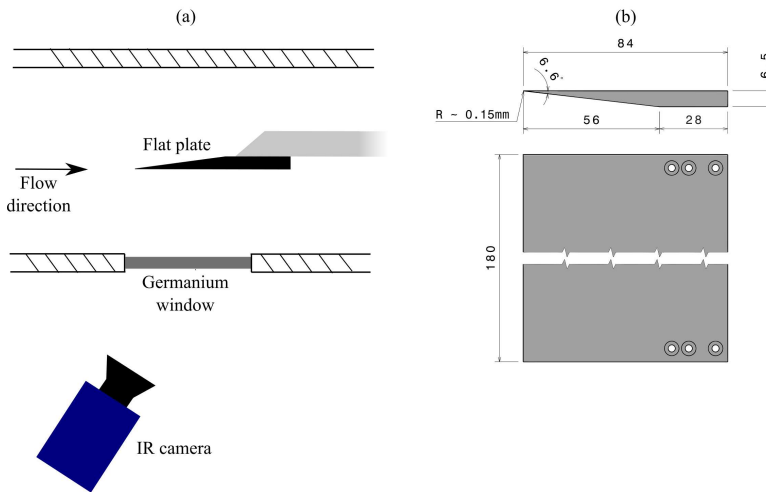


Figure 4.11: Experimental setup. (a) Sketch of the wind tunnel setup (top view) (b) Dimensions of the model in mm

The measurements were performed with a CEDIP Titanium 530L infrared camera, which uses a MCT sensor having 320×256 pixels. The camera is sensitive in the spectral range of $7.7 - 9.3 \mu\text{m}$. A Stirling cycle is used to cool the sensor, which brings down the noise equivalent temperature difference (NETD) to 25 mK . An integration time of $340 \mu\text{s}$ was used and images were recorded at a frequency of 25 Hz . The camera was equipped with a 25 mm objective, delivering a spatial resolution of 0.64 mm/pixel . During the experiments the camera was placed under an angle with respect to the window and the model (see Fig.4.11), in order to avoid any self-reflections from the camera.

Before the wind tunnel was started, the model was heated by means of a 1 kW lamp that increased the temperature of the plate to approximately 65°C. As can be seen in Fig.4.12a, the initial temperature distribution was approximately uniform, showing maximum variations of approximately 5 K. When the wind tunnel is in operation, the flow cools down the model and Fig.4.12b shows the temperature distribution after 17 seconds of running time (including approximately 3 seconds of tunnel start-up time). For a preliminary transition characterization, six 0.2 mm thick zig-zag transition strips were applied at respectively 20, 30, 40, 50, 60 and 70 mm from the leading edge. The purpose of these strips, which are clearly visible in the IR image, is to trigger transition and guarantee a turbulent boundary layer downstream of their location, allowing a qualitative transition location analysis to be inferred directly from the thermograms.

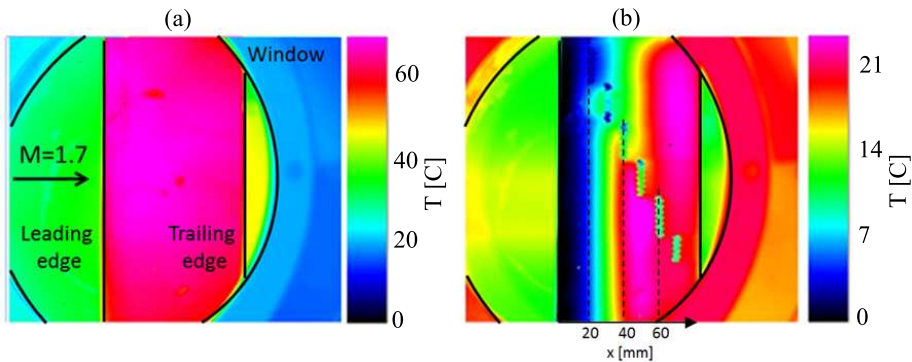


Figure 4.12: Temperature distribution before starting the tunnel (a) and after running the tunnel for 14 seconds (b)

From the raw thermograms, spatial temperature profiles can be extracted along the chord-wise direction of the plate. Fig.4.13 shows some typical temperature distributions for a unit Reynolds number of $35 \cdot 10^6 \text{ m}^{-1}$ (a) and $70 \cdot 10^6 \text{ m}^{-1}$ (b). At the location of the transition strip the temperature profiles are blanked because the measured temperature values are considered not to be valid due to the different optical and thermal properties of the strip with respect to those of the painted stainless steel of the model.

For the case of $Re_\infty = 35 \cdot 10^6 \text{ m}^{-1}$ (Fig.4.13a) the temperature profile for the clean configuration increases up to approximately 43 mm. From that point onwards the temperature decreases in streamwise direction and a plateau exists starting at 59 mm. As can be seen in Fig.4.11, the thickness of the plate increases until 56 mm from the leading edge and then maintains a constant thickness until the trailing edge. Therefore, if the complete boundary layer were laminar one would expect a steep temperature increase to continue until 56 mm. The fact that the temperature profile deviates from this trend and begins to decrease already at 43 mm is an indication that the convective heat transfer must increase there.

Furthermore, notice that the temperatures downstream of the trip at 40 and 50 mm (where a turbulent boundary layer is present) are lower than those of the clean temperature profile, indicating that for the clean configuration the flow is not yet turbulent at

these locations. After 59 mm the clean and tripped profiles again reach the same temperatures, indicating that the transition process for the clean profile is completed. Based upon these observations, it is concluded that transition is confined to the region between $x = 43 - 59$ mm from the leading edge (centered around $x = 51$ mm). The same analysis can also be carried out for the case of having a unit Reynolds number of $Re_\infty = 70 \cdot 10^6 \text{ m}^{-1}$, yielding a transition region from 24 - 32 mm (centered around 28 mm). This corresponds to transitional Reynolds numbers of $1.8 \cdot 10^6$ and $1.9 \cdot 10^6$ for the low and high unit Reynolds case, respectively.

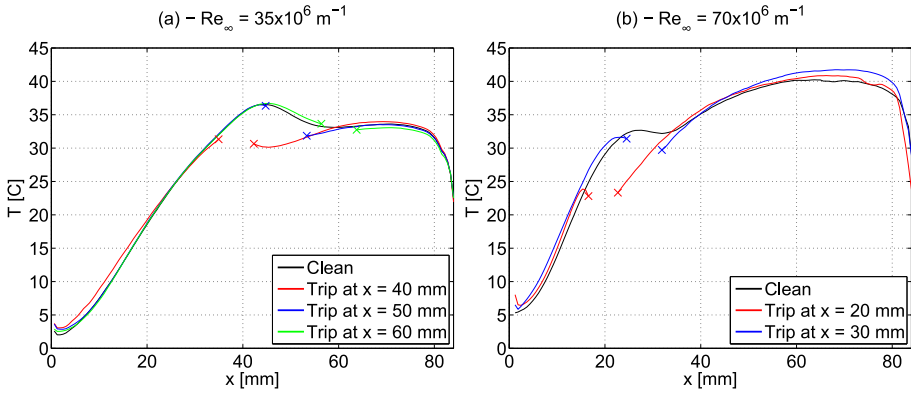


Figure 4.13: Typical temperature profiles measured for unit Reynolds numbers of $35 \cdot 10^6 \text{ m}^{-1}$ (a) and $70 \cdot 10^6 \text{ m}^{-1}$ (b)

From the preceding discussion it is clear that the temperature distribution in combination with reference temperature profiles for which the transition location is known can be useful in providing a first indication of the transition location. However, as was already noted in section 2.3.2, the temperature distribution is only indirectly affected by the transition location (by means of the surface heat flux). The exact transition location may be modulated by a possible movement of the transition front, varying plate thickness and the effects of lateral conduction, which are not accounted for in the analysis of the thermograms.

In order to get a better estimate of the transition location, it is necessary to obtain at least a qualitative impression of the instantaneous convective heat transfer distribution. Therefore, the method outlined in section 2.3.2 is used to calculate the heat flux from the temperature measurements. Fig.4.14a shows the variation of the heat transfer distribution as a function of time (for a non-tripped boundary layer), expressed in terms of the Stanton number: $St = q_w / \rho_\infty U_\infty c_{p_\infty} (T_{aw} - T_w)$, with q_w the wall heat transfer, ρ_∞ the freestream density, U_∞ the freestream velocity, c_{p_∞} the specific heat capacity of the freestream, T_w the wall temperature and T_{aw} the adiabatic wall temperature. As a reference, also the theoretical values are given for a laminar and turbulent boundary layer over an isothermal plate. For the laminar boundary layer the reference temperature concept is used in combination with the correlation of Eckert (1955). For the turbulent boundary layer Kármán-Schoenherr's relation (Schoenherr (1932)) is used in combination with a compressibility correction of Spalding and Chi (1964). For both cases, the

Reynolds analogy is used to convert the skin friction coefficients into heat flux coefficients. The Reynolds analogy, however, only strictly holds true for an isothermal wall and a zero pressure gradient flow. From Fig.4.13(a) it is clear that this does not hold true for the laminar portion of the flow, which encounters a strong temperature gradient from $x = 0 - 40$ mm. The theoretical heat transfer distribution was therefore also determined with a compressible laminar boundary layer computation, using the measured instantaneous wall temperature as boundary condition.

Close to the leading edge (~ 20 mm) a large discrepancy is found between the theoretical laminar estimates and the experiment. Whereas theory predicts a decrease in surface heat flux due to boundary layer development, the experiments actually show an increase when moving in the streamwise direction. This is accounted to the fact that at these locations, the leading edge region is extremely thin (thickness is ~ 2 mm at 20 mm) and shows a relatively high rate of convective heat transfer due to the thin laminar boundary layer. The leading edge region of the plate therefore cools down very rapidly, losing 50 degrees during the start-up phase of the tunnel, complicating the accurate determination of the heat fluxes in this region.

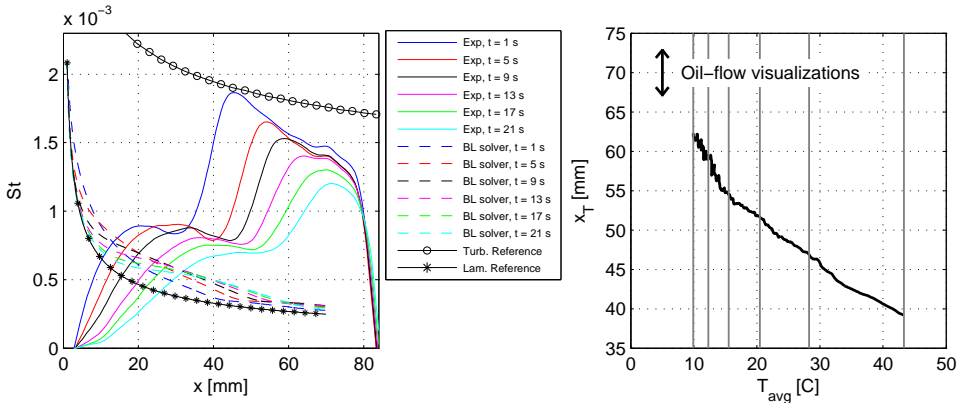


Figure 4.14: Stanton numbers recorded at various times during the run (a) and the movement of the transition location x_T as a function of the average temperature upstream of the transition location T_{avg} (b) The grey vertical lines in (b) correspond to the time instances presented in (a).

Further downstream, the experimental Stanton number can be compared with the solutions from the laminar boundary layer solver. The experimentally determined values in the laminar regime are typically 30-50% larger than those predicted by the boundary layer solver. This is probably due to the assumption that the temperatures are the same on both the top and bottom of the model when calculating the experimental heat flux. In reality there will be a temperature difference between the top and bottom surface, due to the different flow conditions. More in particular, the flow on the bottom surface has to pass an oblique shock wave first, which will increase the mass flow rate in this part. The accompanying higher convective heat flux on the bottom establishes a temperature gradient between the top and bottom surface. This additional heat conduction through the plate is not correctly accounted for by the data-reduction method, which could ex-

plain why the experimentally determined heat flux coefficient values are higher than the values following from the boundary layer solver.

The transition region, which is the main focus, is nevertheless clearly visible for all measurement times. As time progresses and the temperature of the plate drops, the transition location is observed to move downstream. Starting at approximately 39 mm from the leading edge 1 second after the tunnel is fully started and shifting 23 mm downstream to 62 mm from the leading edge after 21 seconds of run time. Fig.4.14(b) shows the transition location $x_{\gamma=0.5}$ versus the average temperature upstream of the transition location T_{avg} , showing a near-linear relation between both quantities ($\sim 0.6 \text{ mm}/^\circ\text{C}$). For temperatures below 15°C it can, however, be noted that the transition location starts to deviate from the linear trend line, showing a stronger response of the transition location to variations in the average wall temperature. As a reference, also the transition locations found by oil-flow visualizations for a cold wall ($T_{avg} \sim 5^\circ\text{C}$) are shown. Both methods are in good agreement with each other, assuming that the general trend determined by infrared thermography can also be extrapolated to lower temperatures.

The data from the current experiment can be compared qualitatively with the data from Higgins and Pappas (1951) (see Fig.4.15). Higgins and Pappas (1951) investigated the effects of wall heating on the transition location of a flat plate boundary layer at Mach 2.4. Dynamic pressure measurements were conducted to determine the start and end of the transition region. The plate was equipped with a series of electrical heaters, which provided a near-constant temperature distribution upstream of the transition location. Although the conditions of their experiment (Mach number, upstream temperature distribution and wind tunnel turbulence level) were different from those of the current study, still qualitatively the same trend is found as shown in Fig.4.15: A lower wall temperature postpones transition and this effect increases in strength when approaching the adiabatic wall temperature T_{aw} .

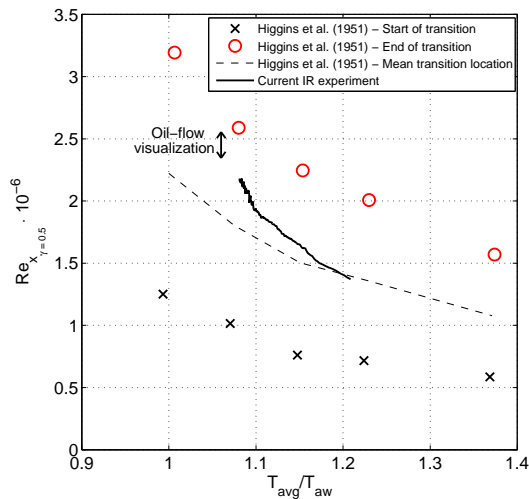


Figure 4.15: Transition Reynolds number $Re_{x_{\gamma=0.5}} = Re_{\infty} \cdot x_{\gamma=0.5}$ as a function of the temperature ratio T_{avg}/T_{aw} .

4.5. COMPARISON OF TECHNIQUES

The transition region has been characterized by means of four different measurement techniques: oil-flow visualizations, spark-light schlieren, particle image velocimetry and infrared thermography. The tunnel operating conditions were the same for all four techniques ($M_\infty = 1.7$ and $Re_\infty = 35 \times 10^6 \text{ m}^{-1}$). The only noticeable difference here is the fact that the infrared thermography measurements were performed on a partial-span (64%) flat plate model, whereas the other measurement techniques were applied to a full-span flat plate. However, both models were designed to have the same leading edge radius ($R \sim 0.15 \text{ mm}$) and were given the same surface treatment. Also the partial-span flat plate is still sufficiently wide for the flow along the centreline to not be affected by the turbulent wedges formed at the spanwise edges of the plate. The results of the infrared thermography measurements should therefore be comparable to those acquired with the other three measurement techniques. The transition locations that were found by means of the four experimental techniques are summarized in Table 4.2.

The transition onset location x_T is found to be approximately 55-60 mm ($Re_{x_T} = 1.9 - 2.1 \times 10^6$) by spark-light schlieren visualizations, oil-flow visualizations and PIV measurements. The average transition location $x_{\gamma=0.5}$ (intermittency of 50%) has been determined by three techniques (oil-flow visualization, infrared thermography and PIV) and equals approximately $\sim 70 \text{ mm}$ ($Re_{x_{\gamma=0.5}} = 2.5 \times 10^6$). The transition length L was derived from the PIV measurements and equals 35 mm. This implies that the process of transition is approximately restricted to the region of $x = 55 - 90 \text{ mm}$ on the flat plate, or in terms of Reynolds numbers from 1.9 to 3.2×10^6 . Finally, infrared thermography also delivered the sensitivity of the average transition location to the average upstream wall temperature. A sensitivity coefficient of $\sim 0.6 \text{ mm}/^\circ\text{C}$ was found. For repeatable measurements it is therefore important that the PIV measurements on the transitional shock wave-boundary layer interaction are performed at approximately the same wall temperature.

Table 4.2: Comparison of the transition locations found with the four different techniques

	x_T	$x_{\gamma=0.5}$	L	$dx_{\gamma=0.5}/dT_w$
Spark-light schlieren	55 mm			
Oil-flow visualizations	55-60 mm	70 mm		
Particle image velocimetry	55 mm	71 mm	35 mm	
Infrared thermography		68 mm		0.6 mm/ $^\circ\text{C}$

5

OBLIQUE SHOCK WAVE REFLECTIONS UNDER NATURAL TRANSITION CONDITIONS

The goal of this study was to develop a database of high-resolution PIV velocity fields of laminar, transitional and turbulent oblique shock wave reflections for a range of Mach numbers, Reynolds numbers and flow deflection angles (shock strengths). First, section 5.1 provides a comparison between the PIV data and a series of oil-flow and schlieren visualizations for the baseline tunnel operating conditions ($M_\infty = 1.7, \theta = 3^\circ$), thereby highlighting the most important differences between laminar, transitional and turbulent interactions. Section 5.2 continues on this topic by discussing the effects of flow deflection angle, Mach and Reynolds number on the topology of the interaction. Special attention is focused here on the connection between flow deflection angle, separation bubble size and transition behaviour. The data furthermore allows for a discussion of the free-interaction theory. Although the free-interaction theory is well-validated for strong interactions (Delery and Marvin (1986)), much less data is available for weak / incipiently separated interactions. Section 5.2 provides convincing evidence for the validity of the free-interaction theory, even for very weak interactions. Finally, section 5.3 provides a brief discussion of the unsteadiness of laminar oblique shock wave reflections.

5.1. LAMINAR, TRANSITIONAL AND TURBULENT INTERACTIONS

An oblique shock wave was positioned to impinge on the laminar ($x_{sh} = 51$ mm), transitional ($x_{sh} = 71$ mm) or turbulent ($x_{sh} = 101$ mm) region of the boundary layer. For the transitional case, the boundary layer has an intermittency level of approximately 50% at the shock impingement location (see Fig.4.6). The shock generator was set to induce a

Parts of this chapter have been published in Experiments in Fluids **56(6)** (Giepman et al. (2015b)) and parts were presented at the 44th AIAA Fluid Dynamics Conference (Giepman et al. (2014c)) and the 17th International Symposium on Application of Laser Techniques to Fluid Mechanics (Giepman et al. (2014a)).

flow deflection angle of 3 degrees, which corresponds to an overall theoretical pressure ratio of 1.35 (based on an inviscid shock reflection). For this particular shock strength it is expected that the laminar SWBLI shows a significant portion of reversed flow, whereas the turbulent SWBLI remains attached (see also section 1.4). The three interactions were investigated by means of oil-flow visualizations, high-speed schlieren visualizations and PIV.

5.1.1. OIL-FLOW VISUALIZATIONS

Oil-flow visualizations were performed to investigate the wall flow topology for the laminar, transitional and turbulent interaction. The images shown in Fig.5.1 were acquired while running the tunnel, because it was observed that shutting down the tunnel has a significant effect on the oil film pattern (in particular the separated regions). For the laminar case (Fig.5.1(a)) a large separation bubble (~ 10 mm in length) is formed. The size of the bubble is significantly reduced for the transitional case and for the turbulent case not more than a vague white line can be distinguished at the shock impingement location. The thin white line is not due to boundary layer separation, but is associated with the change in skin friction coefficient when crossing the interaction.

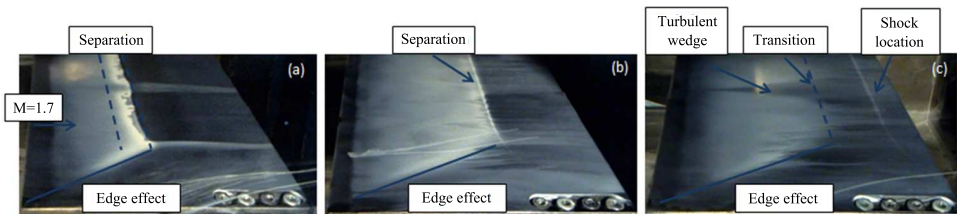


Figure 5.1: Oil-flow visualizations for the interaction between an oblique shock wave and a laminar (a), transitional (b) and turbulent (c) incoming boundary layer

5.1.2. SCHLIEREN VISUALIZATIONS

High-speed (60 kHz) schlieren visualizations provided further information on the flow field of the laminar, transitional and turbulent interactions. The laminar interaction (see Fig.5.2(a)) shows the presence of two compression waves and an expansion fan, a structure which is very similar to what has been reported by other researchers (Gadd et al. (1954) and Hakkinen et al. (1959)) and which is indicative of a separated interaction. The adverse pressure gradient imposed by the incident shock wave causes the incoming laminar boundary layer to separate well upstream of the shock impingement location, which displaces the freestream. The boundary layer therefore effectively acts as a compression ramp, creating a first series of compression waves. The separation bubble reaches its maximum height around the impingement location of the incident shock (see also the PIV results of section 5.1.3). From the top of the separation bubble an expansion fan emanates, which appears as a white region in the schlieren visualizations. Moving downstream, the boundary reattaches again and this is accompanied by a series of reattachment waves, also clearly visible in Fig.5.2(a).

The schlieren visualization for the transitional interaction of Fig.5.2(b) shows a sim-

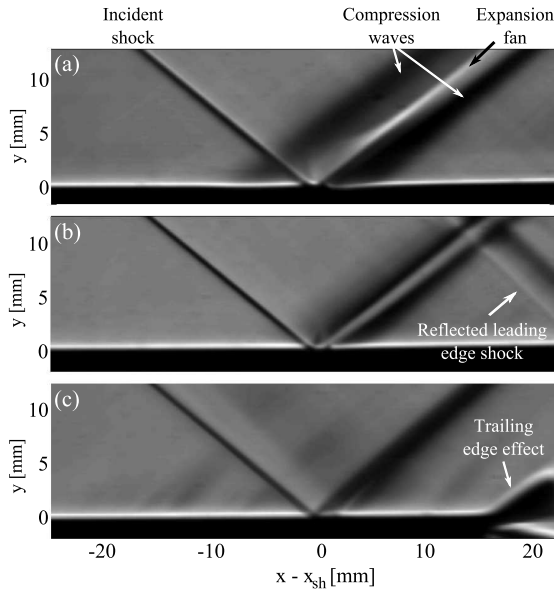


Figure 5.2: Schlieren visualizations (time-averaged) for the interaction between an oblique shock wave ($\theta = 3^\circ$) and a laminar (a), transitional (b) and turbulent (c) incoming boundary layer

ilar structure. For this case, however, the compression waves are confined to a narrower region compared to the laminar interaction. This indicates that the boundary layer is probably still separated, but that the extent of the separated zone is substantially smaller. This conclusion is in line with the oil-flow visualizations reported in the previous section.

Finally, Fig.5.2(c) presents the schlieren visualization for the fully turbulent interaction. An expansion fan is no longer (clearly) visible and the incident shock wave is reflected as a series of compression waves confined within a small (2-3 mm) region in space. This behaviour is typical for a shock wave-boundary layer interaction without separation. The ‘wave’ that is present in the schlieren image around $x - x_{sh} = 16$ mm is a result of the plate trailing edge, but is sufficiently far downstream to not influence the shock wave-boundary layer interaction.

5.1.3. PARTICLE IMAGE VELOCIMETRY

The results of the PIV measurements are presented in Figs.5.3 and 5.4 for the u - and v -component of the mean velocity field, respectively. The results are in good agreement with the schlieren visualizations and the same flow features can be identified.

For the laminar case (Figs.5.3(a) and 5.4(a)) a large separation bubble is present which starts 7.5 mm upstream of the incident shock impingement location and ends 1.4 mm downstream of the impingement location. The total length of the bubble therefore measures 8.9 mm, which corresponds to approximately 96 times the undisturbed incompressible displacement thickness $\delta_{i,0}^*$ recorded upstream of the interaction (see Fig.4.8). According to the velocity profiles, the incoming laminar boundary layer is lifted over the separation bubble and remains in a laminar state up to the impingement location of

the incident shock (see also Fig.5.8). Hereafter transition takes place and the boundary layer quickly reattaches at the wall, closing the separation bubble. The incident shock is reflected from the top of the separation bubble as an expansion fan and compression waves are formed both at the separation and reattachment location of the boundary layer.

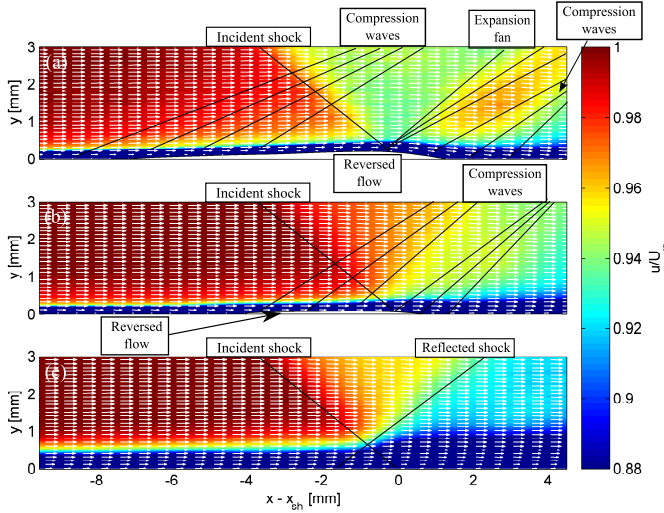


Figure 5.3: Average velocity field (u -component) of an oblique shock wave reflection ($\theta = 3^\circ$) with an incoming laminar (a), transitional ($\gamma = 0.5$) (b) and turbulent (c) boundary layer. The corresponding shock locations are, respectively, $x_{sh} = 51, 71$ and 101 mm. No reliable data could be obtained for the reversed flow region, which has therefore been blanked in Figs.(a) and (b).

The transitional case (Fig.5.3(b) and 5.4(b)) shows a significantly smaller region of reversed flow (4.3 mm; $43\delta_{i,0}^*$), which extends 3.9 mm upstream of the incident shock and 0.4 mm downstream. From the mean velocity field two regions of compression waves can be distinguished, one is formed at the separation location of the boundary layer and the other at the reattachment location. A clear expansion wave, as was found for the laminar interaction, is no longer visible in the velocity field.

For the turbulent case (Fig.5.3(c) and 5.4(c)) no separation is detected in the average flow field, which is in line with the results obtained by schlieren and oil-flow visualizations. The interaction length for the turbulent case equals approximately 1.6 mm ($\sim 11\delta_{i,0}^*$) and is calculated by extrapolating the traces of the incident and reflected shock wave down to the wall.

The seeding difficulties that were encountered when investigating the undisturbed boundary layer (see section 4.3) were also present when investigating the laminar and transitional shock wave boundary layer interactions. Although the situation is slightly alleviated by the presence of a separation bubble, which recirculates a small portion of the particles, the seeding level still remains very low compared to the freestream. Fig.5.5(a) presents the seeding distribution for the laminar shock wave-boundary layer interaction. The boundary layer is lifted over the reversed flow region and due to the initially

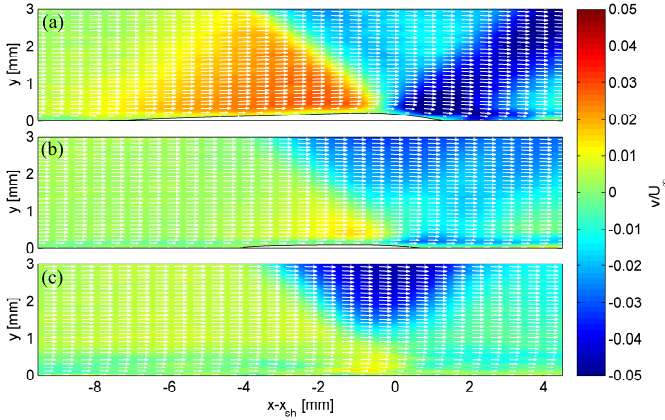


Figure 5.4: Average velocity field (v -component) of an oblique shock wave reflection ($\theta = 3^\circ$) with an incoming laminar (a), transitional ($\gamma = 0.5$) (b) and turbulent (c) boundary layer. The corresponding shock locations are, respectively, $x_{sh} = 51, 71$ and 101 mm. No reliable data could be obtained for the reversed flow region, which has therefore been blanked in Figs.(a) and (b).

laminar character of the interaction, the same applies for the seeding. The seeding density is therefore very low in the separation bubble and the signal is dominated by wall reflections. Consequently, no reliable velocity vectors could be measured in this region of the flow and the data has been blanked in Figs.5.3 and 5.4.

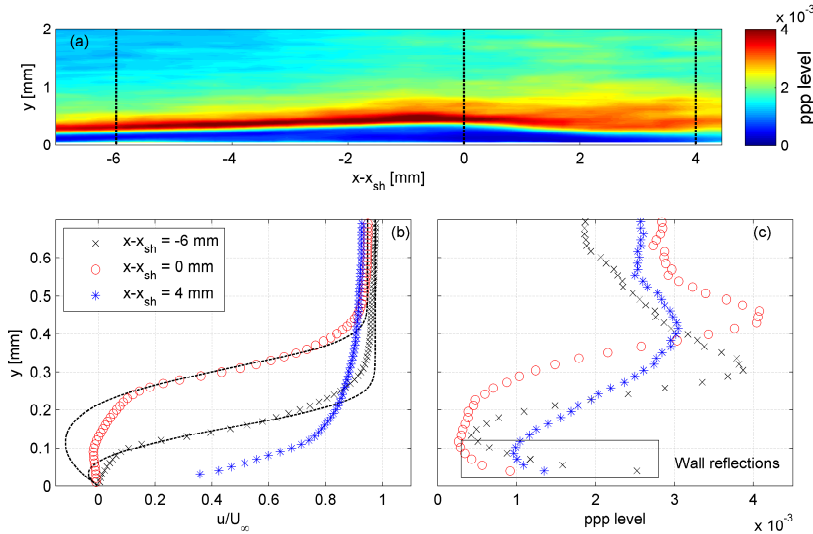


Figure 5.5: Analysis of the seeding distribution and velocity profiles for an oblique shock wave reflection with laminar incoming boundary layer ($x_{sh} = 51$ mm). (a) Seeding distribution (b) Velocity profiles; dashed lines represent fitted Falkner-Skan profiles (c) Seeding level profiles.

Although the velocity field in the separation bubble cannot be reconstructed, the data further away from the wall ($u > 0.2U_\infty$) can still be considered as reliable, because of the higher seeding density and smaller probability of encountering wall reflections. In the work of Lees and Reeves (1964) it was shown that the velocity profiles in the interaction region of a laminar SWBLI may be approximated by Falkner-Skan velocity profiles. It was therefore decided to create a database of Falkner-Skan velocity profiles. The database was created by numerically solving the Falkner-Skan equations for a wide range of pressure gradients and contained both separated (lower branch) and attached (upper branch) solutions. These profiles were fitted (see Fig.5.5(b)) to the experimental data in the velocity range from $0.2 - 0.6U_\infty$ and used to approximate the height of the reversed flow region ($u = 0$ isoline). The same fitting technique was also used for the transitional interactions to determine the height of the reversed flow region. Although Falkner-Skan velocity profiles strictly only hold true for laminar boundary layers, it was found that for mildly transitional boundary layers still a reasonable fit could be obtained between the experimental data outside of the reversed flow region and the Falkner-Skan velocity profile. This approach as such provided a first-order estimate of the height of the reversed flow region also for the transitional interactions.

5

The reversed flow regions for the laminar and transitional interaction are presented in Fig.5.6. For the laminar interaction a maximum height of 0.21 mm ($2.3\delta_{i,0}^*$) is reached approximately 0.7 mm ($7.6\delta_{i,0}^*$) upstream of the shock impingement location x_{sh} , which is defined by linearly extrapolating the incident shock wave to the wall. In practice, the shock will not reflect at the wall, but at the sonic line. Also, the shock will become steeper when entering the boundary layer. These features explain why the maximum height of the reversed flow region is reached slightly upstream of the wall shock impingement location x_{sh} .

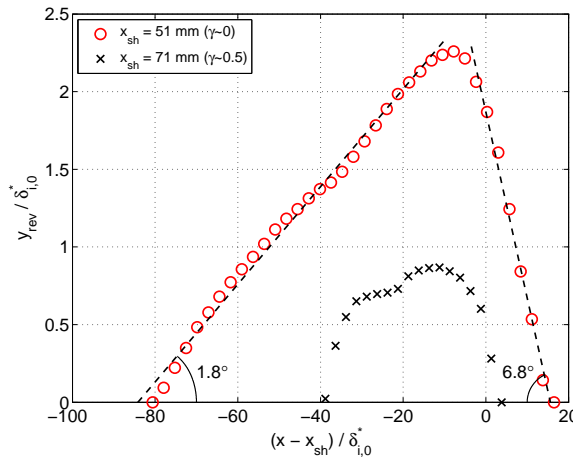


Figure 5.6: Reversed flow region for an interaction with a laminar ($x_{sh} = 51$ mm) and transitional ($x_{sh} = 71$ mm) incoming boundary layer

The reversed flow region has the typical triangular shape expected for a laminar SWBLI (Gadd et al. (1954), Hakkinen et al. (1959)). The flow deflection angle of $\alpha = 1.8^\circ$

for the upstream portion of the reversed flow region agrees very well with the theory of Hakkinen et al. (1959). By applying the principles of conservation of momentum Hakkinen et al. (1959) argues that $\alpha = \text{atan}(0.5\beta C_{ppi})$, with $\beta = \sqrt{M^2 - 1}$ and C_{ppi} the plateau pressure coefficient, for which they have found the following empirical relation: $C_{ppi} = 1.65\sqrt{2C_{f_0}/\beta}$. The skin friction coefficient upstream of the interaction C_{f_0} has been derived from the PIV data and equals 5.5×10^{-4} , which compares favourably with respect to the value of 5.3×10^{-4} predicted by the reference temperature concept for the skin friction coefficient (employing the temperature correlation of Eckert (1955)). Substituting the experimental values into the relations derived by Hakkinen et al. (1959) yields an angle $\alpha = 1.8^\circ$, which is in perfect agreement with the value of 1.8° determined directly from Fig.5.6. The angle of the downstream portion of the reversed flow region is much larger (6.8°), which is at least partially caused by the fact that the boundary layer starts to transition when crossing the incident shock wave.

The transitional case shows a much smaller reversed flow region of $43\delta_{i,0}^*$ in the streamwise direction and the maximum reversed flow height ($0.87\delta_{i,0}^*$) is achieved approximately $11\delta_{i,0}^*$ upstream of the shock impingement location. Also, the reversed flow region is no longer triangular, in contrast to the laminar interaction case.

The PIV data that has been gathered during the experiments can be used to track the state (laminar/transitional/turbulent) of the boundary layer as it develops over the separation bubble. For this purpose an adapted definition of the incompressible shape factor is introduced. In the classical definition of the shape factor, the integration is performed on the velocity field from the wall up to the freestream. This implies that the separation bubble will have a major effect on the value of the shape factor, which is undesirable if it is to be used as a metric to indicate transition. Therefore, to eliminate the contribution of the separation bubble to the shape factor a new 'artificial' wall location y_{aw} is defined by linearly extrapolating the velocity vectors in the range of $0.2-0.6U_\infty$ to 0 m/s. This implies that the data points below y_{aw} are therefore no longer used when calculating the shape factor. This procedure is illustrated in Fig.5.7 for a velocity profile extracted from the laminar SWBLI case at the reattachment location.

Fig.5.8(a) shows the shape factor H_i as calculated by the classical definition (i.e. $y_{wall} = 0$) and Fig.5.8(b) shows the shape factor $H_{i,aw}$ according to the new definition (i.e. $y_{wall} = y_{aw}$). Please keep in mind here that no velocity field data is available inside the separation bubble due to the lack of seeding. A Falkner-Skan type of extrapolation was therefore performed (see Fig.5.5(b)) to obtain an approximate velocity field in the separation bubble. Consequently, Fig.5.8(a) only presents a rough approximation of the development of the true shape factor. It is, however, clear from the figure that in this form the shape factor is not suitable as a transition indicator, as its development is dominated by the peak that results from the separated flow region.

Fig.5.8(b) on the other hand provides more insight in the transition behaviour of the boundary layer. For the laminar interaction it is clear that the boundary layer on top of the separation bubble remains in a laminar state up to the impingement location of the incident shock. After this point, transition sets in and a turbulent boundary layer flow is reached within $80 - 90\delta_{i,0}^*$, which is approximately $60 - 70\delta_{i,0}^*$ downstream of the reattachment location of the boundary layer. For the transitional interaction it can be noticed that the boundary layer shows a strong development over the separation bubble.

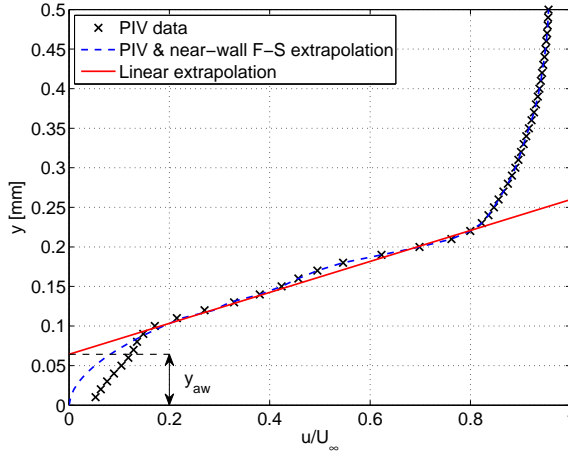


Figure 5.7: Procedure for determining a new ‘artificial’ wall location y_{aw} . The velocity profile has been extracted from the laminar SWBLI case at the reattachment location ($x - x_{sh} = 16\delta_{i,0}^*$).

5

Starting from a nearly laminar boundary layer it develops into a turbulent profile before the point of reattachment. At reattachment the boundary layer profile temporarily becomes slightly less full (with a rise in the shape factor), but a quick recovery is observed and within $\sim 60\delta_{i,0}^*$ a shape factor of 1.4 is reached, typical for a turbulent boundary layer. For the turbulent interaction only a small jump in the shape factor is observed from 1.35 to 1.67 at the shock impingement location, which implies that the turbulent boundary layer is still far removed from separation. The boundary layer shows a steady recovery and within $80\delta_{i,0}^*$ the shape factor has returned to virtually the same level as was observed upstream of the interaction.

5.2. FLOW DEFLECTION ANGLE, MACH AND REYNOLDS NUMBER EFFECTS

A parametric study has been conducted into the effects of the flow deflection angle, Mach number and Reynolds number on laminar and transitional oblique shock wave reflections. The laminar interaction that was described in the previous section will serve here as the baseline test configuration, for which: $\theta = 3^\circ$, $M_\infty = 1.7$, $x_{sh} = 51$ mm and $Re_{x_{sh}} = Re_\infty \cdot x_{sh} = 1.8 \cdot 10^6$. The effects of the flow deflection angle, Mach number and Reynolds number on the flow field were investigated systematically by changing one parameter at a time and keeping the other parameters fixed (see Tables 5.1-5.3).

Flow deflection angles were tested in the range of $\theta = 1 - 5^\circ$, which corresponds to a variation in the inviscid pressure rise over the shock reflection system of $p_3/p_1 = 1.11 - 1.64$. The Mach number was varied from 1.6 to 2.3 and the shock position Reynolds number $Re_{x_{sh}}$ from 1.4×10^6 to 3.5×10^6 . The Reynolds number variation was accomplished by varying the shock impingement location on the flat plate from $x_{sh} = 41-101$ mm, while keeping the unit Reynolds number at a constant value of $Re_\infty = 35 \times 10^6 \text{ m}^{-1}$.

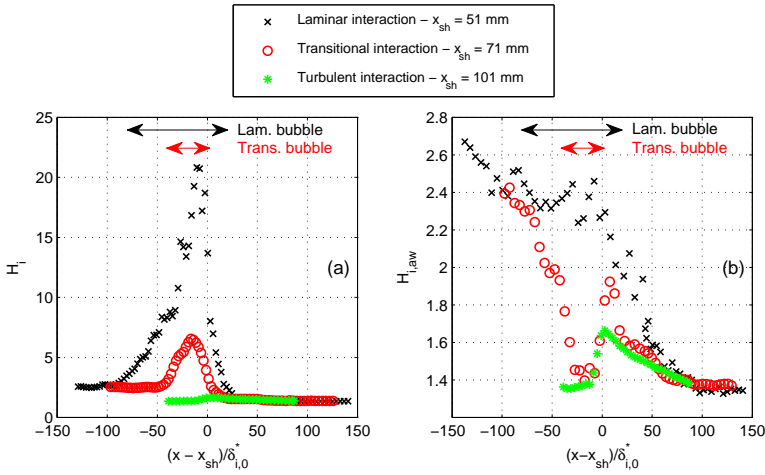


Figure 5.8: Development of the incompressible shape factor throughout a laminar, transitional and turbulent interaction. (a) Shape factor of the full boundary layer H_i (b) Shape factor of the boundary layer developing over the separation bubble $H_{i,aw}$.

The boundary layer is laminar for the $x_{sh} = 41$ and 51 mm cases, transitional for the $x_{sh} = 61, 71, 81$ and 91 mm cases, and turbulent for the $x_{sh} = 101$ mm case. This section will mostly focus though on the laminar and slightly transitional interactions.

Table 5.1: Experimental matrix – Flow deflection angle variation

Shock location	Shock Reynolds number	Mach number	Intermittency at x_{sh}	Flow deflection angle	Inviscid pressure rise
51 mm	1.8×10^6	1.7	0%	1.0°	1.11
51 mm	1.8×10^6	1.7	0%	1.3°	1.14
51 mm	1.8×10^6	1.7	0%	1.5°	1.16
51 mm	1.8×10^6	1.7	0%	1.7°	1.19
51 mm	1.8×10^6	1.7	0%	2.0°	1.22
51 mm	1.8×10^6	1.7	0%	3.0°	1.35
51 mm	1.8×10^6	1.7	0%	4.0°	1.49
51 mm	1.8×10^6	1.7	0%	5.0°	1.64

Table 5.2: Experimental matrix – Mach number variation

Shock location	Shock Reynolds number	Mach number	Intermittency at x_{sh}	Flow deflection angle	Inviscid pressure rise
51 mm	1.8×10^6	1.6	0%	3.0°	1.34
51 mm	1.8×10^6	1.7	0%	3.0°	1.35
51 mm	1.8×10^6	2.0	0%	3.0°	1.39
51 mm	1.8×10^6	2.3	0%	3.0°	1.43

Table 5.3: Experimental matrix – Reynolds number variation

Shock location	Shock Reynolds number	Mach number	Intermittency at x_{sh}	Flow deflection angle	Inviscid pressure rise
41 mm	1.4×10^6	1.7	0%	3.0°	1.35
51 mm	1.8×10^6	1.7	0%	3.0°	1.35
61 mm	2.1×10^6	1.7	8%	3.0°	1.35
71 mm	2.5×10^6	1.7	50%	3.0°	1.35
81 mm	2.8×10^6	1.7	81%	3.0°	1.35
91 mm	3.2×10^6	1.7	96%	3.0°	1.35
101 mm	3.5×10^6	1.7	100%	3.0°	1.35

5.2.1. INTERPRETATION OF THE VELOCITY FIELDS

Figs.5.9 and 5.10 present the velocity field in the interaction region for three different flow deflection angles: $\theta = 1^\circ, 3^\circ$ and 5° . The Mach and Reynolds number were fixed at $M_\infty = 1.7$ and $Re_{x_{sh}} = 1.8 \times 10^6$ ($x_{sh} = 51$ mm), respectively. A very similar flow topology is recorded for all three interactions. The incident shock wave imposes an adverse pressure gradient which separates the incoming boundary layer. For the $\theta = 1^\circ$ case ($p_3/p_1 = 1.11$) the flow is incipiently separated and a small nearly-symmetrical separation bubble is formed. The bubble grows in size with increasing flow deflection angle, with the bubble growing mostly in the direction upstream of the incident shock wave. The thickening and subsequent separation of the laminar boundary layer results in the formation of a series of compression waves, which are clearly visible in the v -component of the velocity field (Fig.5.10). The separation bubble reaches its maximum height close to the shock impingement location. From the top of the separation bubble an expansion fan emanates, which deflects the flow towards the surface. Moving further downstream, the boundary layer reattaches again an a series of compression waves is formed.

The effect of the Mach number on the velocity field is illustrated in the Figs.5.11 and 5.12, for the smallest and largest Mach number tested in this study, $M_\infty = 1.6$ and $M_\infty = 2.3$, respectively. Similar flow topologies are recorded for the low and high-Mach number case, showing the typical features (separation bubble, compression / expansion waves) expected for a separated laminar shock wave-boundary layer interaction. One obvious difference is the lower shock angle that occurs for the higher Mach number case. At $M_\infty = 1.6$ the incident shock makes an angle of 39° with the freestream, whereas for the $M_\infty = 2.3$ case, this has been reduced to 28° . These values compare favourably with those predicted by the oblique shock wave relations, which predict shock angles of 40° and 27° respectively, Also the extent of the interaction has been reduced significantly for the higher Mach number case. The separation bubble for the $M_\infty = 2.3$ case is approximately 35% shorter than the bubble for the $M_\infty = 1.6$ case.

It may be noted that for the $M_\infty = 2.3$ case there exists a small region of positive v -velocity centred around $(x-x_{sh})/\delta_{i,0}^* = 3, y/\delta_{i,0}^* = 10$, which is not present for the $M_\infty = 1.6$ case. This feature is probably the result of aero-optical distortions present in the near-vicinity of the shock wave. The camera configuration (viewing angles, aperture, etc...) was the same for both experiments, but the change in shock angle and Mach

number can still lead to differences in the observed optical distortions (see section 3.6.2). Aero-optical distortions were typically found to be slightly stronger for the higher Mach number case.

Finally, also the effect of the Reynolds number $Re_{x_{sh}}$ on the shock wave-boundary layer interaction was investigated. Figs.5.13 and 5.14 show the velocity field for shock impingement locations of $x_{sh} = 41$ mm and $x_{sh} = 61$ mm, respectively, corresponding to $Re_{x_{sh}} = 1.4 \times 10^6$ and 2.1×10^6 . The undisturbed boundary layer is fully laminar at $x_{sh} = 41$ mm while an intermittency level of $\gamma \sim 0.08$ is recorded at $x = 61$ mm (see section 4.3). The boundary layers at the onset of both interactions are still fully laminar though.

Little differences are to be noted between the two test cases, except for the smaller separation bubble that occurs in the $x_{sh} = 61$ mm case. The separation bubble measures approximately $97\delta_{i,0}^*$ in length for the $x_{sh} = 41$ mm case and $73\delta_{i,0}^*$ for the $x_{sh} = 61$ mm case. This is attributed to the slightly transitional nature of the boundary layer at shock impingement, which makes it easier for the boundary layer to overcome the pressure rise at reattachment, consequently shrinking the separation bubble. The relation between transition and the size of the separation bubble is discussed in more detail in the following section.

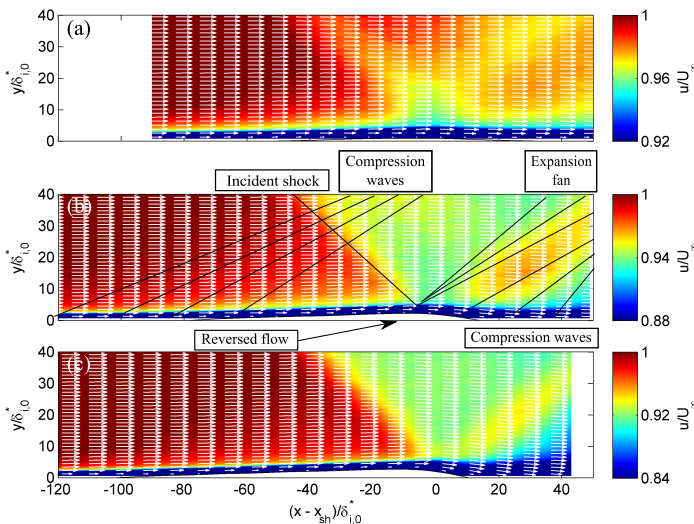


Figure 5.9: The mean streamwise velocity component for three flow deflection angles. The Mach number and Reynolds number were fixed to $M_\infty = 1.7$ and $Re_{x_{sh}} = 1.8 \times 10^6$, respectively. (a) $\theta = 1^\circ$, (b) $\theta = 3^\circ$ and (c) $\theta = 5^\circ$.

5.2.2. THE CONNECTION BETWEEN BOUNDARY LAYER SEPARATION AND TRANSITION

The goal of this section is to investigate the connection between the size and shape of the separation bubble and the state of the boundary layer throughout the interaction. This analysis is supported by the experimental data that was collected for a range of flow de-

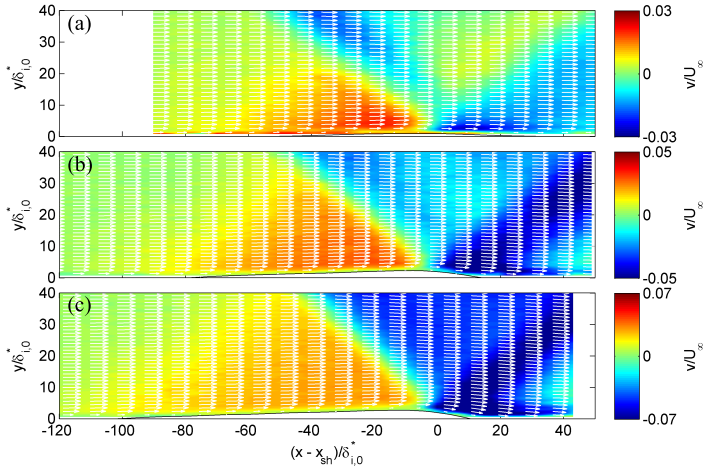


Figure 5.10: The mean wall-normal velocity component for three flow deflection angles. The Mach number and Reynolds number were fixed to $M_\infty = 1.7$ and $Re_{x_{sh}} = 1.8 \times 10^6$, respectively. (a) $\theta = 1^\circ$, (b) $\theta = 3^\circ$ and (c) $\theta = 5^\circ$.

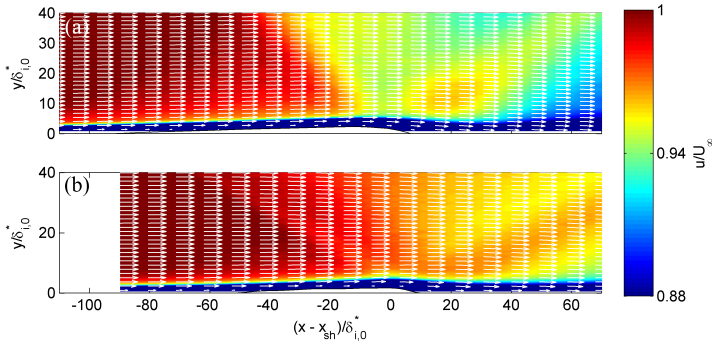


Figure 5.11: The mean streamwise velocity component for two Mach numbers. The flow deflection angle and Reynolds number were fixed to $\theta = 3^\circ$ and $Re_{x_{sh}} = 1.8 \times 10^6$, respectively. (a) $M_\infty = 1.6$ and (b) $M_\infty = 2.3$.

flection angles, Mach numbers and Reynolds numbers. The height of the reversed flow region ($u = 0$ isoline) has been determined by applying a Falkner-Skan based extrapolation procedure on the experimental data and the state of the boundary layer is estimated by calculating the incompressible shape factor over the separation bubble $H_{i,aw}$. Both data analysis techniques have been discussed in detail in section 5.1.3.

Flow deflection angles were considered in the range of $\theta = 1 - 5^\circ$ ($p_3/p_1 = 1.11 - 1.64$). The corresponding extent of the reversed flow regions is presented in Fig.15.15. The Mach and Reynolds number were fixed at $M_\infty = 1.7$ and $Re_{x_{sh}} = 1.8 \times 10^6$ ($x_{sh} = 51$ mm), respectively. The length of the upstream portion of the reversed flow region is designated

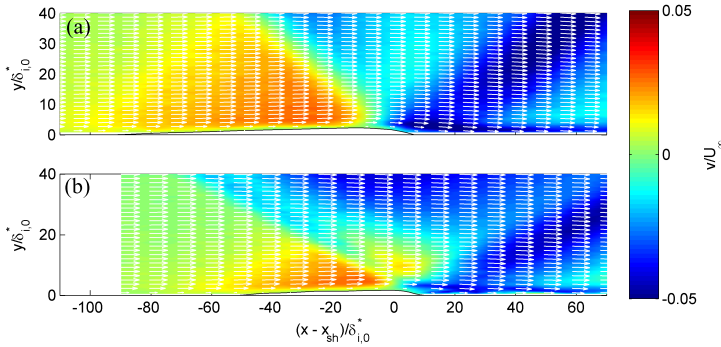


Figure 5.12: The mean wall-normal velocity component for two Mach numbers. The flow deflection angle and Reynolds number were fixed to $\theta = 3^\circ$ and $Re_{x_{sh}} = 1.8 \times 10^6$, respectively. (a) $M_\infty = 1.6$ and (b) $M_\infty = 2.3$.

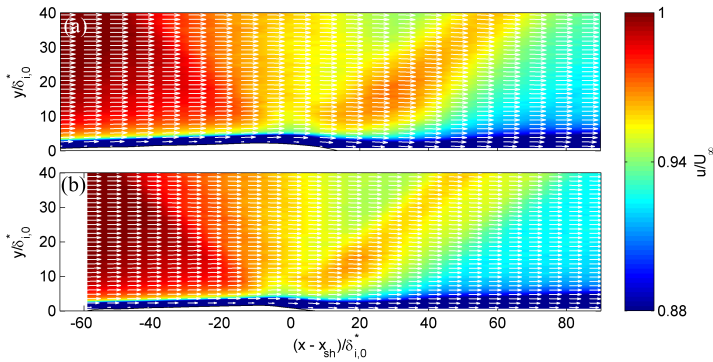


Figure 5.13: The mean streamwise velocity component for two Reynolds numbers. The flow deflection angle and Mach number were fixed to $\theta = 3^\circ$ and $M_\infty = 1.7$, respectively. (a) $Re_{x_{sh}} = 1.4 \times 10^6$ and (b) $Re_{x_{sh}} = 2.1 \times 10^6$.

as L_u and the downstream portion as L_d . These lengths are calculated by fitting straight lines to the experimental data points and calculating the intersection points with the wall (as illustrated in Fig.5.15).

For shock waves stronger than $\theta > 2^\circ$ ($p_3/p_1 > 1.22$) it is observed that the downstream portion of the separation bubble keeps a near-constant length of $20\delta_{i,0}^*$ (see also Fig.5.16). The upstream portion of the separation bubble L_u on the other hand shows a near-linear increase with the flow deflection angle. For weak shock waves ($\theta < 2^\circ$), however, a deviation from these trends is observed, as the upstream portion of the bubble is found to rapidly decrease in size with reducing shock strengths. The downstream portion of the bubble on the other hand increases in size when reducing the shock strength. For flow deflection angles of $\theta = 1^\circ - 1.3^\circ$ ($p_3/p_1 = 1.11 - 1.14$) a near-symmetrical bubble is recorded with L_u and L_d being virtually the same. Even though the $u = 0$ isoline has a symmetrical shape, this does not imply that the velocity field inside of the bubble is also symmetric. This cannot be investigated in the current study due to a lack of

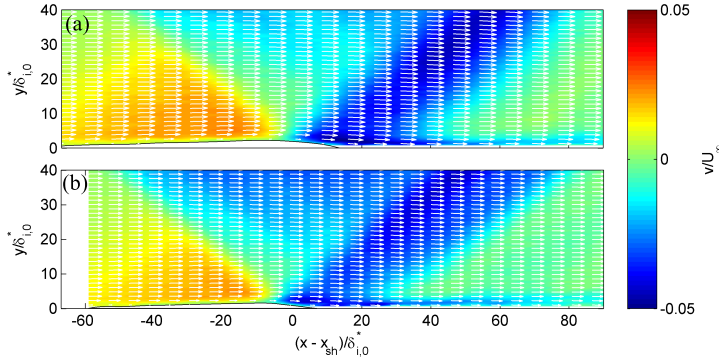


Figure 5.14: The mean wall-normal velocity component for two Reynolds numbers. The flow deflection angle and Mach number were fixed to $\theta = 3^\circ$ and $M_\infty = 1.7$, respectively. (a) $Re_{x_{sh}} = 1.4 \times 10^6$ and (b) $Re_{x_{sh}} = 2.1 \times 10^6$.

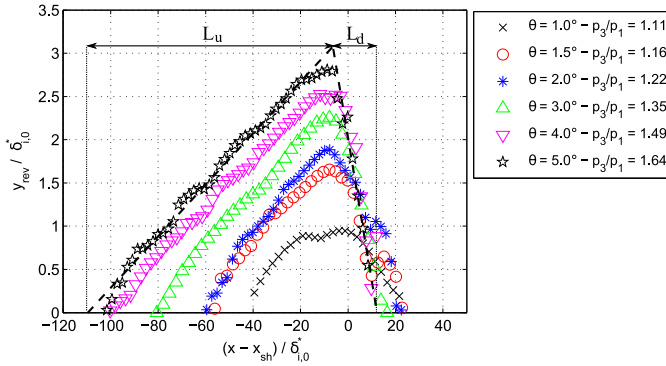


Figure 5.15: The reversed flow region as measured for a range of flow deflection angles ($M_\infty = 1.7$, $x_{sh} = 51$ mm)

particles in the very near-wall portion of the boundary layer (see discussion in section 5.1.3). It has, however, been shown in several numerical studies (Reyhner and Flügge-Lotz (1968); Katzer (1989); Sansica et al. (2014)) that although fully laminar interaction typically show a near-symmetrical $u = 0$ isoline, the velocity field inside of the bubble is found to be asymmetrical.

The incipient separation threshold of Fig.5.16 is derived from the free-interaction of Chapman et al. (1957) and can be written as Eq.5.1

$$\frac{p_{inc}}{p_\infty} = 1 + C_{sep} \gamma M_0^2 \sqrt{\frac{2C_{f_0}}{(M_0^2 - 1)^{0.5}}} \tag{5.1}$$

With C_{f_0} and M_0 being the skin friction coefficient and the freestream Mach number at the interaction onset, respectively. The precise value of the constant C_{sep} is difficult to determine due to the small size of laminar separation bubbles and the accuracy with

which the shock strength can be set. Consequently varying values are found in literature and the incipient separation threshold is presented as a band rather than a sharp line. The lower bound ($C_{sep} = 0.79$, $p_{inc}/p_1 = 1.08$) follows from the theoretical work of Rizzeta et al. (1978) while the upper bound ($C_{sep} = 1$, $p_{inc}/p_1 = 1.11$) from the experimental work of Hakkinen et al. (1959).

For the $\theta = 1^\circ$ case, which is close to the theoretical incipient separation boundary, still a relatively long separation bubble is recorded. A similar result was found in the experiments of Hakkinen et al. (1959), who conjectured that for interactions close to incipient separation there will be a non-linear growth of the separation bubble.

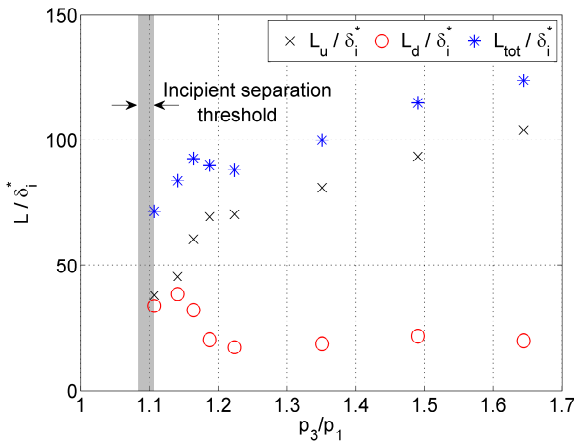


Figure 5.16: The size of the reversed flow region as a function of interaction strength ($M_\infty = 1.7$, $x_{sh} = 51$ mm)

The observed trends in Fig.5.16 are strongly connected with the transition behaviour of the boundary layer, that is presented in Fig.5.17(a). The metric $H_{i,aw}$ represents the incompressible shape factor of the boundary layer growing over the bubble (see also the discussion in section 5.1.3). A shape factor of ~ 2.5 is typical for a laminar boundary layer, whereas a value of ~ 1.4 is typical for a turbulent boundary layer. Even though the measurements are subject to measurement noise (see section 3.6.5), the transition location is clearly identifiable for all shock strengths. With increasing shock strength, the transition front is found to move upstream. However, even for the strongest shock wave ($\theta = 5^\circ$) transition always occurs downstream of the shock impingement location. So, the boundary layer stays in a laminar state over the entire upstream part of the separation bubble.

It is furthermore interesting to notice that transition occurs significantly further downstream for shocks weaker than $\theta = 2^\circ$. A shape factor $H_{i,aw}$ of 2 is reached approximately $100\delta_{i,0}^*$ downstream of the shock impingement location for the $\theta = 1^\circ$ and 1.5° case, whereas for the $\theta = 2^\circ$ case this value is reached already after $35\delta_{i,0}^*$. This implies that for shock angles in the range of $1 - 1.5^\circ$ the boundary layer remains in a close to laminar state throughout the entire interaction. This also explains the longer downstream portion of the separation bubble, which has been observed for weak shock waves in Fig.5.16.

Stronger shocks promote boundary layer transition, which promotes reattachment, consequently shortening the downstream portion of the separation bubble.

Even though transition sets in later for weak shock waves ($\theta = 1 - 1.5^\circ$), the process of transition is still strongly accelerated compared to that of natural transition (see Fig.5.17(b)). Natural transition takes place over the extent of approximately 35 mm, whereas with the presence of an impinging shock wave ($\theta = 1.5^\circ$) this has been reduced to approximately 10 mm. This is likely related to the Kelvin-Helmholtz type of perturbations introduced in the shear-layer of the downstream portion of the separation bubble (Sansica et al. (2014)), which accelerate the subsequent process of transition.

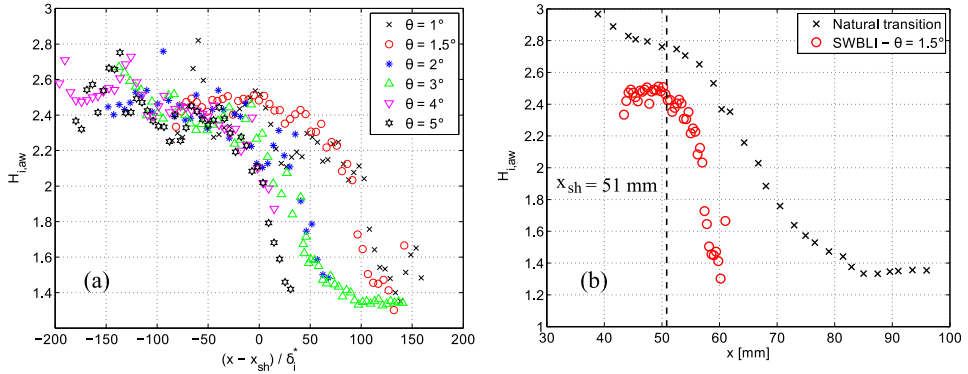


Figure 5.17: Shape factor development over the separation bubble for a range of flow deflection angles (a) and shock-induced transition compared to natural transition (b).

The effect of the Mach number on the interaction zone is presented in Figs.5.18(a) and 5.18(b) for the reversed flow region and the transition behaviour of the boundary layer, respectively. Mach numbers in the range of 1.6 - 2.3 were tested, for a fixed flow deflection angle and shock impingement location ($\theta = 3^\circ$, $x_{sh} = 51$ mm, $Re_{x_{sh}} = 1.8 \times 10^6$). It was already noted in section 5.2.1 that the topology of the interaction does not change substantially when changing the Mach number. The same is also observed when studying the $u = 0$ isolines of Fig.5.18(a). For all Mach numbers a flat near-triangular reversed flow region is recorded, with a long upstream portion and a short downstream portion (i.e. $L_u \gg L_d$). The data for the $M = 2.3$ is slightly noisier than that of the lower Mach number cases, due to increased near-wall seeding difficulties at the higher Mach numbers. The triangular shape can, however, still be recognized.

Two trends with increasing Mach number can be observed in Fig.5.18(a): 1) the length of the reversed flow region shrinks and 2) the angle α between the $u = 0$ isoline and the wall increases (see also Table 5.4). The experimentally determined angles α can be compared with the theoretical model for α by Hakkinen et al. (1959), which has been discussed in detail in section 5.1.3. The experimental values are in very good agreement with the values predicted by the model of Hakkinen et al. (1959) and typically deviate less than 0.1° .

The state of the boundary layer throughout the interaction is presented in Fig.5.18(b). Within the Mach number range considered no clear differences are recorded in the tran-

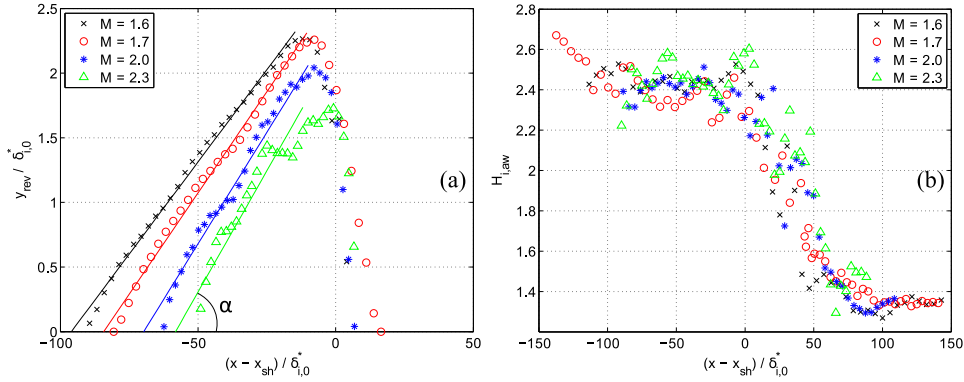


Figure 5.18: The reversed flow region (a) and corresponding shape factor development (b) throughout the interaction region for a range of Mach numbers. ($x_{sh} = 51$ mm, $\theta = 3^\circ$)

Table 5.4: Parameters describing the reversed flow region for a range of Mach numbers

M_∞	$L_u / \delta_{i,0}^*$	$L_d / \delta_{i,0}^*$	$L_{tot} / \delta_{i,0}^*$	α	α_{model}
1.6	87	16	104	1.7°	1.8°
1.7	81	19	100	1.8°	1.8°
2.0	63	12	76	2.1°	2.0°
2.3	58	10	68	2.2°	2.2°

sition behaviour. For all Mach numbers transition sets in directly downstream of the incident shock wave and a fully turbulent boundary layer is reached $\sim 80\delta_{i,0}^*$ downstream of the shock.

Although no clear Mach number effect is observed for this flow deflection angle ($\theta = 3^\circ$), it is speculated that for smaller flow deflection angles ($\theta < 2^\circ$) differences may start to appear between the low and high Mach number cases. For strong shock waves, bypass-transition is expected to occur, whereas for the weaker shock waves the transition process may still be dominated by first-mode oblique Mack waves. As the amplification rate of the first Mack mode becomes smaller with increasing values of the Mach number (Mack (1975)), it could therefore be hypothesized that the transition onset location shifts downstream with increasing Mach numbers for relatively weak interactions. This remains to be investigated.

The effects of the Reynolds number on the reversed flow region are presented in Fig.5.19(a). Shock impingement location in the range of $x_{sh} = 41 - 71$ mm are presented ($Re_{x_{sh}} = 1.4 \times 10^6 - 2.5 \times 10^6$). For the $x_{sh} = 41$ and $x_{sh} = 51$ mm cases virtually the same reversed flow regions are recorded, with both the size and shape of the regions being in good agreement with each other. The reversed flow region for the $x_{sh} = 61$ mm case still shows the characteristic asymmetric triangular shape, but in terms of size it is significantly (37%) smaller than the reversed flow regions recorded for the $x_{sh} = 41$ and 51 mm cases. This probably is due to the slightly transitional nature ($\gamma \sim 0.08$ for the undisturbed boundary layer) for the $x_{sh} = 61$ mm case (see also the discussion in section

5.2.1). For the $x_{sh} = 71$ mm case the boundary layer is clearly transitional ($\gamma \sim 0.5$) and a much smaller reversed flow region is recorded, which is no longer triangular of shape. PIV measurements were also performed for shock impingement locations of $x_{sh} = 81$ mm, 91 mm and 101 mm, but for these locations separation was no longer recorded.

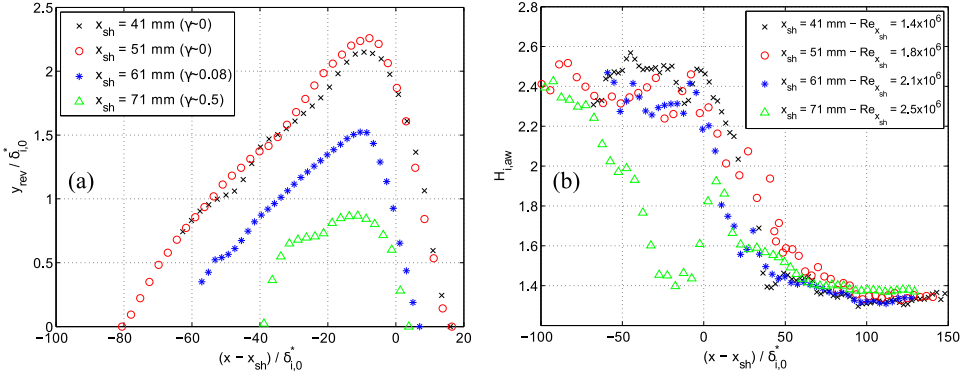


Figure 5.19: The reversed flow region (a) and corresponding shape factor development (b) throughout the interaction region for a range of Reynolds numbers. ($M_\infty = 1.7$, $\theta = 3^\circ$)

The state of the boundary layer throughout the interaction is presented in Fig.5.19(b) for the different shock impingement locations. Virtually the same development is observed for the $x_{sh} = 41$, 51 and 61 mm cases. The boundary layer remains in a laminar state up to the shock impingement location and after passing the shock wave quickly transitions into a turbulent state. The boundary layer for the $x_{sh} = 61$ mm case appears to transition slightly earlier than the boundary layer for the $x_{sh} = 41$ and 51 mm cases. This is probably the result of the already slightly transitional nature of the boundary layer at the moment of crossing the shock wave.

For the transitional interaction ($x_{sh} = 71$ mm), it can be noticed that the boundary layer shows a strong development over the separation bubble. Starting from a nearly laminar boundary layer, it develops into a turbulent profile before the point of reattachment. At reattachment, the boundary layer profile temporarily becomes slightly less full (with a rise in the shape factor), but a quick recovery is observed, and within $\sim 60\delta_{i,0}^*$ a shape factor of 1.4 is reached, typical for a turbulent boundary layer.

5.2.3. THE APPLICABILITY OF THE FREE-INTERACTION THEORY

The goal of this section is to investigate whether the flow field at the onset of the interaction adheres to the principles of the free-interaction theory (Chapman et al. (1957)). The free-interaction theory states that the scaling of the first part of the interaction should only depend upon upstream flow properties and not on the downstream flow conditions. The initial pressure rise through the interaction should therefore, in principle, be independent of the flow deflection angle and the type of interaction (e.g. oblique shock wave reflections or compression corner). From the free-interaction theory it follows that the pressure coefficient C_p through the first part of the interaction can be described by the following relation:

$$C_p(\bar{x}) = F(\bar{x}) \sqrt{\frac{2C_{f0}}{(M_\infty^2 - 1)^{0.5}}} \quad (5.2)$$

Where \bar{x} is defined as $\bar{x} = (x - x_{sep})/L_{sep}$. In this formulation x_{sep} defines the separation location and L_{sep} defines the distance between the interaction onset location (where a pressure rise is first noticed) and the separation location. $F(\bar{x})$ in Eq.5.2 is a universal correlation function, which couples the pressure rise through the interaction to the upstream flow conditions. The correlation function F for laminar interactions that is used in this study has been obtained from the work of Erdos and Pallone (1963) and is plotted in Fig.5.20. At the separation point F equals 0.81 and at the pressure plateau F reaches a value of 1.47.

The free-interaction theory is well-established for low and moderate Reynolds number flows ($Re_{\delta_{99}} < 10^5$), with relatively strong shock waves (Delery and Marvin (1986)). Plenty of data is available which confirms the universal nature of the correlation function F and the validity of Eq.5.2. For weak laminar interactions, on the other hand, much less information is available. In this context, a weak interaction is defined as an interaction where the pressure plateau is not reached. This section provides new evidence that the free-interaction concept also holds true for weak shock waves and even for incipiently separated laminar interactions.

Notwithstanding that no detailed surface pressure data was recorded in the present study, the function F can also be extracted from the PIV velocity data. Supersonic linear theory is used to convert the velocity field upstream of the impinging shock wave to a pressure field. Linear theory is applicable here because of the relatively small flow deflection angles θ_{flow} , which never exceed 2° , allowing the pressure coefficient to be calculated as:

$$C_p = \frac{2\theta_{flow}}{\sqrt{M_\infty^2 - 1}} \quad (5.3)$$

The flow deflection angles are calculated at multiple y -locations to improve the accuracy of the velocity to pressure conversion. Velocity profiles in the range of $y/\delta_{i,0}^* = 5-10$ were typically used for this calculation. The measured flow deflection angles were projected back onto the wall along the Mach angle to account for the horizontal shift in the profiles (see also Fig.5.21). The deflection angles were then averaged and converted to a C_p distribution using Eq.5.3. The correlation function F was obtained by applying Eq.5.2 to the experimental C_p distributions.

Fig.5.20 compares the experimentally obtained correlation functions F for the different interactions, compared with the function F described by Erdos and Pallone (1963). The experimental data for the different interactions is in good agreement with each other: from the weakest interaction ($\theta = 1^\circ$) up to the strongest interaction ($\theta = 5^\circ$) tested in this study, all experiments show virtually the same pressure rise. The sharp drop of the experimental data to the right of the plot is due to the crossing of the horizontal dataline with the incident shock wave, where linear supersonic theory no longer holds true.

It can furthermore be noticed that the initial pressure rise appears to be slightly delayed with respect to the curve of Erdos and Pallone (1963). This is attributed to the

effect of particle slip, which is inherent to any particle-based experiment performed in supersonic flow. To assess if this effect can indeed account for the observed discrepancy, the function F of Erdos and Pallone (1963) was also subjected to the effects of particle slip. This was achieved by converting it to a velocity field upon which a simple particle slip model (Melling (1997)) is used to get an equivalent ‘PIV-filtered’ velocity field. The only input to this model is the particle response time, which for the TiO_2 particles was determined to be $\tau_p = 2.5 \mu\text{s}$. The filtered velocity field is again converted back to a pressure field using linear supersonic theory, yielding a ‘PIV-filtered’ version of the function F . This filtered version of F appears to be in excellent agreement with the experimental data acquired during this study.

Fig.5.20(b) shows a similar comparison for the effects of the Mach number of the function F . Again all the data collapses onto one curve. Figs.5.20(a-b) therefore provide strong experimental evidence that the free-interaction theory also holds for weak laminar interactions, where the pressure plateau is not reached.

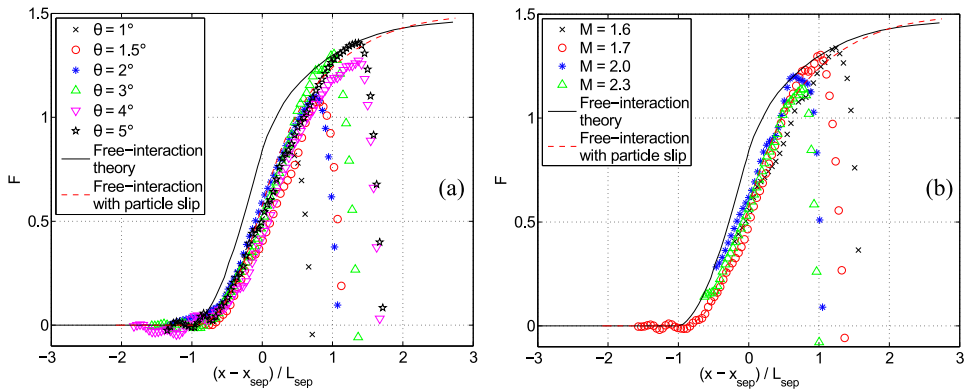


Figure 5.20: Correlation function F for a range of flow deflection angles (a) and a range of Mach numbers (b).

5.3. A NOTE ON THE UNSTEADINESS OF LAMINAR INTERACTIONS

Due to the effects of particle slip it is not possible to accurately reconstruct the velocity fluctuations inside the boundary layer and the interaction region (see also the discussion in section 3.6.1). Some information on the interaction unsteadiness can, however, still be inferred from the PIV snapshots by not focusing on the small scale features of the flow, but instead by looking at its global features. For instance by looking at the compression waves created by the thickening of the laminar boundary layer. If the separation bubble is unsteady and growing / shrinking over time, then the compression waves are also expected to display similar oscillations. The goal of this section is to provide an upper bound on the unsteadiness of the compression waves and thus the separation location.

The PIV velocity fields in the earlier sections were produced by applying the ensemble correlation technique to the full set of image pairs. This approach delivers a high-resolution mean velocity field, which is useful when investigating the boundary layer properties, but is of little use when studying the unsteadiness of the interaction. The PIV

image pairs were therefore also processed with a standard single image pair correlation technique, which delivers a complete set of velocity fields. All processing was done with our in-house built iterative multi-grid window deformation PIV code Fluere, which is based upon the work of Scarano and Riethmuller (2000).

Interrogation windows of 64×64 pixels were used, with an overlap of 75% provided in both the wall-normal and streamwise direction of the flow. This resulted in a vector pitch of 16 pixels or equivalently 0.12 mm. The velocity fields were post-processed with a normalized median filter to remove spurious vectors (Westerweel and Scarano (2005)). Images that were low on seeding and that had many bad vectors (>5%) were removed from the dataset.

Fig.5.21(a) shows the average wall-normal velocity component v for a $M_\infty = 1.7$ flow at a Reynolds number $Re_{x_{sh}} = 1.8 \times 10^6$ and flow deflection angle $\theta = 5^\circ$, as obtained from the single image pair correlation analysis. The compression waves are clearly visible in the velocity field, and leave the surface under the Mach angle of $\sim 36^\circ$. Fig.5.21(b) presents the corresponding r.m.s. field for the v -component of the velocity field. High values are recorded at the shock impingement location, which are, at least partially, due to the effects of boundary layer transition and the associated unsteadiness of the expansion fan and recompression waves. However, bare in mind that this result can only be interpreted in a qualitative sense. The effects of particle slip and the relatively large interrogations windows (compared to the small boundary layer thickness) make it impossible to draw any quantitative conclusions on the unsteadiness measured at and downstream of shock impingement.

The compression waves created at the interaction onset are of a much larger scale than the small scale flow features present in the transitioning boundary layer. A front of compression waves that is moving back and forth should therefore still be resolvable by means of our current PIV approach.

Low r.m.s. values ($\sim 0.7\%$ of U_∞) are recorded upstream of the shock impingement location. Slightly higher values ($\sim 1\%$ of U_∞) are recorded around the Mach line that emanates from the average boundary layer separation location. Although this might indicate some light unsteadiness of the separation location, it should be remarked here that the recorded fluctuation levels are close to the noise floor of our PIV measurements. The PIV measurements are affected by the freestream turbulence level and PIV random errors. The former has been studied by Giepmans et al. (2014a) and equals: $u' \sim 0.6\%$, $v' \sim 0.4\%$ of U_∞ . The latter is estimated to be 0.1 pixel (Scarano and Riethmuller (2000)), which for a freestream displacement of 24 pixels translates into $u' = v' \sim 0.4\%$ of U_∞ .

The relatively low velocity fluctuations in combination with the finite noise floor makes it impossible to accurately calculate the unsteadiness of the compression waves and thus the unsteadiness of the separation location. An upper bound on the range of motion of the separation location can, however, still be provided. To that end it was decided to calculate the wall pressure distribution from the instantaneous velocity snapshots. The same procedure is followed as described in section 5.2.3, where linear supersonic theory was used to convert the small flow deflection angles to pressures. This approach of course fails when the data crosses the incident shock wave.

Fig.5.21(c) shows that again the mean pressure distribution is in good agreement with the free-interaction theory when corrected for the effects of particle slip. The pur-

ple band in Fig.5.21(c) presents the r.m.s. level of the pressure distribution, which can be converted to an r.m.s. level on the separation location by using the average pressure distribution around the expected separation location. The unsteadiness of the separation location equals $\sim 27\%$ of L_{sep} or $\sim 13\delta_{i,0}^*$. These values should be taken as an *upper bound* on the unsteadiness of the separation location, because as mentioned before, the recorded velocity fluctuations are just slightly above the noise floor of the PIV measurements. The actual unsteadiness of the separation location is therefore expected to be substantially smaller.

The same analysis has also been carried out for the other laminar test cases. Very similar results were obtained and fluctuation levels in the compression wave regime were never substantially higher than the PIV noise floor.

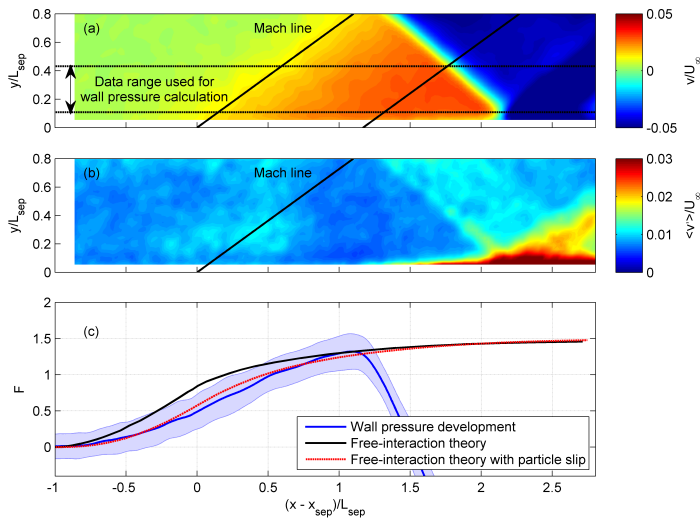


Figure 5.21: Unsteadiness analysis of a laminar shock wave-boundary layer interaction with boundary layer transition at the incident shock wave ($M_\infty = 1.7$, $Re_{x_{sh}} = 1.8 \times 10^6$ and $\theta = 5^\circ$). (a) The mean v -component (b) the r.m.s. level of v and (c) the normalized wall pressure distribution.

5.4. CONCLUSIONS

A parametric study has been conducted into laminar and transitional oblique shock wave reflections, by variation of the Mach number, Reynolds number and interaction strength. The Mach number was varied from 1.6 - 2.3, the Reynolds number from $1.4 - 3.5 \times 10^6$ and the flow deflection angle from $\theta = 1^\circ - 5^\circ$ ($p_3/p_1 = 1.11 - 1.64$). All measurements were performed on a full-span flat plate model, with the oblique shock wave being generated by means of a partial span shock generator. High-resolution particle image velocimetry (PIV) measurements were performed for all test cases, delivering mean velocity field data in the interaction region.

The PIV measurements reveal a long, flat and triangular reversed flow region for the

laminar interactions. For relatively strong shock waves ($\theta > 2^\circ$, $p_3/p_1 > 1.22$) it is found that the horizontal distance L_u between the point of boundary layer separation and the top of the bubble increases linearly with shock strength, whereas the horizontal distance L_d between the top of the separation bubble and reattachment remains virtually constant ($L_d \sim 20\delta_{i,0}^*$) with shock strength. The boundary layer remains laminar over the upstream part of the bubble, but transitions rapidly after passing the incident shock wave.

On the other hand, for relatively weak shock waves the boundary layer is capable of maintaining its laminarity longer and transition sets in approximately $\sim 100\delta_{i,0}^*$ downstream of the incident shock wave. These shock wave-boundary layer interactions can therefore be considered as fully laminar. As a result of the reduced mixing in the shear layer, reattachment is delayed with a corresponding increase in the downstream length of the separation bubble L_d , from approximately 20 to 38 when reducing the flow deflection angle from $\theta = 2^\circ$ to 1.3° , respectively. This clearly shows the strong connection between boundary layer transition, separation bubble size and flow deflection angle. Even though transition sets in later for weak shock waves ($\theta = 1 - 1.5^\circ$), the process of transition is still strongly accelerated compared to that of natural transition. Natural transition takes place over the extent of approximately 35 mm, whereas with the presence of an impinging shock wave ($\theta = 1.5^\circ$) this has been reduced to approximately 10 mm.

Increasing the Mach number while keeping the Reynolds number and flow deflection angle constant ($Re_{x_{sh}} = 1.8 \times 10^6$, $\theta = 3^\circ$) leads to a monotonic decrease in the size of the reversed flow region. On the other hand, the angle α between the $u = 0$ isoline and the wall is found to monotonically increase with Mach number, from 1.7° to 2.2° for $M_\infty = 1.6$ to 2.3 , respectively. These values are in good agreement with the predictions from the empirical scaling model of Hakkinen et al. (1959) for laminar oblique shock wave reflections.

The shock-location Reynolds number $Re_{x_{sh}}$ was varied from $1.4 \times 10^6 - 3.5 \times 10^6$ ($x_{sh} = 41 - 101$ mm). The boundary layer study of chapter 4 revealed that the boundary layer is laminar for $Re_{x_{sh}} = 1.4 \times 10^6$ and 1.8×10^6 , transitional for $Re_{x_{sh}} = 2.1 \times 10^6 - 3.2 \times 10^6$ mm and fully turbulent for $Re_{x_{sh}} = 3.5 \times 10^6$. Separation is only recorded for $Re_{x_{sh}} = 1.4 \times 10^6 - 2.5 \times 10^6$ ($\gamma = 0 - 0.5$), with the largest bubble recorded for the laminar cases. The two laminar cases deliver virtually the same size / shape of separation bubble and also the recorded transition process appears to be very similar. This shows that the interaction is relatively insensitive to changes in the Reynolds number, as long as the incoming boundary layer is fully laminar. The size of the bubble is reduced significantly when the boundary layer is (slightly) transitional. Although the intermittency level for $Re_{x_{sh}} = 2.1 \times 10^6$ equals only $\gamma = 0.08$, the recorded bubble size nevertheless is 24% smaller than the bubble size recorded for the $Re_{x_{sh}} = 1.8 \times 10^6$ case, for which the boundary layer is still fully laminar.

The flow deflection angles upstream of the incident shock wave are relatively small ($\theta_{flow} < 2^\circ$) and justify the use of linear supersonic theory to convert the measured velocities to wall pressures. The calculated pressure distributions compare favourably with the free-interaction theory of Chapman et al. (1957) after a correction was applied for the effects of particle slip. Although the free-interaction theory is well-established for relatively strong shock waves (Delery and Marvin (1986)), much less information is available

in literature for weak interactions, where a pressure plateau is never reached. The data of this study provides convincing evidence that the free-interaction concept also holds for incipiently separated laminar oblique shock wave reflections.

Due to the extremely thin laminar boundary layer ($\delta_{99} \sim 0.2$ mm) and thus high particle Stokes number ($St = \tau_p U_\infty / \delta_{99} \sim 5.6$) it was not possible to accurately reconstruct the velocity fluctuations inside the boundary layer and interaction region. Some information on the unsteadiness of the interaction could, however, still be inferred by looking at its global flow features instead of the small scale features present in the boundary layer. The velocity fluctuations were assessed in the region upstream of the incident shock wave, which is dominated by the compression waves that are generated by the thickening and separation of the laminar boundary layer. The velocity fluctuations values were found to be quite small, with typical values: $v' = 0.7 - 1\%$ of U_∞ for all laminar test cases. This translates into typical uncertainties on the separation location of $\sim 0.27L_{sep}$ or equivalently $\sim 13\delta_{i,0}^*$, where L_{sep} is the distance between the interaction onset and boundary layer separation location. The measured velocity fluctuations were, however, close to the noise floor of our PIV measurements and the recorded uncertainties should therefore be considered as a conservative upper bound on the unsteadiness of the compression waves and separation location.

6

OBLIQUE SHOCK WAVE REFLECTIONS UNDER FORCED TRANSITION CONDITIONS

This chapter discusses the effects of boundary layer tripping on an oblique shock wave reflection ($M = 1.7$, $Re_\infty = 35 \times 10^6 \text{ m}^{-1}$, $\theta = 3^\circ$) by means of particle image velocimetry and schlieren visualizations. Although laminar boundary layers are typically beneficial because of their low drag contribution, they are also very sensitive to adverse pressure gradients as seen in the previous chapter. Boundary layer separation in general is to be avoided, because of losses in the total pressure and an increased pressure drag contribution. It therefore seems optimal to trip the laminar boundary layer a short distance upstream of the impinging shock wave. This idea, however, raises the following questions.

1. How far should the transition control devices be placed upstream of the interaction to completely avoid separation?
2. What is the most effective way of tripping the boundary layer?
3. How do the results of the tripped interaction compare with the baseline laminar interaction?

To answer these questions, three types of transition control devices were investigated: a stepwise trip, a patch of distributed roughness and a zig-zag strip (see section 6.1). The PIV camera configuration is discussed in section 6.2 and section 6.3 presents the velocity fields downstream of the transition control devices, in the absence of an

Parts of this chapter have been presented at the 45th AIAA Fluid Dynamics Conference (Giepmans et al. (2015a)).

impinging shock wave. The process of transition is analyzed by calculating the integral boundary layer parameters and tracking the development of the shape factor downstream of the trips. Section 6.4 builds further upon these result and discusses the control authority of the tripping devices for two trip to shock wave distances ($30\delta_{95}$ and $55\delta_{95}$).

6.1. TRANSITION CONTROL DEVICES

The natural development of the boundary layer along the flat plate has been studied extensively in chapter 4 by means of infrared thermography, particle image velocimetry, oil-flow and schlieren visualizations. It was found that the flat plate boundary layer remains laminar up to $x_T = 55$ mm from the leading edge ($Re_{x_T} = 1.9 \times 10^6$). Natural transition takes place over a length of 35 mm and a fully turbulent boundary layer is established at approximately $x_{turb} = 90$ mm ($Re_{x_{turb}} = 3.2 \times 10^6$) from the leading edge.

For the current study it was decided to place the transition control devices at $x_{trip} = 40$ mm from the leading edge ($Re_{x_{trip}} = 1.4 \times 10^6$). The velocity profile of the undisturbed laminar boundary layer profile at this location is presented in Fig.4.4(b), with the corresponding boundary layer parameters summarized in Table 4.1.

Three types of tripping devices were investigated in this study: a step-wise 2D trip, a patch of distributed roughness (carborundum particles) and a zig-zag strip. Fig.6.1 shows a schematic representation of the trips and Fig.6.2 shows the details of the trips as imaged with a confocal microscope. All devices spanned the entire width of the plate and had a roughness height of $k = 0.1$ mm, which corresponds to half the boundary layer thickness ($0.5\delta_{95}$) or equivalently: $Re_k = U_\infty k / \nu_\infty = 3.5 \times 10^3$, $Re_{kk} = U_k k / \nu_k = 1.4 \times 10^3$ or $Re_{k2} = \rho_k U_k k / \mu_w = 1.2 \times 10^3$. These values can be compared with the classical experimental work of Hicks and Harper (1970) and the more recent DNS study by Bernardini et al. (2014)

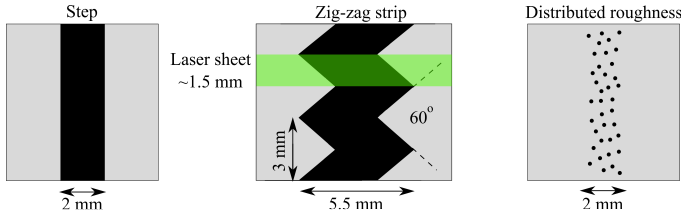


Figure 6.1: Schematic representation of the tripping devices

Hicks and Harper (1970) investigated the effects of an isolated roughness element on a Mach 1.58 laminar boundary layer for a range of roughness Reynolds numbers Re_k . For spherical roughness elements they found that the transition location is virtually unaffected by the presence of the roughness element for $Re_k < 1.5 \times 10^3$ (critical Re_k). Increasing Re_k above this critical value gradually shifts the transition location upstream with respect to the natural transition location, up to the point where transition occurs at a short distance downstream of the trip, while a further increase of Re_k leads to no further change in the transition location (effective Re_k). The effective roughness Reynolds number was found to depend on $Re_{x_{trip}}$: it equals $Re_k = 2.7 \times 10^3$ for $Re_{x_{trip}} = 2.2 \times 10^4$ and increases up to $Re_k = 3.6 \times 10^3$ for $Re_{x_{trip}} = 3.6 \times 10^5$. For the current experiment

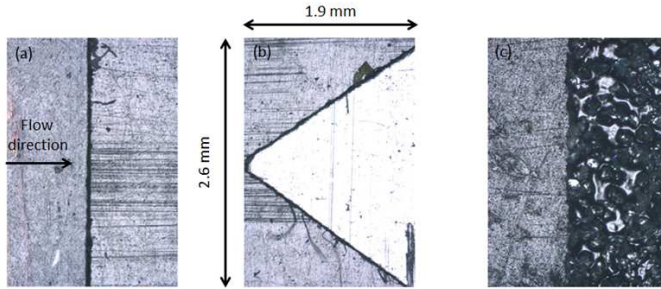


Figure 6.2: Tripping devices imaged with a confocal microscope (a) Step (b) Zig-zag tooth (c) Distributed roughness

these results would translate into a critical roughness height of 0.04 mm and an effective roughness height of at least 0.1 mm.

Bernardini et al. (2014) investigated, amongst others, hemispherical isolated roughness elements at $M = 2$. They found a critical roughness Reynolds number $Re_{k2} = 4.4 \times 10^2$ and an effective roughness Reynolds number Re_{kk} of at least 1.1×10^3 (the highest Re_{kk} investigated in their work). For the current work these results would translate into a critical roughness height of 0.06 mm and an effective roughness height of at least 0.09 mm.

Based upon the work of Hicks and Harper (1970) and Bernardini et al. (2014) it is therefore expected that the $k = 0.1$ mm trips used for the current experiment introduce boundary layer (bypass) transition in close proximity of the trip, without significantly overtripping the boundary layer. This is desirable since one wants to minimize the required distance between the tripping device and the incident shock, in order to maximize the portion of laminar flow upstream of the tripping device. Of course one should bear in mind that the works of Hicks and Harper (1970) and Bernardini et al. (2014) investigated isolated spherical and hemi-spherical roughness elements, respectively. The tripping heights found from these studies therefore do not translate directly to the zig-zag strip, the 2D step and the patch of distributed roughness investigated in this study, but they do provide a first-order estimate for the tripping heights required to introduce transition. The patch of distributed roughness is expected to initiate a relatively clean and uniform transition process, whereas the zig-zag strip will enforce transition by the introduction of a series of longitudinal vortices, therefore resulting in an initially non-uniform turbulence field.

6.2. PIV CAMERA CONFIGURATION

The PIV measurements were performed with two Lavision Imager LX cameras, placed on either side of the tunnel. One of the cameras observed the region upstream of the tripping device ($x = 30 - 42.5$ mm) to verify that the incoming boundary layer is laminar. The second camera was positioned downstream of the tripping device (see also Fig.6.3). To cover the interaction region to a sufficient extent, multiple wind tunnel runs were performed, with the second camera positioned at different locations downstream of the

tripping device. An overlap of ~ 4 mm was provided between the fields of view of the different runs to allow a proper recombination of the velocity fields afterwards. In this manner, the region from $x = 40 - 75$ mm was covered, however, due to strong laser light reflections from the trip it was only possible to measure the velocity field starting from ~ 3 mm downstream of the trip. Additional information regarding the camera / laser settings and the processing of PIV data can be found in chapter 3.

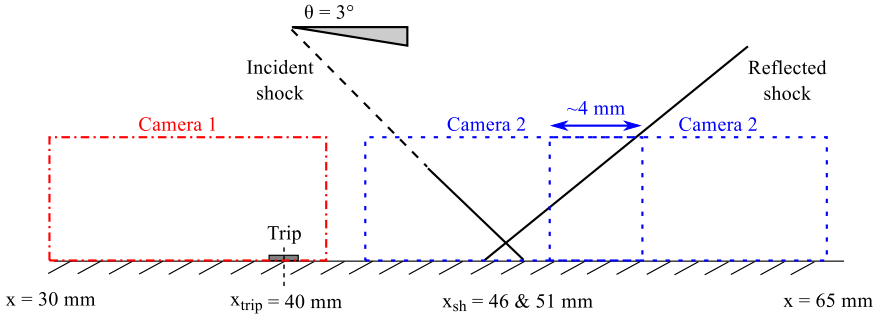


Figure 6.3: Schematic overview of the experimental setup, including the PIV field of views

6.3. STUDY OF TRANSITION CONTROL DEVICES

The velocity field downstream of the tripping devices is presented in Fig.6.4 for the zig-zag strip (a), step (b) and distributed roughness patch (c). Velocity field data is missing for the step in the region from 50.6 - 53.4 mm due to improper flow conditions for this specific measurement (incoming boundary layer was found to be already transitional instead of laminar). For all other datasets included in Fig.6.4 it has been confirmed that the incoming boundary layer is indeed laminar. To provide more insight in the flow field downstream of the tripping devices, velocity profiles were extracted at $x = 45$ and 50 mm (see Fig.6.5). The trips were centred on $x = 40$ mm and the trip to measurement station distance for Figs.6.5a-b therefore equals 5 and 10 mm, respectively. Or equivalently: 25 and 50 undisturbed boundary layer thicknesses δ_{95} downstream of the centreline of the trip.

The laminar boundary layer upstream of the tripping devices is lacking seeding in the near-wall region (< 0.1 mm) of the flow. The boundary layer undergoes transition when crossing the trips, which has a positive effect on the seeding distribution in the boundary layer. This process is, however, not instantaneous and the seeding conditions are found to only gradually improve when moving downstream from the trip. For the first measurement station ($x = 45$ mm) it is therefore still difficult to accurately determine the velocity field in the near-wall region of the flow and some outliers may be observed in the velocity vectors close to the wall. In order to calculate the integral boundary layer parameters from the experimental data it is therefore necessary to extrapolate the velocity data in this region. A power-law fit is used for this purpose, which is included in the Figs.6.5(a-b).

For $x = 45$ mm (Fig.6.5a) it is interesting to observe that the boundary layer displays a turbulent character for both the zig-zag strip and the distributed roughness, whereas

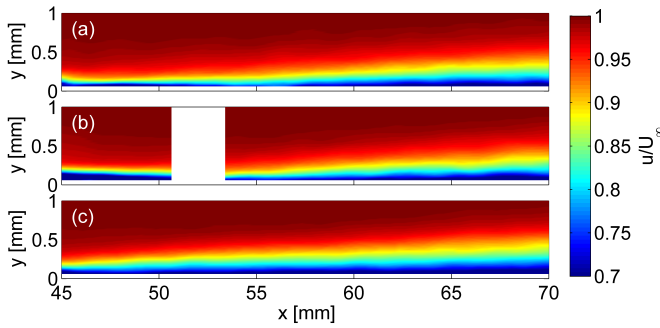


Figure 6.4: Streamwise component of the velocity field downstream of the transition control devices. (a) Zig-zag strip (b) step (c) distributed roughness patch

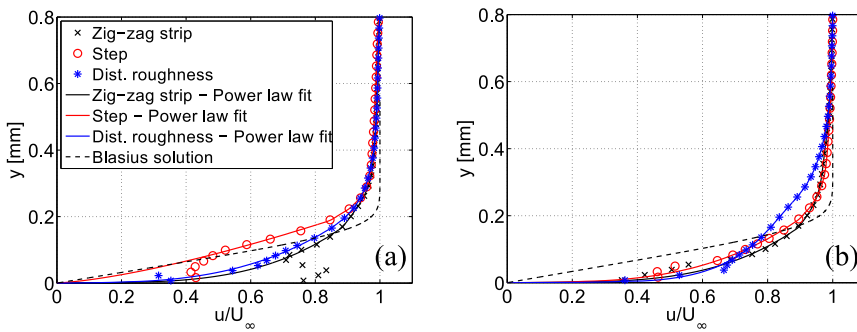


Figure 6.5: Velocity profiles at $x = 45$ mm (a) and $x = 50$ mm (b)

for the case of the step the boundary layer is emptier and closer to a laminar profile. This difference disappears when moving further downstream ($x = 50$ mm) and the boundary layer is observed to be turbulent for each of the trips. Although all three trips result in a turbulent boundary layer, it may be noticed that the patch of the distributed roughness results in a substantially thicker boundary layer than the zig-zag strip and the step.

These observations are clearly reflected in Figs.6.6a-c, which display the development of the incompressible displacement thickness δ_i^* , incompressible momentum thickness θ_i and the incompressible shape factor H_i , respectively. For the computation of the integral boundary parameters, a power-law fit is used for the velocity data points close to the wall. Although the transition process is different for the zig-zag strip and the step, they both eventually result in a turbulent boundary layer with approximately the same displacement and momentum thickness. The distributed roughness on the other hand results in a turbulent boundary layer with a displacement thickness which is typically $10 \mu\text{m}$ larger ($\sim 10\%$) than that of the zig-zag strip or the step. The momentum thickness is typically about $8 \mu\text{m}$ larger ($\sim 10\%$) for the patch of distributed roughness than for the other two tripping devices.

Figs.6.6a-b also show the development of δ_i^* and θ_i as a ratio of the undisturbed (laminar) values ($\delta_{i,0}^*$ and $\theta_{i,0}$) measured at the location of the trip (right-hand scales).

The displacement thickness temporarily becomes smaller than its undisturbed value due to the process of transition, which fills up the boundary layer profile. On the other hand, the momentum thickness downstream of the trip is always larger than its undisturbed value.

Finally, the shape factor development of Fig.6.6c clearly shows that the zig-zag strip and the distributed roughness patch deliver a turbulent boundary layer that originates much closer to the trip than is the case for the step. A shape factor of 1.4 is reached approximately 6 mm downstream of the centreline of the zig-zag strip and the distributed roughness patch. The same shape factor is reached only after approximately 11 mm for the step. This implies that for the same degree of effectiveness the step should be placed further upstream of an impinging shock wave than the other two tripping devices, therefore reducing the laminar part of the incoming boundary layer.

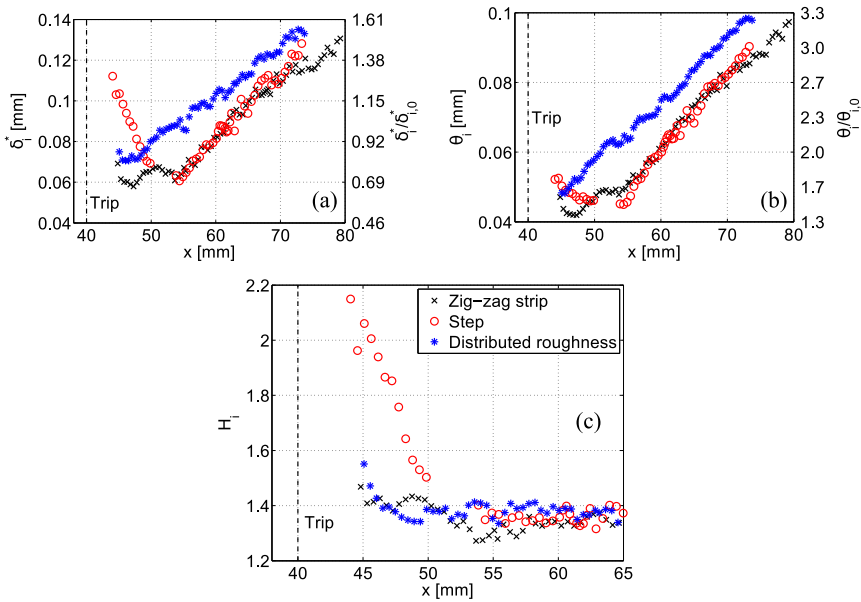


Figure 6.6: Development of the incompressible displacement thickness δ_i^* (a), incompressible momentum thickness θ_i (b) and incompressible shape factor H_i (c) downstream of the tripping devices

6.4. THE EFFECTS OF FORCED TRANSITION ON AN OBLIQUE SHOCK WAVE REFLECTION

SHOCK IMPINGEMENT TO TRIP DISTANCE: $55\delta_{95}$

Schlieren visualizations were performed for the three tripping devices to provide a qualitative understanding of the flow field. Fig.6.7a-c shows that the schlieren visualizations look similar for the different tripping devices, in terms of the overall flow features. Upstream of the trip a series of compression waves is observed. As the flow passes over the top of the device, it expands and downstream it is compressed again. The inci-

dent shock wave impinges on the surface 11 mm downstream of the centreline of the trips and does not appear to cause separation of the incoming boundary layer. In case of a large separation bubble one would expect to see a clear expansion (compression waves and expansion fan emanating from top of the separation bubble) similar to those present in Fig.6.7d, which represents the shock wave-boundary layer interaction with an undisturbed laminar incoming boundary layer (see also chapter 5). Notwithstanding the overall similarity between the three tripped cases, it may be observed, that for the step in Fig.6.7(b) a slightly wider reflected shock region is observed than for the other two trips. This might indicate a larger interaction region and a less effective tripping.

PIV measurements were performed in the interaction region for the three tripping devices. The average velocity fields shown in Fig.6.8 indicate no sign of boundary layer separation, implying that all three trips are effective in removing the large separation bubble that occurs for the laminar interaction case (see Fig.6.9). On a qualitative basis, the velocity fields look very similar. They all clearly show the presence of the incident and reflected shock wave in the domain. Upstream of the incident shock wave also the effects of the trip on the freestream are apparent. From the schlieren visualization, it was observed that the trip induces several shocks and expansion waves. In the PIV results the expansion fan and the succeeding compression waves, which originate from the trailing edge of the trip are clearly visible. For the zig-zag strip the expansion / compression waves occupy a rather wide band, which is due to the fact that measurements are averaged in spanwise direction over a ~ 1.5 mm thick lasersheet. This corresponds to half a zig-zag tooth (see Fig.6.1) and consequently leads to the spreading of the expansion and compression wave features visible in the velocity field. For the other two trips the results are also averaged over the ~ 1.5 mm laser sheet, but because of the (quasi) two-dimensionality of the flow field, the flow features remain rather sharp.

For the case of distributed roughness a relatively high value for the upwash velocity ($0.010 - 0.013U_\infty$) is recorded in the region between the trip and the impinging shock wave. This observation can be linked to the fact that the boundary layer downstream of the distributed roughness initially shows a stronger growth than observed for the other two trips (see section 6.3).

From the velocity fields of Fig.6.8 it is, however, hard to draw conclusions on the effectiveness of the tripping devices. The integral boundary layer parameters were therefore calculated for all tripping devices to analyze the state of the boundary layer. Figs.6.10a-c shows the development of δ_i^* , θ_i and H_i downstream of the zig-zag strip and throughout the interaction region. Figs.6.11a-c show these parameters for the step and Figs.6.12a-c for the distributed roughness. As a reference, all figures also show the data that was acquired for the case without an impinging shock wave.

The thickening of the boundary layer over the interaction region is clearly reflected in the development of the incompressible displacement and momentum thickness. To quantify the increase in the integral parameters due to the presence of the interaction, their values were evaluated 10 mm downstream of the shock impingement location and the difference between the dataset with and without an impinging shock wave was computed. The results were normalized by the displacement / momentum thickness measured at x_{sh} for the case without an impinging shock wave. The displacement thickness increases by approximately 58% over the shock system for the zig-zag strip and by 56%

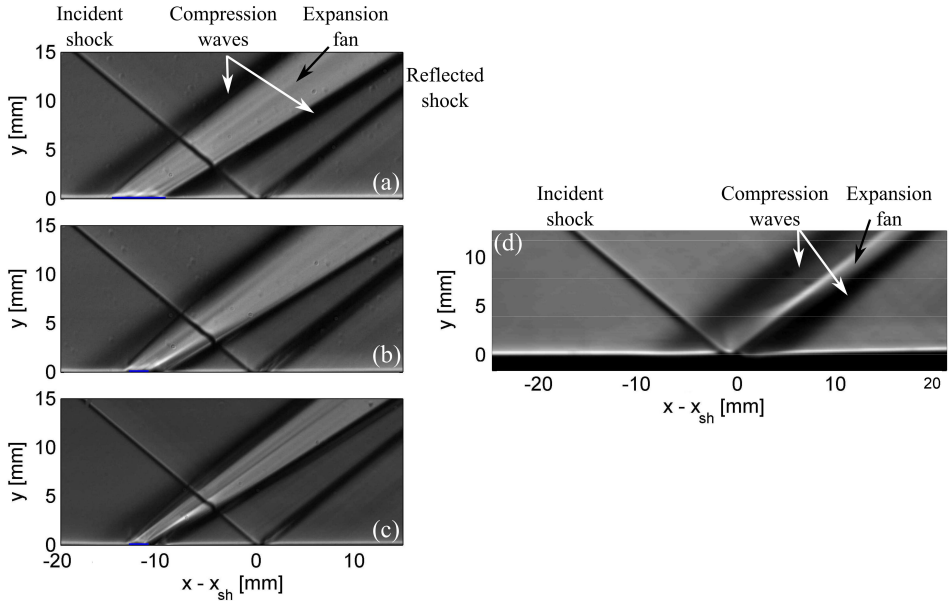


Figure 6.7: Schlieren visualizations for three tripping devices positioned 10 mm upstream of an impinging oblique shock wave ($x_{sh} = 51$ mm). (a) Zig-zag strip; (b) step; (c) distributed roughness; (d) untripped laminar interaction

6

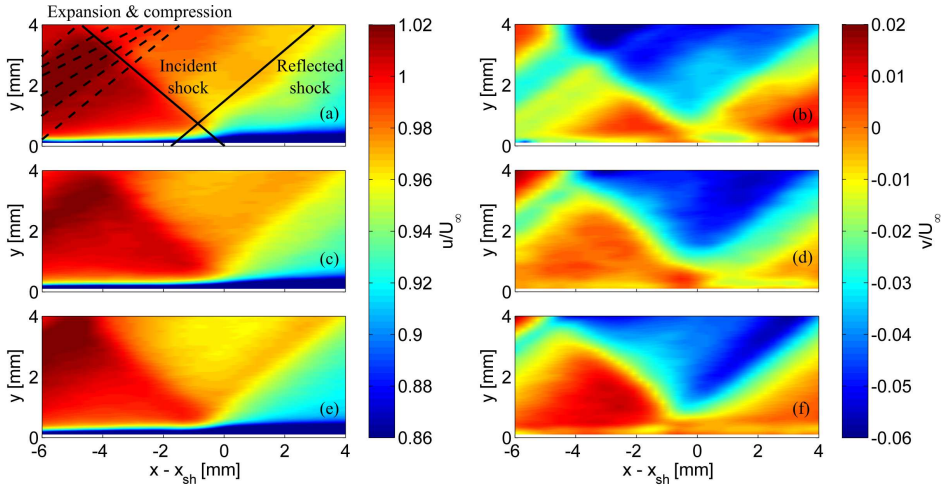


Figure 6.8: The u- and v-component of the velocity field in the interaction region for the zig-zag strip (a,b), step (c,d) and distributed roughness (e,f).

for the step. The distributed roughness case on the other hand displays a much smaller increase in the displacement thickness by only 34%. The exact reason for this difference

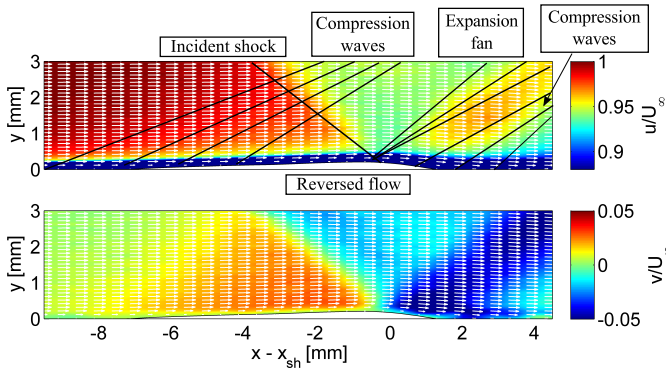


Figure 6.9: Velocity field in the interaction region for a non-tripped (laminar) incoming boundary layer ($x_{sh} = 51$ mm)

remains to be investigated, but may be related to the strong initial boundary layer growth downstream of the distributed roughness patch. The absolute and relative increases in the displacement and momentum thickness are summarized in Table 6.1.

Inside the interaction region the boundary layer velocity profile becomes less full, with the emptiest profiles (highest shape factors) reached at the shock impingement location. For the step a maximum shape factor of 1.80 is reached in the interaction region, for the distributed roughness this is 1.72 while for the zig-zag strip a maximum shape factor of 1.61 is recorded. The flow downstream of the step is therefore concluded to be closest to separation in the interaction region (largest shape factor), whereas the flow downstream of the zig-zag strip is furthest removed from separation (smallest shape factor). The differences in shape factor are, however, relatively small (1.80 vs 1.61). This agrees with the previous observation that 11 mm downstream of the centreline of the trip all three trips yield a fully turbulent boundary layer (see section 6.3).

Finally, a comparison is made between the development of the boundary layer downstream of the interaction for the tripped and untripped case. For the untripped (laminar) interaction a large separation bubble is formed, which extends mostly upstream (7.5 mm) of the incident shock wave (see also Fig.6.9). It was found in chapter 5 that the boundary layer developing over the separation bubble remains in a laminar state up to the shock impingement location. Transition only sets in after crossing the incident shock and this results in a quick reattachment of the separated boundary layer. This phenomenon is reflected in Fig.6.13c, which compares the development of the incompressible shape factor downstream of the interaction for the tripped boundary layers and the untripped boundary layer. The boundary layer for the untripped case recovers rapidly and within 5 mm downstream of the shock wave it reaches the same level of fullness as recorded for the tripped interactions.

The development of the incompressible displacement and momentum thickness are presented in Figs.6.13a and 6.13b, respectively. From these figures it is apparent that tripping the boundary layer upstream of the interaction results in a substantially thicker boundary layer downstream of the interaction. On average, tripping leads to an increase

of the displacement thickness by 0.04 mm and an increase of the momentum thickness by 0.03 mm. In relative terms, this corresponds to a boundary layer that is ~50% thicker than the untripped boundary layer. This substantial difference is presumably caused by the following three effects:

- Losses at the tripping devices (e.g. wave drag, flow separation, etc. . .)
- Lower shock-induced losses for the untripped interaction due to a more gradual compression in the interaction region. The tripped interaction shows a sharp reflected shock wave, whereas the untripped interaction shows a combination of compression and expansion waves, which results in lower entropy losses.
- For the untripped case a laminar boundary layer is maintained over a larger portion of the plate. A laminar boundary layer has a smaller skin friction coefficient than a turbulent (tripped) boundary layer, which translates into a reduction of the boundary layer growth.

The above observations confirm that the transition control devices are able to remove the separation bubble, however, at the price of producing a substantially thicker boundary layer downstream of the interaction. A similar result was obtained in the work of Davidson and Babinsky (2015), who investigated the effects of forced transition on a flat plate normal shock wave-boundary layer interaction. By tripping the boundary layer they were able to remove the shock-induced separation bubble, but accompanied by a thicker downstream boundary layer (~40%). In this context it is important to note that both the laminar oblique shock wave reflection (chapter 5) and the laminar normal SWBLI (Davidson and Babinsky (2015)) showed no sign of any large-scale unsteadiness.

Table 6.1: Increase in the incompressible displacement and momentum thickness when crossing the shock system for the different tripping devices

	$\Delta\delta_i^*$	$\Delta\delta_i^*/\delta_i^*(x_{sh})$	$\Delta\theta_i$	$\Delta\theta_i/\theta_i(x_{sh})$	H_{max}
Zig-zag	39 μm	58%	26 μm	55%	1.61
Step	39 μm	56%	26 μm	57%	1.80
Dist. roughness	28 μm	34%	16 μm	28%	1.72

SHOCK IMPINGEMENT TO TRIP DISTANCE: $30\delta_{95}$

For a more upstream location of the shock impingement ($x_{sh} = 46$ mm), Fig.6.14 shows the velocity field inside the interaction region for the case of the distributed roughness patch (a) and the step (b). For the sake of clarity, the y -axis was scaled with a factor of three with respect to x -axis. The most important difference between both velocity fields is the presence of a separation bubble for the case of the step. Although a small separation bubble will always be present at the downstream edge of the trip, for this particular configuration it appears that this separation bubble is now connected with the interaction region, creating one large separation bubble extending for ~5.5 mm from the trailing edge of the step downwards.

By visual inspection of Fig.6.14b it appears that a laminar profile is recorded on top of the separation bubble and that transition occurs downstream of the shock impingement location. To further substantiate this observation it was decided to calculate the incompressible shape factor $H_{i,aw}$ throughout the interaction region (see Fig.6.15). The classical definition of the shape factor involves an integration of the velocity field from the wall up to the freestream. The presence of a separation bubble will therefore have a major impact on the calculated value of the shape factor, which is undesirable if it is to be used as a metric to indicate transition. Therefore, to eliminate the contribution of the separation bubble to the shape factor a new 'artificial' wall location y_{aw} is defined by linearly extrapolating the velocity vectors in the range of $0.2 - 0.6U_\infty$ to 0 m/s. This implies that the data points below y_{aw} are therefore no longer used when calculating the shape factor. The incompressible shape factor calculated according to this new definition will be designated with the symbol $H_{i,aw}$. More information on this alternative shape factor definition can be found in section 5.1.3.

Fig.6.15 confirms that the boundary layer remains in a laminar state up to the shock impingement location. Transition sets in after passing the incident shock wave and a rapid decrease in the shape factor can be observed. It should be noted here that the measurement conditions for this particular case were challenging. The shock wave was positioned close to the tripping device, which caused laser reflections to enter the region of interest. Also, the near-wall seeding conditions were rather poor due to the tracer particles being lifted over the laminar separation bubble formed downstream of the trip. The shape factor presented in Fig.6.15 should therefore only be interpreted in a qualitative sense, as an indicator of boundary layer transition.

The situation is quite different for the case of distributed roughness (Fig.6.14a). The boundary layer just upstream of the shock wave is already in a turbulent state ($H_i \sim 1.55$ at $x = 45$ mm) and does not separate inside the interaction region. These results again confirm that the step is not optimal as a tripping device under these conditions. Tripping devices that introduce three-dimensionality in the flow are more effective at rapidly transitioning the boundary layer and therefore minimizing the trip-to-shock wave distance to achieve suppression of boundary layer separation. Finally, one may notice that the boundary layer downstream of the interaction ($x - x_{sh} = 3$ mm) is substantially thicker ($\sim 18\%$ of δ_{95}) for the case of the distributed roughness than for the case of the step. This probably is due to the effects of shock smearing in the interaction regime for the case of the step and due to the laminar boundary layer that is maintained for a longer streamwise distance (see also the discussion in section 6.4).

6.5. CONCLUSIONS

This study investigated the effects of forced transition on an oblique shock wave reflection ($\theta = 3^\circ$) at a freestream Mach number of 1.7 and unit Reynolds number of 35×10^6 m⁻¹. Three transition control devices were investigated: a zig-zag strip, a step-wise trip and a patch of distributed roughness. The tripping devices had a height of $k = 0.1$ mm, which corresponds to a $Re_k = U_\infty k / \nu_\infty = 3.5 \times 10^3$ or equivalently a $Re_{kk} = U_k k / \nu_k = 1.4 \times 10^3$. The tripping devices spanned the entire width of the plate and were positioned 40 mm from the leading edge of the flat plate ($Re_{x_{trip}} = 1.4 \times 10^6$).

The devices were first tested in the absence of an impinging shock wave. It was

found that the zig-zag strip and the patch of distributed roughness are most effective at tripping the boundary layer; a turbulent boundary layer was obtained approximately 6 mm ($\sim 30\delta_{95}$) downstream of the centreline of the device. The step also transitioned the boundary layer, but a longer streamwise distance of 11 mm ($\sim 55\delta_{95}$) was needed to reach a fully turbulent state. Based upon these results it was therefore decided to carry out the tests with the oblique shock wave positioned at 6 and 11 mm from the tripping device.

For the $x_{sh} - x_{trip} = 11$ mm case, all three tripping devices were able to eliminate the separation bubble in the interaction region. This was expected, since all trips yield a turbulent boundary layer 11 mm downstream of the trip, which for the current operating conditions does not separate when disturbed by a $\theta = 3^\circ$ shock wave (see section 5.1). Small differences can be noted though in the interaction region for the different trips. For the zig-zag strip, the patch of distributed roughness and the step maximum shape factors of, respectively, 1.6, 1.7 and 1.8 were recorded in the interaction region. This implies that the boundary layer for the case of the step was closest to separation and for the zig-zag strip it was furthest removed from separation.

The differences were more pronounced for a shock impingement location 6 mm downstream of the trip. For these conditions, a large separation bubble is recorded for the case of the step, whereas no separation is recorded for the distributed roughness case. This result confirms that under the present measurement conditions it is more effective to apply a 3D type of trip instead of a 2D trip.

In conclusion, the shock-induced separation bubble present for the laminar interaction can effectively be removed by tripping the boundary layer a short distance upstream of the interaction. However, this comes at the price of having a substantially thicker ($\sim 50\%$) boundary layer downstream of the interaction ($x - x_{sh} = 10$ mm). It is expected that this is caused partially by losses at trip (e.g. wave drag, flow separation) and partially by the reduced wave and friction drag of the laminar SWBLI. The tripped interaction shows a single reflected shock wave, whereas the laminar interaction shows a combination of compression and expansion waves, which results in lower entropy losses. Furthermore, for the laminar interaction, the boundary layer remains in a laminar state (i.e. low skin friction coefficient) up to the shock impingement location. The shock acts as an effective tripping device, triggering transition, which helps the boundary layer in overcoming the pressure rise towards reattachment. Given the fact that no large-scale unsteadiness was recorded for the laminar interaction (see section 5.3), it appears that tripping for this case mainly has a negative effect on the flow properties downstream of the interaction.

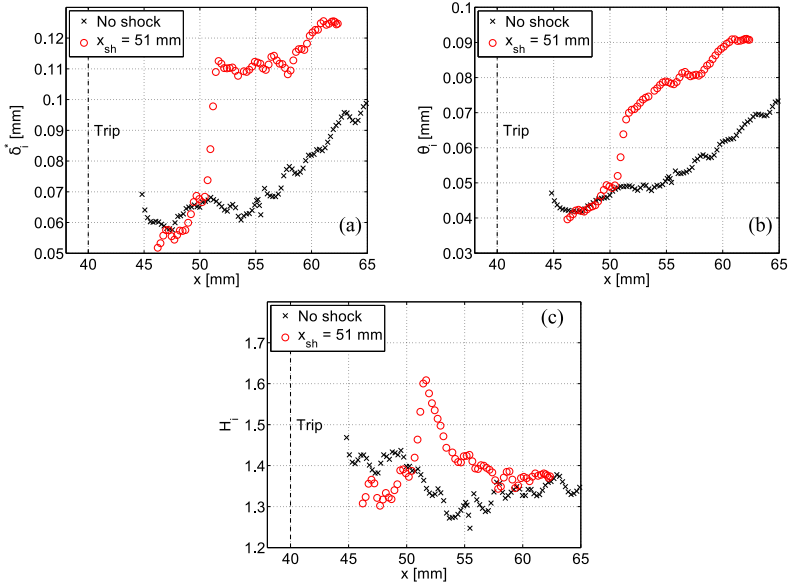


Figure 6.10: Development of the incompressible displacement thickness δ_i^* (a), incompressible momentum thickness θ_i (b) and incompressible shape factor H_i^- (c) downstream of the zig-zag strip, with an impinging shock at $x_{sh} = 51$ mm

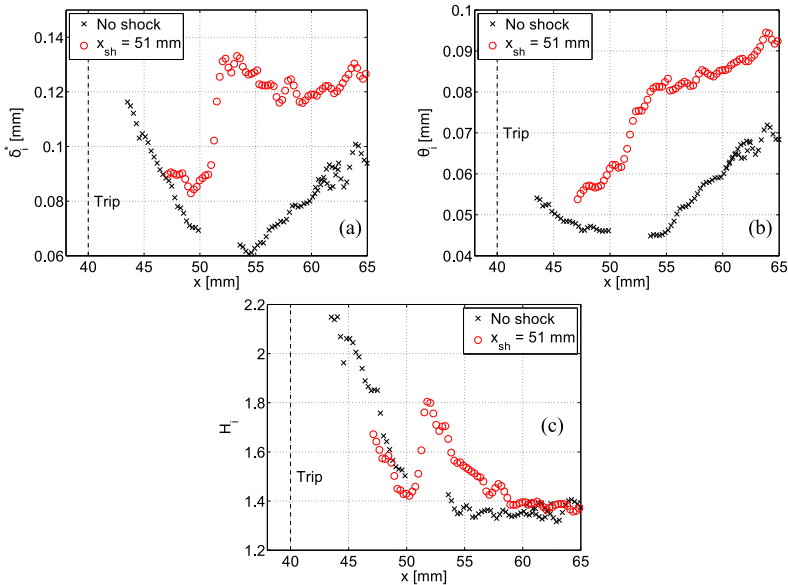


Figure 6.11: Development of the incompressible displacement thickness δ_i^* (a), incompressible momentum thickness θ_i (b) and incompressible shape factor H_i^- (c) downstream of the step, with an impinging shock at $x_{sh} = 51$ mm

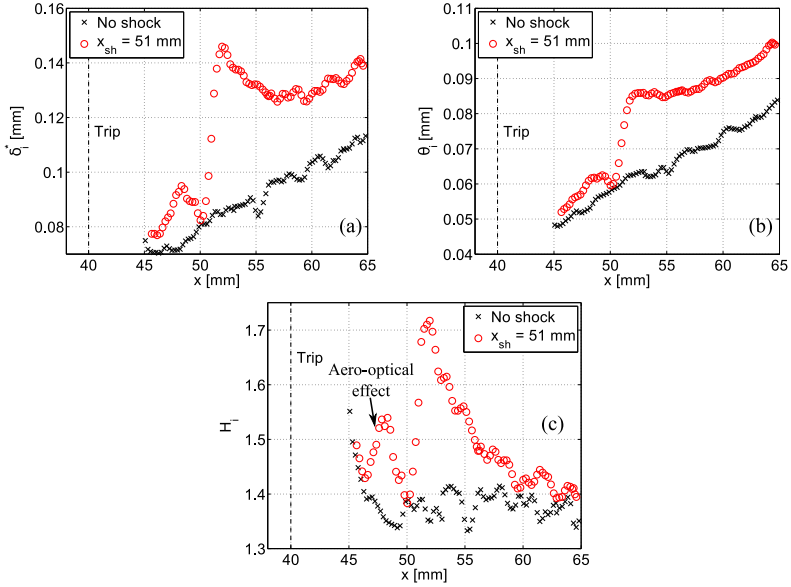


Figure 6.12: Development of the incompressible displacement thickness δ_i^* (a), incompressible momentum thickness θ_i (b) and incompressible shape factor H_i (c) downstream of the patch of distributed roughness, with an impinging shock at $x_{sh} = 51$ mm

6

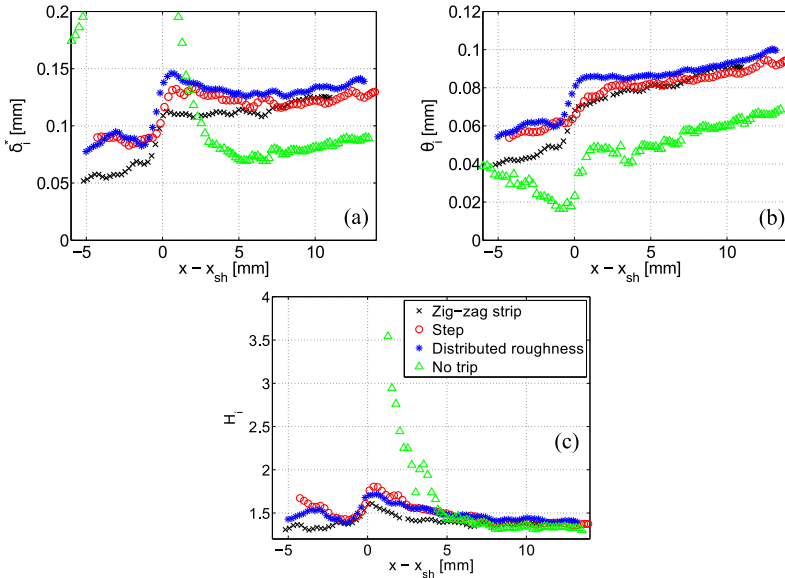


Figure 6.13: Development of the incompressible displacement thickness δ_i^* (a), incompressible momentum thickness θ_i (b) and incompressible shape factor H_i (c) for the three tripping devices and the untripped laminar interaction ($x_{sh} = 51$ mm)

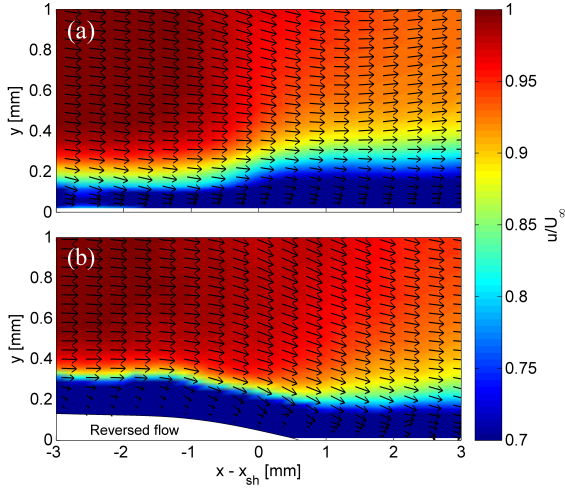


Figure 6.14: The u -component of the velocity field in the interaction region ($x_{sh} = 46$ mm) (a) Distributed roughness (b) Step

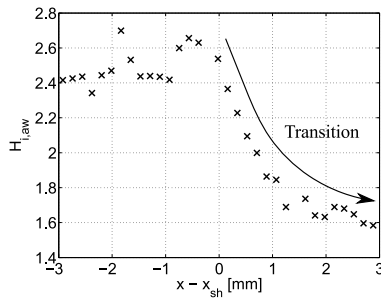


Figure 6.15: Development of the incompressible shape factor $H_{i,aw}$ throughout the interaction region for the case of the step and a shock impingement location $x_{sh} = 46$ mm.

II

FLOW CONTROL FOR TURBULENT OBLIQUE SHOCK WAVE REFLECTIONS

7

NEW INSIGHTS IN THE FLOW TOPOLOGY OF MICRO-RAMP VORTEX GENERATORS

This part of the thesis looks into the control of turbulent oblique shock wave reflections with micro-ramp vortex generators. A micro-ramp is a small triangular, wedge-shaped type of vortex generator (see Fig.7.1) that has specifically been designed for supersonic operating conditions (Anderson et al. (2006)). The typical height of such devices is in the order of $\sim 50\%$ and their control effectiveness comes primarily from the two counter-rotating vortices they introduce in the flow. These vortices redistribute momentum throughout the boundary layer, where high-momentum fluid is transported towards the wall and, vice versa, low-momentum fluid is carried away from the wall. The end result is a fuller velocity profile that is less prone to separation and that can pass through a shock wave-boundary layer interaction with potentially lower losses and lower levels of flow unsteadiness.

Micro-ramps have therefore been identified by several researchers as a promising alternative to boundary layer bleed (Anderson et al. (2006); Blinde et al. (2009); Babinsky et al. (2009); Panaras and Lu (2015)). The latter technique is often employed in supersonic jet intakes (see also section 1.2) and although proven to be effective at reducing the total pressure losses associated with SWBLIs, it does have the main disadvantage that part of the mass flow needs to be removed from the inlet. This requires the frontal area of the engine to be increased, thus increasing the weight and drag contribution of the engine.

The flow topology around micro-ramps has been studied extensively by a number of researchers (e.g. Babinsky et al. (2009); Lu et al. (2012); Sun et al. (2012)) and their findings were summarized in section 1.5 of this thesis. This chapter forms an extension on their work and presents some new insights in the flow field around micro-ramp vortex generators. First, the horseshoe vortex at the leading edge of the micro-ramp (see Fig.7.1) is discussed in section 7.1, based upon a series of oil-flow visualizations.

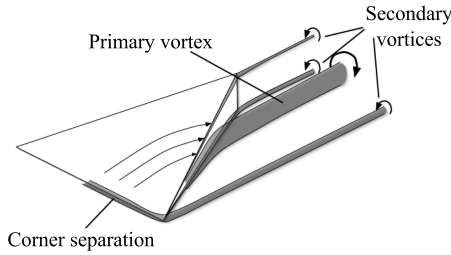


Figure 7.1: Conceptual model of the flow topology around micro-ramp vortex generators by Babinsky et al. (2009).

The second topic to be discussed in this chapter is the formation of Kelvin-Helmholtz vortices in the shear layer of the micro-ramp's wake. Sun et al. (2014) performed an extensive study into the evolution of these vortices and was able to produce a conceptual model of the vortical organization in a micro-ramp's wake (see Fig.7.2). For their study they solely relied upon the use of particle image velocimetry measurements. Section 7.2 shows that many of their results can be easily reproduced by means of simple spark-light schlieren visualizations. This technique has the additional advantage that measurements can be made very close to the trailing edge of the micro-ramp. This is often not possible when performing PIV measurements, because of the strong laser light reflections coming from the trailing edge of the micro-ramp. New information has therefore become available on the early stage development of Kelvin-Helmholtz vortices in a micro-ramp's wake.

7

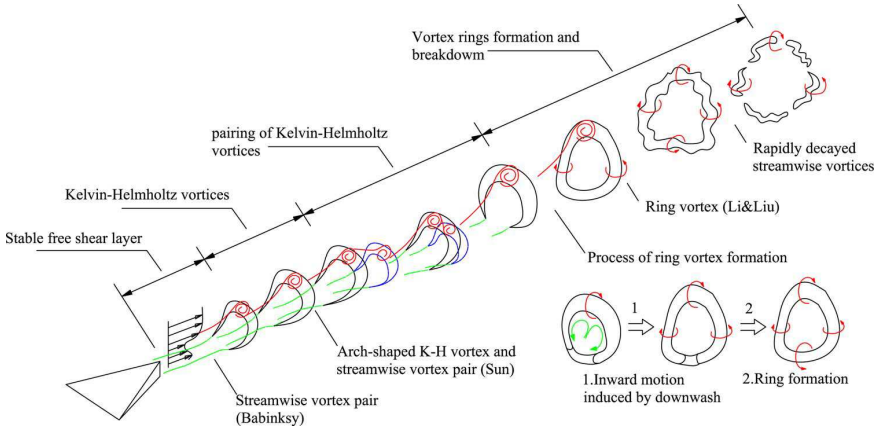


Figure 7.2: Conceptual model of the development and decay of Kelvin-Helmholtz vortices in a micro-ramp's wake by Sun et al. (2014).

7.1. THE ABSENCE / PRESENCE OF A LEADING-EDGE HORSESHOE VORTEX

Oil-flow visualizations have been employed by several researchers (Babinsky et al. (2009); Herges et al. (2009); Saad et al. (2012); Lu (2015)) to study the intricate flow behaviour around micro-ramp vortex generators. Fig.7.3 presents a compilation of their results, clearly visualizing the presence of a primary vortex pair and several secondary vortices formed around the slanted edges of the micro-ramp. Additionally, all four researchers recorded the presence of a weak horseshoe vortex, which wraps around the leading edge of the micro-ramp and trails downstream. It is important to mention here that oil was applied both upstream and downstream of the micro-ramp for the experiments of Babinsky et al. (2009), Herges et al. (2009) and Lu (2015) and only upstream of the micro-ramp for the experiments of Saad et al. (2012).

The initial oil film distribution can, however, have a significant impact on the final oil-flow pattern and in this section it will be shown that the horseshoe vortex is not present / non-detectable when the oil is only applied downstream of the micro-ramp. In fact, the horseshoe type of feature that is present in Fig.7.3 is not due to the active presence of a horseshoe vortex, but due to oil being transported around the corners of the ramp and further downstream. The longer the wind tunnel run lasts, the longer this horseshoe type of feature becomes in the final oil-flow visualizations. However, this does not necessarily imply that the horseshoe vortex is non-existent, only that it is a very weak feature of the flow, which is non-detectable by our oil-flow visualizations. A more elaborate discussion on this topic is given in section 7.1.2 and the experimental arrangement for the current study is presented in section 7.1.1.

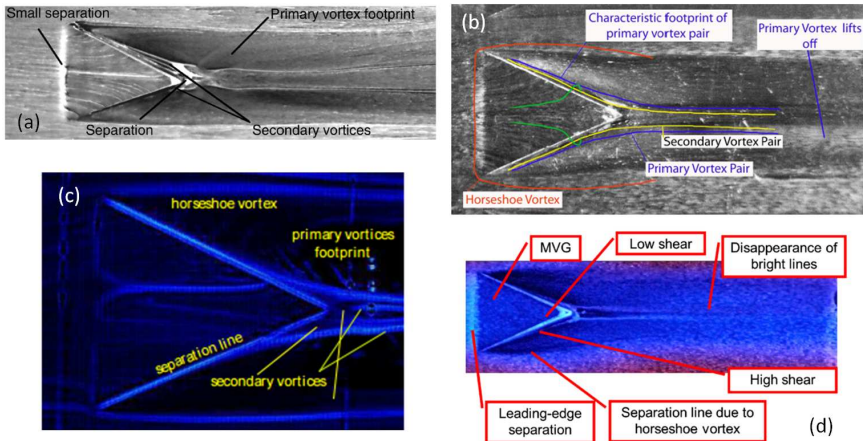


Figure 7.3: Oil-flow visualizations on micro-ramp vortex generators in supersonic flow. (a) Babinsky et al. (2009), (b) Herges et al. (2009), (c) Saad et al. (2012) and (d) Lu (2015).

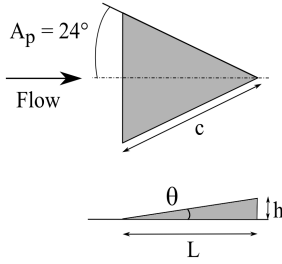


Figure 7.4: Micro-ramp geometry

Table 7.1: Micro-ramp geometrical parameters

θ	L	c
4.3°	$13.2h$	$14.5h$
8.6°	$6.6h$	$7.2h$
13.0°	$4.3h$	$4.8h$
17.3°	$3.2h$	$3.5h$
21.6°	$2.5h$	$2.8h$

7.1.1. EXPERIMENTAL ARRANGEMENT

The experiments were performed in the ST-15 supersonic blow-down wind tunnel of the TU Delft. The tunnel was operated at Mach 2.0, a total pressure of 3.2 bars and a total temperature of approximately 290 K. This results in a freestream velocity of 524 m/s and a unit Reynolds number of $42 \times 10^6 \text{ m}^{-1}$. The tunnel wall boundary layer, at these conditions, has a thickness of $\delta_{99} = 5.2 \text{ mm}$, an incompressible displacement thickness of $\delta_i^* = 0.63 \text{ mm}$ and an incompressible momentum thickness of $\theta_i = 0.52 \text{ mm}$. More information on the tunnel wall boundary layer properties can be found in section 8.1.1.

The micro-ramps were mounted on the bottom wall of the tunnel and were aligned with the centreline. The geometry of the micro-ramps is based on the optimization study of Anderson et al. (2006) for minimizing the incompressible shape factor H_i downstream of the micro-ramp. The shape of the micro-ramp is presented in Fig.7.4 and its dimensions are listed in Table 7.1. The ramp angle of the ‘standard’ Anderson et al. (2006) micro-ramp equals $\theta = 8.6^\circ$. Additionally, also smaller and larger ramp angles were tested, covering the range from $\theta = 4.3^\circ - 21.6^\circ$. The ramp angle was altered by changing the length of the micro-ramps, while keeping the micro-ramp height h and semi-angle A_p fixed at $h = 3 \text{ mm}$ and $A_p = 24^\circ$, respectively.

For the oil-flow visualizations a mixture of Shell Tellus type 22 oil and TiO_2 particles (Sachtleben UV-TITAN L-530, 30 nm crystal size) was used. To this mixture a couple of drops of oleic acid were added in order to obtain an oil film layer with the right viscosity for the current application.

7.1.2. RESULTS

Fig.7.5c presents the oil-flow visualization that was performed on the standard Anderson et al. (2006) micro-ramp ($\theta = 8.6^\circ$), with oil applied both upstream and downstream of the micro-ramp. The visualization reveals a type of structure, which could be attributed to the presence of a horseshoe vortex and which shows a close similarity with the results recorded by Babinsky et al. (2009), Herges et al. (2009), Saad et al. (2012) and Lu (2015). This horseshoe type of feature, however, disappears from the results when the oil is applied only downstream (Fig.7.5d) of the leading edge.

Intuitively it might be tempting to associate a large accumulation of oil with a low skin friction coefficient and, vice versa, a region with little oil to a high skin friction coefficient. However, this interpretation does not hold true under all circumstances. The oil flows in the direction of the local skin friction vector (except in regions with large

pressure gradients) and as such maps out the skin friction lines (Squire (1961)). The oil flowing between two skin friction lines must be conserved which means that the oil film height can increase by two factors: 1) a reduction of the skin friction coefficient, which lowers the convection speed of the oil and 2) converging skin friction lines. A large accumulation of oil therefore does not necessarily have to be associated with a low skin friction coefficient or the presence of a vortex, instead it can also be the result of closely spaced skin friction lines. This is exactly what happens for the case of the micro-ramp. The oil upstream of the micro-ramp is pushed around the edges of the ramp (converging skin friction lines) and continues to trail downstream as long as the wind tunnel is running, therefore creating long streaks which closely resemble a horseshoe vortex.

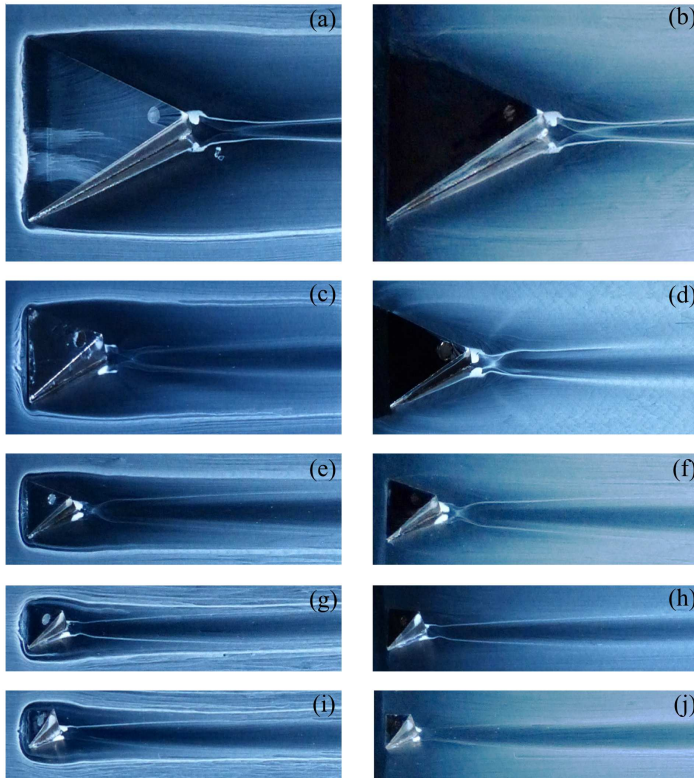


Figure 7.5: Oil-flow visualizations on micro-ramp vortex generators with flow deflection angles of $\theta = 4.3^\circ$ (a,b), $\theta = 8.6^\circ$ (c,d), $\theta = 13.0^\circ$ (e,f), $\theta = 17.3^\circ$ (g,h) and $\theta = 21.6^\circ$ (i,j), with and without oil applied upstream of the micro-ramp, respectively. The $\theta = 8.6^\circ$ case corresponds to the standard Anderson et al. (2006) micro-ramp.

Based upon topological arguments (Tobak and Peake (1982)) one would expect that a horseshoe vortex is formed if an open separation bubble is present at the leading edge of the micro-ramp. From the oil-flow visualizations on the Anderson et al. (2006) micro-ramp (Fig.7.5c-d) one can, however, not conclude that the flow is separated at the lead-

ing edge. The accumulation of oil that is recorded may also be the result of the reduced (but not necessarily negative) skin friction coefficient in the shock wave-boundary layer interaction. Whether or not the flow separates upstream of the micro-ramp depends on the flow deflection angle of the micro-ramp and the upstream boundary layer properties (e.g. boundary layer fullness, Mach number). The standard Anderson micro-ramp has a flow deflection angle of 8.6° , which is significantly lower than the incipient separation threshold of $\theta_{inc} \approx 15^\circ$ recorded by Kuehn (1959) at the given operating conditions ($M = 2.0$, $Re_{\delta_{99}} = 2.2 \times 10^5$). It should, however, be remarked here that Kuehn's experiments apply to a 2D object that extends far outside of the boundary layer. This separation criterion therefore does not hold true for a 3D object, which is completely embedded in the boundary layer, as also concluded by Lu (2015).

Therefore to further investigate the connection between the formation of a horseshoe vortex and the leading edge separation bubble, oil-flow visualizations were performed on micro-ramps with flow deflection angles of 4.3° , 13.0° , 17.3° and 21.6° (see Fig.7.5). As expected, the streamwise extent of the interaction region increases with increasing flow deflection angle. Although not very clear from the oil-flow visualizations, it appears that the flow is separated at the leading edge of the micro-ramp for the $\theta = 21.6^\circ$ case (Fig.7.5(i-j)). The separation line for this particular case is displaced by 2.8 mm ($4.5\delta_i^*$) with respect to the leading edge of the micro-ramp at its symmetry plane. If oil is applied both upstream and downstream of the micro-ramp, a clear 'horseshoe' type of feature appears in the oil-flow pattern. Again this feature is, not visible when the oil is applied only downstream of the leading edge. On topological grounds one would expect the formation of a horseshoe vortex since the flow is separated at the leading edge of the micro-ramp. The fact that it is not detectable in the oil-flow visualization of Fig.7.5(j) again shows that it is a very weak feature of the flow, which probably dissipates quickly downstream of the micro-ramp's leading edge.

A further CFD study would be recommended here to study the development of the horseshoe vortex in more detail. Such a study would be more of scientific interest than of actual industrial relevance, since it is already clear from the current results that the horseshoe vortex is a negligible feature of the flow which is of no relevance to the final flow control purpose of the micro-ramp.

7.2. SCHLIEREN VISUALIZATIONS OF KELVIN-HELMHOLTZ VORTEX SHEDDING

Spark-light schlieren visualizations were used to study the development of Kelvin-Helmholtz vortices on the shear layer of a micro-ramp's low-momentum wake. The experiments were performed in the TST-27 transonic-supersonic blow-down wind tunnel of the TU Delft at the baseline operating conditions described in chapter 9, so $M_\infty = 2$ and $Re_\infty = 39 \times 10^6 \text{ m}^{-1}$. A $h = 8 \text{ mm}$ micro-ramp was mounted first on the bottom wall of the wind tunnel and next on the side wall of the tunnel, where the micro-ramp was aligned with the centerline of the wind tunnel for both experiments. The first experiment allows for a side-view visualization of the micro-ramp's wake (see Fig.7.6(a)) and the latter for a top-view visualization (see Fig.7.6(b)). The schlieren knife was oriented vertically for both experiments and a total of 300 spark-schlieren visualizations were obtained per test

case.

The spark-schlieren visualizations of Fig.7.6 reveal the presence of some intermittent, large-scale coherent structures in the wake of the micro-ramp, which are likely to be the imprint of the Kelvin-Helmholtz vortices. In principle, the observed coherent structures could also be the result of some hairpin type of structures propagating in the turbulent boundary and thus not be due to the anticipated Kelvin-Helmholtz vortices. Later analysis in this section will, however, show that both the wavelength and the shape of the observed structures are in good agreement with the Kelvin-Helmholtz vortices measured by Sun et al. (2012) during their Tomographic-PIV study on the wakes of micro-ramp vortex generators, thereby confirming our initial assumption of visualizing Kelvin-Helmholtz vortices in the spark-light schlieren images of Fig.7.6.

So, although the Kelvin-Helmholtz vortices are identifiable from the raw images, their structure and typical wavelength remains rather elusive. That is because the schlieren visualizations present a spanwise average of the flow field and the Kelvin-Helmholtz vortices are therefore obscured by density variations occurring elsewhere in the tunnel. This is especially problematic for the side-view visualizations of Fig.7.6(a), which present an average of the full tunnel wall boundary layer.

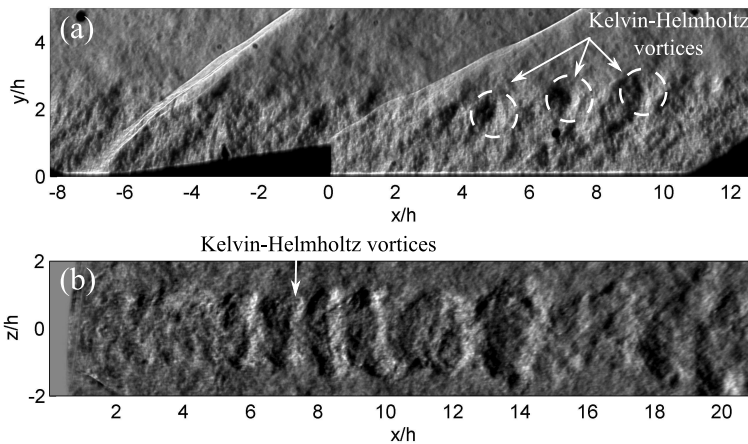


Figure 7.6: Spark-schlieren visualizations of the flow field around micro-ramp vortex generators. Side-view (a) and top-view (b).

Extra information can be obtained from the raw schlieren visualizations by performing a proper orthogonal decomposition (POD) of the full dataset. A POD analysis extracts the most energetic modes of the system (Berkoos et al. (1993)) and therefore allows for a much clearer visualizations of the Kelvin-Helmholtz vortices. Fig.7.7 and 7.8 show a selected number of POD modes for the side-view and top-view schlieren visualizations, respectively. The POD modes typically come in pairs, so mode 1 is similar to mode 2 and mode 3 is similar to mode 4, etc... The main difference between between these modes is a 180° phase shift (e.g. see Figs.7.7(a-b)), which places the modes in anti-phase of each other. In theory, the combination of a sufficient number of mode pairs in an appropriate reduced order model would allow for the reconstruction of the convecting motion of the

Kelvin-Helmholtz vortices. The aim of the current analysis is, however, not to construct such a model, but to use the POD modes to get a better qualitative understanding of the shape and development of the Kelvin-Helmholtz vortices downstream of the micro-ramp.

Figs.7.7 and 7.8 reveal an intermittent train of Kelvin-Helmholtz vortices, which over-arch the two primary vortices. Fig.7.7 shows that the Kelvin-Helmholtz vortices are inclined with respect to the surface by an angle of approximately $19^\circ \pm 2^\circ$. Near the wall, there appears to be the formation of a vortex leg, which is inclined over a substantially larger angle and tends to align with the wall. These observations are in general agreement with the conceptual model of Sun et al. (2014) presented in Fig.7.2.

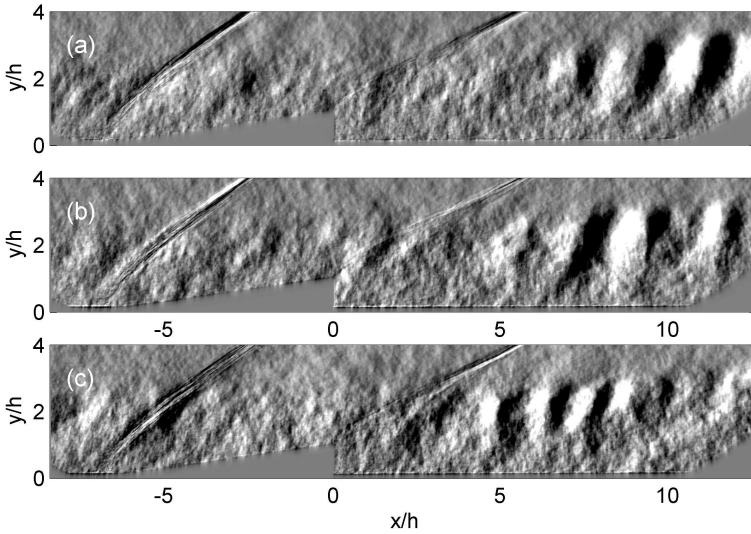


Figure 7.7: POD modes of the side-view spark-schlieren visualizations. Mode 1 (a), mode 7 (b) and mode 9 (c).

The top-view POD modes of Fig.7.8 show that the wavelength of the Kelvin-Helmholtz vortices increases when moving downstream of the micro-ramp. Around $x = 10h$, a typical wavelength λ of $1.5h$ is recorded, whereas at $x = 20h$, this wavelength has increased to a value of $\lambda = 2h$. To further substantiate this result it was decided to perform a two-point correlation analysis on the raw schlieren visualizations. In this analysis, one point was fixed in space and the correlation coefficient R was calculated with respect to its neighbouring points. Fig.7.9 shows the spanwise averaged correlation coefficient at $x = 10h$, where results were averaged over a region of $-h \leq z \leq h$ in span. The typical width of the Kelvin-Helmholtz vortices at this location is $\pm 1.2h$, which implies that in the averaging procedure only data is used that is affected by the presence of Kelvin-Helmholtz vortices.

If a zero shift ($\Delta x = 0$) is applied, then the signal is correlated with itself and, of course, a correlation coefficient of $R = 1$ is obtained. A substantial drop in correlation coefficient can be observed when moving to the left or right of the reference point. Two minima are recorded in Fig.7.9, one at $x = -0.67h$ and the other at $x = 0.78h$, which

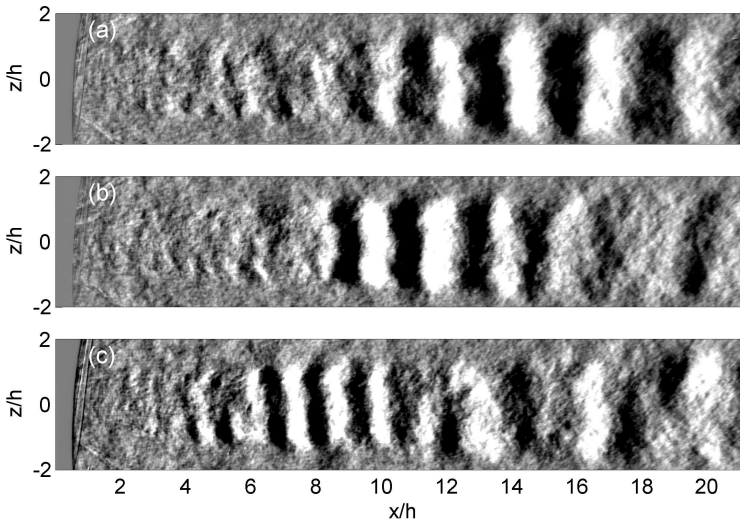


Figure 7.8: POD modes of the top-view spark-schlieren visualizations. Mode 1 (a), mode 7 (b) and mode 9 (c).

were determined by fitting a smoothing spline to the data. The distance between the two minima ($0.67h + 0.78h = 1.45h$) then provides an indication of the wavelength λ of the Kelvin-Helmholtz vortices.

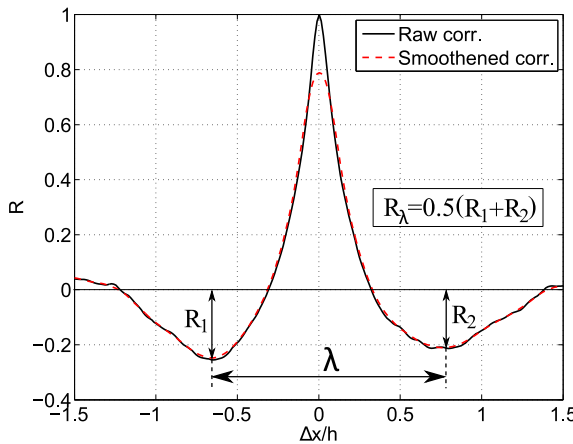


Figure 7.9: Two-point correlation coefficient R between a point $(10h, y)$ and $(10h - \Delta x, y)$ for the top-view spark-schlieren visualizations. Results are averaged in the z -direction over $-h \leq z \leq h$.

The procedure outlined in Fig.7.9 can now be repeated for an entire range of x -locations, starting from the trailing edge of the micro-ramp towards the end of the measurement domain. Fig.7.10(a) shows the wavelengths that were calculated from the top-view and side-view schlieren visualizations. The calculated wavelengths are in good

agreement with each other and with the data of Sun et al. (2014), which was obtained for virtually the same operating conditions ($M_\infty = 2.0$, $Re_\infty = 41 \times 10^6 \text{ m}^{-1}$), but in a different wind tunnel (ST-15 at the TU Delft) with a thinner turbulent boundary layer ($\delta_{99} = 5.2 \text{ mm}$ instead of $\delta_{99} = 17.3 \text{ mm}$). Smaller micro-ramps of $h = 3$ and 4 mm were therefore used in their study. From this data it was found that the wavelength of the K-H vortices scales proportionally with the micro-ramp height (see also Fig.7.10(a)).

The data of Sun et al. (2014) reveals a sudden jump in wavelength around $x = 20h$, which they argue can be attributed to the pairing process of Kelvin-Helmholtz vortices. This process was, however, not captured in the current experiment due to limited size of the measurement domain (constrained by the size of the schlieren windows). It would, however, be worthwhile to repeat the current measurements on either a $h = 8 \text{ mm}$ micro-ramp that is located further upstream in the wind tunnel or on a smaller $h = 4 \text{ mm}$ micro-ramp positioned at the same location. Such experiments would also yield data for $x > 20h$ and should therefore accommodate a study into the vortex pairing process proposed by Sun et al. (2014).

Fig.7.10(a) shows that there is a virtually linear increase in the K-H wavelength when moving from $x = 5h - 20h$, where λ increases by $\sim 67\%$ from $1.2h$ to $2.0h$. This increase in wavelength is in part due to the higher convection velocities in the upper shear layer further downstream of the micro-ramp. The PIV measurements of chapter 9 revealed that the mean streamwise velocity at the inflection point of the upper shear layer measures $\sim 0.8U_\infty$ at $x = 5h$ and $\sim 0.9U_\infty$ at $x = 20h$. This translates into a percentual increase of $\sim 13\%$ and can therefore only partially explain the observed growth in the K-H wavelength. The additional growth is probably due to the effects of dissipation, but this remains to be investigated.

The Kelvin-Helmholtz vortices are not created instantaneously at the trailing edge of the micro-ramp. Stability theory predicts that there is a linear amplification stage of the instabilities in the upper shear layer of the low-momentum wake, followed by non-linear amplification and the roll-up of the instabilities into Kelvin-Helmholtz vortices (White (2005)). This predicted behaviour is reflected in the development of the correlation coefficient R_λ , which is presented in Fig.7.10(b). The coefficient R_λ is calculated as the average of the correlation coefficients R_1 and R_2 measured at the left and right minima of Fig.7.9, respectively. A high value of R_λ indicates a strong / coherent instability that clearly stands out of the freestream background noise, whereas a low value of R_λ indicates the exact opposite. Lower correlation coefficients are typically recorded for the side-view schlieren visualizations due to a higher level of 'background noise' in the images. The side-view schlieren visualizations are averaged over the entire span of the tunnel's bottom wall boundary layer, whereas the light rays for the top view schlieren visualizations pass through a large portion of freestream, where density fluctuations are expected to be substantially smaller than in the turbulent wall boundary layer.

From the results of Fig.7.10(b) it appears that there is an initial amplification stage of approximately $6-8h$, after which the K-H instabilities become saturated and start to roll-up, resulting in near-constant levels of R_λ . Of course, correlation coefficients cannot be translated directly to vortex strengths or velocity fluctuations, but they can give a general idea of K-H vortex development in the near-vicinity of the micro-ramp, which has, to the author's knowledge, not been investigated yet in any experimental study on micro-ramp

vortex generators.

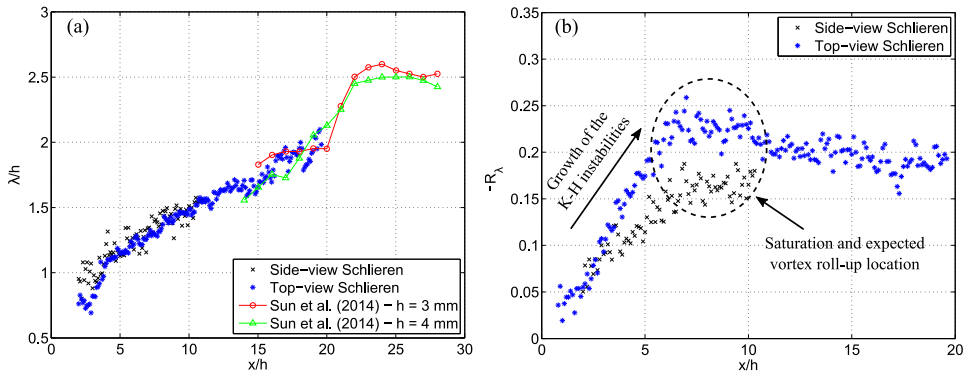


Figure 7.10: Results of the correlation analysis for the side-view and top-view schlieren visualizations, showing the Kelvin-Helmholtz wavelength λ development (a) and the corresponding correlations coefficients R_λ (b).

8

MICRO-RAMP FLOW CONTROL

This chapter investigates the influences of micro-ramp size and location on its effectiveness as a flow control device for turbulent oblique shock wave reflections. The effectiveness is measured in terms of the size of the shock-induced separation bubble and the level of reflected shock unsteadiness. Planar particle image velocimetry measurements were performed to instantaneously capture the separation bubble and inflow conditions. The results of the parametric study are interpreted by analyzing the effects of the micro-ramp on the boundary layer entering the interaction. A phenomenological description is provided of the mixing processes downstream of a micro-ramp and a criterion is derived for the minimum distance required between the micro-ramp and the interaction.

8.1. EXPERIMENTAL ARRANGEMENT

8.1.1. FLOW FACILITY

The experiments were carried out in the ST-15 blow-down supersonic wind tunnel of the Delft University of Technology. The test section measures $150 \times 150 \text{ mm}^2$ and the tunnel is operated at Mach 2, a total pressure p_0 of 3.2 bars, and a total temperature T_0 of 290 K. This results in a freestream velocity U_∞ of 524 m/s and a unit Reynolds number of 42.2 million. The incident shock wave is created by a nearly full-span 12 degree shock generator. The shock generator is designed such that the expansion fan emanating from its shoulder does not interfere with the shock wave-boundary layer interaction (see Fig.8.1).

The boundary layer on the bottom wall of the tunnel is used for all the experiments in this study. It develops along a smooth surface for approximately 1 m under nearly adiabatic conditions and reaches a thickness $\delta_{99} = 5.2 \text{ mm}$ in the test section. The properties of the undisturbed boundary layer were measured by means of a dedicated PIV experiment at high resolution. A spatial resolution of 59 pixels/mm was used and the

Parts of this chapter have been published in *Physics of Fluids* **26(6)** (Giepmans et al. (2014b)) and parts have been presented at the 20th International Shock Interaction Symposium (Giepmans et al. (2012)) and the 5th European Conference for Aeronautics and Space Sciences (Giepmans et al. (2013)).

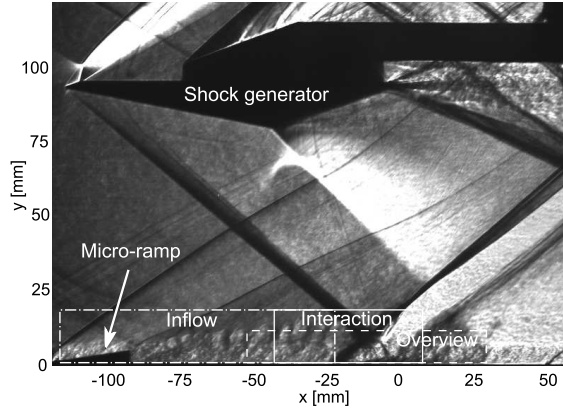


Figure 8.1: Spark-light schlieren visualization of the tunnel setup; the field of views used for the different camera configurations are overlaid.

laser pulse separation was set to $1 \mu\text{s}$, resulting in a freestream particle displacement of 31 pixels. The incompressible displacement thickness δ_i^* is determined to be 0.63 mm, the incompressible momentum thickness $\theta_i = 0.52 \text{ mm}$ and the incompressible shape factor $H_i = 1.23$. The Reynolds number based on the incompressible momentum thickness equals: $Re_{\theta_i} = \rho_{\infty} U_{\infty} \theta_i / \mu_{\infty} = 21.8 \times 10^3$, with μ_{∞} being the dynamic viscosity of the freestream.

By using the Van Driest II transformation in combination with the Crocco-Busemann relation (recovery factor $r = 0.89$), the skin friction coefficient c_f and friction velocity u_{τ} are determined from a log-law fit which yields 1.9×10^{-3} and 20.8 m/s, respectively. The experimental conditions and boundary layer properties are summarized in Table 8.1.

Table 8.1: Experimental conditions and undisturbed boundary layer properties

Parameter	Quantity	Parameter	Quantity
M_{∞}	2.0	θ_i (mm)	0.52
U_{∞} (m/s)	524	H_i	1.23
p_0 (N/m ²)	3.2×10^5	u_{τ} (m/s)	20.8
T_0 (K)	290	c_f	1.9×10^{-3}
δ_{99} (mm)	5.2	Re (1/m)	42.2×10^6
δ_i^* (mm)	0.63	Re_{θ_i}	21.8×10^3

8.1.2. MICRO-RAMP CONFIGURATIONS AND EXPERIMENTAL MATRICES

The geometry of the micro-ramps used in this study are based on the recommendations of Anderson et al. (2006) for minimizing H_i downstream of the micro-ramp. The dimensions of this micro-ramp are presented in Fig.8.2 and are normalized with the micro-ramp height h .

Table 8.2 provides an overview of the different measurement configurations considered. Three different micro-ramp heights were investigated in this study, namely 2, 3 and

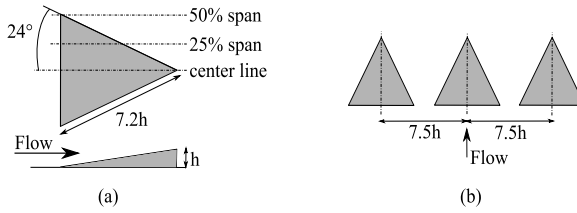


Figure 8.2: Dimensions of a single micro-ramp (a) and an array of three ramps (b)

4 mm (set A-C). They were mounted at a range of distances d : the distance between the trailing edge of the micro-ramp and the inviscid impingement location of the incident shock wave. All the measurements in sets A-C were carried out along the centerline plane of the micro-ramp. Set D considers the flow behavior at two off-center location, namely 25% and 50% span (see Fig.8.2(a)). In set E, three 4 mm micro-ramps were mounted next to each other in the tunnel (see Fig.8.2(b)). The spacing s between the center lines of the micro-ramps equals $7.5h = 30$ mm, which is the value recommended by Anderson et al. (2006) and the one commonly used by other researchers Babinsky et al. (2009); Blinde et al. (2009); Lee et al. (2010). Finally, in set F, the undisturbed shock wave-boundary layer interaction is investigated, which will serve as a reference for all other cases.

All measurements were performed along the centerline of the tunnel. So, for measurements A-C the centerline of the micro-ramp coincided with the centerline of the tunnel and for measurements D-E the ramps were shifted with respect to the tunnel's centerline. For all the configurations investigated in this parametric study, 150 image pairs were recorded. For statistical purposes, the measurements on two configurations were repeated (see Table 8.3) and two datasets of 500 image pairs were obtained.

Table 8.2: Experimental matrix for the parametric study

	Number of ramps	Spacing s	Height h	Distance d/δ_{99}	Plane z/δ_{99}
A	1	-	2 mm	8.1, 10.4, 13.8, 17.3, 20.8	0
B	1	-	3 mm	10.4, 13.8, 17.3, 20.8	0
C	1	-	4 mm	10.4, 13.8, 17.3, 20.8	0
D	1	-	4 mm	17.3	1.15, 2.3
E	3	$7.5h$	4 mm	17.3	0, 1.15, 2.3
F	Clean configuration - No micro-ramp				

Table 8.3: Experimental matrix for the overview measurements

	Number of ramps	Spacing s	Height h	Distance d/δ_{99}	Plane z/δ_{99}
G	1	-	4 mm	17.3	0
H	Clean configuration - No micro-ramp				

8.1.3. PIV ARRANGEMENT

Planar PIV measurements were carried out to capture the instantaneous flow field downstream of the micro-ramp and inside the interaction region. For the parametric study (Table 8.2), two 16 MP Lavision Imager Pro LX cameras were used simultaneously. One of the cameras was zoomed in on the interaction region and the other was focused on the inflow into the interaction. An overlap of 20 mm was provided to allow proper combination of the datasets (See Fig.8.1).

On the ‘interaction’ camera a 105 mm Nikkor objective was used with $f_{\#}$ set to 5.6. Cropping and binning (2x2) were applied to accelerate data acquisition (see Table 8.4). This resulted in a field of view (FOV) of 50x20 mm and 48 pixels/mm for the interaction camera. On the ‘inflow’ camera, a 60 mm Nikkor objective was used with $f_{\#}$ also set to 5.6 and the image was cropped to fit the laser sheet, which resulted in a FOV of 95x20 mm and 35 pixels/mm. However, due to strong laser reflections from the micro-ramp, it was not possible to use the full FOV, and no data could be acquired within 10 mm of the ramp. For the ‘overview’ measurements of Table 8.3, only one of the cameras was used. To speed up the acquisition process, the camera was zoomed out and cropped in the wall normal direction. A 60 mm Nikkor objective was used with $f_{\#}$ set to 5.6. This resulted in a FOV of 80x13 mm and a digital resolution of 25 pixels/mm.

Table 8.4: Viewing configuration for the PIV measurements

Configuration	FOV		Resolution		Particle displacement
	mm	pixels	$\mu\text{m}/\text{pix}$	mm/vec	pixels
Interaction	50 × 20	2416 × 967	21	0.16	25
Inflow	95 × 20	3291 × 693	29	0.17	18
Overview	80 × 13	1955 × 333	41	0.25	13

Illumination was provided by a Quantel Evergreen double-pulsed Nd:YAG laser with a pulse energy of 200 mJ, a pulse duration of <10 ns and a pulse rate of 5.5 Hz (limited by the camera). A pulse separation of 1 μs was used, resulting in particle displacements of 25, 18 and 13 pixels for the interaction, inflow and overview field of view, respectively. The flow was seeded with DEHS particles, having a nominal diameter of 1 μm and a relaxation time τ of 2 μs , as determined by Ragni et al. (2010). In the region of the incident shock wave this translates into a relaxation length of 1 mm. The ratio of the particle relaxation time with respect to the flow time scales is defined as the Stokes number: $\tau U_{\infty}/\delta_{99} = 0.2$, which according to Samimy and Lele (1991) translates into maximum slip velocities of $0.02U$.

Davis 7.4 was used for data acquisition and Davis 8.1 for processing the data. As pre-processing steps, a sliding minimum filter over time was applied to remove wall laser reflections and a min-max filter was used to normalize particle intensities. A multi-pass cross-correlation approach was used with final interrogation windows of 32×32 pixels and 75% overlap for the interaction camera. For the inflow and overview camera, 24×24 windows with 75% overlap were used. The resulting vector pitches are summarized in Table 8.4. Spurious vectors were removed using the universal outlier detection Westerweel and Scarano (2005) approach implemented in Davis.

8.1.4. UNCERTAINTY ANALYSIS

The experimental results are subject to uncertainties introduced by the data ensemble size, the measurement technique, and micro-ramp positioning errors.

For the parametric study, 150 image pairs were recorded per case. The flow properties converged slowest in the region of the separation bubble, where the uncertainties on \bar{u} and u' are estimated to be 0.5% and 0.9%, respectively. The uncertainty on A_{sep} is estimated to be 0.7%; A_{sep} being the average separated area, an important parameter that will be introduced in section 8.2.2 to quantify the amount of separation per test case.

In the cross-correlation procedure, the location of the peak can only be determined with a finite accuracy of ~ 0.1 pixel. As a consequence, the instantaneous velocities measured are expected to be off by $\sim 0.4\%$ for the interaction field of view and by $\sim 0.6\%$ for the inflow field of view.

Particle slip has already been discussed in the previous section and for the DEHS particles used, slip velocities of $<2\%$ of the freestream velocity are expected. The effect of particle slip is most pronounced in regions where the particles are subjected to strong velocity gradients, for instance when passing a shock wave or inside vortices.

The micro-ramps were mounted in the tunnel by hand and although this was done with great precision, small positioning errors with respect to the laser sheet cannot be avoided. An offset of, for instance, 0.5 mm will significantly affect the velocity field that is measured, because the streamwise vortices that are responsible for the mixing process are of the same scale Sun et al. (2012). Even if the micro-ramp is perfectly aligned with the laser sheet, results will still be averaged due to the finite laser sheet thickness of approximately 1 mm. To investigate the sensitivity of the solution, several measurements were repeated; the uncertainty in the average separated area is expected to be 10-25%.

All the uncertainty parameters discussed are summarized in Table 8.5 together with the values for the overview field of view. For the overview field of view, 500 image pairs were recorded and consequently the statistical errors are smaller than for the parametric study.

Table 8.5: Uncertainty analysis

Parameter	Parametric study ($N = 150$)	Overview measurements ($N = 500$)
Statistical uncertainty		
• Average velocity $\epsilon_{\bar{u}}/U_{\infty}$	0.5%	0.1%
• Velocity fluctuations $\epsilon_{u'}/U_{\infty}$	0.9%	0.5%
• Average separated area $\epsilon_{A_{sep}}/A_{sep}$	0.7%	0.3%
Cross correlation uncertainty ϵ_{CC}	0.1 pixel	0.1 pixel
Instantaneous velocity $\epsilon_{u(\epsilon_{CC})}/U_{\infty}$	0.4 - 0.6%	0.8%
Particle slip $\epsilon_{\tau}/U_{\infty}$	$<2\%$	$<2\%$
Repeatability $\epsilon_{\Delta A_{sep}}/A_{sep}$	10 - 25%	

8.2. RESULTS

8.2.1. ASSESSMENT OF THE UNDISTURBED BOUNDARY LAYER

Before investigating the effects of a micro-ramp on the boundary layer and the interaction region, the undisturbed boundary layer profile will be assessed in more detail. A dedicated PIV measurement was carried out and the results are presented in Figs.8.3(a) and (b).

Fig.8.3(a) shows the mean velocity profile in terms of the inner variables $u^+ = u_{eq} / u_\tau$ and $y^+ = y u_\tau / \mu_w$. Here u_τ presents the friction velocity, μ_w the kinematic viscosity at the wall and u_{eq} the Van Driest effective velocity. The latter is obtained by applying the Van Driest II transformation in combination with the Crocco-Busemann relation (recovery factor $r = 0.89$) to the boundary layer profile. From Fig.8.3(a) it is clear that an excellent agreement between the boundary layer profile and the log law is obtained in the region from $y^+ = 200$ to $y^+ = 900$, for a friction velocity u_τ of 20.8 m/s. For $y^+ > 900$, a wake component can be distinguished, which can be described in terms of the law of the wake by Coles (1956). Coles' wake parameter Π is calculated to be 0.54, which falls within the range found in the study of Fernholz and Finley (1980). They reported that for flat-plates with $1.7 < M < 10.3$ and $Re_\theta > 2000$, Coles' wake parameter equals $\Pi = 0.55 \pm 0.05$.

Fig.8.3(b) shows the velocity fluctuations in the boundary layer in both streamwise and wall-normal direction. In order to allow a direct comparison with the classical incompressible data of Klebanoff (1955), the velocity components are normalized with respect to the friction velocity and scaled with $\sqrt{\rho / \rho_w}$ (Morkovin scaling). The density ratio is calculated from the mean velocity profile by using the adiabatic Crocco-Busemann relation with a recovery factor r of 0.89. Besides Klebanoff's data, the results from the tomographic PIV study of Humble et al. (2009) and the hot wire anemometry (HWA) study of Elena and Lacharme (1988) are also shown in the figure. The measurements reported in this study are in good agreement with these reference cases.

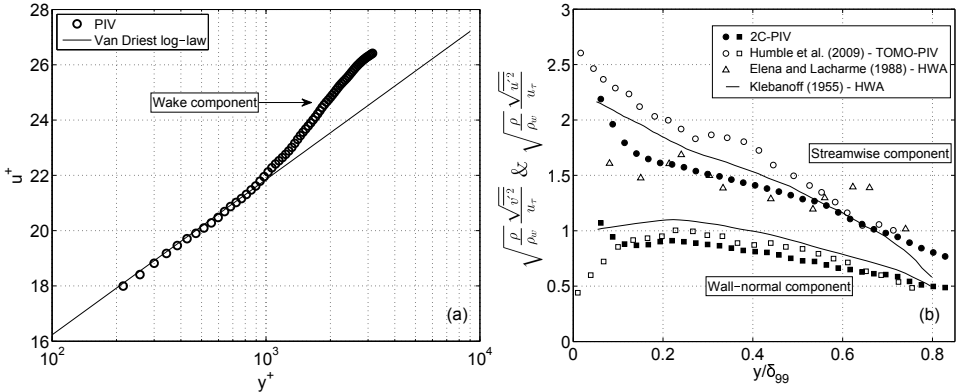


Figure 8.3: Assessment of the undisturbed boundary layer. Comparison with a log law fit (a) and the velocity fluctuations in Morkovin scaling (b)

8.2.2. EFFECTS OF THE MICRO-RAMP ON THE INTERACTION REGION

Before zooming in on the interaction region, it is illustrative to first consider the global features of the flow in the schlieren visualization of Fig.8.1. A 12 degree, nearly full-span shock generator is used to create the incident shock wave, which by definition impinges on the wall at $x = 0$ mm. The reflected shock is formed approximately 25 mm upstream. For this measurement, a 4 mm micro-ramp was placed 90 mm ($17.3\delta_{99}$) upstream of the incident shock impingement point. The micro-ramp is completely embedded in the boundary layer, and both the leading edge shock and the lip shock (terminating the expansion wave over the micro-ramp's corner) are clearly visible. Furthermore, it can be observed that the boundary layer thickens after passing the micro-ramp.

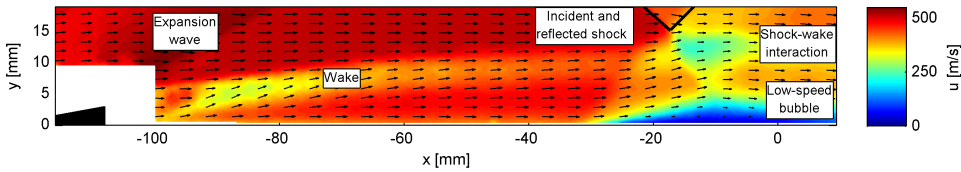


Figure 8.4: Flow field overview for a $h = 3$ mm micro-ramp at $x = -20.8\delta_{99}$. Presented is the u -component of the velocity field.

By combining the inflow and interaction field of view, an overview of the velocity field from micro-ramp until interaction can be constructed. Fig.8.4 presents the u -velocity component for the case of a 3 mm micro-ramp located at $x = -108$ mm ($20.8\delta_{99}$). For this case, the measurements are performed in the symmetry plane of the ramp. The region close to the micro-ramp is blanked, because reflections were too strong to allow a proper measurement. Behind the ramp, a wake can be distinguished which lifts away from the surface and weakens when moving downstream. Around $x = -20$ mm, the wake interacts with the shock system, and a low-velocity pocket is formed. Another important feature revealed in Fig.8.4 is the low-speed bubble formed at the wall, which is caused by the strong adverse pressure gradient imposed on the incoming boundary layer by the reflected shock wave. On average there is no separation taking place for this particular configuration, however, instantaneously there can still be separated regions (see Fig.8.7 for instantaneous snapshots).

Fig.8.5 compares the flow topology for a case with ($h = 4$ mm & $d = 17.3\delta_{99}$) and without a micro-ramp. The average velocity fields (u -component) are compared in Figs.8.5(a) and (b) and the turbulence intensities are compared in Figs.8.5(c) and (d). The solid black line in Figs.8.5(a) and (c) represents the dividing streamline, which discriminates the separation bubble from the outer flow, while the dashed black line represents the sonic line. Note that on average no separation takes place for the case with a micro-ramp. Consequently, this results in a shear layer with smaller velocity gradients, reduced production of vorticity, and therefore lower turbulence levels. The turbulence intensity recorded in the center of the shear layer is approximately 15% smaller for the case with a micro-ramp. Lower turbulence levels are, however, also recorded downstream of the interaction, within the recovering boundary layer. The highest values for the turbulence intensity are recorded in the region enclosed by the dividing streamline and the sonic

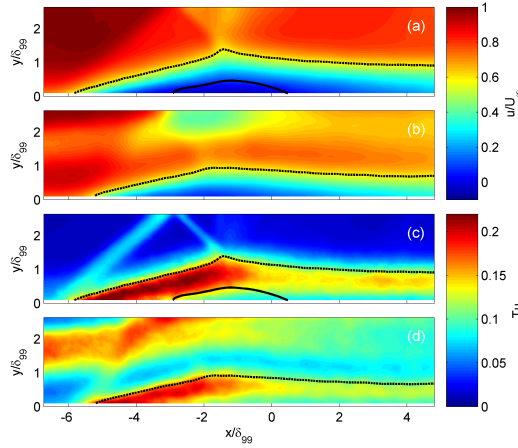


Figure 8.5: The interaction region for a case with ($h = 4$ mm and $d = 17.3\delta_{99}$) and without micro-ramp. (a) U/U_∞ without and (b) with a micro-ramp (c) Turbulence intensity $Tu = \sqrt{u'^2 + v'^2}/U_\infty$ without and (d) with a micro-ramp.

line, as was also observed by Souverein (2010).

Since the flow field that is generated by the micro-ramp is highly three-dimensional, it is insufficient to only consider the velocity field in the symmetry plane. PIV measurements were performed at three spanwise planes: the centerline, 25% span and 50% span. For these measurements, the micro-ramp was moved with respect to the centerline of the tunnel and the lasersheet was kept aligned with the centerline of the tunnel. From Fig.8.6 it is clear that as the measurement plane is shifted away from the center, the separated region increases. At $z/\delta_{99} = 2.3$ (50% span), the mean flow field and size of the separated region are similar to that of a flow without a micro-ramp (exact values are presented in Fig.8.9(a)). The micro-ramp therefore does not remove separation completely, but instead creates a spanwise modulation in the bubble size. A similar observation was also made by Babinsky et al. (2009), by means of oil-flow visualizations they showed that the effect of the micro-ramp does not reach far beyond its span and that attached flow is only observed within the centerline region.

The unsteady behavior of the separation bubble is illustrated in Fig.8.7, showing three snapshots of the interaction region. For this measurement, a 4 mm micro-ramp was located at $d/\delta_{99} = 17.3$. The three snapshots represent the typical variability of the extent of flow separation that occurs. In Fig.8.7(a) the flow is attached down to $y/\delta_{99} = 0.07$. Fig.8.7(b) shows a small separation bubble of approximately 6 mm^2 and Fig.8.7(c) indicates the presence of a large bubble of approximately 44 mm^2 . The size of the separation bubble is determined as the region of the flow that shows flow reversal and therefore falls within the zero-velocity iso-line. Separation and flow reversal are strictly speaking not the same, because separation encompasses all the flow within the dividing streamline and flow reversal only the area within the zero-velocity iso-line. For individual snapshots it can, however, be difficult to accurately construct the dividing streamline, espe-

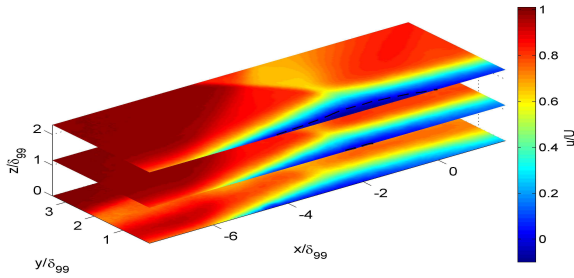


Figure 8.6: Velocity distribution in the interaction region for a 4 mm micro-ramp located at $d = 17.3\delta_{99}$. The three planes correspond to a cut through the centerline ($z = 0$), at 25% span ($z = 1.15\delta_{99}$) and 50% span ($z = 2.3\delta_{99}$). The dashed line presents the zero-velocity iso-line.

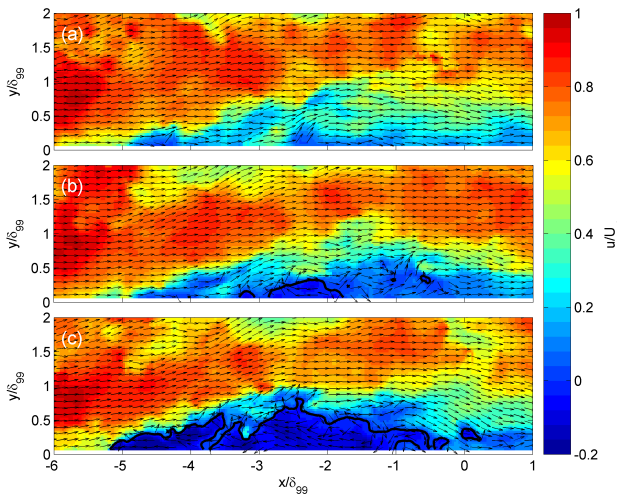


Figure 8.7: Three uncorrelated PIV snapshots of the low-speed bubble for a 4 mm micro-ramp located at $d/\delta_{99} = 17.3$ ($z/\delta_{99} = 0$). The solid black line presents the zero-velocity iso-line. (a) No separation (b) Small separation bubble (c) Large separation bubble

cially for very small separation bubbles. Flow reversal on the other hand forms a less sensitive criterion and is therefore used throughout this paper for calculating the (to be defined) separation probability and average separated area.

From the individual snapshots, the local separation probability P_{sep} can be obtained, which is defined as the probability that a certain point (x, y) shows reversed flow. For example, when $P_{sep}(x, y)$ equals 50%, then half of the time reversed flow occurs at (x, y) . Fig.8.8 compares the separation probability with (a) and without a micro-ramp (b). Without a micro-ramp, flow reversal is observed in a region spanning the entire field of view in the streamwise direction, which is approximately $9\delta_{99}$. By placing a 4 mm micro-ramp

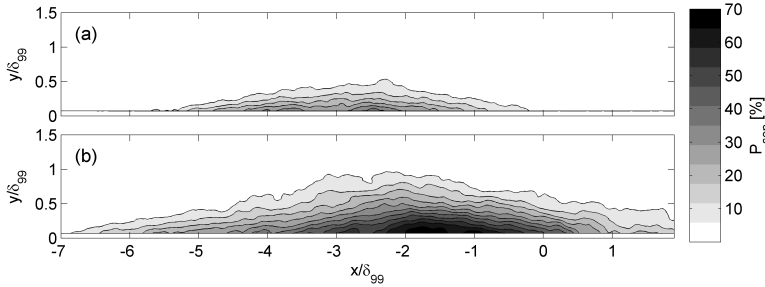


Figure 8.8: The separation probability P_{sep} with a micro-ramp ($h = 4 \text{ mm}$, $d = 17.3\delta_{99}$) upstream of the interaction (a) and without a micro-ramp (b).

$17.3\delta_{99}$ upstream of the interaction, this is reduced to $\sim 5.5\delta_{99}$ within the centerline region of the ramp. The probability of encountering reversed flow is also reduced. Without a micro-ramp, there are regions close to the wall that show flow reversal 75% of the time. With a micro-ramp, this peak value has been reduced to 41%. By integrating the separation probability over the entire domain, an average separated area A_{sep} can be calculated. Without a micro-ramp, A_{sep} equals 37.4 mm^2 while with a micro-ramp ($h = 4 \text{ mm}$ and $d = 17.3\delta_{99}$) it decreases to 8.1 mm^2 , which is a reduction of 78%.

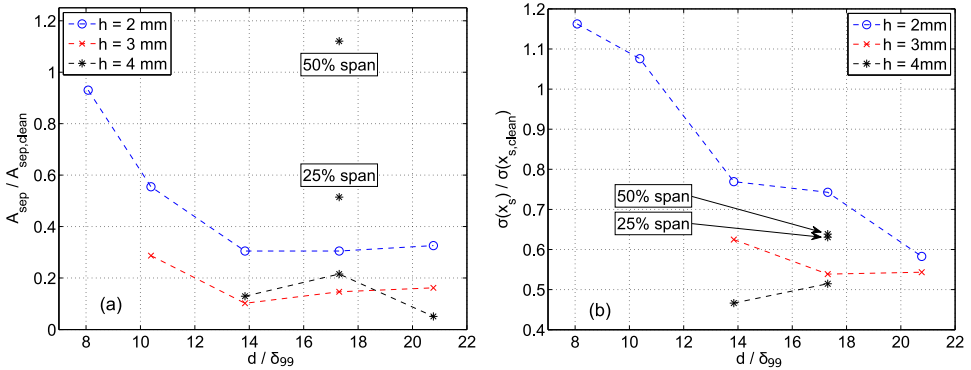


Figure 8.9: Results of the parametric study along the micro-ramp's centerline and at two off-centerline locations, in terms of the average separated area (a) and the reflected shock unsteadiness (b).

Micro-ramp height and location have a pronounced effect on the unsteadiness of the interaction and the amount of reversed flow. A parametric study was therefore carried out, in which both parameters were investigated (See Table 8.2). The results of this study are summarized in Figs.8.9(a) and (b), which show the average separated area and the shock unsteadiness in the centerline region of the ramp, respectively. In Fig.8.9(a) A_{sep} is normalized with $A_{sep, clean} = 37.4 \text{ mm}^2$, which is the average separated area present for a clean configuration. For all cases measured in the centerline plane of the micro-ramp, an improvement with respect to the clean configuration is observed.

For the 2 mm micro-ramp, the average separated area is relatively constant for $d/\delta_{99} >$

13.8 and equals approximately $0.31A_{sep, clean}$. A distinct increase in the average separated area is however noticed when the micro-ramp is placed any closer to the interaction. When it is placed at $x = 8.1\delta_{99}$ an average separated area of $0.93A_{sep, clean}$ is recorded. The larger 3 and 4 mm micro-ramp deliver a stronger control effect and typical values of $0.13A_{sep, clean}$ are recorded for $d/\delta_{99} > 13.8$. Off-centerline measurements are also shown in Fig.8.9(a) for the case of a 4 mm micro-ramp placed at $d/\delta_{99} = 17.3$. This again confirms that the effectiveness of the micro-ramp is reduced when moving away from the centerline, as was also observed in Fig.8.6. At 50% span, the average separated area is even increased by 12% compared to the clean configuration. Again we notice that the micro-ramp is not able to completely remove the separation bubble, but instead is spanwise modulated by the presence of the ramp.

The ultimate consequence of the loss of control authority when moving the micro-ramp closer to the interaction, as indicated by the rising trend in Fig.8.9(a), was evidenced by an experiment where a 4 mm micro-ramp was placed at $d/\delta_{99} = 10.4$. The corresponding datapoint is not presented in Fig.8.9(a). The separation bubble for this particular case was too large to fit completely within the field of view and therefore no accurate estimate could be given for A_{sep} . This large separation bubble, however, does make it an interesting configuration to study. The average velocity field is presented in Fig.8.10 and the zero-velocity contour (solid black line) is compared to the zero-velocity contour for a clean configuration (dashed black line). Clearly, the reversed flow region is multiple times larger with a micro-ramp than without a micro-ramp. From the oil-flow measurements of Babinsky et al. (2009), we know that there is a small region of reversed flow directly behind the micro-ramp. For this particular case, this region has linked up with the shock-induced separation bubble, resulting in a completely separated interaction.

So, micro-ramp location clearly is an important parameter, which determines to a large extent the effectiveness of the micro-ramp. For all micro-ramp heights (2, 3 and 4 mm) it is noticed that the best performance is achieved for $d/\delta_{99} > 13.8$. This observation will be further substantiated in section 8.2.3, which discusses the effects of a micro-ramp on the incoming boundary layer.

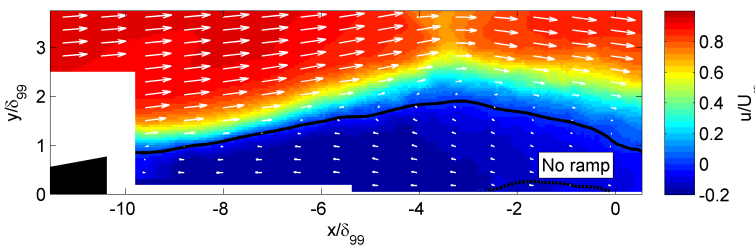


Figure 8.10: Mean velocity field for a 4 mm micro-ramp placed at $d = 10.4\delta_{99}$. Solid black line: zero-velocity iso-line. Dashed black line: zero-velocity iso-line for the clean configuration.

Since the size of the separation bubble is correlated with the location of the reflected shock wave (Dussauge et al. (2006); Van Oudheusden et al. (2011)), it is expected that by reducing the size/unsteadiness of the separation bubble, the unsteadiness of the reflected shock wave is also reduced. In order to assess the unsteadiness of the reflected

shock wave in the current experiments, its location is obtained from the measurement data by finding the maximum of dV/dx along the horizontal line $y = 3.5\delta_{99}$. The same procedure is repeated for the five rows of vectors above and below this line. After removing obvious outliers, the shock locations are used in a least squares fitting procedure. The resulting linear fit is used to calculate the shock location at $y = 3.5\delta_{99}$. This process is repeated for all the snapshots, and the shock unsteadiness is then quantified by the standard deviation σ of the list of shock locations x_s .

Fig.8.9(b) shows the reflected shock wave unsteadiness $\sigma(x_s)$ normalized by $\sigma(x_{s, clean}) = 1.87$ mm for the clean configuration. In some cases ($h = 4$ mm, $d/\delta_{99} = 10.4$ & 20.8 and $h = 3$ mm, $d/\delta_{99} = 10.4$) the wake coming from the micro-ramp and/or vortices being shed from the separation bubble obscured the velocity gradient imposed by the shock wave. It was therefore not possible to accurately resolve the instantaneous location of the shock wave and no reliable value of the shock unsteadiness could be obtained.

The data points for a 2 mm micro-ramp show that shock unsteadiness is reduced when the ramp is moved away from the interaction. Furthermore, the larger micro-ramps appear to be more effective in reducing the unsteady behavior of the reflected shock wave. With a 4 mm ramp placed at $d/\delta_{99} = 13.8$ or $d/\delta_{99} = 17.3$, the shock unsteadiness is approximately halved. The shock unsteadiness is not only reduced in the symmetry plane of the ramp, but also at 25% and 50% span reductions of, respectively, 37% and 36% are obtained. It is especially interesting to see that at 50% span, the micro-ramp still reduces the shock unsteadiness, whereas the average separated area at this location has been found to increase by 12% compared to a case without micro-ramp. It appears that the spanwise modulation of the separation bubble has a beneficial effect on the reflected shock unsteadiness.

8.2.3. INTERACTION CONTROL MECHANISM

In the previous section it has been observed that there is an optimal micro-ramp configuration to reduce the average separated area. So, in order to gain insight into the working principles of the micro-ramp, the velocity profiles downstream of the ramp are analyzed in more detail. To this end, the development of the boundary layer profile behind a 3 mm micro-ramp is presented in Fig.8.11. Profiles are shown at four locations behind the ramp, with x_{MR} defined as the distance between the measurement location and the trailing edge of the ramp. As a reference, the undisturbed boundary layer profile is presented as well. As expected, the wake region becomes less intense when traveling downstream and moves away from the surface. Furthermore, notice that momentum is added to the near-wall region of the boundary layer. Since it is anticipated that the effectiveness of the micro ramp is primarily related to the near-wall region, the wake region and the near-wall region are analyzed separately. First, the wake region is discussed and in particular the scaling of wake location and intensity. Second, the momentum increase in the near-wall region is treated. Finally, conditional averaging is applied to show the effects of both regions on the separation bubble.

Fig.8.12(a) shows the wake height y_{wake} (location of minimum velocity) as a function of the distance behind the micro-ramp x_{MR} . The wake height scales with micro-ramp height, and the results from the 2, 3 and 4 mm micro-ramp are shown to collapse on one curve for the given Mach and Reynolds number. The same observation was made by

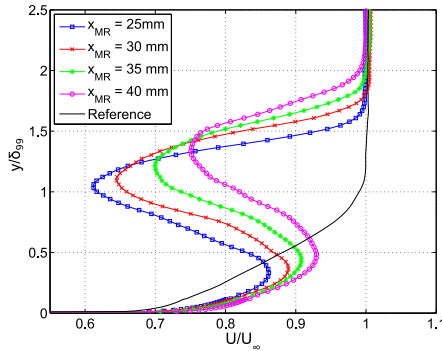


Figure 8.11: Velocity profiles downstream of a 3 mm micro-ramp.

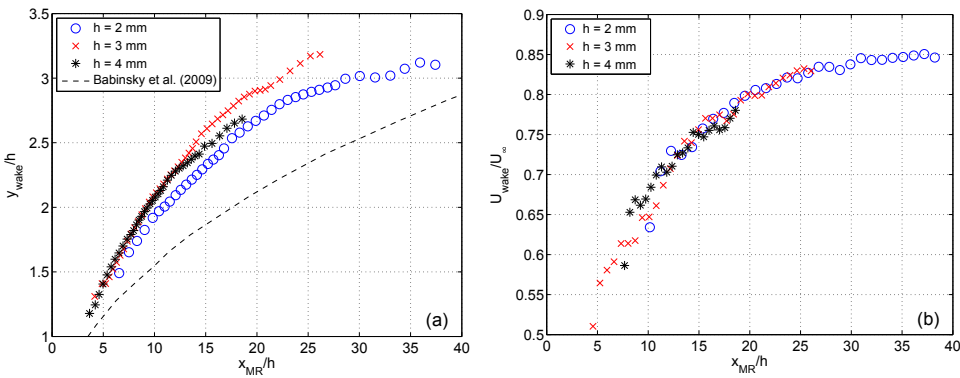


Figure 8.12: Behavior of the micro-ramp's wake, in terms of wake height (a) and velocity (b).

Ashill et al. (2005) in incompressible flows and by Babinsky et al. (2009) for supersonic free stream conditions. As a reference, the fit from Babinsky is also shown, which shows the same trend, but with an offset of approximately $1h$ for $x/h \geq 15$. The micro-ramp heights investigated in this study ($0.38 - 0.77\delta_{99}$) fall within the range of heights investigated by Babinsky ($0.33 - 1\delta_{99}$). So, this cannot be the cause for the offset measured in Fig.8.12(a). The offset could, however, be due to the different freestream conditions. Babinsky's experiments were carried out at a higher Mach number of 2.5 and a higher Re_{θ_i} of 28.8×10^3 . A further discussion of the Mach number effect on the micro-ramp's wake properties is provided in chapter 9.

The wake velocity U_{wake} is defined as the minimum velocity recorded inside the micro-ramp's wake at a particular downstream location x_{MR} . Fig.8.12(b) shows that the wake velocities for the 2, 3 and 4 mm micro-ramp all collapse on one curve, when the streamwise distance is normalized with the micro-ramp height h .

In Fig.8.11 it was noticed that momentum is added to the near-wall region of the flow. To track the development of the added momentum flux downstream of the micro-ramp, the following metric is introduced:

$$E(x) = \int_0^Y \frac{U^2 - U_{clean}^2}{U_\infty^2} dy \quad (8.1)$$

In which U_{clean} is the velocity field for the clean configuration without micro-ramp. The integration is performed from the wall up to a value of $Y = 0.43\delta_{99}$. A value of $0.43\delta_{99}$ is used, because it was found that the separation bubble is mostly sensitive to the momentum flux contained in the lower 43% of the boundary layer. The exact value was obtained by computing the correlation coefficient R between the bubble size and the added momentum flux E (data from set G is used, see Table 8.3), which is plotted in Fig.8.13. A clear maximum can be distinguished for a value of around $Y = 0.43\delta_{99}$. The negative value for the correlation coefficient implies that an increase in the added momentum flux is correlated with a reduction in the bubble size. The relatively modest correlation ($R = -0.18$) is a result of the inherent time delay of the shock interaction system, which was reported in more detail by Van Oudheusden et al. (2011). They used a high-speed PIV system to perform a time correlation between the bubble size and the incoming boundary layer momentum. For a zero time separation $\Delta t = 0 \mu s$ (boundary layer momentum and bubble size are determined from the same snapshot), a correlation coefficient of -0.19 was found, which is close to the value of -0.18 found in this study. However, for a time delay of 200 μs , the correlation coefficient reached a maximum value of -0.47. This result clearly shows that there is a time delay present within the system. Although the value of $Y = 0.43\delta_{99}$ seems rather specific, it was found that the development of E is relatively independent of the upper integration boundary that is used.

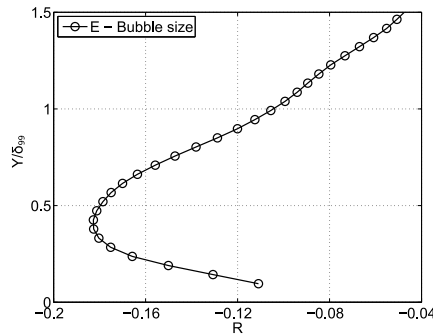


Figure 8.13: Correlation coefficient R between the bubble size and added momentum flux E , as a function of the upper integration bound Y of Eq.8.1.

Fig.8.14(a) shows the development of the normalized added momentum flux E/h for a 2, 3 and 4 mm micro-ramp placed at $d = 17.3\delta_{99}$ along its centerline. The bottom axis shows the distance from the micro-ramp x_{MR} and the top axis indicates the distance x to the incident shock. Clearly all three datasets collapse to one curve, which implies that the added momentum flux scales linearly with micro-ramp height. A possible explanation for this behavior can be found in the work of Ashill et al. (2005). Here, a range of vortex generators (VGs) was investigated and it was noticed that vortex circulation scales linearly with VG height. Additionally it was found that this is only valid for non-

dimensional VG heights of $h_e^+ = u_\tau h_e / \nu > 1400$, in which h_e is the effective height of the VG, which is the same as its physical height for forward wedges like the micro-ramp. A h_e^+ of 1400 corresponds to a micro-ramp height of 0.84 mm for the present case. So, a linear increase in the vortex circulation may be expected when moving from a 2 to 3 and 4 mm micro-ramp. A vortex that is twice as strong should also be able to transport twice the amount of momentum flux to the wall, which would explain why scaling E with h causes all the curves to collapse in Fig.8.14(a).

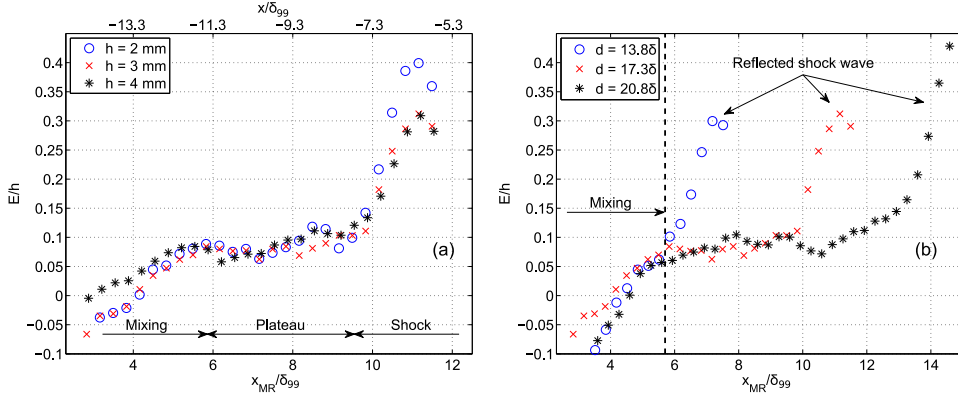


Figure 8.14: Development of the normalized added momentum flux E/h downstream of the micro-ramp along its centerline. In (a) the micro-ramp location is fixed to $d/\delta_{99} = 17.3$ and in (b) micro-ramp height is fixed to 3 mm.

When looking more closely at Fig.8.14(a), three regions can be distinguished: a mixing region extending up to $x_{MR}/\delta_{99} = 5.7$, a plateau having a length of $3.8\delta_{99}$, and a shock region which becomes apparent at $x_{MR}/\delta_{99} = 9.5$ (which corresponds to a distance of approximately $7.8\delta_{99}$ upstream from the inviscid shock location). During the initial mixing phase, high-momentum fluid is transported towards the surface by streamwise vortices and at the same time the wake moves away from the surface. After this mixing region, E/h becomes approximately constant and little momentum flux is added to the near-wall region. This plateau extends over $3.8\delta_{99}$ until the point where the reflected shock wave is encountered. The effect of the added momentum flux is amplified when crossing the reflected shock wave. Remember that the quantity E represents the difference between the momentum flux in a controlled and uncontrolled situation. The extra momentum flux present in the near-wall region greatly helps in overcoming the adverse pressure gradient posed by the reflected shock wave, therefore resulting in the steep rise of E/h as recorded around $x_{MR}/\delta_{99} = 9.5$.

So, the micro-ramp requires a fixed length of $5.7\delta_{99}$ (for the operating conditions considered in this study) to allow maximum momentum to be injected in the near-wall region. This implies that if the micro-ramps are placed closer than $5.7\delta_{99} + 7.8\delta_{99} = 13.5\delta_{99}$ to the incident shock (mixing distance plus region of influence of the shock wave), reduced micro-ramp effectiveness may be expected. This is exactly what was noticed in Fig.8.9(a), where the average separated area remains relatively constant for $d > 13.8\delta_{99}$ and increases for $d < 13.8\delta_{99}$.

As has already been mentioned, the mixing distance of $5.7\delta_{99}$ is relatively independent of the upper integration bound Y used in Eq.8.1: for values of Y in between 0.2 and 0.7, the mixing distance varies between 5.5 and $5.9\delta_{99}$. Furthermore, it appears that the mixing distance is independent of the location of the micro-ramp. Fig.8.14(b) shows the results for a 3 mm micro-ramp situated 13.8 , 17.3 and $20.8\delta_{99}$ upstream of the incident shock. The mixing distance remains constant and only the plateau length varies. Notice that for the $13.8\delta_{99}$ case, no plateau can be observed and the boundary layer encounters the reflected shock wave directly after the mixing region.

The boundary layer has now been investigated in terms of the wake intensity / location and the amount of momentum flux that is transported to the near-wall region. In order to relate these properties to the behavior of the interaction region, conditional averaging is applied (see also Van Oudheusden et al. (2011)). First the images are sorted based upon a certain metric, for instance the boundary layer momentum flux. Then the images are grouped into two sets, one for which this metric has a large value and another for which the value is small. By subtracting the conditionally averaged 'small' dataset from the 'large' dataset one can visualize the impact that the metric has on the flow field. In this analysis, images are grouped within the 'large' / 'small' set when their value is 1-3 standard deviations above / below the mean.

Fig.8.15 shows the differential velocity fields Δu for four different conditions. Fig.8.15(a) is conditioned on the boundary layer momentum flux in the near-wall region ($0 < y < 0.43\delta_{99}$). The higher speeds in the interaction region imply that one is likely to have a weaker separation bubble when the incoming boundary layer is rich in momentum. Furthermore, higher speeds are also recorded in the region of the reflected shock wave. The reflected shock wave causes a deceleration of the flow, so higher values in this region imply a downstream displacement of the shock wave. So, when the boundary layer is rich in momentum, the reflected shock is likely to be displaced downstream, as has been observed before Humble et al. (2009); Ganapathisubramani et al. (2007).

Fig.8.15(b) is conditioned on the size of the low-speed ($U < 0.2U_{\infty}$) bubble. The effect of the bubble size is not only observed in the interaction region, but is also clearly visible $5\delta_{99}$ downstream of the incident shock. There is, however, no direct relation visible between bubble size and features of the incoming boundary layer. A similar observation was also made by Van Oudheusden et al. (2011), who employed the same technique on a shock wave-boundary layer interaction without micro-ramp. In that study it was hypothesized that this might be due to an attenuated response of the bubble to the inflow conditions.

In Figs.8.15(c) and (d), the effects of the instantaneous wake location and speed are investigated. When the wake enters the interaction relatively far away from the wall, one is likely to encounter a weaker separation bubble. The wake speed has the exact opposite effect, higher wake speeds appear to be correlated with a stronger separation bubble.

8.3. CONCLUSIONS

A planar PIV study has been carried out in order to quantify the effects of micro-ramp height and location on the separation probability of the flow and the reflected shock wave unsteadiness. Conditional averaging showed that the separation bubble is sensitive to the momentum flux contained in the near-wall region ($<0.43\delta_{99}$) of the incoming

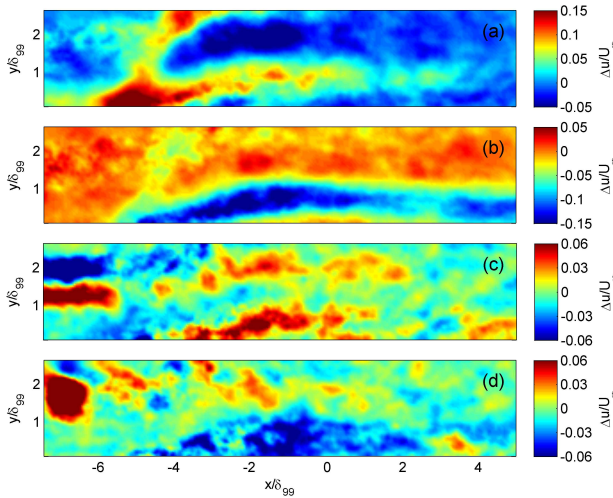


Figure 8.15: Results from conditional averaging, differential velocity fields Δu between large and small criterion events. Conditioned on (a) boundary layer momentum flux (b) size of the low-speed bubble (c) wake location (d) wake velocity

boundary layer. The momentum flux added to this region scales linearly with micro-ramp height and keeps increasing up to $5.7\delta_{99}$ downstream of the ramp. After $5.7\delta_{99}$, a plateau is reached and virtually no extra momentum is added or removed. The mixing distance of $5.7\delta_{99}$ is found to be independent of micro-ramp height and location. Therefore, if the distance between the micro-ramp's trailing edge and the start of the interaction region is less than $5.7\delta_{99}$, full boundary layer mixing is not attained and reduced performance is expected.

The measurements that were carried out on the interaction region indeed confirm this result. The average separated area is relatively constant for $d > 13.8\delta_{99}$ (micro-ramp and reflected shock wave were separated by $6.1\delta_{99}$) and increased when the micro-ramp was placed closer to the interaction. For the special case of a 4 mm micro-ramp placed $10.4\delta_{99}$ upstream of the incident shock wave, a very large separation bubble appeared, multiple times larger than the bubble recorded without a micro-ramp. So, if micro-ramps are to be used for shock wave-boundary layer interaction control (e.g in a supersonic jet inlet), it is important to maintain a certain minimum distance between the micro-ramp and the interaction for all flow conditions. The dependence of this minimum distance on the Mach and Reynolds number is investigated in chapter 9.

The 3 and 4 mm micro-ramps were more effective in reducing the average shock-induced separated area than the 2 mm micro-ramp. Typical reductions in the average separated area by 87% were recorded in the centerline of the micro-ramp. Larger micro-ramps were also more effective in reducing the reflected shock wave unsteadiness. A 4 mm micro-ramp ($d = 13.8\delta_{99}$) was able to reduce the shock unsteadiness by 53%. Although the larger micro-ramps perform better than their smaller counterparts, this most likely also comes at the price of a higher drag contribution (not investigated in this

study).

Micro-ramps are less effective at off-center locations. On the outer edge of a micro-ramp ($h = 4 \text{ mm}$, $d = 17.3\delta_{99}$), the average separated area was measured to be 12% larger than for a clean configuration. A micro-ramp therefore does not remove separation completely, but instead creates a spanwise modulation in the bubble. However, for the same case, the shock unsteadiness was reduced by 36% compared to a clean configuration.

9

MACH AND REYNOLDS NUMBER EFFECTS

The previous chapter evaluated the performance of micro-ramp vortex generators for one particular operating condition ($M_\infty = 2.0$, $Re_\infty = 42 \times 10^6 \text{ m}^{-1}$). However, for micro-ramps to be of industrial relevance, it is important to have a clear understanding of how its performance is improved / deteriorated when changing the operating Mach or Reynolds number. A large parametric study was therefore conducted into the effects of Mach ($M_\infty = 1.5 - 3.0$) and Reynolds number ($Re_\infty = 28 - 63 \times 10^6 \text{ m}^{-1}$), the results of which are presented in the current chapter. The flow field in the symmetry plane of the micro-ramp was studied by means of planar PIV measurements, and the three-dimensional features of the flow field were captured by means of a series of oil-flow and schlieren visualizations.

9.1. EXPERIMENTAL SETUP

9.1.1. TEST MATRIX

All measurements were performed in the TST-27 transonic-supersonic blow-down tunnel of the TU Delft. The micro-ramp was mounted on the top wall of the test section and was aligned with the centreline of the tunnel. The geometry of the micro-ramps used in this study is based on the optimization study performed by Anderson et al. (2006) for minimizing the incompressible shape factor H_i downstream of the micro-ramp. The dimensions of the micro-ramp are presented in Fig.9.1 and are normalized with the micro-ramp height h . The flow field downstream of the micro-ramps was measured by means of particle image velocimetry and all measurements were performed along the symmetry plane of the micro-ramp. Additionally, schlieren and oil-flow visualizations were performed to study the effects of the Mach number on the (spanwise) trajectory of the primary and secondary vortices.

Parts of this chapter have been presented at the 45th AIAA Fluid Dynamics Conference (Giepmans et al. (2015d)).

As a baseline configuration a $h = 8$ mm micro-ramp was used, which was tested at a Mach number $M_\infty = 2$ and a unit Reynolds number of $Re_\infty = 39 \times 10^6 \text{ m}^{-1}$. The effects of micro-ramp height, Mach number and Reynolds number on the flow field were investigated systematically by changing one parameter at a time while keeping the other parameters fixed (see Table 9.1). The micro-ramp height was varied from 6 to 10 mm, the Mach number from 1.5 to 2.5 and the unit Reynolds number from 28 to $63 \times 10^6 \text{ m}^{-1}$. To clearly identify the mixing properties of the micro-ramp, reference measurements were also performed on the tunnel wall boundary layer without a micro-ramp (see section 9.3).

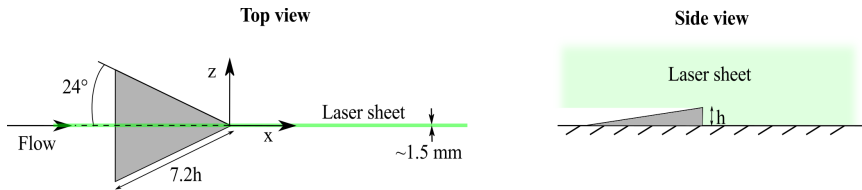


Figure 9.1: Micro-ramp geometry

Table 9.1: Test matrix for the measurements with micro-ramp

Set	M_∞	$Re_\infty [\text{m}^{-1}]$	$Re_{\delta_{99}}$	$h [\text{mm}]$	h/δ_{99}	Measurements technique
1	2.0	39.5×10^6	6.8×10^5	6	0.35	PIV
	2.0	39.5×10^6	6.8×10^5	8	0.46	PIV, schlieren, oil-flow
	2.0	39.5×10^6	6.8×10^5	10	0.58	PIV
2	1.5	39.1×10^6	6.4×10^5	8	0.49	PIV, schlieren, oil-flow
	2.0	39.5×10^6	6.8×10^5	8	0.46	PIV, schlieren, oil-flow
	2.5	39.4×10^6	7.3×10^5	8	0.44	PIV, schlieren, oil-flow
3	2.0	27.7×10^6	4.9×10^5	8	0.45	PIV
	2.0	39.5×10^6	6.8×10^5	8	0.46	PIV, schlieren, oil-flow
	2.0	51.3×10^6	8.8×10^5	8	0.47	PIV
	2.0	63.4×10^6	10.5×10^5	8	0.48	PIV

9.1.2. PIV SETUP

Four 2 Mega-pixel Lavisision Imager LX cameras were used to capture the flow field downstream of the micro-ramp. Two cameras were equipped with a 35 mm Nikkor objective and the other two cameras with a 50 mm Nikkor objective. All four cameras were operated at the same magnification of 0.13 and a $f_\#$ of 8. This resulted in a spatial resolution of 30 pixels/mm and a field of view per camera of $54 \times 37 \text{ mm}^2$ in streamwise and wall-normal direction, respectively. An overlap of approximately 9 mm was provided between the fields of view of the individual cameras to allow for a proper recombination of the velocity fields. The total field of view of the four cameras combined therefore equalled $190 \times 37 \text{ mm}^2$. The laser light reflection from the micro-ramp makes it impossible to measure very close to the trailing edge of the ramp. The first field of view was therefore po-

sitioned approximately 18 mm downstream of the trailing edge of the micro-ramp. A sketch of the four fields of view and their position with respect to the micro-ramp is provided in Fig.9.2. Notice from the figure that the fields of view are overlapping the wall by approximately 4 mm, which allows for identifying the wall location from the PIV images afterwards.

Illumination was provided by a double-pulse Nd:YAG Spectra Physics Quanta Ray PIV-400 laser. A series of lenses was used to shape the laser beam into a sheet of approximately 1.5 mm thick (see also Fig.9.1) The pulse separation time between pulse A and B was set to 1.4 μs for the Mach 1.5 and 2.0 test cases and was lowered to 1.3 μs for the Mach 2.5 case in order to have a free stream particle displacement of approximately 20 pixels for all conditions. The flow was seeded with DEHS tracer particles having a nominal diameter of $\sim 1 \mu\text{m}$. The response time of the particles was evaluated by means of an oblique shock wave test (Ragni et al. (2010)) and equals $\tau_p = 1.9 \mu\text{s}$, which translates into a Stokes number of $U_\infty \tau_p / \delta_{99} = 0.06$. According to Samimy and Lele (1991) this results in particle slip velocities of $< 1\%$. All operating settings are summarized in Table 9.2.

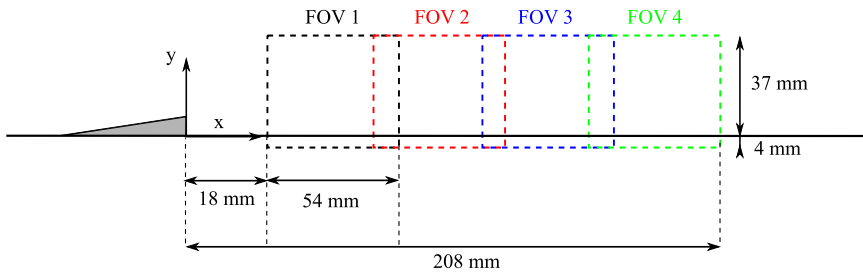


Figure 9.2: Fields of view (FOV) of the four cameras used for the PIV measurements

Table 9.2: PIV experimental settings

Parameter	Value
Measurement area	54 x 41 mm 1624 x 1236 pixels
Laser sheet thickness	1.5 mm
Digital imaging resolution	30 pixels/mm
Magnification	0.13
Object focal length	2x 35 mm and 2x 50 mm
F-number	8
Laser pulse separation time	1.4 μs ($M_\infty = 2.0$)
Freestream particle displacement	21 pixels ($M_\infty = 2.0$)

9.2. DATA REDUCTION

This section covers the PIV processing techniques used for converting the raw PIV images to velocity fields (section 9.2.1). Also a description is given of how PIV and schlieren data can be combined to give an estimate of the primary vortex strength (section 9.2.2).

Finally, a discussion is given on the uncertainties related to the PIV measurement technique and the subsequent processing steps (section 9.2.3).

9.2.1. PIV PROCESSING

The PIV images were processed with an in-house built iterative multi-grid window deformation PIV code Fluere, which is based upon the work of Scarano and Riethmuller (2000). Stretched interrogation windows of 128x64 pixels were used for processing the data (stretching applied in the streamwise direction) and Gaussian window weighting was applied to further reduce the correlation noise (Astarita (2007)). A window overlap of 75% was used in both the wall normal and streamwise direction, resulting in a vector pitch of 32 by 16 pixels, or equivalently 1.07 by 0.54 mm.

The velocity fields were post-processed with a normalized median filter to remove spurious vectors (Westerweel and Scarano (2005)) and vector relocation (Theunissen et al. (2008)) was performed on vectors for which the interrogation window is overlapping the wall mask.

9.2.2. VORTEX MODELLING

The vortex strength was not measured directly in this study, but can be derived from the Burgers vortex model (see also the work of Nolan and Babinsky (2012)):

$$u_{\theta} = \frac{\Gamma}{2\pi r} \left[1 - \exp\left(-1.26 \frac{r^2}{r_{vor}^2}\right) \right] \quad (9.1)$$

This model requires four inputs: the vortex strength (circulation Γ), the vortex core radius r_{vor} and the location of the vortex core in the y - z plane. As output it delivers the circumferential velocity u_{θ} around the centreline axis of the vortex. The flow field that is measured in the symmetry plane of the micro-ramp can be modelled as the result of four Burgers vortices: the two primary vortices and two mirror vortices located on the opposite side of the wall (see also Fig.9.3). The mirror vortices are necessary to ensure a zero v -velocity component at the wall.

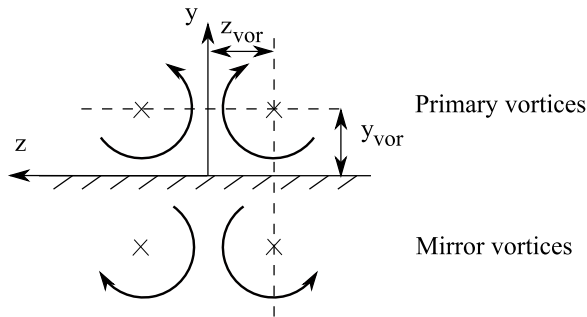


Figure 9.3: Inviscid vortex model, showing the primary vortices and the mirror vortices.

The location of the vortex in the x - z plane can be derived from schlieren visualizations (see discussion section 9.4.1). The vortex core height y_{vor} has not been measured

directly in this study, but can be approximated from the velocity field in the symmetry plane of the micro-ramp. In the works of Sun et al. (2012) and Nolan and Babinsky (2011), it has been shown that the location of maximum upwash y_{vmax} is virtually the same as the height of the vortex core y_{vor} above the wall. This leaves the circulation Γ and the vortex core radius r_{vor} as the two remaining unknowns. A fitting procedure can then be employed to estimate the circulation strength and vortex core radius from the upwash velocity profile in the symmetry plane of the micro-ramp.

This method has been validated by using the tomographic PIV data of Sun et al. (2012) The circulation has been calculated both directly from the full 3D velocity field as well as approximated by only using the data in the symmetry plane and by fitting a Burgers vortex model to the upwash velocity profile, by the procedure indicated above. Both approaches yield very similar values for the circulation (r.m.s. $\sim 4\%$) as can be seen in Fig.9.19. It should be noted here that for the study of Sun et al. (2012) no schlieren visualizations were available. The spanwise vortex trajectories were therefore derived directly from the tomographic PIV data. In section 9.4.1 it is discussed that the typical uncertainty on the schlieren-derived vortex trajectories equals $\sim 12\%$, which translates into an uncertainty of approximately 6% on the calculated circulation strengths.

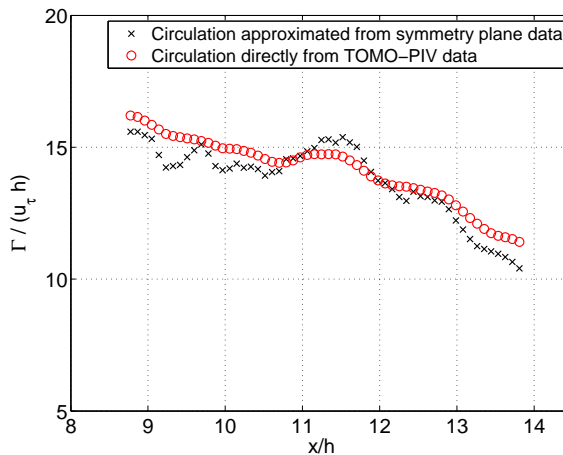


Figure 9.4: Vortex strength calculation from the TOMO-PIV data of Sun et al. (2012)

9.2.3. PIV UNCERTAINTY ANALYSIS

The PIV measurements are subject to uncertainties introduced by the finite ensemble size, limitations of the measurement technique and the subsequent processing steps.

Based on the ensemble size of 150 image pairs it is estimated that the statistical component of the uncertainty on the mean streamwise velocity field \bar{u} equals $\sim 1.0\%$ of U_∞ in the wake region of the micro-ramp (at $x/h = 10$), where the highest velocity fluctuations are recorded. The velocity fluctuations are smaller in the near-wall region of the boundary layer, consequently resulting in a lower uncertainty on \bar{u} of $\sim 0.4\%$ of U_∞ (at $x/h = 10$ and $y/h = 0.5$).

The laser sheet was aligned with the centreline of the micro-ramp and had a thickness of ~ 1.5 mm ($0.19h$) for all the experiments described in this study. The measured velocity field therefore presents a spanwise average over $0.19h$ in space and is, as such, not exactly equal to the velocity field in the centreline of the micro-ramp. To estimate the potential error introduced by the finite thickness of the laser sheet a comparison was made with the data of Sun et al. (2012), who performed TOMO-PIV measurements on the flow field downstream of a similar micro-ramp. From the 3D TOMO-PIV data it is possible to derive the velocity field at the centreline of the micro-ramp, which can be compared with the velocity field that is obtained when averaging the data over a $0.19h$ thick virtual laser sheet. The differences between the 'exact' velocity field at the centreline and the spanwise averaged velocity field turned out to be less than 0.1% of the freestream velocity. The finite laser sheet thickness is therefore not expected to have a significant impact on the velocity fields measured in this study.

Uncertainties are furthermore introduced by the finite size of the interrogation windows (Schrijer and Scarano (2008)). For processing the PIV images, interrogation windows with a size of 128×64 pixels ($0.53h \times 0.27h$) were used (see also section 9.2.1). This window size was selected as a trade-off between having a low noise level and obtaining a high spatial resolution. Fig.9.5 shows profiles of the average streamwise velocity component at three locations ($x/h = 8, 10$ and 12) for four different window sizes ($32 \times 16, 64 \times 32, 128 \times 64, 256 \times 128$). The velocity profiles for the 32×16 and 64×32 interrogation windows show a light amount of scatter, which is reduced when going to larger windows of 128×64 and 256×128 pixels. However, the large 256×128 windows have a too strong smoothing effect on the data and the wake velocities are clearly overestimated for this window size. It was therefore decided to use 128×64 windows, which deliver a clean result for the current ensemble size of 150 image pairs, without significantly modulating the wake and boundary layer profile.

Finally, it may be noted that even the very large 256×128 pixel interrogation windows ($1.07h \times 0.53h$) still yield relatively good results in the near-wall region of the flow. That is because the PIV code that we used features a vector-relocation algorithm (see appendix A), which automatically adjusts the size and location of very near-wall interrogation windows. The near-wall interrogation windows are effectively a factor of 2 smaller in the wall-normal direction than the windows used further away from the wall.

9

9.3. UNDISTURBED BOUNDARY LAYER MEASUREMENTS

PIV measurements were performed on the undisturbed tunnel wall boundary layer for all flow conditions considered in this study. Fig.9.6a shows the boundary layer profile for a range of freestream Mach numbers while Fig.9.6(b) presents the same profiles in terms of the inner variables $u^+ = u_{eq}/u_\tau$ and $y^+ = yu_\tau/\mu_w$. Here u_τ represents the friction velocity, μ_w the kinematic viscosity at the wall and u_{eq} the Van Driest effective velocity. The latter is obtained by applying the Van Driest II transformation in combination with the Crocco-Busemann relation (recovery factor $r = 0.89$) to the boundary layer profile. From Fig.9.6(b) it is clear that an excellent agreement between the boundary layer profile and the log-law is obtained for all three Mach numbers in the region of $y^+ \sim 2 \times 10^2$ to $y^+ \sim 3 \times 10^3$, where the log-law can be described by the following relation ($\kappa = 0.41, B = 5$):

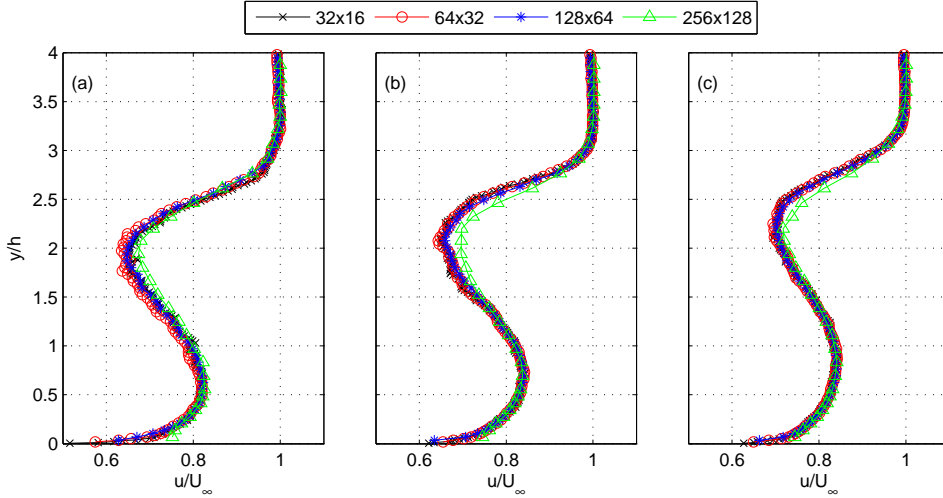


Figure 9.5: Velocity profiles obtained for different interrogation window sizes at three different locations: (a) $x/h = 8$ (b) $x/h = 10$ and (c) $x/h = 12$

$$\frac{u_{eq}}{u_\tau} = \frac{1}{\kappa} \ln(y^+) + B \quad (9.2)$$

The boundary layer thickness δ_{99} increases slightly with the freestream Mach number, from 16.3 mm to 18.4 mm, for $M_\infty = 1.5$ and $M_\infty = 2.5$, respectively. The skin friction coefficient C_f on the other hand decreases with increasing Mach number, from 1.72×10^{-3} to 1.40×10^{-3} , for $M_\infty = 1.5$ and $M_\infty = 2.5$, respectively. These trends are in agreement with results reported before by, amongst others, Schlichting and Gersten (2000) and Cousteix (1989). A summary of the boundary layer properties can be found in Table 9.3.

Fig.9.7 presents the undisturbed boundary layer profiles for the Reynolds number variation that was considered in this study, at a constant value of the Mach number. Again the boundary layer profiles are found to be in excellent agreement with the log-law and from Fig.9.7(b) it is clear that the size of the log-region (in terms of y^+) increases when going to higher freestream Reynolds numbers. In agreement with theory, both the boundary layer thickness and skin friction coefficient are found to decrease with increasing Reynolds number (see Table 9.3).

The fullness of the boundary layer profiles does not vary much with Mach and Reynolds number, and the incompressible shape factor H_i is found to range between 1.23-1.25 for all operating conditions tested.

9.4. RESULTS

The PIV measurements in this study were confined to the symmetry plane of the micro-ramp. The flow field downstream of a micro-ramp is, however, inherently three-dimensional. To gain a better understanding of the effects of the Mach number on the vor-

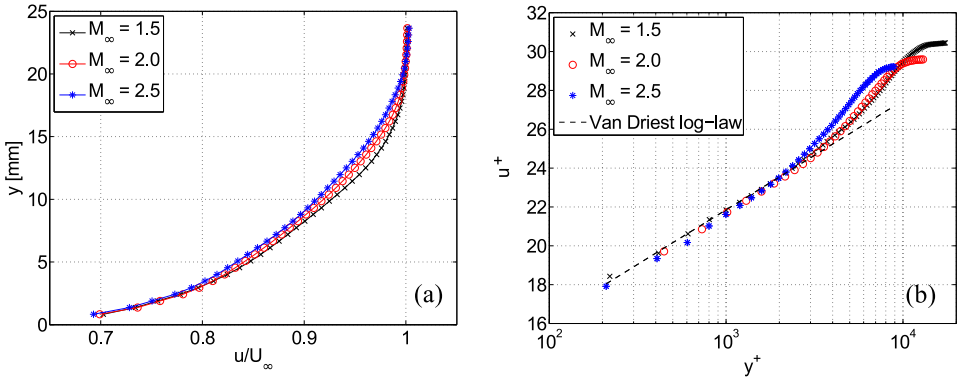


Figure 9.6: Undisturbed boundary layer profiles for a range of freestream Mach numbers for $Re_\infty \sim 39 \times 10^6 \text{ m}^{-1}$. (a) Linear representation (b) Inner-variable scaling

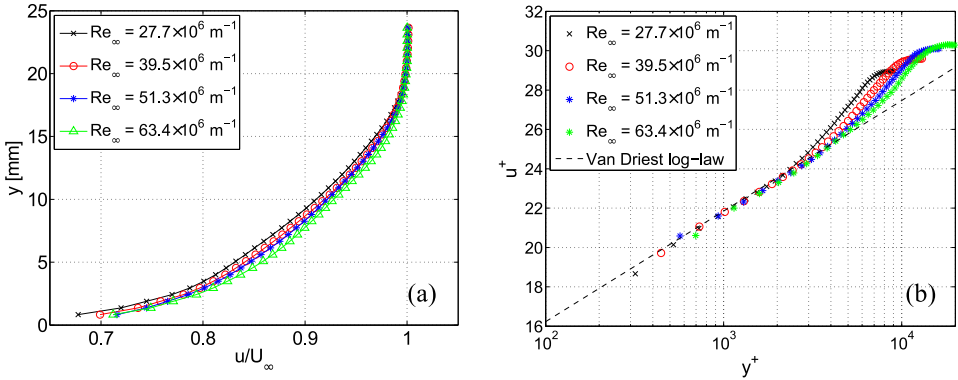


Figure 9.7: Undisturbed boundary layer profiles for a range of freestream Reynolds numbers for $M_\infty = 2.0$. (a) Linear representation (b) Inner-variable scaling

tex trajectories, the PIV measurements were complemented with top-view schlieren and surface oil-flow visualizations. The schlieren and oil-flow visualizations are described in section 9.4.1 and the PIV measurements in section 9.4.2. Finally, section 9.4.3 presents a comparison of the current results with the data reported by other researchers.

9.4.1. SCHLIEREN AND OIL-FLOW VISUALIZATIONS

For the schlieren measurements, the micro-ramp was mounted on the side-wall of the tunnel, just upstream of the test section window to allow a visualization of the micro-ramp wake through the test section window. Fig.9.8 presents a schlieren visualization for an $h = 8 \text{ mm}$ micro-ramp in a Mach 2.0 flow at a unit Reynolds number of $39 \times 10^6 \text{ m}^{-1}$. The schlieren knife was oriented horizontally (i.e. parallel to the wake axis) in order to visualize the density gradients in the spanwise direction. The largest density gradients are present at the shear layer between the wake and freestream which explains the presence of a dark / white band on the bottom / top of the image. A smaller density gradient

Table 9.3: Undisturbed boundary layer properties for all operating conditions considered in this study

Tunnel operating conditions							
M_∞		1.5	2.0	2.0	2.0	2.0	2.5
$Re_\infty \times 10^{-6}$	[1/m]	39.1	27.7	39.5	51.3	63.4	39.4
U_∞	[m/s]	409	493	493	493	494	550
$p_0 \times 10^{-5}$	[N/m ²]	2.48	2.06	2.94	3.82	4.70	3.72
T_0	[K]	278	278	278	278	278	278
Tunnel wall boundary layer properties							
δ_{99}	[mm]	16.3	17.7	17.3	17.1	16.5	18.4
δ_i^*	[mm]	2.02	2.24	2.10	2.05	1.92	2.23
θ_i	[mm]	1.61	1.80	1.70	1.66	1.56	1.80
H_i		1.25	1.25	1.24	1.23	1.23	1.24
u_τ	[m/s]	14.2	18.5	18.1	17.8	17.7	21.2
$C_f \times 10^3$		1.72	1.65	1.58	1.53	1.50	1.40
$Re_{\delta_{99}} \times 10^{-5}$		6.4	4.9	6.8	8.8	10.5	7.3

is also present between the two vortex cores. This again creates a dark and a light band in the image, which are most clearly visible for the first $10h$ downstream of the ramp. The vortex location is identified from the schlieren images as the transition point from the white to dark band. It should be highlighted here though that the wake flow consists of a highly 3D mixture of low and high-momentum regions. A schlieren visualization provides only a vertically averaged representation of these density gradients. An exact determination of the vortex trajectories is therefore not possible, but a reasonable approximation can still be inferred.

In this context it is useful to compare the schlieren visualizations of the current study with the tomographic PIV data from Sun et al. (2012), which was acquired under very similar conditions: $M_\infty = 2.0$ and $Re_\infty = 41 \times 10^6 \text{ m}^{-1}$. The velocity field of Fig.9.8 has been constructed by extracting the velocities at the height of the local wake location. Two streaks of low-momentum fluid can be very clearly identified in the velocity field. Also indicated in the figure are the vortex trajectories (Q-criterion) that were derived from the PIV data of Sun et al. (2012) The vortex trajectories that were derived from the schlieren visualizations are seen to be in reasonable agreement (the r.m.s. error in the spanwise position is $\sim 12\%$) with the trajectories measured in the PIV study of Sun et al. (2012). The same technique for determining the vortex trajectories has therefore also been applied to the schlieren visualizations that were acquired at the other Mach numbers (1.5, 2.5 and 3.0).

Fig.9.9 presents the vortex trajectories projected on the corresponding schlieren visualizations and Fig.9.10 presents the vortex trajectories for the different Mach numbers compared with the CFD data of Lee et al. (2009) (see Table 9.4 for the details of their simulations). The vortex trajectories look qualitatively very similar for the different Mach numbers. Downstream of the micro-ramp the vortices are first moving closer to each other, reach a certain minimum separation distance ($\sim 0.9h$) and then move apart again. For incompressible flows Ashill et al. (2001) showed that the first part of the trajectory can be described, with reasonable accuracy, by the combination of inviscid theory (Jones

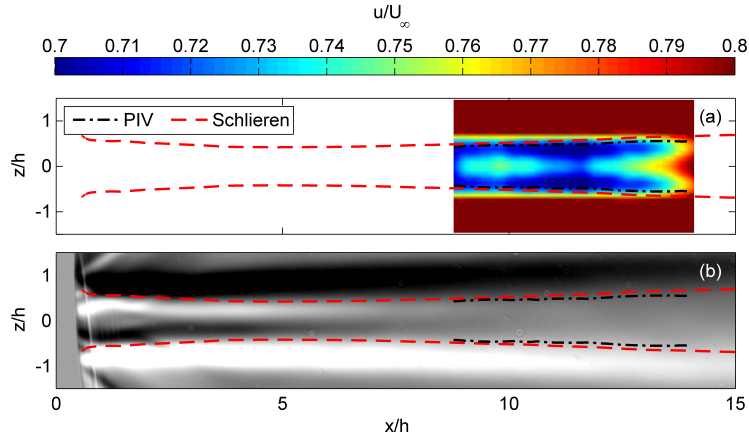


Figure 9.8: Comparison between the tomographic PIV data of Sun et al. (2012) (a) and a schlieren visualization of the vortex trajectories obtained during the current study (b).

(1955)) with an exponential vortex decay model (Wendt et al. (1991)). In modelling the vortices one has to take into account the effects of the wall (i.e. $v(y=0) = 0$) on the vortex trajectories. This is done by introducing a counter-rotating vortex pair of equal strength on the opposite side of the wall (see Fig.9.3), where the mirror vortices are responsible for pushing the primary vortices towards the centreline of the micro-ramp. This inviscid description, however, does not capture the fact that the vortices start to move apart after approximately five micro-ramp heights. That is because, inviscid theory does not model the dissipation that is developed between the two approaching vortices. As also highlighted in the work of Lee et al. (2009), it is dissipation which is responsible for increasing the vortex core radius and for moving the vortices away from the centreline.

The location where the vortices are closest to each other depends on the Mach number. The higher the Mach number, the further this location is moved downstream. For $M_\infty = 1.5$, the vortices reach their minimum separation distance $\sim 4.2h$ downstream of the micro-ramp, whereas for the $M_\infty = 3.0$ case this has become significantly larger: $\sim 6.8h$. Also for the lower Mach numbers ($M_\infty = 1.5$ and $M_\infty = 2.0$) it is observed that the vortices move apart faster than for the higher Mach numbers. For example, the center of the vortex core at $x/h = 20$ is located at $z \sim 0.72h$ for the $M_\infty = 1.5$ case and at $z \sim 0.57h$ for the $M_\infty = 3.0$ case. The same trend is also clearly visible in the numerical data of Lee et al. (2009).

For the same conditions, also oil-flow visualizations were carried out (see Fig.9.11). Downstream of the micro-ramp two white lines are recorded, which form the separation lines between the primary and secondary vortices introduced by the micro-ramp. The primary vortices are the result of the positive pressure difference between the micro-ramp's top surface and its slanted side-walls. Secondary vortices are introduced by the strong primary vortices at the side-wall / tunnel wall junction and at the side-wall / top surface junction (see also the work of Lu et al. (2011)). The primary vortices push the oil towards the centreline of the ramp, whereas the smaller secondary vortices (tunnel-wall

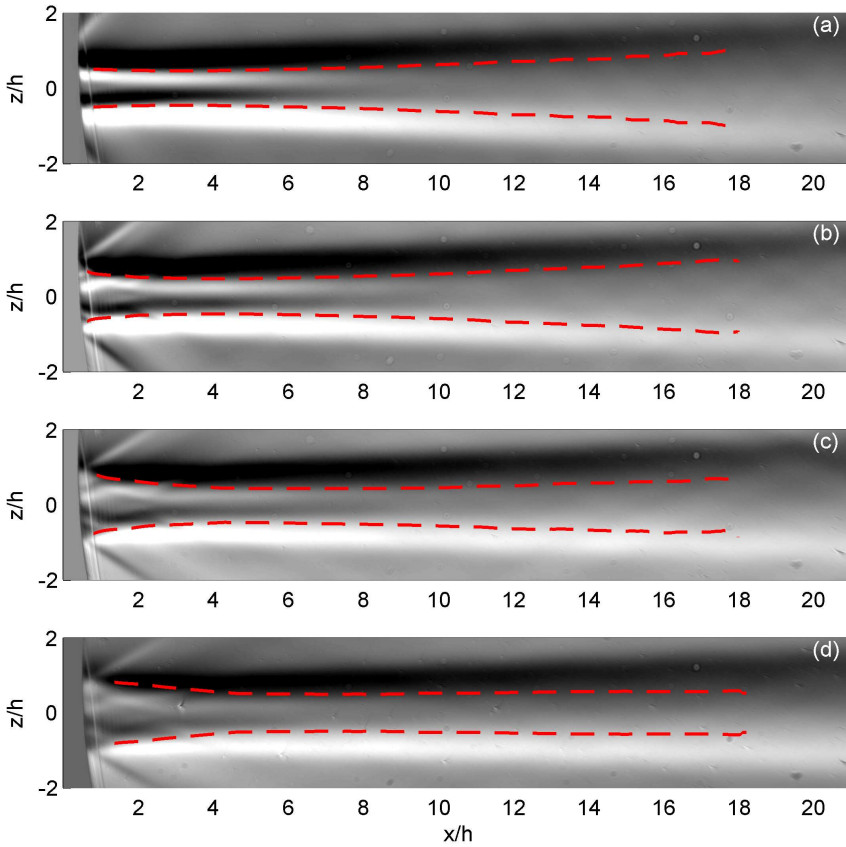


Figure 9.9: Schlieren visualizations of the micro-ramp vortex trajectories for $M_\infty = 1.5, 2.0, 2.5$ and 3.0 (a-d)

/ side-wall junction) push the oil away from the centreline. As such, the oil flow pattern provides an approximation of the trajectory of the primary vortices downstream of the ramp. Also it should be remarked here that the vortices lift-off from the surface when moving downstream (typically after 2 micro-ramp lengths, see also the work of Babinsky et al. (2009)), which further alters the wall skin friction distribution and thus the recorded oil-flow patterns.

The oil tracks are nevertheless in good agreement with the vortex trajectories derived from the schlieren images (red dashed line) for $x > 5h$. Closer to the ramp some differences can be noticed between the trajectories derived from the two techniques. The oil tracks show a kink (minimum vortex separation distance) around $x/h = 1-2$, whereas for the schlieren visualizations this minimum is reached significantly further downstream, around $x/h = 4-6$, depending upon the Mach number. This difference can be attributed to the measurement technique, with schlieren visualizations the primary vortices are tracked directly, whereas in the oil-flow visualizations an oil track created by the mutual effects of the primary and secondary vortices is used as indicator. It should be remarked

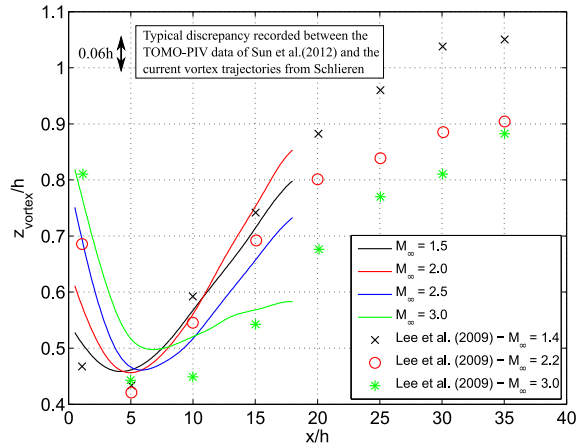


Figure 9.10: The estimated vortex core location (z_{vor}) for a range of Mach numbers ($Re_\infty = 39 \times 10^6 \text{ m}^{-1}$), compared with the numerical data of Lee et al. (2009).

here, that Lee et al. (2009) in their LES simulations also found that the distance between the primary vortices is minimal $\sim 5h$ downstream of the trailing edge of the micro-ramp.

9.4.2. PIV RESULTS

All PIV measurements were performed in the symmetry plane of the micro-ramp. The baseline configuration is that of a $h = 8 \text{ mm}$ micro-ramp at a freestream Mach number of 2.0 and unit Reynolds number of $39 \times 10^6 \text{ m}^{-1}$. The effects of micro-ramp height, Mach number and Reynolds number on the induced flow field were investigated systematically by varying one parameters at a time, keeping the other two parameters constant (see section 9.1.1).

Fig.9.12 shows the velocity field downstream of a 6, 8 and 10 mm micro-ramp, where both x and y are scaled with the micro-ramp height h . Close to the micro-ramp it was not possible to perform accurate measurements due to strong laser reflections and a relatively low seeding level. This part of the data has therefore been blanked in the velocity fields of Fig.9.12. In the top left corner of the velocity field one can clearly distinguish a region with higher velocities, which is the result of an expansion wave created at the trailing edge of the ramp. This region is terminated by a shock wave, which is inclined by an angle of $\sim 28^\circ$. This is slightly smaller than the Mach angle $\mu = 30^\circ$ at this Mach number ($M_\infty = 2.0$). Downstream of the micro-ramp a strong wake is observed, which gradually lifts off from the surface and weakens in strength when moving downstream.

Similarly, Fig.9.13 and 9.14 display the PIV results for the Mach and Reynolds number variations. From the contour plots some trends may be noted, where it appears that larger micro-ramps introduce higher velocities close to the wall at the same x/h distance from the ramp, which indicates stronger mixing effects for the larger micro-ramps. The opposite holds true for the effect of the Mach number on the flow field, a higher Mach number appears to reduce the effects of mixing and introduces a stronger wake (a larger velocity deficit), which is located closer to the wall at the same x/h distance.

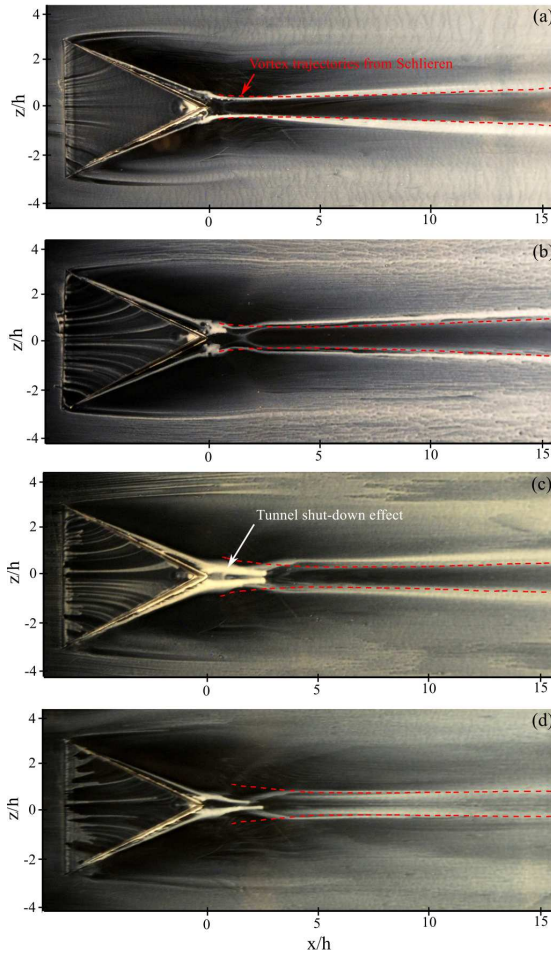


Figure 9.11: Oil flow visualizations for a $h = 8$ mm micro-ramp at $M_\infty = 1.5$ (a), $M_\infty = 2.0$ (b), $M_\infty = 2.5$ (c) and $M_\infty = 3.0$ (d).

These trends are elaborated further in Figs.9.16, Figs.9.17 and Figs.9.18. These figures, respectively, show the wake height y_{wake} , the wake velocity U_{wake} , the maximum upwash location y_{vmax} , the maximum upwash velocity V_{max} , the incompressible shape factor H_i and the added momentum flux E . The definition of the wake properties can be found in Fig.9.15, which shows some typical velocity profiles downstream of the $h = 8$ mm micro-ramp. The incompressible shape factor H_i is a measure of the fullness of the boundary layer and is often used to assess the 'health' of the boundary layer and its resilience to separation (Titchener and Babinsky (2015)). The added momentum flux E is a metric that was introduced in section 8.2.3 and provides a measure of the momentum flux that has been added to the near-wall region ($<0.43\delta_{99}$) of the flow by the action of the micro-ramp. In section 8.2.3 it was found that the added momentum flux $E(x/\delta_{99})$

scales linearly with the micro-ramp height h , whereas the streamwise development (x -coordinate) scales with δ_{99} and not with h . In this definition δ_{99} is the boundary layer thickness of the undisturbed boundary layer as listed in Table 9.3. The added momentum flux was found to increase up to $x \sim 5.7\delta_{99}$, after which a plateau is reached and virtually no extra momentum is added or removed.

$$H_i(x) = \frac{\delta_i^*}{\theta_i} = \frac{\int_0^\infty \left(1 - \frac{u}{U_\infty}\right) dy}{\int_0^\infty \frac{u}{U_\infty} \left(1 - \frac{u}{U_\infty}\right) dy} \quad (9.3)$$

$$E(x) = \int_0^{0.43\delta_{99}} \frac{u^2 - u_{clean}^2}{U_\infty^2} dy \quad (9.4)$$

MICRO-RAMP HEIGHT EFFECTS

Fig.9.16(a-b) shows that the wake height and wake velocity collapse nearly exactly on top of each other for the different micro-ramp heights, when scaling both x and y by h . The maximum upwash location also scales nearly perfectly with micro-ramp height (see Fig.9.17(a)). The maximum upwash velocity on the other hand shows a weak dependence on the micro-ramp height (see Fig.9.17(b)). For the larger micro-ramps, higher upwash velocities are recorded at the same x/h location, which indicates stronger flow mixing. This observation is further supported by the development of the incompressible shape factor and the added momentum flux. Fig.9.18(a) shows that a larger micro-ramps leads to a lower shape factor and thus a fuller boundary layer profile. The shape factor was reduced below the undisturbed reference value for all three micro-ramp heights, so all three micro-ramps tested have a positive effect on the ‘health’ of the boundary layer in the symmetry plane of the ramp. However, for the same x/h distance, larger micro-ramps consistently record lower values of the shape factor. For $x/h = 20$, the $h = 6$ mm micro-ramp records $H_i = 1.23$, the $h = 8$ mm micro-ramp records $H_i = 1.20$ and the $h = 10$ mm micro-ramp records $H_i = 1.18$.

The added momentum flux is presented in Fig.9.18(b), with E normalized by h and x normalized by δ_{99} . The data of the three micro-ramp heights collapses nearly exactly on top of each other, which agrees with the observations made in the previous chapter. The latter experiments were also performed at the TU Delft, but in a different supersonic wind tunnel (ST-15) and under different tunnel operating conditions (see Table 9.4). The normalized added momentum flux E/h becomes positive after $\sim 5\delta_{99}$ and a plateau is reached after $\sim 7\delta_{99}$.

MACH NUMBER EFFECTS

The effects of the Mach number on the flow field downstream of the micro-ramp are presented in Figs.9.16(c-d), 9.17(c-d) and 9.18(c-d). A higher Mach number tends to lower the location of the wake as well as the location of maximum upwash. Also for the higher Mach number a slightly stronger wake is recorded for the same x/h distance from the micro-ramp. Figs.9.18(c-d) reveal that for higher Mach numbers a longer mixing distance is needed to reach the same level of boundary layer fullness / added momentum flux in the symmetry plane of the micro-ramp. Also the plateau level of E is significantly lower for $M_\infty = 2.5$ ($E/h \sim 0.02$) than for $M_\infty = 1.5$ ($E/h \sim 0.05$).

These observations are closely linked to the evolution of the primary vortices in the streamwise direction. The method described in section 9.2.2 was used to obtain the development of the vortex strength for the different Mach numbers (see Fig.9.19). The $M = 1.5$ and $M = 2$ case deliver virtually the same circulation at every x/h location, whereas the $M = 2.5$ case delivers a lower value of the circulation, especially within $10h$ of the micro-ramp. The circulation strength calculated by Nolan and Babinsky (2012) (from LDV measurements, same type of micro-ramp) is slightly higher for all x/h locations. Furthermore their data shows no significant Mach number effect on the circulation Γ , when normalized with hu_r .

REYNOLDS NUMBER EFFECTS

The Reynolds number range considered in the present investigation has a much smaller effect on the flow field than the micro-ramp height and the Mach number (see 9.16(e-f), 9.17(e-f), 9.18(e-f)). All plots show a good collapse of the data for the different Reynolds numbers. Only for the shape factor a small Reynolds number may be observed, with the higher Reynolds number resulting in a slightly fuller velocity profile. At $x/h = 20$, shape factor of 1.21, 1.20, 1.19 and 1.18 are recorded for unit Reynolds numbers of 27.7×10^6 , 39.5×10^6 , 51.3×10^6 and $63.4 \times 10^6 \text{ m}^{-1}$, respectively.

9.4.3. COMPARISON WITH OTHER STUDIES

Micro-ramp vortex generators have been studied by numerous researchers, but all at different operating conditions. The objective of this section is to compare the results of some of these earlier studies with the current dataset and to investigate the variability between the experiments and to identify trends related to the micro-ramp height, Mach number and Reynolds number. Three wake characteristics are investigated: the wake height y_{wake} , the maximum upwash velocity V_{max} and the maximum upwash location y_{vmax} . Eight studies were considered for this comparison (see Table 9.4), with Mach numbers varying between $M_\infty = 1.4 - 3.0$, micro-ramp heights in the range of $x/\delta_{99} = 0.33 - 1.0$ and Reynolds numbers of $Re_{\delta_{99}} = 1.7 \times 10^4 - 1.1 \times 10^6$. The wide range of operating conditions considered supports the generalization of the conclusions. Both numerical (Reynolds Averaged Navier Stokes (RANS), Large Eddy Simulations (LES)) and experimental (Laser Doppler Velocimetry (LDV), Particle Image Velocimetry (PIV)) studies are included in the discussion.

Fig.9.20 presents the wake location recorded by the different researchers in terms of the x/h , y_{wake}/h - scaling. The same general trend is recorded by all researchers, subject to some scatter between the datasets. Irrespective of the operating conditions, it can be noticed that all data points fall within a $\sim 0.8h$ uncertainty band, which corresponds to approximately 30% of y_{wake} at $x/h = 20$. It is interesting to observe that the data of Nolan and Babinsky (2011) ($M_\infty = 1.5$) lies systematically above the data of Babinsky et al. (2009) ($M_\infty = 2.5$). Both datasets were acquired in the same experimental facility at only a slightly different Reynolds number ($Re_{\delta_{99}} = 1.8 \times 10^5$ vs $Re_{\delta_{99}} = 2.4 \times 10^5$). So, also from the University of Cambridge experiments it appears that a higher Mach number tends to lower the location of the wake.

The maximum upwash velocity is presented in Fig.9.21 for three different datasets and a range of micro-ramp heights. The datasets are in good agreement and show a

near-exponential decay of the maximum upwash velocity with x/h . Additionally one can notice that the current dataset and the dataset of Giepman et al. (2014b), show a weak dependence on the micro-ramp height. A larger micro-ramp results in higher upwash velocities at the same x/h distance for $x/h < 20$.

Finally, Fig.9.22 shows the normalized maximum upwash location y_{vmax}/h as a function of x/h . In the works of Sun et al. (2012) and Nolan and Babinsky (2011), it has been shown that the location of maximum upwash is virtually the same as the height of the vortex core above the wall. Since several researchers have investigated the trajectory of the vortex core (Nolan and Babinsky (2012); Lee et al. (2009); Galbraith et al. (2009)) it was decided to compare their data with the maximum upwash location recorded in the current study and that of a previous study by the authors (Giepman et al. (2014b)). The datasets are in good agreement and all data points fall within an uncertainty band of $\sim 0.5h$, which at $x/h = 20$ corresponds to an uncertainty of $\sim 25\%$ on the vortex core location / maximum upwash location. A weak Mach number effect can be observed for both the current dataset and the dataset of Nolan and Babinsky (2012), where a higher Mach number tends to lower the location of the vortex core. The LES simulations of Lee et al. (2009), on the other hand do not show any Mach number effect. This could be due to the relatively low Reynolds number of their LES simulations, which is an order of magnitude smaller than that of the experiments presented in Fig.9.22.

9.5. CONCLUSIONS

A parametric study has been conducted to investigate the effects of micro-ramp height, freestream Mach number and Reynolds number on the wake and mixing properties of micro-ramp vortex generators. As a baseline configuration, a $h = 8$ mm ($h/\delta_{99} = 0.46$) micro-ramp was used, which was tested at a Mach number of $M_\infty = 2.0$ and a Reynolds number of $Re_\infty = 39 \times 10^6 \text{ m}^{-1}$. The effects of these parameters were investigated systematically by changing one parameter at a time, while keeping the other fixed. The micro-ramp height was varied between 6 and 10 mm (corresponding to $h/\delta_{99} = 0.35$ and 0.58), the Mach number from 1.5 to 2.5 and the unit Reynolds number from $28 - 63 \times 10^6 \text{ m}^{-1}$. The latter corresponds to a $Re_{\delta_{99}}$ range of $4.9 - 10.5 \times 10^5$. Particle image velocimetry has been used as the primary flow diagnostics tool of this study and all measurements were performed in the symmetry plane of the micro-ramp. Additional oil-flow and top-view schlieren visualizations were performed to document the vortex trajectories in the spanwise plane.

Most flow features were found to scale linearly with the micro-ramp height: the wake location, wake velocity deficit and the maximum upwash location (equivalent to the vortex core height, see also the work of Sun et al. (2012); Nolan and Babinsky (2011)), all scale linearly with h . Larger micro-ramps are substantially more effective at mixing the boundary layer than smaller ramps and at the same x/h location a fuller velocity profile is recorded for the larger micro-ramps. The momentum flux that is added to the near-wall region ($y < 0.43\delta_{99}$) of the flow (with respect to the undisturbed boundary layer) is found to scale linearly with micro-ramp height for $0.35 < h/\delta_{99} < 0.58$. The added momentum flux E increases steadily up to $\sim 7\delta_{99}$ ($M_\infty = 2.0$, $Re_\infty = 39 \times 10^6 \text{ m}^{-1}$) downstream of the micro-ramp, after this point a plateau is reached and virtually no momentum is added or removed from the near-wall portion of the boundary layer. Similar re-

sults were reported in the chapter 8, but results were obtained in a different wind tunnel under different operating conditions. In this previous work a high value of E was found to be correlated with a lower (shock-induced) boundary layer separation probability.

Increasing the Mach number has a negative impact on the wake / mixing properties of the micro-ramp, as judged from the velocity field that is recorded in the symmetry plane of the micro-ramp. The profile is less full (higher H_i) and less momentum is added to the near-wall region of the flow (lower E). Additionally, a stronger wake is recorded for the higher Mach numbers, which stays closer to the wall for a longer distance. Schlieren and oil-flow visualizations furthermore revealed that for higher Mach numbers, the two primary vortices move apart slower (in span direction) than for the lower Mach numbers, which is a direct consequence of the weaker vortices at the higher Mach numbers (especially $M_\infty = 2.5$). An evaluation of the normalized vortex strength (Γ/hu_τ) showed that for $M_\infty = 1.5$ and $M_\infty = 2.0$ vortices of virtually the same strength are recorded. The vortices recorded for $M_\infty = 2.5$ are weaker, with the differences being most pronounced (20 - 30%) in the vicinity of the micro-ramp ($x/h < 10$).

The Reynolds number has no effect on the wake properties (wake location, velocity etc. . .) of the micro-ramp, but it does have a small effect on the mixing properties of the ramp. At higher Reynolds numbers the micro-ramp becomes slightly more effective and a fuller velocity profile is recorded at the same x/h location downstream of the micro-ramp. For $Re_\infty = 28 \times 10^6 \text{ m}^{-1}$ and $Re_\infty = 63 \times 10^6 \text{ m}^{-1}$ shape factors of respectively 1.21 and 1.18 are recorded $20h$ downstream of the trailing edge of the micro-ramp.

Finally, the results for the wake location, maximum upwash velocity and the maximum upwash location were compared with the results of eight earlier studies on micro-ramps. Here it has been assumed that the maximum upwash location can be compared to the vortex core height, an assumption supported by the work of Sun et al. (2012) and Nolan and Babinsky (2011). The studies incorporated in the comparison cover a wide range of operating conditions: $M_\infty = 1.4 - 3.0$, Reynolds numbers of $Re_{\delta_{99}} = 1.7 \times 10^4 - 1.1 \times 10^6$ and micro-ramp heights of $x/\delta_{99} = 0.33 - 1.0$. After scaling the data with the micro-ramp height h a typical variability of 25% is recorded between the studies for the three different parameters. This variability can partially be explained by the different operating conditions (in particular the Mach number). Data that was acquired at the same wind tunnel with the same measurement technique usually revealed some Mach number dependence. The wake and vortex core location are lowered for higher Mach numbers and also the mixing strength is reduced. However, between the datasets of different researchers no clear Mach or Reynolds number dependence could be discovered. It appears that other factors (for instance tunnel turbulence intensity and measurement / simulation uncertainties) in this respect may play a greater role than the nominal flow conditions and inhibit a further collapse of the data.

Table 9.4: Previous studies on micro-ramp vortex generators

Study	Technique	M_∞	Re_∞	Re_δ	h/δ
Babinsky et al. (2009)	1-component LDV	2.5	$40 \times 10^6 \text{ m}^{-1}$	2.4×10^5	0.33, 0.5, 0.66, 1.0
Galbraith et al. (2009)	RANS	2.5	$36 \times 10^6 \text{ m}^{-1}$	1.1×10^5	0.4
Giepman et al. (2014b)	PIV	2.0	$42 \times 10^6 \text{ m}^{-1}$	2.2×10^5	0.38, 0.58, 0.77
Herges et al. (2009)	PIV	1.4	$30 \times 10^6 \text{ m}^{-1}$	1.3×10^5	0.4
Lee et al. (2009)	LES	1.4	-	0.17×10^5	0.76
		2.2	-	0.18×10^5	0.72
		3.0	-	0.17×10^5	0.74
Nolan and Babinsky (2011)	2-component LDV	1.5	$26 \times 10^6 \text{ m}^{-1}$	1.8×10^5	0.57
Nolan and Babinsky (2012)	2-component LDV	1.5	$26 \times 10^6 \text{ m}^{-1}$	1.8×10^5	0.57
		1.8	$24 \times 10^6 \text{ m}^{-1}$	1.7×10^5	0.57
		2.5	$31 \times 10^6 \text{ m}^{-1}$	2.2×10^5	0.57
Sun et al. (2014)	PIV	2.0	$41 \times 10^6 \text{ m}^{-1}$	2.1×10^5	0.58, 0.77

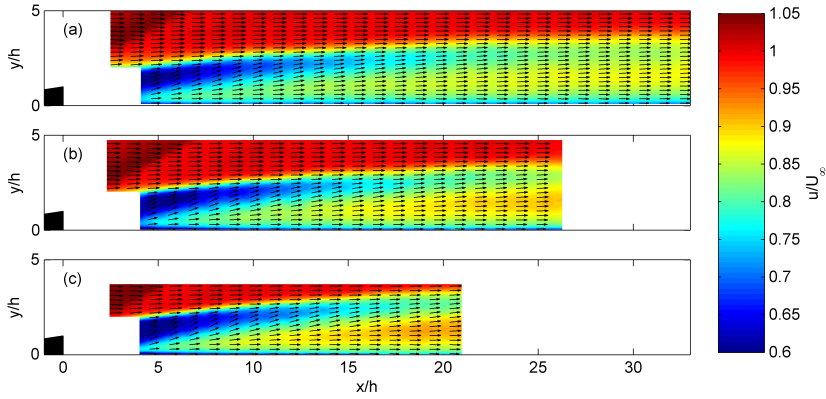


Figure 9.12: Average velocity field (u-component) downstream of a $h = 6$ mm (a), $h = 8$ mm (b) and $h = 10$ mm (c) micro-ramp. Tunnel operating conditions: $M_\infty = 2.0$ and $Re_\infty \sim 39 \times 10^6 \text{ m}^{-1}$

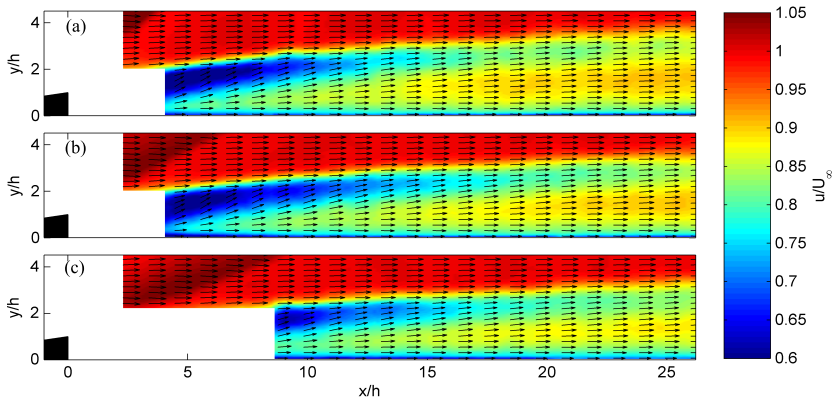


Figure 9.13: Average velocity field (u-component) downstream of a $h = 8$ mm micro-ramp for a fixed Reynolds number ($Re_\infty \sim 39 \times 10^6 \text{ m}^{-1}$) and a range of Mach numbers: $M_\infty = 1.5$ (a), $M_\infty = 2.0$. (b) and $M_\infty = 2.5$ (c).

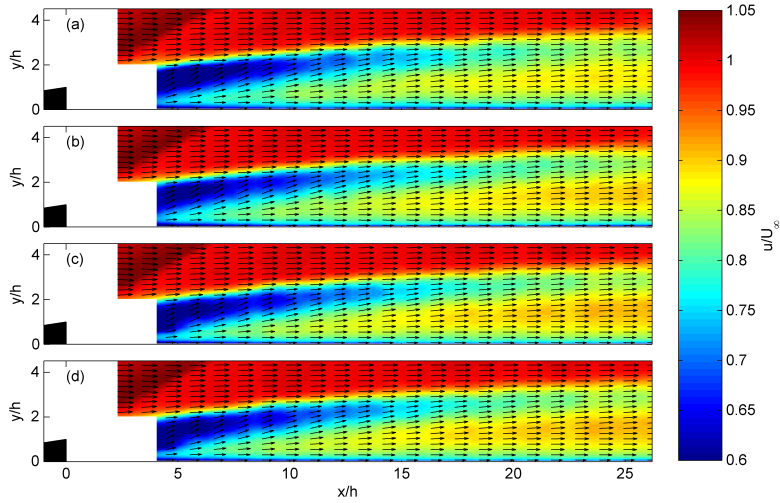


Figure 9.14: Average velocity field (u -component) downstream of a $h = 8$ mm micro-ramp for a fixed Mach number ($M_\infty = 2.0$) and a range of Reynolds numbers: $Re_\infty \sim 27.7 \times 10^6 \text{ m}^{-1}$ (a), $Re_\infty \sim 39.5 \times 10^6 \text{ m}^{-1}$ (b), $Re_\infty \sim 51.3 \times 10^6 \text{ m}^{-1}$ (c) and $Re_\infty \sim 63.4 \times 10^6 \text{ m}^{-1}$ (d).

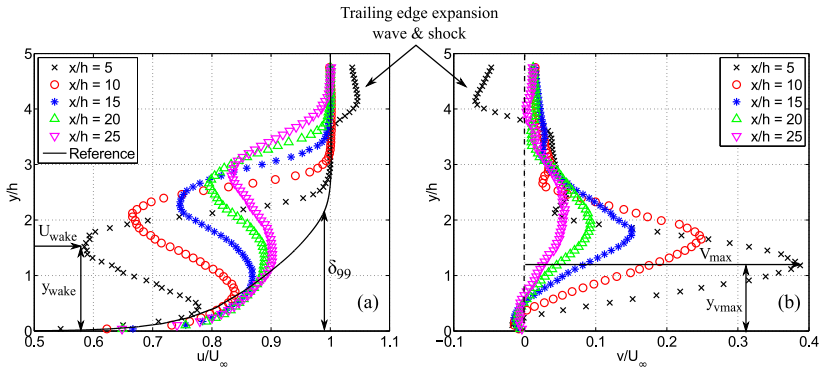


Figure 9.15: Velocity profiles along the symmetry plane of the micro-ramp, showing (a) the u -component and (b) the v -component. Experimental conditions: $M_\infty = 2.0$ and $Re_\infty \sim 39.5 \times 10^6$, for a $h = 8$ mm micro-ramp.

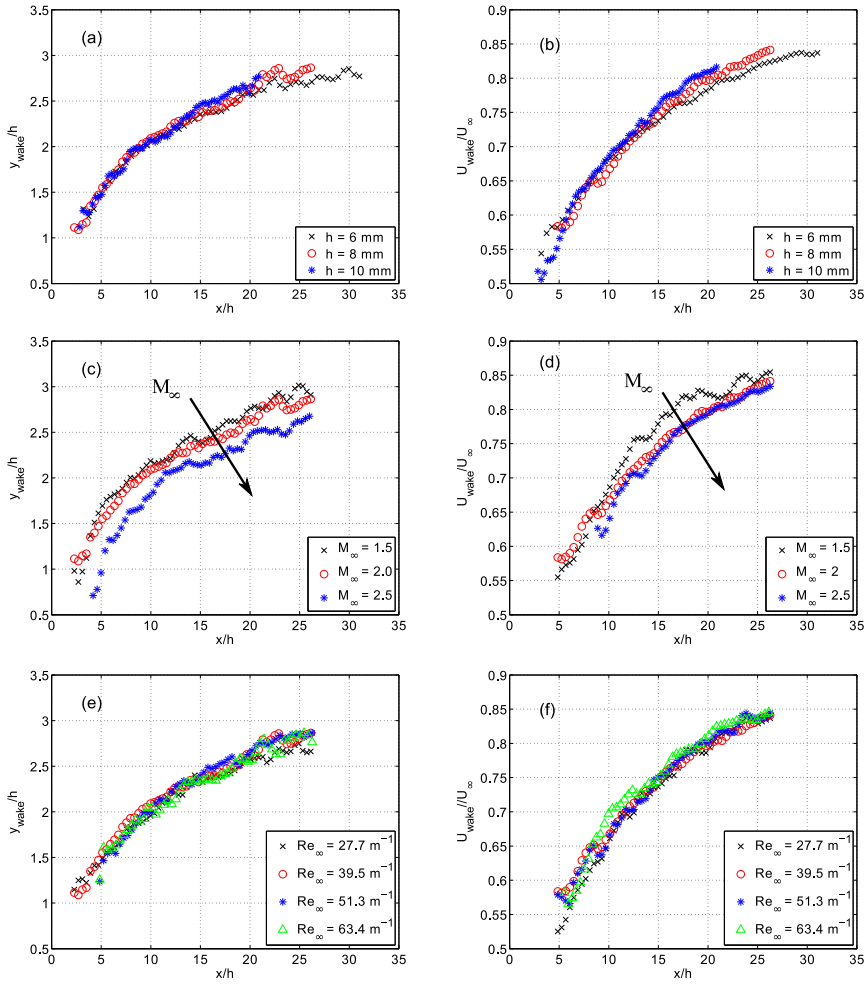


Figure 9.16: The wake location (a,c,e) and wake velocity (b,d,f) for a range of micro-ramp heights, Mach numbers and Reynolds numbers, respectively.

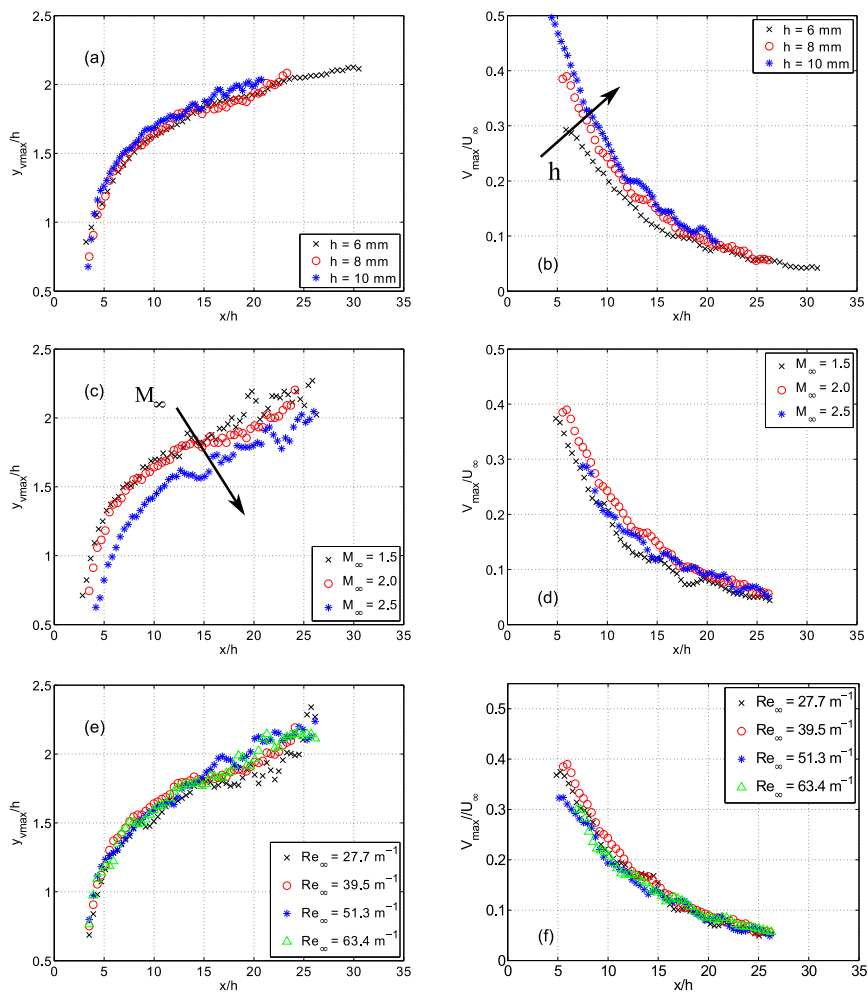


Figure 9.17: The maximum upwash location (a,c,e) and the maximum upwash velocity (b,d,f) for a range of micro-ramp heights, Mach numbers and Reynolds numbers, respectively.

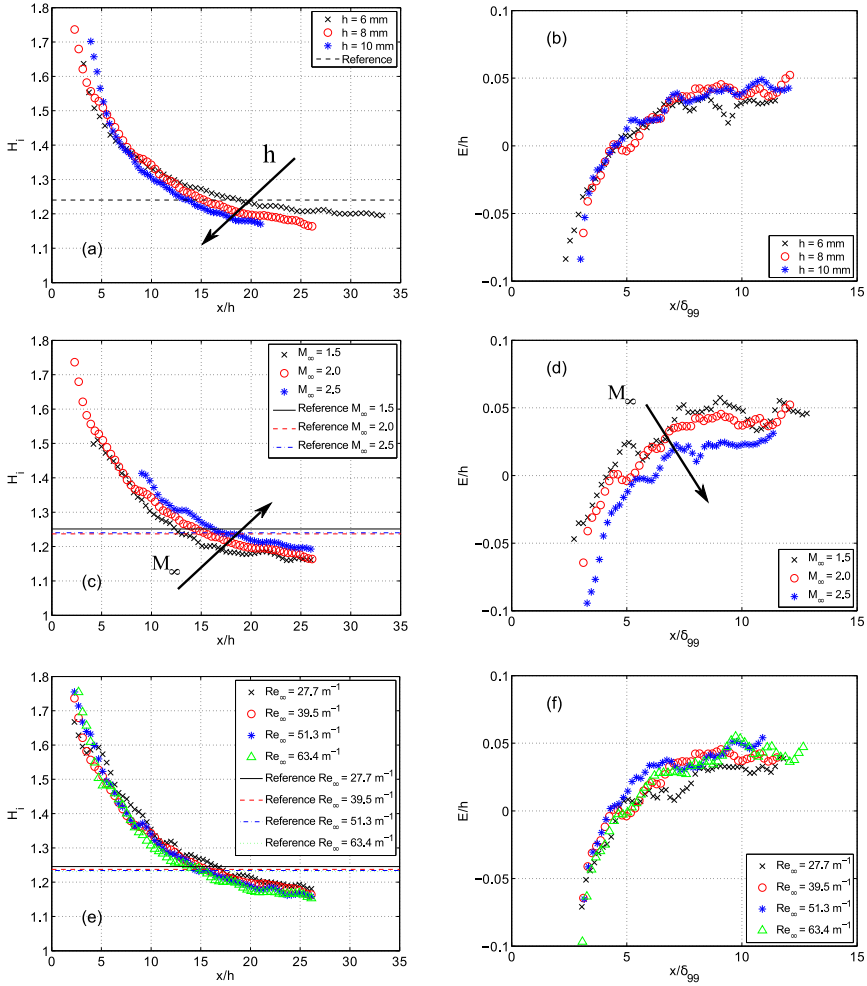


Figure 9.18: The incompressible shape factor (a,c,e) and the normalized added momentum flux (b,d,f) for a range micro-ramp heights, Mach numbers and Reynolds numbers, respectively.

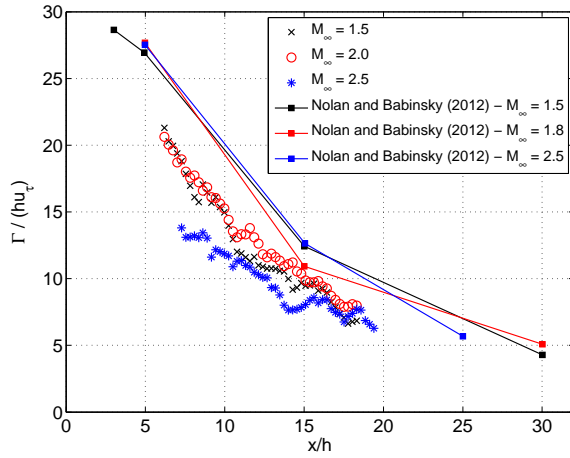


Figure 9.19: Vortex strength calculation for a range of Mach numbers

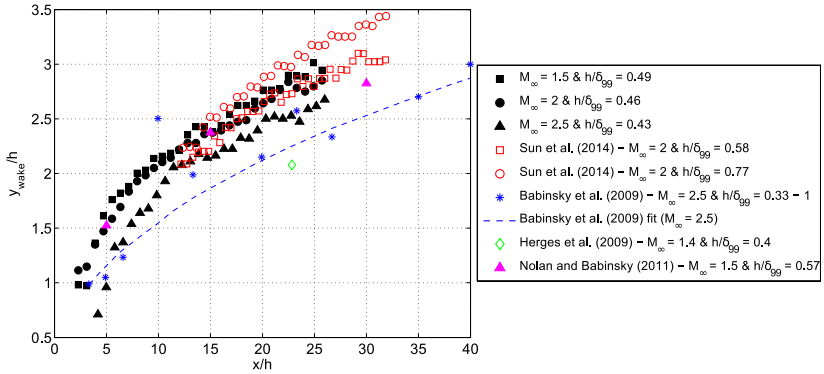


Figure 9.20: The wake location reported in different studies.

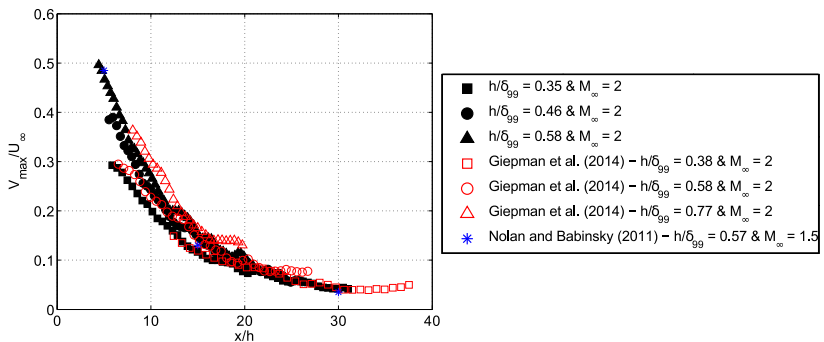


Figure 9.21: The maximum upwash velocity reported in different studies.

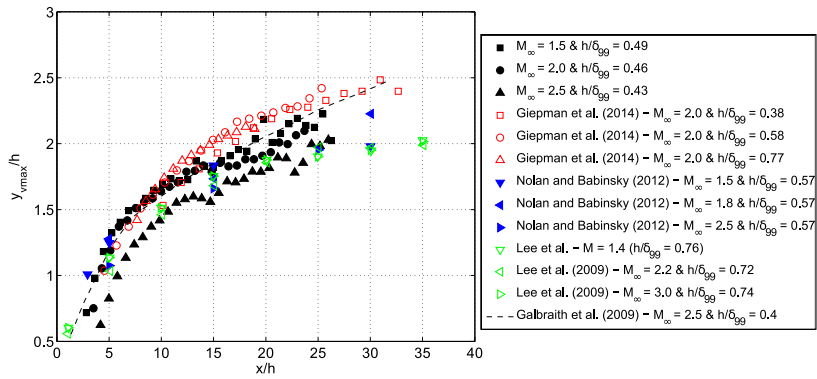


Figure 9.22: The location of maximum upwash reported in different studies. For constructing this figure it has been assumed that the location of maximum upwash (along the $z = 0$ mm plane) is approximately the same as the vortex core height.

10

CONCLUSIONS

This PhD thesis focused on the characterization of flow control devices for oblique shock wave reflections at relatively low supersonic Mach numbers ($M_\infty = 1.5 - 3.0$). Oblique shock wave reflections can be encountered in supersonic intakes, on the blades of compressor and turbine cascades and in other situations of relevance for the high-speed flight regime. These type of interactions can generate undesirable features, such as a high-degree of flow unsteadiness, a large drag contribution and increased total pressure losses. Many of these features can be (in)directly linked to the occurrence of flow separation. In this PhD thesis separation control techniques were investigated for both laminar and turbulent oblique shock wave reflections, the results of which are summarized in sections 10.1 and 10.2, respectively.

10.1. FLOW CONTROL FOR LAMINAR OBLIQUE SHOCK WAVE REFLECTIONS

Laminar boundary layers are beneficial because of their low skin friction contribution, which can help to further reduce the fuel consumption of air and space vehicles. The main disadvantage of laminar boundary layers is, however, their sensitivity to adverse pressure gradients; even very weak shock waves ($p_3/p_1 = 1.11$) can already result in the formation of large separation bubbles. In general, boundary layer separation is regarded as detrimental, because of the associated unsteadiness and potential system performance losses. It therefore seems optimal to enforce boundary layer transition a short distance upstream of the interaction. Such a strategy would benefit from the low skin friction laminar boundary layer for as long as possible, while still avoiding the adverse effects of boundary layer separation. This concept, however, raises the following questions:

1. How detrimental is the baseline laminar SWBLI?
2. How far should the transition control devices be placed upstream of the interaction to completely avoid separation?

3. What is the most effective way of tripping the boundary layer?

Attention was first directed to the baseline uncontrolled oblique shock wave reflection. A parametric study was carried out for laminar and transitional oblique shock wave reflections, by variation of the Mach number, Reynolds number and the flow deflection angle. The Mach number was varied from $M_\infty = 1.6 - 2.3$, the Reynolds number from $Re_{x_{sh}} = 1.4 - 3.5 \times 10^6$ and the flow deflection angle from $\theta = 1^\circ - 5^\circ$ ($p_3/p_1 = 1.11 - 1.64$). All measurements were performed on a full-span flat plate model and the oblique shock wave was generated by a partial span shock generator. High-resolution particle image velocimetry (PIV) measurements were performed for all test cases, supported by oil-flow and schlieren visualizations.

The PIV measurements proved to be challenging due to the thin laminar boundary layer ($\delta_{99} \sim 0.2$ mm), the high shear rate (~ 0.9 pix/pix) and the highly non-uniform seeding distribution. The seeding particles were found to migrate away from the wall close to the leading edge of the flat plate, due to the effects of the high local streamline curvature and the high level of rotation (large $\partial u / \partial y$) in the newly formed laminar boundary layer. Since a laminar boundary layer shows virtually no mixing effects, there is no mechanism to redistribute the particles into the laminar boundary layer and a near-wall region of very low seeding persists until the moment of boundary layer transition. This region comprised approximately 40% of the laminar boundary layer thickness at $x = 40$ mm ($Re_x = 1.4 \times 10^6$) from the leading edge. The top 60% of the velocity profile could still be reconstructed reliably by using a combination of several newly developed pre-processing techniques and an ensemble correlation approach.

Seeding difficulties were also encountered when studying laminar shock wave boundary layer interactions. The laminar boundary layer is lifted over the separation bubble and so are the incoming tracer particles, which rendered it impossible to obtain reliable velocity data inside of the separation bubble, even when using an ensemble correlation approach. Although the velocity field in the separation bubble cannot be reconstructed from the particle image data, the data further away from the wall ($u > 0.2U_\infty$) can still be considered as reliable, because of the higher seeding density and smaller probability of encountering wall reflections. Since the size of the separation bubble is a key parameter in this study it was decided to develop an extrapolation technique based upon Falkner-Skan velocity profiles to estimate the height of the reversed flow region (i.e. the $u = 0$ isoline). This procedure was validated with DNS data of Sansica et al. (2014), who simulated a laminar oblique shock wave reflection ($\theta = 2^\circ$) at a Mach number of 1.5. It was found that with this approach the length and height of the reversed flow region can be predicted with a $\sim 4\%$ and $\sim 10\%$ accuracy, respectively.

The PIV measurements revealed a long, flat and triangular reversed flow region for the laminar interactions, as sketched in Fig.10.1. The separation bubble acts as a ramp for the incoming flow, resulting in the formation of a series of compression waves. The incident shock reflects as an expansion wave from the top of the separation bubble shear layer, and at reattachment, again a series of compression waves is created. Although the overall topology of laminar interactions is well-known within the research community from wall-pressure measurements, schlieren visualizations and pitot probe measurements, the effects of boundary layer transition on the interaction remained a difficult topic to tackle with these traditional measurement techniques. The PIV measurements

performed in the course of this work provided several new insights in this respect, especially regarding the connection between shock strength, separation bubble size and boundary layer transition. The following results, unless mentioned otherwise, refer to the baseline laminar operating conditions ($M_\infty = 1.7$, $Re_{x_{sh}} = 1.8 \times 10^6$).

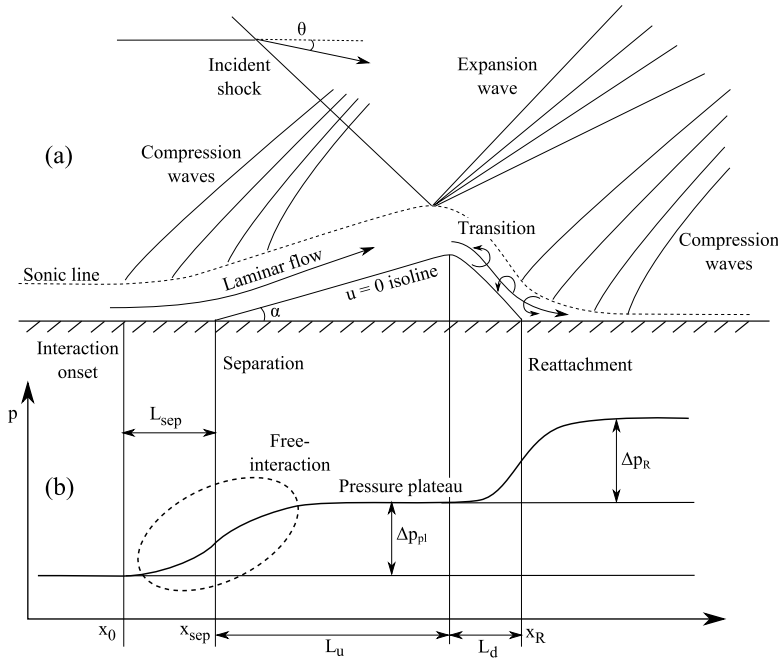


Figure 10.1: A sketch of an oblique shock wave reflection with a laminar incoming boundary layer and transition on the rear part of the bubble (a); the corresponding pressure distribution (b).

1. For sufficiently strong shock waves ($p_3/p_1 > 1.22$), boundary layer transition occurs directly after passing the oblique shock wave, resulting in higher mixing levels in the detached shear layer and a quick reattachment ($L_d \sim 20\delta_{i,0}^*$) of the boundary layer. The distance L_d remains virtually constant with shock strength, whereas the upstream length of the separation bubble L_u grows linearly with shock strength for $p_3/p_1 > 1.22$.
2. For relatively weak shock waves ($p_3/p_1 = 1.11 - 1.16$), the boundary layer is capable of maintaining its laminarity longer and transition occurs approximately $\sim 100\delta_{i,0}^*$ downstream of the incident shock wave. These shock wave-boundary layer interactions can therefore be considered as fully laminar. As a result of the reduced mixing in the shear layer, reattachment is delayed with a corresponding increase in the downstream length of the separation bubble L_d , from approximately $20\delta_{i,0}^*$ to $38\delta_{i,0}^*$ when reducing the shock strength from $p_3/p_1 = 1.22$ to 1.14, respectively. Even though transition sets in later for weak shock waves, the process of transition is still strongly accelerated compared to that of natural transition. Natural

transition takes place over the extent of approximately $4.0 \times 10^2 \delta_{i,0}^*$, whereas with the presence of an impinging shock wave ($\theta = 1.5^\circ$, $p_3/p_1 = 1.16$) this has been reduced to approximately $1.2 \times 10^2 \delta_{i,0}^*$.

3. Increasing the Mach number while keeping the Reynolds number and flow deflection angle constant ($Re_{x_{sh}} = 1.8 \times 10^6$, $\theta = 3^\circ$) leads to a monotonic decrease in the size of the reversed flow region. On the other hand, the angle α between the $u = 0$ isoline and the wall is found to monotonically increase with Mach number, from 1.7° to 2.2° for $M_\infty = 1.6$ to 2.3 , respectively. Virtually the same predictions are given by the analytical model of Hakkinen et al. (1959).
4. The shock Reynolds number $Re_{x_{sh}}$ was varied from $1.4 \times 10^6 - 3.5 \times 10^6$ ($x_{sh} = 41 - 101$ mm). The boundary layer was laminar for $Re_{x_{sh}} = 1.4 \times 10^6$ and 1.8×10^6 test cases, transitional for $Re_{x_{sh}} = 2.1 \times 10^6 - 3.2 \times 10^6$ and fully turbulent for $Re_{x_{sh}} = 3.5 \times 10^6$. Separation is only recorded for $Re_{x_{sh}} = 1.4 \times 10^6 - 2.5 \times 10^6$ ($\gamma = 0 - 0.5$), with the largest bubble recorded for the laminar cases. The two laminar cases deliver virtually the same size / shape of separation bubble and also the recorded transition process appears to be very similar. This shows that the interaction is relatively insensitive to changes in the Reynolds number as long as the incoming boundary layer is laminar. The size of the bubble is reduced significantly when the boundary layer is (slightly) transitional. Although the intermittency level for $Re_{x_{sh}} = 2.1 \times 10^6$ equals only $\gamma = 0.08$, the recorded bubble size nevertheless is 24% smaller than the bubble size recorded for the $Re_{x_{sh}} = 1.8 \times 10^6$ case, for which the boundary layer is still fully laminar.
5. The free-interaction theory (Chapman et al. (1957)) states that the initial pressure rise at separation should only depend upon upstream flow properties and not on downstream flow properties for both laminar and turbulent shock wave-boundary layer interactions. Although the free-interaction theory is well-established for relatively strong shock waves (Delery and Marvin (1986)), much less information is available in literature for weak interactions, where a pressure plateau is not reached. The data of this thesis, however, provides convincing evidence that the free-interaction concept also holds true for weak near-incipiently separated laminar oblique shock wave reflections.
6. Due to the extremely thin laminar boundary layer ($\delta_{99} \sim 0.2$ mm) and thus high particle Stokes number ($St = \tau_p / \delta_{99} \sim 5.6$) it was not possible to accurately reconstruct the velocity fluctuations inside the boundary layer and interaction region. Some information on the unsteadiness of the interaction could, however, still be inferred by looking at its global flow features instead of the small scale features present in the boundary layer. The velocity fluctuations were assessed in the region upstream of the incident shock wave, which is dominated by the compression waves that are generated by the thickening and separation of the laminar boundary layer. The velocity fluctuations values were found to be quite small, with typical values: $v' = 0.7 - 1\%$ of U_∞ for all laminar test cases. This translates into typical variations in the separation location of $\sim 0.27 L_{sep}$ at $M_\infty = 1.7$, $Re_{x_{sh}} = 1.8 \times 10^6$ and $\theta = 5^\circ$, where L_{sep} is the distance between the interaction onset and boundary

layer separation location (see Fig.10.1). The measured velocity fluctuations were, however, close to the noise threshold of the PIV measurements and the recorded uncertainties should therefore only be considered as a *conservative upper bound* on the unsteadiness of the compression waves and separation location.

After having gained a thorough understanding of the uncontrolled laminar interaction, the next step was to study the effects of transition control devices on the flat plate laminar boundary layer. Three devices were considered for this study: a 2D stepwise trip, a patch of distributed roughness and a zig-zag strip. The trips were located 40 mm from the leading edge of the plate, which corresponds to a $Re_x = 1.4 \times 10^6$. The laminar boundary layer at this location is approximately 0.2 mm thick and the height of the trip was $k = 0.1$ mm ($k/\delta_{99} = 0.5$, $Re_k = U_\infty k/\nu_\infty = 3.5 \times 10^3$ or $Re_{kk} = U_k k/\nu_k = 1.4 \times 10^3$). For these conditions it is expected (Hicks and Harper (1970); Bernardini et al. (2014)), that transition sets in directly downstream of the trip, without substantially overtripping the boundary layer.

The devices were first tested in the absence of an impinging shock wave. It was found that the zig-zag strip and the patch of distributed roughness are most effective at tripping the boundary layer; a turbulent boundary layer was obtained approximately 6 mm ($\sim 30\delta_{95}$) downstream of the centreline of the device. The step also transitioned the boundary layer, but a longer streamwise distance of 11 mm ($\sim 55\delta_{95}$) was needed to reach a fully turbulent state. Based upon these results it was therefore decided to carry out the tests with the oblique shock wave positioned at 6 and 11 mm from the tripping device.

For the $x_{sh} - x_{trip} = 11$ mm case, all three tripping devices were able to eliminate the separation bubble in the interaction region. This was expected, since all trips yield a turbulent boundary layer 11 mm downstream of the trip, which for the current operating conditions does not separate when disturbed by a $\theta = 3^\circ$ shock wave. The differences were, however, more pronounced for a shock impingement location 6 mm downstream of the trip. For these conditions, a large separation bubble is recorded for the case of the step, whereas no separation is recorded for the distributed roughness case. This result confirms that under the present conditions it is more effective to apply a 3D type of trip instead of a 2D trip.

Although the shock-induced separation bubble present for the laminar interaction can effectively be removed by tripping the boundary layer a short distance upstream of the interaction, this does come at the price of having a substantially thicker ($\sim 50\%$) boundary layer downstream of the interaction ($x - x_{sh} = 10$ mm). It is expected that this is caused partially by losses at trip (e.g. wave drag, flow separation) and partially by the reduced wave and friction drag of the laminar SWBLI compared to the turbulent one. The tripped interaction shows a single reflected shock wave, whereas the laminar interaction shows a combination of compression and expansion waves, which results in lower entropy losses. Furthermore, for the laminar interaction, the boundary layer remains in a laminar state (i.e. low skin friction coefficient) up to the shock impingement location. The shock acts as an effective tripping device, triggering transition, which helps the boundary layer in overcoming the pressure rise towards reattachment. Furthermore given the fact that the laminar interaction shows no large-scale type of unsteadiness, it appears that tripping for this case mainly has a negative effect on the flow properties

downstream of the interaction.

10.2. FLOW CONTROL FOR TURBULENT OBLIQUE SHOCK WAVE REFLECTIONS

Micro-ramp vortex generators were studied in this PhD thesis as flow control devices for fully turbulent oblique shock wave reflections. A micro-ramp is a small ($\sim 0.5\delta_{99}$), triangular, wedge-type shaped of device that redistributes streamwise momentum throughout the boundary layer by the action of two counter-rotating streamwise vortices. The purpose of the device is to create a fuller boundary layer profile that is more capable of withstanding the adverse pressure gradient imposed by the shock system. In the introduction of this thesis the following questions were identified regarding the application of micro-ramps in supersonic flows:

1. How do micro-ramp height and location affect the size of the shock-induced separation bubble and the interaction unsteadiness?
2. What is the physical mechanism behind the (in)effectiveness of micro-ramp vortex generators?
3. How do the Mach and Reynolds number affect the flow mixing properties of micro-ramp vortex generators?

These questions were addressed by performing two PIV measurement campaigns; both of which were supported by oil-flow and schlieren visualizations. A correlation analysis was carried out on the velocity field data acquired inside and upstream of the shock-induced separation bubble. From this analysis it followed that the separation bubble is mostly sensitive to the momentum contained in the lower 43% of the incoming boundary layer. The momentum flux added to this region scales linearly with micro-ramp height and keeps increasing until $\sim 6\delta_{99}$ downstream of the ramp. After $\sim 6\delta_{99}$, a plateau is reached and virtually no extra momentum is added or removed. The mixing distance of $\sim 6\delta_{99}$ is found to be virtually independent of micro-ramp height, micro-ramp location, Mach number and Reynolds number within the investigated parameter space. Therefore, if the distance between the micro-ramp's trailing edge and the start of the interaction region is less than $\sim 6\delta_{99}$, full boundary layer mixing is not attained and reduced performance is recorded. Reduced performance in this context implies a larger separation bubble and a higher degree of reflected shock unsteadiness.

The size of the separation bubble was expressed in this study in terms of the average separated area, which is calculated by integrating the local reversed flow probability over the full measurement domain (e.g. a region of 10 mm^2 that shows reversed flow 50% of the time has an average separated area of 5 mm^2). The shock unsteadiness was calculated as the r.m.s. movement of the reflected shock wave at $y = 3.5\delta_{99}$ from the wall. The reflected shock wave is identified from the PIV images as the location where dV/dx reaches a maximum value and a least-squares fitting procedure is employed to accurately estimate the location of the shock wave at $y = 3.5\delta_{99}$.

However, even when positioned correctly, the micro-ramp is not able to completely remove the separation bubble. Instead the micro-ramp introduces a spanwise modulation in the separation bubble, with the strongest reduction in bubble size recorded along the micro-ramp's centreline. Typical reductions in the average separated area by 87% were recorded along the centerline of the micro-ramp ($h/\delta_{99} = 0.77$), whereas along the micro-ramp's spanwise edges the average separated area in the interaction was found to be 12% larger than for the uncontrolled case. The reflected shock unsteadiness on the other hand was found to be reduced over the entire span of the micro-ramp, by ~50% along the centreline and by ~36% at the edge of a $h/\delta = 0.77$ micro-ramp.

Most of the geometric flow features were found to scale linearly with micro-ramp height h : the wake height, wake strength, vortex core height and the momentum flux added to the near-wall region of the flow all increase linearly with h . Consequently, slightly better results (i.e. a smaller separation bubble, lower reflected shock unsteadiness) were typically recorded for the larger micro-ramps.

The control effectiveness of the micro-ramp in the symmetry plane is reduced for higher Mach numbers ($M_\infty > 2$) as the strength of the vortices (circulation Γ) is reduced, which adds less momentum to the near-wall region of the flow. Also a stronger wake is recorded for the higher Mach number cases. Only a weak Reynolds number effect was observed, with the micro-ramp becoming slightly more effective at higher Reynolds numbers.

Although this PhD thesis mostly focused on the control application of micro-ramp vortex generators, two noteworthy discoveries were also made regarding the flow topology induced by these devices:

1. Oil-flow visualizations have been a popular tool in the scientific community to study the surface flow topology of the micro-ramp vortex generator (Babinsky et al. (2009); Herges et al. (2009); Saad et al. (2012); Lu (2015)). Although very useful, special care must be taken when it comes to the interpretation of the oil-flow patterns. A horseshoe type of feature can be identified from the oil-flow visualizations when the oil is applied both upstream and downstream of the micro-ramp. That is because, the oil upstream of the micro-ramp is pushed around the edges of the ramp (converging skin friction lines) and continues to trail downstream as long as the wind tunnel is running, therefore creating long streaks which closely resemble a horseshoe vortex. If the oil is only applied downstream of the micro-ramp's leading edge, then no horseshoe vortex is recorded in the results. This implies that the horseshoe vortex is either non-existent or a very weak (non-detectable) feature of the flow field for the Anderson et al. (2006) type of micro-ramp when tested in a $M = 2$ supersonic turbulent boundary layer.

On pure topological grounds (Tobak and Peake (1982)) one would expect the formation of a horseshoe vortex when the incoming boundary layer separates at the leading edge of the micro-ramp. Boundary layer separation is, however, hard to detect for the small sub-boundary layer micro-ramps that were tested in this and other studies. It was therefore decided to also test a set of adjusted micro-ramps for which the flow deflection angle at the leading edge was increased from $\theta = 8.6^\circ$ for the Anderson type of micro-ramp upto $\theta = 13.0, 17.3$ and 21.6° , while keeping

the height of the micro-ramp constant. For the largest flow deflection angles, it appears that a small separation bubble is formed upstream of the micro-ramp. However, still no horseshoe vortex is detected in the oil-flow visualizations, whereas it should exist if separation occurs at the leading edge of the micro-ramp. This result again shows that the horseshoe vortex is a very weak feature of the flow, which probably dissipates quickly downstream of the micro-ramp, even for large ramp angles.

2. Spark-light schlieren visualizations were used for the first time to study the development of Kelvin-Helmholtz vortices on the upper shear layer of the low-momentum wake downstream of a micro-ramp. From a POD and correlation analysis it appears that the K-H instabilities are amplified over a distance of $\sim 6h$, directly downstream of the micro-ramp. After this initial stage, saturation occurs which is probably linked to the process of vortex roll-up. The initiated K-H vortices are convected with the flow and display a near-linear growth in wavelength in the region from $x = 5h - 20h$, where λ increases from $1.2h$ to $2.0h$.

11

RECOMMENDATIONS

11.1. THE UNSTEADINESS OF LAMINAR OBLIQUE SHOCK WAVE REFLECTIONS

The unsteadiness of laminar oblique shock wave reflections was investigated in this thesis by means of particle image velocimetry. However, due to the extremely thin laminar boundary layer (~ 0.2 mm) and the limited response time of the tracer particles ($\tau_p \sim 2.5 \mu\text{s}$), it was not possible to accurately measure velocity fluctuations inside the boundary layer and the interaction region. Some information on the unsteadiness of the interaction could, however, still be inferred from the movement of the compression waves generated at the interaction onset. From this analysis it was found that the separation location fluctuates by $\sim 0.27L_{sep}$ (r.m.s.) for a laminar interaction at $M_\infty = 1.7$, $Re_{x_{sh}} = 1.8 \times 10^6$ and $\theta = 5^\circ$, where L_{sep} defines the distance between the interaction onset and boundary layer separation location. The measured velocity fluctuations were, however, close to the noise floor of the PIV measurements and the recorded uncertainties should therefore only be considered as a conservative upper bound on the unsteadiness of the compression waves and separation location.

It would therefore be useful to re-evaluate the unsteadiness of the separation point by means of hot wire anemometry measurements. It is suggested by the author to position the hot wire a small distance (~ 2 mm) above the wall, within the region of compression waves generated at the interaction onset. If the separation point is unsteady, then this should translate into an equivalent oscillatory movement of the front of compression waves. The hot wire would have to be operated at a high overheat ratio ($a_w > 0.9$) to make sure that the wire is mostly sensitive to fluctuations in the mass flux $(\rho u)'$. The resulting spectrum could be compared with the spectrum obtained for freestream tunnel conditions (see section 3.1), the respective differences in spectra could then be attributed to the unsteadiness of the laminar oblique shock wave reflection.

From the mass flux spectrum one could, in principle, also derive the oscillation amplitude of the boundary layer's separation point. The free-interaction theory (see section 5.2.3) could be used to make the conversion between fluctuations in $(\rho u)'$ and the fluctu-

tuations of the separation point. This approach only works well if the location of the hot wire probe with respect to the mean separation location (both horizontally and vertically) is known with good accuracy. The vertical distance may change when starting the tunnel, because of the forces acting on the models / hot wire sting. It would therefore be recommendable to have a camera recording the distance between the plate and hot wire probe during the wind tunnel run. The horizontal distance between the separation point and the hot wire probe is difficult to measure directly, but could be inferred from a translation of the hot wire probe in the streamwise direction. The correlation function F (see Fig.5.20) could be fitted to this data, as such delivering a reasonable estimate of the separation location.

11.2. A SYNTHESIS OF ALL FLAT PLATE TFAST DATA

The measurements on laminar oblique shock wave reflections were carried out within the collaborative framework of TFAST (as part of the European FP7 program), which investigates the effects of boundary layer transition on a shock wave-boundary layer interaction. Several test cases were considered within the project, ranging from fundamental flat plate interactions (normal / oblique SWBLIs) to SWBLIs on more complex geometries, such as compressor / turbine cascades and on transonic wings.

Within the scope of this project, data was acquired for a wide range of tunnel operating conditions (Mach number, Reynolds number, shock strengths and freestream turbulence levels) with an equally wide range of experimental / numerical techniques (pressure measurements, particle image velocimetry, large eddy simulations and several more). It would be of great interest to both the scientific and industrial community to compare the fundamental flat plate cases with each other and analyse the relevant trends in the data. In particular, it would be useful to study the dependency of the separation bubble size and the transition location on the freestream turbulence level of the tunnel. Such a comparison could lead to a further generalization of the conclusions presented in section 10.1.

11.3. KELVIN-HELMHOLTZ VORTEX FORMATION DOWNSTREAM OF MICRO-RAMPS

Spark-light schlieren visualizations were used in section 7.2 of this thesis to study the development of Kelvin-Helmholtz vortices on the shear layer of the micro-ramp's low-momentum wake. POD and correlation analyses were applied to the raw Schlieren visualizations to extract both the shape and wavelength development of the K-H vortices. The results were found to be in excellent agreement with the (TOMO)-PIV measurements of Sun et al. (2014). The work Sun et al. (2014) also predicts the occurrence of vortex pairing approximately $20 - 24h$ downstream of the micro-ramp. The measurement domain for the current exploratory schlieren study was, however, limited to $x = 21h$. It was therefore not possible to confirm or reject the occurrence of K-H vortex pairing from the current dataset.

Given the good results obtained in this exploratory study it would be of interest to repeat the measurements of section 7.2 for a smaller micro-ramp, for instance $h = 4$

mm, instead of the $h = 8$ mm micro-ramp used in the current study. The measurement domain would then measure $\sim 42h$, which would be large enough to capture the process of vortex pairing and maybe also the formation of K-H ring vortices observed in the numerical work of Li and Liu (2010). Also given the relative simplicity of spark-light Schlieren visualization, it would be of interest to test the micro-ramp at a range of Mach and Reynolds numbers. Such a database could be useful for the validation of, for instance, stability codes.

11.4. A 3D VISUALIZATION OF A MICRO-RAMP CONTROLLED INTERACTION

The planar PIV measurements of chapter 8 revealed that the interaction region downstream of the micro-ramp is highly three-dimensional. The micro-ramp induces a spanwise modulation in the mean shape of the separation bubble, with the micro-ramp being most effective along its centreline. In fact, the average separated area at a plane aligned with the edge of the micro-ramp was recorded to be 12% larger than that recorded for the uncontrolled shock wave-boundary layer interaction. It is therefore not yet entirely clear if the total volume of separated flow increases or decreases by the use of micro-ramp vortex generators. Tomographic PIV measurements in a volume spanning at least the entire width of the micro-ramp could help to answer this question. Such measurements would also be useful when investigating the unsteadiness of the reflected shock wave. Micro-ramps are known for having a stabilizing effect on the reflected shock wave (see section 8.2.2) and tomographic PIV measurements would allow for a study into the dynamics of the reflected shock wave. Is the reflected shock wave for instance oscillating as one front, or is its behaviour decoupled left and right of the micro-ramp's centreline?

11.5. TOTAL PRESSURE MEASUREMENTS OF A MICRO-RAMP CONTROLLED INTERACTION

If micro-ramps are to be installed in a supersonic jet intake, then an important output parameter is the total pressure recovery over the shock system. A smaller separation bubble will, in general, result in lower viscous losses and thus lower total pressure losses. However, as discussed in section 1.5, total pressure losses are also introduced by the low-momentum wake of the micro-ramp. A large separation bubble furthermore leads to a smearing of the reflected shock wave and thus lower entropy / total pressure losses. It is therefore difficult to gauge the net effect of micro-ramp vortex generators on the total pressure recovery over a shock system by purely analysing PIV results. It would therefore be useful to install a rake with pitot tubes downstream of the interaction and measure the total pressure recovery directly, with and without the presence of a micro-ramp.

11.6. VARIATIONS ON THE MICRO-RAMP GEOMETRY

The micro-ramp geometry that was used in this PhD thesis is based upon the work of Anderson et al. (2006), who performed Reynolds-averaged Navier Stokes (RANS) simulations for a range of micro-ramp geometries. They found that micro-ramps with an angle

$A_p = 24^\circ$ and chord length $c = 7.2h$ (see Fig.7.4) are optimal in the sense that they deliver a downstream boundary layer with the lowest incompressible shape factor. Their recommendations formed the basis for many publications in this field and were also used throughout this PhD thesis.

Lee et al. (2010) studied the flow field downstream of the Anderson et al. (2006) type of micro-ramp by means of RANS simulations, large eddy simulations (LES) and pitot probe measurements. The LES data was, in general, in good agreement with the experimental data, whereas the RANS data was typically much further off. Especially the fullness of the velocity profile was underpredicted by the RANS simulations.

Since the optimization study of Anderson et al. (2006) was based upon RANS simulations, one may put into doubt the optimality of the currently 'accepted' micro-ramp geometry. It would therefore be interesting to perform a similar optimization study by means of wind tunnel experiments. Such an experimental campaign should involve total pressure measurements downstream of the shock interaction and ideally also some particle image velocimetry measurements directly downstream of the micro-ramp and inside the interaction zone. The important output variables here are the total pressure recovery over the shock system, the flow non-uniformity downstream of the interaction, the interaction unsteadiness and the size of the separation bubble. It would be interesting to also include some 'ramped vanes' in this study. Ramped vanes (Lee et al. (2011)) are a split-type of micro-ramp, which combines the micro-ramp's robust design with the good mixing properties of micro-vanes.

A

PIV WALL TREATMENT

Three modifications are made with respect to standard iterative image deformation analysis (Scarano and Riethmuller (2000)) in order to improve the accuracy and resolution near the wall. Many of these modifications were inspired by the work of Theunissen et al. (2008), but adapted for use with structured (rather than unstructured) grids and with interrogation window weighting functions which are now standard practice in PIV (Astarita (2007)).

The first modification is an imposed zero-velocity boundary condition which is applied during predictor-corrector iterations. At the beginning of each iteration, grid points are identified which lie fully within a defined mask. All components of the predictor are set to zero at these gridpoints. This constrains the magnitude of image deformation near the wall and is also physically consistent with the no-slip condition expected at the wall. This reduces the formation of outliers near and at the wall as also reported by Theunissen et al. (2008).

The second modification is a window weighting function which adapts to the wall. A mask window M equal to the size of the interrogation window is defined, set to 0 inside of the wall (masked) and 1 outside of the wall (unmasked). The window weighting function W is calculated as a Gaussian with parameters set by the first and second moments of the mask distribution (for x , also identical for y),

$$\mu_x = \frac{\sum_i M_i \cdot x_i}{\sum_i M_i} \quad (\text{A.1})$$

$$\sigma_x = \sqrt{\frac{\sum_i M_i \cdot (x_i - \mu_x)^2}{\sum_i M_i}} \quad (\text{A.2})$$

$$W(x, y) = e^{-\left(\frac{(x_i - \mu_x)^2}{2c\sigma_x^2} + \frac{(y_i - \mu_y)^2}{2c\sigma_y^2}\right)} \quad (\text{A.3})$$

Parts of this appendix have been presented at the 17th International Symposium on Application of Laser Techniques to Fluid Mechanics (Giepmans et al. (2014a)).

where x_i is the pixel coordinate corresponding to pixel with linear index i , and c is a coefficient specified to shrink/grow the Gaussian accordingly. This is set $c = 0.5$ for all calculations which corresponds well to a Gaussian of $\alpha = 2.5$ (Astarita (2007)). An example of window M , weighting function W , and correlation plane are given in Fig.A.1 using a reference uniform weighting window and the adapted Gaussian window. This corresponds to experimental data in the turbulent region with a reduced set of 5 image pairs used for the ensemble correlation.

A comparison between the two correlation planes shows a far greater signal peak for the adapted Gaussian window due to the reduction in signal truncation effects caused by the interface region as noted by Theunissen et al. (2008). In contrast to their work which focused on reduction of signal truncation by using direct correlation, the current work is applied directly to existing FFT correlation analysis. Furthermore, no Fourier-domain filtering (i.e., symmetric phase-only filtering, SPOF; Wernet (2005)) is required. As a final note, the current technique is similar to the non-isotropic PIV analysis technique (Scarano (2003)), but applied near the wall and using the distance from the wall as the window adaptive parameter rather than the velocity gradient tensor.

The final modification is vector relocation, originally proposed by Usera et al. (2004) and Theunissen et al. (2008), which positions the resulting velocity vector which is nominally defined at the array center of the window to the window centroid position (see equation A.1). This is performed as the final step in the processing, where the final predictor is evaluated at the window centroid position, and the corrector is added to this value. Non-uniform grid interpolation in the image deformation is therefore avoided.

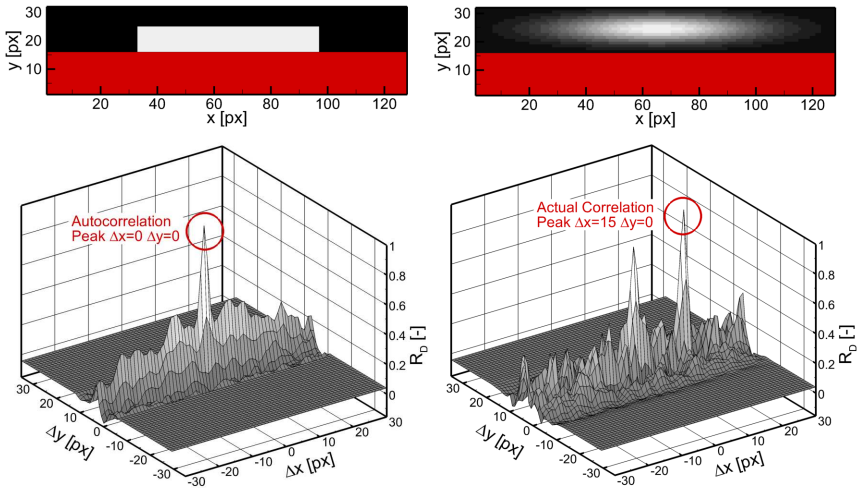


Figure A.1: Comparison of masked uniform weighting window (left column) and adaptive Gaussian weighting (right column). First row, weighting function W with mask M outlined in red; second row, associated correlation planes.

REFERENCES

- Anderson, B., Tinapple, J., and Surber, L. (2006). Optimal Control of Shock Wave Turbulent Boundary Layer Interactions Using Micro-Array Actuation. In *3rd AIAA Flow Control Conference*, San Francisco, California. AIAA 2006-3197.
- Anderson, J. (1999). *A History of Aerodynamics: And Its Impact on Flying Machines*. Cambridge University Press, Cambridge.
- Ashill, P., Fulker, J., and Hackett, K. (2001). Research at DERA on Sub Boundary Layer Vortex Generators (SBVGs). In *39th Aerospace Sciences Meeting and Exhibit*, Reno, Nevada. AIAA 2001-0887.
- Ashill, P., Fulker, J., and Hackett, K. (2005). A Review of Recent Developments in Flow Control. *Aeronautical Journal*, 109(1095):205–232.
- Astarita, T. (2007). Analysis of weighting windows for image deformation methods in PIV. *Experiments in Fluids*, 43(6):859–872.
- Auton, T. (1987). The lift force on a spherical body in a rotational flow. *J. Fluid Mechanics*, 183:199–218.
- Babinsky, H. and Harvey, J. (2011). *Shock Wave-Boundary-Layer Interactions*. Cambridge University Press, Cambridge.
- Babinsky, H., Li, Y., and Pitt Ford, C. (2009). Microramp Control of Supersonic Oblique Shock-Wave/Boundary-Layer Interactions. *AIAA Journal*, 47(3):668–675.
- Berkooz, G., Holmes, P., and Lumley, J. (1993). The proper orthogonal decomposition in the analysis of turbulent flows. *Annu. Rev. Fluid Mech.*, 25:539–575.
- Bernardini, M., Pirozzoli, S., Orlandi, P., and Lele, S. (2014). Parameterization of Boundary-Layer Transition Induced by Isolated Roughness Elements. *AIAA Journal*, 52(10):2261–2269.
- Blinde, P., Humble, R., van Oudheusden, B., and Scarano, F. (2009). Effects of micro-ramps on a shock wave/turbulent boundary layer interaction. *Shock Waves*, 19(6):507–520.
- Brown, L. and Naughton, W. (1999). *The Thin Oil Film Equation*. NASA/TM-1999-208767.
- Bruun, H. (1995). *Hot-Wire Anemometry: Principles and Signal Analysis*. Oxford University Press, Oxford.

- Caldwell, F and Fales, E. (1921). *Wind tunnel studies in aerodynamic phenomena at high speed*. NACA report 83.
- Chapman, D., Kuehn, D., and Larson, H. (1957). Investigation of separated flows in supersonic and subsonic streams with emphasis on the effect of transition. NACA report no 1356, NACA report 1356.
- Clemens, N. and Narayanaswamy, V. (2014). Low-Frequency Unsteadiness of Shock Wave/Turbulent Boundary Layer Interactions. *Annual Review of Fluid Mechanics*, 46(1):469–492.
- Coles, D. (1956). The law of the wake in the turbulent boundary layer. *J. Fluid Mechanics*, 1:191–226.
- Cook, W. and Felderman, E. (1966). Reduction of data from thin-film heat-transfer gages - A concise numerical technique. *AIAA Journal*, 4(3):561–562.
- Cousteix, J. (1989). *Aérodynamique turbulence et couche limite*. Cépaduès.
- Davidson, T. and Babinsky, H. (2015). Transition location effects on normal shock wave - boundary layer interactions. In *53rd AIAA Aerospace Sciences Meeting*, Kissimmee, Florida. AIAA 2015-1975.
- Délery, J. and Bur, R. (2000). The physics of shock wave / boundary layer interaction control: last lessons learned. In *ECCOMAS*, Barcelona, Spain.
- Delery, J. and Marvin, J. (1986). *Shock-Wave Boundary Layer Interactions*. AGARDograph No. 280.
- Dewey, C. (1965). A correlation of convective heat transfer and recovery temperature data for cylinders in compressible flow. *Int. J. Heat Mass Transf*, 8.
- Dhawan, S. and Narasimha, R. (1958). Some properties of boundary layer flow during the transition from laminar to turbulent motion. *Journal of Fluid Mechanics*, 3(4):418–436.
- Dolling, D. (2001). Fifty Years of Shock-Wave/Boundary-Layer Interaction Research: What Next? *AIAA Journal*, 39(8):1517–1531.
- Duan, L., Choudhari, M., and Wu, M. (2014). Numerical study of acoustic radiation due to a supersonic turbulent boundary layer. *Journal of Fluid Mechanics*, 746:165–192.
- Dussauge, J., Dupont, P., and Debiève, J. (2006). Unsteadiness in shock wave boundary layer interactions with separation. *Aerospace Science and Technology*, 10(2):85–91.
- Eckert, E. (1955). Engineering relations for friction and heat transfer to surfaces in high velocity flow. *Journal of Aeronautical Sciences*, 22:585–587.
- Elena, M. and Lacharme, J. (1988). Experimental study of a supersonic turbulent boundary layer using a laser Doppler anemometer. *Journal de mécanique théorique et appliquée*, 7(2):175–190.

- Elsinga, G., van Oudheusden, B., and Scarano, F. (2005a). Evaluation of aero-optical distortion effects in PIV. *Experiments in Fluids*, 39(2):246–256.
- Elsinga, G., Van Oudheusden, B., and Scarano, F. (2005b). The effect of particle image blur on the correlation map and velocity measurement in PIV. In Hanssen, L. M. and Farrell, P. V., editors, *SPIE*, volume 5880.
- Elsinga, G., van Oudheusden, B., Scarano, F., and Watt, D. (2003). Assessment and application of quantitative schlieren methods: Calibrated color schlieren and background oriented schlieren. *Experiments in Fluids*, 36(2):309–325.
- Erdos, J. and Pallone, A. (1963). Shock-boundary layer interaction and flow separations. In *Proceedings of the 1962 Heat Transfer and Fluid Mechanics Institute*.
- Erengil, M. and Dolling, D. (1993). Physical causes of separation shock unsteadiness in shock wave turbulent boundary layer interactions. In *AIAA Fluid Dynamics Conference*, Orlando, Florida. AIAA 1993-3134.
- Fernholz, H. and Finley, P. (1980). *A Critical Commentary on Mean Flow Data for Two-Dimensional Compressible Turbulent Boundary Layers*. AGARDograph 253.
- Florentie, L. (2015). Efficient CFD simulations of vortex generator induced flow phenomena. In *Woudschoten Conference*, Zeist, Netherlands.
- Gad-el Hak, M. (2000). *Flow control - Passive, active and reactive flow management*. Cambridge University Press, Cambridge.
- Gadd, G., Holder, D., and Regan, J. (1954). An Experimental Investigation of the Interaction between Shock Waves and Boundary Layers. *Proc. R. Soc. Lond. A*, 226(1165):227–253.
- Galbraith, M., Orkwis, P., and Benek, J. (2009). Multi-Row Micro-Ramp Actuators for Shock Wave Boundary-Layer Interaction Control. In *47th AIAA Aerospace Sciences Meeting*, number January, pages 1–30, Orlando, Florida. AIAA 2009-321.
- Ganapathisubramani, B., Clemens, N., and Dolling, D. (2007). Effects of upstream boundary layer on the unsteadiness of shock-induced separation. *Journal of Fluid Mechanics*, 585:369–394.
- Ghosh, S., Choi, J., and Edwards, J. (2010). Numerical Simulations of Effects of Micro Vortex Generators Using Immersed-Boundary Methods. *AIAA Journal*, 48(1):92–103.
- Giepman, R., De Giovanni, G., Schrijer, F., and Van Oudheusden, B. (2012). Experimental investigation into the effects of micro-ramps on the separation bubble of shock wave / boundary layer interactions. In *20th International Shock Interaction Symposium*, Stockholm, Sweden.
- Giepman, R., Louman, R., Schrijer, F., and Van Oudheusden, B. (2015a). Experimental investigation of boundary layer tripping devices for shock wave-boundary layer control. In *45th AIAA Fluid Dynamics Conference*, Dallas, Texas. AIAA 2015-2780.

- Giepmans, R., Lynch, K., Schrijer, F., and Van Oudheusden, B. (2014a). Investigation of a transitional oblique shock wave reflection using PIV. In *17th International Symposium on Application of Laser Techniques to Fluid Mechanics*, Lisbon, Portugal.
- Giepmans, R., Schrijer, F., and Van Oudheusden, B. (2013). Flow control of an oblique shock wave reflection with micro-ramp vortex generators: Effects of location and size. In *European Conference for Aeronautics and Space Sciences (EUCASS)*, Munich, Germany.
- Giepmans, R., Schrijer, F., and van Oudheusden, B. (2014b). Flow control of an oblique shock wave reflection with micro-ramp vortex generators: Effects of location and size. *Physics of Fluids*, 26(6):066101.
- Giepmans, R., Schrijer, F., and Van Oudheusden, B. (2014c). High-resolution PIV measurements of a transitional shock wave-boundary layer interaction. In *44th AIAA Fluid Dynamics Conference*, Atlanta, Georgia. AIAA 2014-3333.
- Giepmans, R., Schrijer, F., and Van Oudheusden, B. (2014d). Tracking a moving boundary layer transition front in supersonic flow using infrared thermography. In *12th International Conference on Quantitative Infrared Thermography*, Bordeaux, France.
- Giepmans, R., Schrijer, F., and Van Oudheusden, B. (2015b). High-resolution PIV measurements of a transitional shock wave-boundary layer interaction. *Experiments in Fluids*, 56(6):113.
- Giepmans, R., Schrijer, F., and Van Oudheusden, B. (2015c). Infrared Thermography Measurements on a Moving Boundary-Layer Transition Front in Supersonic Flow. *AIAA Journal*, 53(7).
- Giepmans, R., Srivastava, A., Schrijer, F., and Van Oudheusden, B. (2015d). The effects of Mach and Reynolds number on the flow mixing properties of micro-ramp vortex generators in a supersonic boundary layer. In *45th AIAA Fluid Dynamics Conference*, Dallas, Texas. AIAA 2015-2779.
- Graham, C. and Kost, F. (1979). Shock Boundary Layer Interaction on High Turning Transonic Turbine Cascades. In *ASME International Gas Turbine Conference and Exhibit and Solar Energy Conference*, San Diego, California, USA.
- Groot, K., Pinna, E., and van Oudheusden, B. (2014). On closing the streamwise BiGlobal stability problem: the effect of boundary conditions. In *IUTAM-ABCM Symposium on Laminar-Turbulent Transition*, Rio de Janeiro, Brazil.
- Hakkinen, R., Greber, I., Trilling, L., and Abarbanel, S. (1959). *The interaction of an oblique shock wave with a laminar boundary layer*. NASA Memo 2-18-59W.
- Henderson, L. (1967). The reflexion of a shock wave at a rigid wall in the presence of a boundary layer. *J. Fluid Mechanics*, 30(4):699-722.

- Herges, T., Kroeker, E., Elliott, G., and Dutton, C. (2009). Micro-Ramp Flow Control of Normal Shock/Boundary Layer Interactions. In *47th AIAA Aerospace Sciences Meeting*, Orlando, Florida. AIAA 2009-920.
- Herges, T., Kroeker, E., Elliott, G., and Dutton, C. (2010). Microramp Flow Control of Normal Shock/Boundary-Layer Interactions. *AIAA Journal*, 48(11):2529–2542.
- Hicks, R. and Harper, W. (1970). *A comparison of spherical and triangular boundary-layer trips on a flat plate at supersonic speeds*. NASA TM X-2146.
- Higgins, R. and Pappas, C. (1951). *An experimental investigation of the effect of surface heating on boundary-layer transition on a flat plate in supersonic flow*. NACA TN2351.
- Hugoniot, P. (1887). Mémoire sur la propagation du mouvement dans les corps et plus spécialement dans les gaz parfaits, 1e Partie. *J. École Polytech*, 57:3–97.
- Hultmark, M., Ashok, A., and Smits, A. (2011). A new criterion for end-conduction effects in hot-wire anemometry. *Measurement Science and Technology*, 22(5):055401.
- Humble, R., Elsinga, G., Scarano, F., and Van Oudheusden, B. (2009). Three-dimensional instantaneous structure of a shock wave/turbulent boundary layer interaction. *Journal of Fluid Mechanics*, 622:33.
- Humble, R., Scarano, F., and Van Oudheusden, B. (2007). Particle image velocimetry measurements of a shock wave/turbulent boundary layer interaction. *Experiments in Fluids*, 43(2-3):173–183.
- Illingworth, C. (1950). Some solutions of the equations of flow of a viscous compressible fluid. *Proc. Cambridge Philos. Soc.*, 46:469–478.
- Janke, E. and Wolf, T. (2010). Aerothermal Research for Turbine Components: An Overview of the European AITEB-2 Project. In *ASME Turbo Expo 2010: Power for Land, Sea, and Air*, Glasgow, UK.
- Jones, J. (1955). *The calculation of the paths of vortices from a system of vortex generators, and a comparison with experiment*. ARC 361.
- Katzer, E. (1989). On the lengthscales of laminar shock/boundary- layer interaction. *J. Fluid Mechanics*, 206:477–496.
- Kendall, D., Dixon, P., and Schulte, E. (1967). Semiconductor Surface Thermocouples for Determining Heat-Transfer Rates. *IEEE Transactions on Aerospace and Electronic Systems*, AES-3(4):596–603.
- Kistler, A. (1964). Fluctuating wall pressure under a separated supersonic flow. *J. Fluid Mechanics*, 36(3):543–550.
- Klebanoff, P. (1955). *Characteristics of Turbulence in a Boundary Layer with Zero Pressure Gradient*. NACA Report 1247.

- Kuehn, D. (1959). *Experimental investigation of the pressure rise required for the incipient separation of turbulent boundary layers in two-dimensional supersonic flow*. NASA Memo 1-21-59A.
- Laplace, P. (1816). Sur la vitesse du son dans l'aire et dans l'eau. *Annales de Chimie et de Physique*, 3:238–241.
- Laufer, J. (1961). Aerodynamic noise in supersonic wind tunnels. *J. Aerospace Sciences*, 28(9):685–692.
- Laufer, J. (1964). Some Statistical Properties of the Pressure Field Radiated by a Turbulent Boundary Layer. *Physics of Fluids*, 7(8):1191.
- Le Balleur, J. and Déleroy, J. (1973). Etude expérimentale de l'effet de la réflexion d'une onde de choc sur la transition de la couche limite. In *Congrès Français de Mécanique*, Poitiers, France.
- Lee, S., Goettke, M., Loth, E., Tinapple, J., and Benek, J. (2010). Microramps Upstream of an Oblique-Shock/Boundary-Layer Interaction. *AIAA Journal*, 48(1):104–118.
- Lee, S., Loth, E., and Babinsky, H. (2011). Normal shock boundary layer control with various vortex generator geometries. *Computers & Fluids*, 49(1):233–246.
- Lee, S., Loth, E., Georgiadis, N., and Debonis, J. (2009). Effect of Mach number on Flow Past Micro-Ramps. In *39th AIAA Fluid Dynamics Conference*, San Antonio, Texas. AIAA 2009-4181.
- Lees, L. and Reeves, B. (1964). Supersonic separated and reattaching laminar flows: I. General theory and application to adiabatic boundary-layer/shock-wave interactions. *AIAA Journal*, 2:1907–1920.
- Li, Q. and Liu, C. (2010). LES for Supersonic Ramp Control Flow Using MVG at $M=2.5$ and $Re\theta = 1440$. In *AIAA Aerospace Sciences Meeting*, Orlando, Florida. AIAA 2010-592.
- Liepmann, H. and Roshko, A. (1957). *Elements of Gasdynamics*. John Wiley & Sons.
- Lin, J. (2002). Review of research on low-profile vortex generators to control boundary-layer separation. *Progress in Aerospace Sciences*, 38(4-5):389–420.
- Lu, F. (2015). Visualization of supersonic flow around a sharp-edged, sub-boundary-layer protuberance. *Journal of Visualization*.
- Lu, F., Li, Q., and Liu, C. (2012). Microvortex generators in high-speed flow. *Progress in Aerospace Sciences*, 53:30–45.
- Lu, F., Li, Q., Shih, Y., Pierce, A., and Liu, C. (2011). Review of Micro Vortex Generators in High-Speed Flow. In *49th AIAA Aerospace Sciences Meeting*. AIAA 2011-31.
- Mach, E. (1887). Photographische Fixierung der durch Projektile in der Luft eingeleiteten Vorgänge. In *Akademie der Künsten under der Wissenschaft, Vienna*, volume 95.

- Mack, L. (1975). Linear Stability Theory and the Problem of Supersonic Boundary-Layer Transition. *AIAA Journal*, 13(3):278–289.
- Mayer, R. (2000). *Wall-shear stress measurements with quantitative infrared thermography*. PhD thesis, Delft University of Technology.
- McCormick, D. (1993). Shock/Boundary-Layer Interaction Control with Vortex Generators and Passive Cavity. *AIAA Journal*, 31(1):91–96.
- Meinhart, C., Wereley, S., and Santiago, J. (2000). A PIV Algorithm for Estimating Time-Averaged Velocity Fields. *Journal of Fluids Engineering*, 122(June):285–289.
- Melling, A. (1997). Tracer particles and seeding for particle image velocimetry. *Meas Sci Technol*, 8:1406–1416.
- Merzkirch, W. (1987). *Flow visualization*. Academic Press, New York.
- Meunier, P. and Leweke, T. (2003). Analysis and treatment of errors due to high velocity gradients in particle image velocimetry. *Experiments in Fluids*, 35(5):408–421.
- Morkovin, M. (1956). *Fluctuations and hot-wire anemometry in compressible flows*, volume 24. AGARDograph 24.
- Narasimha, R. (1957). On the distribution of intermittency in the transition region of a boundary layer. *Journal of Aeronautical Sciences*, 24:711–712.
- Nolan, W. and Babinsky, H. (2011). Characterization of Micro-Vortex Generators in Supersonic Flows. In *49th AIAA Aerospace Sciences Meeting*, Orlando, Florida.
- Nolan, W. and Babinsky, H. (2012). Comparison of Micro-Vortex Generators in Supersonic Flows. In *6th AIAA Flow Control Conference*, New Orleans, Louisiana.
- Özisik, M. and Orlande, H. (2000). *Inverse Heat Transfer – Fundamentals and Applications*. Taylor & Francis, New York.
- Panaras, A. and Lu, F. (2015). Micro-vortex generators for shock wave/boundary layer interactions. *Progress in Aerospace Sciences*, 74:16–47.
- Piponniau, S., Dussauge, J., Debiève, J., and Dupont, P. (2009). A simple model for low-frequency unsteadiness in shock-induced separation. *Journal of Fluid Mechanics*, 629:87.
- Priebe, S. and Martin, M. (2012). Low-frequency unsteadiness in shock wave–turbulent boundary layer interaction. *Journal of Fluid Mechanics*, 699:1–49.
- Raffel, M. and Kost, F. (1998). Investigation of aerodynamic effects of coolant ejection at the trailing edge of a turbine blade model by PIV and pressure measurements. *Experiments in Fluids*, 24:447–461.
- Raffel, M., Willert, C., Wereley, S., and Kompenhans, J. (2007). *Particle image velocimetry - A practical guide*. Springer-Verlag, Berlin.

- Ragni, D., Schrijer, F., Van Oudheusden, B., and Scarano, F. (2010). Particle tracer response across shocks measured by PIV. *Experiments in Fluids*, 50(1):53–64.
- Rankine, W. (1870). On the thermodynamic theory of waves of finite longitudinal disturbances. *Phil. Trans. Roy. Soc. London*, 160:277–286.
- Reyhner, T. and Flügge-Lotz, I. (1968). The interaction of a shock wave with a laminar boundary layer. *J. Non-Linear Mechanics*, 3(2):173–199.
- Rizzeta, D., Burggraf, O., and Jenson, R. (1978). Triple-deck solutions for viscous supersonic and hypersonic flow past corners. *Journal of Fluid Mechanics*, 89(3):535–552.
- Robinet, J. (2007). Bifurcations in shock-wave/laminar-boundary-layer interaction: global instability approach. *Journal of Fluid Mechanics*, 579:85–112.
- Saad, M., Zare-Behtash, H., Che-Idris, A., and Kontis, K. (2012). Micro-Ramps for Hypersonic Flow Control. *Micromachines*, 3(4):364–378.
- Samimy, M. and Lele, S. (1991). Motion of particles with inertia in a compressible free shear layer. *Physics of Fluids A: Fluid Dynamics*, 3(8):1915–1923.
- Sansica, A., Sandham, N., and Hu, Z. (2014). Forced response of a laminar shock-induced separation bubble. *Physics of Fluids*, 26(9):093601.
- Saric, W., Reed, H., and Kerschen, E. (2002). Boundary-layer receptivity to freestream disturbances. *Annu. Rev. Fluid Mech.*, 34:291–319.
- Scarano, F. (2003). Theory of non-isotropic spatial resolution in PIV. *Experiments in Fluids*, 35(3):268–277.
- Scarano, F. and Riethmüller, M. (2000). Advances in iterative multigrid PIV image processing. *Experiments in Fluids*, 29(7):S051–S060.
- Scharnowski, S., Hain, R., and Kähler, C. (2011). Reynolds stress estimation up to single-pixel resolution using PIV-measurements. *Experiments in Fluids*, 52(4):985–1002.
- Schlichting, H. and Gersten, K. (2000). *Boundary-layer theory*. Springer, Berlin, 8th edition.
- Schoenherr, K. (1932). Resistance of plates. *Trans. Soc. Nav. Architects Mar. Eng.*, 40.
- Schrijer, F. (2010). Investigation of Görtler vortices in a hypersonic double compression ramp flow by means of infrared thermography. *Quantitative InfraRed Thermography Journal*, 7(2).
- Schrijer, F. F. J. and Scarano, F. (2008). Effect of predictor–corrector filtering on the stability and spatial resolution of iterative PIV interrogation. *Experiments in Fluids*, 45(5):927–941.
- Smits, J., Hayakawa, K., and Muck, K. (1983). Constant Temperature Hot-wire Anemometer Practice in Supersonic Flows - Part 1: The Normal Wire. *Experiments in Fluids*, 1(2):83–92.

- Souverein, L. (2010). *On the scaling and unsteadiness of shock induced separation*. PhD thesis, Delft University of Technology.
- Souverein, L., Dupont, P., Debieve, J., Dussauge, J., and Van Oudheusden, B.W. Scarano, F. (2010). Effect of interaction strength on unsteadiness in turbulent shock-wave induced separations. *AIAA Journal*, 48:1480–1493.
- Spalding, D. and Chi, S. (1964). The drag of a compressible turbulent boundary layer on a smooth flat plate with and without heat transfer. *Journal of Fluid Mechanics*, 18:117–143.
- Squire, L. (1961). The motion of a thin oil sheet under the steady boundary layer on a body. *Journal of Fluid Mechanics*, 11(2):161–179.
- Stack, J. (1933). *The N.A.C.A. high-speed wind tunnel and tests of six propeller sections*. NACA TR 463.
- Sun, Z., Schrijer, F., Scarano, F., and van Oudheusden, B. (2012). The three-dimensional flow organization past a micro-ramp in a supersonic boundary layer. *Physics of Fluids*, 24:1–22.
- Sun, Z., Schrijer, F., Scarano, F., and van Oudheusden, B. (2014). Decay of the supersonic turbulent wakes from micro-ramps. *Physics of Fluids*, 26(2):025115.
- Theunissen, R., Scarano, F., and Riethmuller, M. (2008). On improvement of PIV image interrogation near stationary interfaces. *Experiments in Fluids*, 45(4):557–572.
- Titchener, N. and Babinsky, H. (2015). A review of the use of vortex generators for mitigating shock-induced separation. *Shock Waves*, 25(5).
- Tobak, M. and Peake, D. (1982). Topology of three-dimensional separated flows. *Annu. Rev. Fluid Mech.*, 14:61–85.
- Touber, E. and Sandham, N. (2009). Large-eddy simulation of low-frequency unsteadiness in a turbulent shock-induced separation bubble. *Theoretical and Computational Fluid Dynamics*, 23(2):79–107.
- Touber, E. and Sandham, N. (2011). Low-order stochastic modelling of low-frequency motions in reflected shock-wave/boundary-layer interactions. *Journal of Fluid Mechanics*, 671:417–465.
- Tropea, C., Yarin, A., and Foss, J. (2007). *Springer Handbook of Experimental Fluid Mechanics*. Springer, Berlin.
- Usera, G., Vernet, A., and Ferre, J. (2004). Considerations and improvements of the analysing algorithms used for time resolved PIV of wall bounded flows. In *Proceedings of the 12th international symposium on applications of laser techniques to fluid mechanic*, Lisbon, Portugal.
- Van Driest, E. (1951). Turbulent Boundary Layer in Compressible Fluids. *J. Aeronaut. Sci.*, 18(3):145–160.

- Van Driest, E. and Blumer, C. (1962). Boundary-layer transition at supersonic speeds - three-dimensional roughness effects (spheres). *Journal of Aerospace Sciences*, 29:909–916.
- Van Oudheusden, B., Jöbbsis, A., Scarano, F., and Souverein, L. (2011). Investigation of the unsteadiness of a shock-reflection interaction with time-resolved particle image velocimetry. *Shock Waves*, 21(5):397–409.
- Walker, D. and Scott, E. (1998). Evaluation of Estimation Methods for High Unsteady Heat Fluxes from Surface Measurements. *Journal of Thermophysics and Heat Transfer*, 12(4):543–551.
- Wasserbauer, J., Shaw, R., and Neumann, H. (1975). *Design of a very-low-bleed Mach 2.5 mixed-compression inlet with 45 percent internal contraction*. NASA TM X-3135.
- Weber, A., Schreiber, H., Fuchs, R., and Steinert, W. (2002). 3-D Transonic Flow in a Compressor Cascade With Shock-Induced Corner Stall. *Journal of Turbomachinery*, 124(3):358–366.
- Wendt, B., Greber, I., and Hingst, W. (1991). *The structure and development of streamwise vortex arrays embedded in a turbulent boundary layer*. NASA Tech Memo 105211.
- Wernet, M. (2005). Symmetric phase only filtering: a new paradigm for DPIV data processing. *Measurement Science and Technology*, 16(3):601–618.
- Westerweel, J. and Scarano, F. (2005). Universal outlier detection for PIV data. *Experiments in Fluids*, 39(6):1096–1100.
- White, F. (2005). *Viscous fluid flow*. McGraw-Hill Education, New York, 3rd edition.
- Wilcox, D. (1994). *Turbulence Modeling for CFD*. DCW Industries.
- Willert, C. and Gharib, M. (1991). Experiments in Fluids Digital particle image velocimetry. *Experiments in Fluids*, 10:181–193.
- Wu, M. and Martin, M. (2007a). Analysis of shock motion in shockwave and turbulent boundary layer interaction using direct numerical simulation data. *Journal of Fluid Mechanics*, 594:71–83.
- Wu, M. and Martin, M. (2007b). Direct Numerical Simulation of Supersonic Turbulent Boundary Layer over a Compression Ramp. *AIAA Journal*, 45(4):879–889.

ACKNOWLEDGEMENTS

This thesis marks the end of a 4.5 year long journey from MSc to PhD, on which I look back with great pleasure. It has been a time during which I got to work with some of the best people in the field, during which I made some life-long friends and during which I met my soon to-be-wife Mathilde. Of course there were also times of frustration, where I felt I was stuck and where my research was not heading in the right direction. However, during those times I could always rely upon the help, support and understanding of my supervisors, friends and family. I would like to take this section to acknowledge those persons that directly or indirectly made their impact on this PhD work.

First, I would like to thank my direct supervisors during my time as a PhD student, Bas and Ferry. Thanks for giving me the freedom to set out my own research plan and for providing me with the opportunity to supervise multiple master students during the course of my PhD. Your doors were always open and you were always available to quickly discuss some new ideas or to brainstorm about new ways of handling the experimental difficulties that we encountered in the wind tunnel. Your ‘approachability’ has been very helpful throughout my time as a PhD student and has been key in getting valuable data out of my experiments.

To Fulvio, my promotor, for always being supportive of my work and for the many times you dropped by in the lab and provided me with feedback on my PIV setup and experimental results. You have a great talent for simplifying problems and for making the right connections between different physical concepts. Your excitement for PIV, aerodynamics and research in general is contagious and was really appreciated during those times that my measurements were delivering far from optimal results.

I am grateful for all the support that I got from the technical staff during the many experimental campaigns that I have carried out. Major thanks go out to Frits, Peter and Eric for the hundreds of times that you had to start the ST15 or the TST27 and for always being ready to do some last-minute tweaks and fixes to my experimental setup.

When it comes to the staff of the HSL, then the name of Colette should definitely not go unmentioned. One phone call to Colette and you know that your problem, document or thesis is in good hands. I would especially like to thank you for helping me out with the many forms and procedures surrounding the PhD defence and for taking care of the printing of my thesis.

During my PhD I had the opportunity to work together with some amazing fellow PhD-students. Some of which who have turned into life-long friends.

First of all, Kyle Lynch, you have been my American comrade, favourite PIV expert and partner-in-crime right from the start of my PhD time. As we both know, the processing aspect of my PIV data has been quite a challenge and the standard processing

algorithms available in commercial software packages did not suffice here. It was incredibly helpful to try out our new and wild processing ideas directly in your PIV processing code Fluere. If it wasn't for Fluere and your programming skills, then my PIV results wouldn't have been nearly half as good as they are right now. Our friendship was and is, however, not limited to the walls of the high-speed laboratory, but stretches across the entire globe. Backpacking across the jungle of Indonesia, roadtripping across the USA and many other city trips across Europe, we have done it all. Kyle, you are an amazing friend, both through good and bad times and I always will look back with great pleasure on our nights at de Kaasmarkt. I am sure the future holds great things for both of us and I am looking forward to meet up again in September of this year for an event even bigger than my promotion: my wedding & bachelor party!

Mister Wouter van der Velden, what a pleasure it has been to meet you about half way during the course of my PhD. I appreciate your appetite for adventure, for discovering new places, for work, for making time to hang-out with friends, for simply trying to make the most out of life. Your talents reach far beyond the computer screen and your near 1 billion cell CFD simulations, I am sure that your organizational and communicational skills will take you great places. I wouldn't be surprised to meet you once again as the CEO of Siemens (or GE maybe?). However, before that time we should definitely schedule many more holiday trips, drinks and social events.

Koen, the man, the myth, the storyteller. I am still amazed by your skill of turning a simple 10 second fact into a 5 minute romantic novel. Our many discussions on boundary layer transition have been very useful for the interpretation of my experimental results and I look forward to continue our joint transition work, also now that I have moved to Munich. Although boundary layer transition often formed the main thread in our stories, there were tons of other topics that passed the scene during the many coffees and beers that we consumed. We both had our highs/lows over the past years and it has been a pleasure to share / live through them with you.

Jan, you are the best at spicing up every conversation, either by means of your colourful pants or by dropping some opinion or idea in the group that gets everyone upset. One thing is for sure, life is never boring with Jan around.

Iliass, we met at the age of 18 as first-year aerospace students and we stayed close friends all the way throughout our studies and now having our PhD defences scheduled just two days after each other. I greatly valued our many discussions on technical / non-technical topics, either at work or during our regular gym training sessions, although, to be honest, they were a bit more regular for you than they were for me. I admire your incredible discipline not only at the gym, but mostly at work, there is very little that can distract you from the goals that you have set and I am sure you will do great things in F1.

Of course there are several other great colleagues that should not go unmentioned here. Andrea, Daniele, David, Giuseppe, Ilya, Jacopo, Liesbeth, Mehmet, Mirja, Mustafa, Paul, Thijs, Tiago, Valeria, Zhengzhong, and many more, you all played your part in making my PhD such a great time.

Also I would like to thank the excellent master students that I got to work with during my time as a PhD student: Aabhas, Felipe, Giovanni, Renee, Shruthi, Wouter and Yang. It has been a pleasure to work together with you and much of your work has directly or indirectly affected my PhD thesis. Your sharp questions often made me view problems

from a different perspective and helped me to also improve my own understanding of the topic / technique, thank you for that.

To my roommates at the Hugo de Grootstraat: Danique, Fabian, Liza, Louise, Mark, Melissa, Robbert, Tom, Wietske and Yara. Thanks for providing me with an always welcoming home and for all the dinners and great conversations we had together. After a long day at the lab it was always a pleasure to come home and share my stories with you guys.

To David, Haiyun & Maartje, Henri, Lars, Marcus & Tijana, Martijn & Paula, Michelle, Peter, Sven, Wieke and many more, thanks for your support during my time as a PhD student. You were always available for a good conversation, dinner, drinks or all of them at the same time. Your friendship is very valuable to me and I am looking forward to welcome all of you in Munich, either for visiting Biergartens, for skiing trips, sightseeing or just for meeting up again.

I would like to thank my parents for giving me the best childhood I could have wished for. A carefree, loving childhood, during which my curiosity has always been stimulated. Since a young age you have motivated me to chase my passions and interests. Also after moving out of Leidschendam I have always felt your love and support, whether it was in Delft, Göttingen, Munich, San Francisco or somewhere in the middle of Peru, you were always there for me. Also I would like to thank Nathalie, my one and only sister, for listening to my stories and for always being supportive of my work.

Last but definitely not least is Mathilde, my lovely girlfriend and soon to-be-wife. We met about 4.5 years ago on the train after just being two weeks into my PhD. During those years you have been incredibly supportive, always asking about my work and along the way gaining quite a bit of expertise yourself on boundary layer transition, shock waves and particle image velocimetry. I would have probably bored every other person with my stories, but you were always listening and you very often gave me the inspiration to try new things and to keep pushing my experiments. I am grateful for having such a beautiful, loving and caring fiancée and I am looking forward to our life in Munich.

Rogier Hendrikus Maria Giepman
München, May 2016

LIST OF PUBLICATIONS

JOURNAL ARTICLES

- Giepman, R., Srivastava, A., Schrijer, F., and Van Oudheusden, B. (2016). Mach and Reynolds number effects on the wake properties of micro-ramps, *AIAA Journal*, accepted.
- Giepman, R., Louman, R., Schrijer, F., and Van Oudheusden, B. (2016). Experimental study into the effects of forced transition on a shock-wave/boundary-layer interaction, *AIAA Journal*, 54(4).
- Giepman, R., Schrijer, F., and Van Oudheusden, B. (2015). High-resolution PIV measurements of a transitional shock wave-boundary layer interaction, *Experiments in Fluids*, 56(6).
- Giepman, R., Schrijer, F., and Van Oudheusden, B. (2015). Infrared thermography measurements on a moving boundary-layer transition front in supersonic flow, *AIAA Journal*, 53(7).
- Giepman, R., Schrijer, F., and Van Oudheusden, B. (2014). Flow control of an oblique shock wave reflection with micro-ramp vortex generators: Effects of location and size, *Physics of Fluids*, 26(6).
- Kotsonis, M., Giepman, R., Hulshoff, S., and Veldhuis, L. (2013). Numerical study of the control of Tollmien-Schlichting waves using plasma actuators, *AIAA Journal*, 51(10).
- Giepman, R., and Kotsonis, M. (2011). On the mechanical efficiency of dielectric barrier discharge plasma actuators, *Applied Physics Letters*, 98(22).

CONFERENCE PROCEEDINGS

- Van Veen, W., Giepman, R., Schrijer, F., and Van Oudheusden, B. (2015). RANS modeling of shock wave-boundary layer interactions, In *3rd ECCOMAS Young Investigators Conference*, Aachen, Germany.
- Giepman, R., Louman, R., Schrijer, F., and Van Oudheusden, B. (2015). Experimental investigation of boundary layer tripping devices for shock wave-boundary layer control, In *45th AIAA Fluid Dynamics Conference*, Dallas, Texas. AIAA 2015-2780.
- Giepman, R., Srivastava, A., Schrijer, F., and Van Oudheusden, B. (2015). The effects of Mach and Reynolds number on the flow mixing properties of micro-ramp vortex generators in a supersonic boundary layer, In *45th AIAA Fluid Dynamics Conference*, Dallas, Texas. AIAA 2015-2779.

- Szubert, D., Van Veen, W., Grossi, F., Hoarau, Y., Braza, M., Giepman, R., Srivastava, A., Schrijer, F., and Van Oudheusden, B. (2014). Physics and modelling of the transonic and supersonic shock wave boundary layer interaction of oblique and normal shock at high Reynolds number, In *10th International ERCOFTAC Symposium on Engineering Turbulence Modelling and Measurements*, Marbella, Spain.
- Giepman, R., Lynch, K., Schrijer, F., and Van Oudheusden, B. (2014). Investigation of a transitional oblique shock wave reflection using PIV, In *17th International Symposium on Application of Laser Techniques to Fluid Mechanics*, Lisbon, Portugal.
- Giepman, R., Schrijer, F., and Van Oudheusden, B. (2014). Tracking a moving boundary layer transition front in supersonic flow using infrared thermography, In *Quantitative InfraRed Thermography*, Bordeaux, France.
- Giepman, R., Schrijer, F., and Van Oudheusden, B. (2014). High-resolution PIV measurements of a transitional shock wave-boundary layer interaction, In *44th AIAA Fluid Dynamics Conference*, Atlanta, Georgia. AIAA 2014-3333.
- Giepman, R., Schrijer, F., and Van Oudheusden, B. (2013). Flow control of an oblique shock wave reflection with micro-ramp vortex generators: Effects of location and size, In *European Conference for Aeronautics and Space Sciences (EUCASS)*, Munich, Germany.
- Giepman, R., De Giovanni, G., Schrijer, F., and Van Oudheusden, B. (2012). Experimental investigation into the effects of micro-ramps on the separation bubble of shock wave / boundary layer interactions, In *20th International Shock Interaction Symposium*, Stockholm, Sweden.
- Kotsonis, M., Veldhuis, L. and Giepman, R. (2011). Numerical study on control of Tollmien-Schlichting waves using plasma actuators, In *29th AIAA Applied Aerodynamics Conference*, Honolulu, Hawaii. AIAA 2011-3175.
- Kotsonis, M., Ghaemi, S., Giepman, R., and Veldhuis, L. (2010). Experimental study on the body force field of dielectric barrier discharge actuators, In *41st Plasmadynamics and Lasers Conference*, Chicago, Illinois. AIAA 2010-4630.
- Nitzsche J., and Giepman, R. (2010), Numerical experiments on aerodynamic resonance in transonic airfoil flow. In *17th STAB/DGLR Symposium*, Berlin, Germany.

BOOK CHAPTERS

- Nitzsche, J., and Giepman, R. (2013). Numerical Experiments on Aerodynamic Resonance in Transonic Airfoil Flow, In *New results in numerical and experimental fluid mechanics VIII*. By Dillman, A., Heller, G., Kreplin, H., Nitsche, W., and Peltzer, I. Springer, Berlin. ISBN: 978-3-642-35680-3.

MAGAZINES

- Giepman, R., Schrijer, F., and Van Oudheusden, B. (2014). Shock wave-boundary layer interactions - Flow control by micro-ramp vortex generators, *Leonardo Times*, June edition.

BIOGRAPHICAL NOTE

Rogier Giepmans was born on the 27th of December 1986 in Den Haag, the Netherlands. Since a young age he showed great interest for engineering, mathematics and physics, which translated itself into thousands of hours spent on designing, building and improving Lego models, many visits to automotive & aerospace musea and reading dozens of books on rocket design and space travel.

It therefore came as no surprise that Rogier decided to study Aerospace Engineering at the Technical University of Delft in the Netherlands. He graduated with honors for both his Bachelor and Master degree and was awarded the P-prize for the student that obtains his propaedeutic exam with the highest average grade of his year. His MSc thesis on 'Transition Delay with Plasma Actuators - PIV Diagnostics, Reduced Order Modeling and Adaptive Control' received the NVvL & KIVI NIRIA graduation award for the best aerospace-related MSc thesis in the Netherlands of the year 2011.

In December 2011 he started his PhD on the topic of 'Flow Control for Oblique Shock Wave Reflections' in the Aerodynamics department of the TU Delft under the supervision of Bas van Oudheusden and Ferry Schrijer. During his PhD he gained a deep understanding of high-speed compressible flows and mastered a wide range of experimental techniques. Up to date he has published 7 journal articles and has presented his work at numerous conferences across the globe.

Currently he is working at the turbomachinery department of General Electric Global Research in Munich, where he is involved in multiple applied research projects, ranging from cost-effective water pump applications to film-cooled supersonic turbine cascade experiments.